

# In-vivo investigation of electrochemical behavior of Ti and CoCrMo alloy in human synovial fluids

Présentée le 1er février 2023

Faculté des sciences et techniques de l'ingénieur  
Groupe SCI STI SM  
Programme doctoral en science et génie des matériaux

pour l'obtention du grade de Docteur ès Sciences

par

**Yueyue BAO**

Acceptée sur proposition du jury

Prof. A. Mortensen, président du jury  
Dr S. Mischler, directeur de thèse  
Dr P. Schmutz, rapporteur  
Dr C. Rieker, rapporteur  
Dr C. Roussel, rapporteur

# Acknowledgements

First of all, I would like to express my deep gratitude to my thesis supervisor Dr. Stefano Mischler for giving me the opportunity to conduct my PhD thesis in his group. Throughout these years, I am extremely grateful for his professional guidance, trust, patience, and encouragement. He always encourages and trusts on me when I face difficulties and setbacks on the project, even when I do not trust myself. His professional guidance inspires me to think outside the box and he is my father of science who leads me into the corrosion field. He also impressed me with his respect for students and humor both in research and daily life. Without his strong support, I could not accomplish my thesis.

I would like to acknowledge the jury members of my defense: Prof. Andreas Mortensen, Dr. Christophe Roussel, Dr. Claude Rieker, Dr. Patrik Schmutz for their careful review, precious time and insightful comments, which are very helpful in improving the quality of the thesis.

Many thanks to the Swiss National Science Foundation for the founding of MESYNIC project, and China Scholarship Council for the financial support for my PhD study.

I wish to thank the secretary of our group, Ms. Sylvie Vaucher, and the administrative staff of Material science doctoral school, Ms. Anne Kolly and Ms. Chrystelle Demierre, for their help with the administrative problems, which make my studies at EPFL much easier.

I also want to thank Dr. Brigitte M. Jolles for the help with experiments in the hospital. Thank Dr. Jonathan Paz Montoya for the help of sample preservation and the nice talks.

Many thanks to Pierre Mettraux for the XPS analysis and the help on technical issues. It was a pleasure working with him and he will be deeply missed. Rest in peace.

My specially thank goes to Dr. Anna Igual Muñoz and Dr. Alex Roda Buch. Anna is the most energetic and optimistic person I have ever met. She helped me a lot with the understanding and the progress of the project. She always cheered me up when I was down and her enthusiasm in science and life deeply affected me. Alex is gentle and always ready for help. They are such a sweet couple with adorable kids Lara and Pau. I greatly appreciate your kind support during my PhD studies.

My heartfelt thank to my colleagues and friends in the lab for generous help, insightful discussion and joyful chatting, specifically Shoufan for introducing me to the lab and life in Switzerland at the first two months. Leili for her kind help in daily life. She is so sweet and warmhearted by always ready for help. I am grateful for her kindness in comforting me in the group when I was too shy to socialize with people. Valentine for the delicious birthday cakes



and desserts. Vance for the kind help on my project and encouragement when I was frustrated with the results. Oksana for discussing the good or bad results and sharing life with each other. Park for Korean culture and delicious foods. Claes for teaching EQCM techniques. Marija, the most hard-working girl, for the lunches and beers. Calixe for her kind help on my thesis writing and her optimistic personality. She is always positive and brings much energy to me, especially at the end of my thesis. Marian for her generous spirit and the wonderful Bachelor party. Pranav for his black humor, which brings lots of joy and laughs. Ayush for his kind help on my thesis writing and the wonderful games. Alba for the lunches and coffees. Enrico for introducing Italian foods. Yakob for introducing various sports. Beñat for already ready for help. Pierre and Arthur for the excellent semester project they did.

I learned a lot from your guys on how to balance work and life and on how to enjoy my life. Thank you all for the beautiful hiking, beers, parties, games, etc. With all your company and support, my life in Switzerland and in the group is much more colorful and meaningful.

I also want to thank my Chinese friends Yiru, Huaiyu, Fangshu, Jinhui, Qiao, Xiang, Chaoqi for the fantastic hiking and meals.

My big thanks go to my family, parents, sisters, and cute niece and nephews. They are always there to support me without any conditions.

My last but not least thanks to my fiancé Yi, to whom I cannot even express my gratitude with words. He is always there supporting me, encouraging me and believing in me. He is patient, trustworthy, and accepts all my negative emotions and flaws. With him, I can be simply myself. Thank you for always being here!

# Abstract

With the development of modern medical techniques, the application of orthopedic implants has been continually increasing in recent years. Passive materials, such as Ti and its alloys as well as CoCrMo alloys, are widely used in artificial joints due to their excellent mechanical properties, corrosion resistance and biocompatibility. Despite their excellent performance, the release of harmful metal ions, due to tribocorrosion and corrosion of artificial joints operating in human synovial fluids, remains a critical issue. Although numerous research on the electrochemical behavior of metal in simulated body fluids has been published, only few studies were conducted directly in real human body fluids. Interestingly, the only systematic in-vivo corrosion investigation has shown that the electrochemical response of a CoCrMo alloy in human synovial fluids significantly differs from that observed in simulated body fluids. To understand the corrosion of metals in the human body, a study on the electrochemical behavior of metal directly in human synovial fluids is therefore needed. Thus, this thesis aims to determine the electrochemical behavior of pure Ti and CoCrMo alloy in human synovial fluids and understand the corresponding mechanisms for a series of patients undergoing primary total knee/hip arthroplasty (TKA/THA), puncture of patients with TKA and TKA/THA revision surgery.

To achieve this goal, a systematic experimental protocol was designed and validated to perform the electrochemical tests on a cohort of 154 patients. A wide palette of electrochemical techniques was used, including open circuit potential (OCP), potentiodynamic methods, electrochemical impedance spectroscopy (EIS) and electrochemical quartz crystal microbalance (EQCM). After the electrochemical testing, selected surfaces were analyzed using Fourier Transform Infrared Spectroscopy (FTIR), Scanning Electron Microscopy (SEM), Energy Dispersive X-Ray Spectrometry (EDS) and Auger Electron Spectroscopy (AES). The same tests were conducted in a series of simulated body fluids to contribute to an understanding of the in-vivo results.

The electrochemical results show that the electrochemical behavior of Ti and CoCrMo in human synovial fluids varies between patients, especially for Ti. The corrosion rates of Ti vary up to two orders of magnitude, while the variability for CoCrMo alloy lies within one order of magnitude. The obtained corrosion rates of both materials correspond well with the metal ion release rates clinically detected in patients with hip and knee implants. For both materials, the corrosion behavior is likely controlled by the combined action of dissolved oxygen and the adsorption of organic molecules. The electrochemical behavior of Ti surface exposed to synovial fluids is significantly affected by surface roughness. No significant risk

of galvanic corrosion between Ti and CoCrMo alloy in human synovial fluids is anticipated by the present results.

**Keywords:**

Electrochemistry; Ti; CoCrMo Alloy; Human Synovial Fluids, Corrosion

## Résumé

Avec le développement des techniques médicales modernes, la pose d'implants orthopédiques n'a cessé d'augmenter ces dernières années. Les matériaux passifs, tels que le Ti et ses alliages ainsi que les alliages CoCrMo, sont largement utilisés dans les articulations artificielles en raison de leurs excellentes propriétés mécaniques, de leur résistance à la corrosion et de leur biocompatibilité. Malgré leurs performances exceptionnelles, la libération d'ions métalliques nocifs, en raison de la tribocorrosion et de la corrosion des articulations artificielles opérant au sein de fluides synoviaux humains, reste un problème critique. Bien que de nombreuses recherches sur le comportement électrochimique du métal dans des fluides corporels simulés aient été menées, une petite part seulement ont été réalisées directement dans les fluides synoviaux humains. Par ailleurs, la seule étude systématique de la corrosion *in-vivo* a montré que la réponse électrochimique d'un alliage CoCrMo dans des fluides synoviaux humains diffère significativement de ce qui est observé dans les fluides simulés. Pour comprendre la corrosion des métaux dans le corps humain, une étude sur le comportement électrochimique du métal directement dans les liquides synoviaux humains est nécessaire. Ainsi, cette thèse vise à déterminer le comportement électrochimique du Ti pur et de l'alliage CoCrMo dans les liquides synoviaux humains et à comprendre les mécanismes correspondants pour une série de patients dans différents états cliniques : lors d'une première arthroplastie totale du genou ou de la hanche (TKA/THA), de la ponction de patients ayant déjà subi une TKA ainsi que lors d'opérations de révisions de TKA/THA.

Pour y parvenir, un protocole expérimental systématique a été conçu et validé pour réaliser les tests électrochimiques sur un groupe de 154 patients. Une large palette de techniques électrochimiques a été utilisée, y compris le potentiel de circuit ouvert (OCP), les méthodes potentiodynamiques, la spectroscopie d'impédance électrochimique (EIS) et la microbalance électrochimique à cristal de quartz (EQCM). Après les tests électrochimiques, des surfaces sélectionnées ont été analysées par spectroscopie infrarouge à transformée de Fourier (FTIR), microscopie électronique à balayage (SEM), spectrométrie des rayons X à dispersion d'énergie (EDS) et spectroscopie électronique Auger (AES). Les mêmes tests ont été menés dans une série de fluides corporels simulés pour contribuer à la compréhension des résultats *in-vivo*.

Les résultats électrochimiques montrent que le comportement à la corrosion du Ti et du CoCrMo dans les fluides synoviaux humains varie significativement selon les patients, particulièrement pour le Ti. Les vitesses de corrosion du Ti varient jusqu'à deux ordres de grandeur, tandis que la variabilité de l'alliage CoCrMo est d'environ un ordre de grandeur. Les taux de corrosion obtenus pour les deux matériaux correspondent bien aux taux de libération

d'ions métalliques détectés cliniquement chez les patients porteurs d'implants de hanche et de genou. Pour les deux matériaux, le comportement à la corrosion est vraisemblablement contrôlé par l'action combinée de l'oxygène dissous et de l'adsorption de molécules organiques. Le comportement électrochimique de la surface de Ti exposée aux fluides synoviaux est significativement affecté par la rugosité de la surface. Aucun risque significatif de corrosion galvanique entre l'alliage Ti et CoCrMo dans les fluides synoviaux humains n'est anticipé par les présents résultats.

**Mots-clés:**

Électrochimie; Ti; Alliage CoCrMo; Liquides synoviaux humains, Corrosion

# Contents

<b>Acknowledgements .....</b>	<b>i</b>
<b>Abstract.....</b>	<b>iii</b>
<b>Résumé.....</b>	<b>v</b>
<b>Contents .....</b>	<b>vii</b>
<b>List of Figures.....</b>	<b>x</b>
<b>List of Tables .....</b>	<b>xv</b>
<b>List of Acronyms &amp; Symbols .....</b>	<b>xvii</b>
<b>Chapter 1      Introduction .....</b>	<b>1</b>
1.1    Motivation.....	1
1.2    Challenges.....	1
1.3    Thesis Structure .....	2
<b>Chapter 2      State of the art.....</b>	<b>4</b>
2.1    Metallic Implants .....	4
2.2    Degradation of metallic Implants.....	6
2.2.1 Retrieved Implants Analysis.....	7
2.2.2 Metallic Ions Release in the Human Body .....	7
2.3    Human Synovial Fluids.....	8
2.4    Interfacial Reactions of Metallic Implants in Simulated Human Fluids.....	10
2.4.1 Reactions between Metals and Water/Dissolved Oxygen.....	10
2.4.2 Reactions between Metals and Ions .....	12
2.4.3 Reactions between Metals and Organic Molecules.....	14
2.4.4 Reactions between Metals and Reactive Oxygen Species.....	18
2.4.5 Reactions between Metals and Cells .....	19
2.5    Comparison Between In-Vivo and In-Vitro Results.....	20
2.6    Statement of the Problem.....	22
2.7    Objectives of the Thesis.....	22
<b>Chapter 3      Experimental Setup and Protocol .....</b>	<b>24</b>
3.1    Characterization of Human Synovial Fluids.....	25
3.2    Design of the Multi-electrode Electrochemical Cell.....	26
3.3    Sample Preparation .....	27
3.4    In-vivo Electrochemical Measurements.....	28
3.4.1 OCP and Potentiodynamic Polarization .....	28
3.4.2 EIS .....	29
3.4.3 EQCM.....	30
3.5    Ex-situ Surface Characterization .....	32
3.5.1 FTIR .....	33
3.5.2 SEM/EDS .....	33
3.5.3 AES.....	34
<b>Chapter 4      Characterization of Synovial Fluids .....</b>	<b>35</b>
4.1    Color of Human Synovial Fluids .....	35

4.2	Volume and pH of Human Synovial Fluids.....	37
4.3	Homogeneity of Human Synovial Fluids .....	39
4.4	Correlation between Color and Consistency of Synovial Fluids .....	40
4.5	Summary .....	41
<b>Chapter 5</b>	<b>Electrochemical Behaviour of Ti and CoCrMo Alloy in Human Synovial Fluids .....</b>	<b>42</b>
5.1	Electrochemical Results of Ti and CoCrMo Alloy in Human Synovial Fluids.....	42
5.1.1	OCP of Ti and CoCrMo Alloy .....	42
5.1.2	Rp of Ti and CoCrMo Alloy .....	44
5.1.3	Rs of Synovial Fluids .....	46
5.1.4	Potentiodynamic Polarization Curve of Ti and CoCrMo alloy .....	47
5.1.5	EIS Measurements on Ti and CoCrMo Alloy .....	56
5.2	Discussion .....	62
5.2.1	Electrochemical Reactions of Ti and CoCrMo Alloy in Synovial Fluids ...	62
5.2.2	Comparison with Measurements in Simulated Fluids .....	66
5.3	Summary .....	73
<b>Chapter 6</b>	<b>Ex-situ Surface Analysis of Ti and CoCrMo alloy in Human Synovial Fluids 74</b>	
6.1	Ex-situ Surface Analysis of Ti .....	74
6.1.1	FTIR .....	74
6.1.2	SEM/EDS .....	79
6.1.3	AES.....	82
6.2	Ex-situ Surface Analysis of CoCrMo Alloy .....	85
6.2.1	FTIR .....	85
6.2.2	SEM/EDS .....	88
6.3	Discussion .....	90
6.3.1	Organic adsorption/deposition.....	90
6.3.2	Particles containing calcium.....	91
6.3.3	Correlation between surface analysis and in-vivo electrochemical results ..	92
6.4	Summary .....	94
<b>Chapter 7</b>	<b>Influence of Surface Roughness on the Electrochemical Behavior of Ti in Human Synovial Fluids .....</b>	<b>95</b>
7.1	Sample Preparation .....	95
7.2	Electrochemical Results .....	96
7.2.1	OCP of Ti and Ti-1200 samples .....	96
7.2.2	Potentiodynamic Polarization Curve of Ti samples .....	97
7.2.3	EIS Measurements on Ti-1200 .....	101
7.3	Discussion .....	103
7.4	Summary .....	106
<b>Chapter 8</b>	<b>Discussion .....</b>	<b>107</b>
8.1	Improvement of the Experimental Protocol.....	107
8.2	Corrosion Mechanisms .....	108
8.3	Galvanic Corrosion Between Ti and CoCrMo Alloy in Human Synovial Fluids	110
<b>Chapter 9</b>	<b>Conclusions .....</b>	<b>115</b>

<b>Appendix A EQCM Study of Ti in Human Synovial Fluids.....</b>	<b>116</b>
A.1. Theory.....	116
A.2. Experimental.....	117
A.2.1. Quartz Crystal Characterization.....	117
A.2.2. Calibration of the Sauerbrey Constant.....	118
A.2.3. Calibration of the Viscous Loading.....	119
A.3. Results.....	120
A.3.1. OCP of Ti Crystal.....	120
A.3.2. Potentiodynamic Polarization Curves of Ti Crystal.....	122
A.4. Discussion.....	122
A.5. Summary.....	123
<b>Appendix B Validation of the Multi-electrode Electrochemical Cell.....</b>	<b>124</b>
<b>Appendix C Electrochemical Behavior of Ti and CoCrMo Alloy in Simulated Fluids .</b>	<b>127</b>
C.1. Electrochemical Behavior of Ti in Simulated Solutions.....	128
C.2. Electrochemical Behavior of Ti-1200 in Simulated Solutions.....	136
C.3. EQCM Measurements of Ti.....	140
C.4. Influence of the Scan Rate on the $R_p$ Measurements.....	142
C.5. Electrochemical Behavior of CoCrMo Alloy in Simulated Solutions.....	143
<b>Appendix D Fourier Transform Infrared Spectroscopy of BSA and HA .....</b>	<b>150</b>
<b>References.....</b>	<b>151</b>
<b>Curriculum Vitae .....</b>	<b>165</b>



# List of Figures

Figure 2.1 Normal and rheumatoid arthritis joint [9] .....	4
Figure 2.2 (a) hip replacements and (b) materials couplings for the cup on head in implants (adapted from [10]).....	5
Figure 2.3 Interfacial reactions of metal immersed in bioenvironment [40] .....	10
Figure 2.4 Typical equilibrium potential ranges of Ti, Co, Cr and Mo in H <sub>2</sub> O at 25 °C and pH 7.4 (physiological conditions) extracted from Pourbaix diagrams in different domains: immunity (i), active dissolution (a), passivity (p) and transpassivity (t) [43] .....	11
Figure 2.5 Interaction mechanisms between phosphate ions and the metallic surface under different pH (P: positive charge; I: isoelectric point; N: negative charge).....	13
Figure 2.6 3D structures of HAS and BSA with tryptophan residues [76].....	15
Figure 2.7 Polarization curves of Ti6Al4V (a) and CoCrMo alloy (b) in PBS solution at different concentrations of BSA with a scan rate of 0.167 mV/s at 37°C [81] .....	16
Figure 2.8 Interfacial reactions between protein and metallic surface with different applied potential, adapted from [89] .....	17
Figure 2.9 Chemical structure of HA.....	18
Figure 2.10 Cathodic and anodic polarization curves of Ti6Al4V in 0.5M NaCl solution at various amount of H <sub>2</sub> O <sub>2</sub> [103] .....	19
Figure 2.11 Scheme of the time response after implantation of a metallic implant [112, 113] .....	19
Figure 2.12 The (a) cathodic and (b) anodic polarization curves of CoCrMo alloy in synovial fluids from different patients [5] .....	20
Figure 2.13 The polarization curves of CoCrMo alloy in synovial fluid from patient 13 and in BCS (30 g/L) at a pH of 7.6 [5].....	21
Figure 2.14 Schematic view of the surface composition on retrieved prosthesis [117].....	22
Figure 3.1 Scheme for the research programs (*EQCM measurements were conducted in EQCM cell on a rough crystal).....	25
Figure 3.2 (a) Schematic diagram of the multi-electrode cell. A: working electrode, B: counter electrode, C: reference electrode, D: air evacuation hole, E: sealing O-ring, F: tested synovial fluid, G: vessel, H: injection hole, I: vessel cover. (b) The picture of the cell.....	27
Figure 3.3 SEM images of microstructure for Ti (left) and CoCrMo alloy (right) .....	28
Figure 3.4 Experimental sequence 1 .....	29
Figure 3.5 Experimental sequence 2 .....	30
Figure 3.6 Experimental sequence 3 .....	30

Figure 4.1 Pictures of human synovial fluids inside the syringe (PS, TKA: P17 and P100, R: P6, P32, P68, P88, P104, P108 and P109) .....	36
Figure 4.2 The color of synovial fluids obtained through CIELAB color space.....	37
Figure 4.3 OCP measurement of Pt electrodes in synovial fluid from P2.....	39
Figure 4.4 Standard deviation of OCP results of Pt rods immersed in different synovial fluids from PS, TKA (P17 and P100) and R (P6, P104 and P108) group.....	40
Figure 4.5 Correlation between the color and consistency of synovial fluids (liquid-like fluids are labeled in red) .....	41
Figure 5.1 OCP measurement of Ti and CoCrMo samples for P23, and OCP evolution of Ti with time for P2, P3, and P4.....	43
Figure 5.2 Stabilized OCP results of Ti after 20 minutes' immersion in different synovial fluids from PS, TKA (P17 and P100), and R (P6, P32, P68 and P88) group.....	43
Figure 5.3 Stabilized OCP results of CoCrMo after 20 minutes' immersion in different synovial fluids from PS, TKA (P100) and R (P32 and P88) groups.....	44
Figure 5.4 Rp measurement of Ti for P6 .....	45
Figure 5.5 Comparison of Rp value of Ti in all synovial fluids from PS, TKA (P17 and P100), and R (P6, P32, P68 and P88) group .....	45
Figure 5.6 Comparison of Rp values of CoCrMo alloy in tested synovial fluids from PS, TKA (P100) and R (P32 and P88) groups .....	46
Figure 5.7 Bode plot of Ti in synovial fluid from P3 .....	47
Figure 5.8 Rs of synovial fluids from different patients from PS, TKA (P17 and P100), and R (P6, P32, P68 and P88) group .....	47
Figure 5.9 Cathodic polarization curves (logarithmic scale of the absolute current density) of Ti tested in synovial fluids from PS, TKA and R group .....	49
Figure 5.10 Anodic polarization curves (logarithmic scale of the absolute current density) of Ti tested in synovial fluids from PS, TKA and R group .....	50
Figure 5.11 Cathodic polarization curves (logarithmic scale of the absolute current density) of CoCrMo tested in synovial fluids from from PS, TKA (P100) and R (P32 and P88) groups .....	54
Figure 5.12 Anodic polarization curves (logarithmic scale of the absolute current de density) of CoCrMo tested in synovial fluids from from PS, TKA (P100) and R (P32 and P88) groups .....	55
Figure 5.13 Stabilized OCP results of Ti after immersion in different synovial fluids from PS, TKA (P100), and R (P108 and P109) group .....	57
Figure 5.14 Nyquist and Bode plot of Ti in tested synovial fluids.....	59
Figure 5.15 Nyquist and Bode plots of CoCrMo alloy in different synovial fluids .....	61
Figure 5.16 Metal ion release rates obtained from this work and from literature [28].....	65
Figure 5.17 Polarization curves of Ti tested in synovial fluids and simulated solutions.....	67
Figure 5.18 Nyquist and Bode plots of Ti in synovial fluids and simulated solutions.....	68

Figure 5.19 Cathodic and anodic polarization curves of CoCrMo alloy tested in synovial fluids and simulated fluids.....	70
Figure 5.20 Nyquist and Bode plots of CoCrMo alloy for P95, P99 and simulated solutions	71
Figure 5.21 Rp measurements of Ti tested in simulated fluids and in synovial fluids with different scan rates.....	72
Figure 6.1 Representative absorption spectra on the Ti surface immersed in human synovia	75
Figure 6.2 FTIR spectra of samples for patients with the presence of amide groups together with that of BSA and HA (left), and C=O as well as C-H group present in in-vivo samples and HA (right).....	77
Figure 6.3 Representative SEM images of the Ti sample surface in low and high magnification for patients and simulated fluids .....	80
Figure 6.4 Representative SEM images of Ti sample surface after immersing in simulated fluids with different BSA concentrations .....	81
Figure 6.5 SEM images of the calcium particles for Ti exposure to synovial fluids from P3 and P16 .....	82
Figure 6.6 Atomic concentration of the particles observed on the Ti surface after being immersed in the synovia from several patients .....	82
Figure 6.7 Auger sputter depth profiles from the reference sample before exposure and after contact with the synovial fluid from P4 and P5. (Sputter rate: 0.6 nm/min).....	84
Figure 6.8 Passive film thickness of the reference Ti sample and the samples after contact with the synovial fluid from some patients .....	85
Figure 6.9 Representative absorption spectra on the CoCrMo surface immersed in the human synovial fluids from patients .....	86
Figure 6.10 FTIR spectra of CoCrMo samples for patients with the presence of amide groups together with that of BSA and HA, and C=O as well as C-H group present in in-vivo samples and HA.....	88
Figure 6.11 Representative SEM images of the CoCrMo sample surface in low and high magnification for patients and simulated fluids .....	89
Figure 6.12 SEM image of the calcium particles on CoCrMo surface for P21 and P22 .....	89
Figure 6.13 Atomic concentration of the particles observed on the CoCrMo surface after being immersed in the synovia from several patients.....	90
Figure 6.14 Correlation between organic adsorption/deposition and OCP as well as Rp of Ti in tested synovial fluids .....	93
Figure 6.15 Correlation between Rp and OCP of Ti in tested synovial fluids and simulated solutions.....	93
Figure 7.1 SEM and 3D images of polished smooth and rough Ti surface .....	96
Figure 7.2 Stabilized OCP of Ti and Ti-1200 samples immersed in different synovial fluids from PS, and R (P108 and P109) groups.....	97

Figure 7.3 Cathodic polarization curves (logarithmic scale of the absolute current density) of Ti and Ti-1200 samples in tested synovial fluids from PS, and R (P108 and P109) groups .....	98
Figure 7.4 Anodic polarization curves (logarithmic scale of the absolute current density) of Ti and Ti-1200 samples in tested synovial fluids from PS, and R (P108 and P109) groups .....	100
Figure 7.5 Nyquist and Bode plots of Ti-1200 in tested synovial fluids .....	102
Figure 7.6 Anodic scan of the polarization curves of Ti and Ti-1200 in simulated solutions .....	104
Figure 7.7 Auger depth profiles from the smooth and rough surfaces before exposure to solutions.....	105
Figure 8.1 Oxygen reduction rate as a function of concentration of protein and dissolved oxygen (arbitrary units) .....	109
Figure 8.2 OCP of Ti and CoCrMo alloy immersed in human synovial fluids from PS, TKA (P100) and R (P32 and P88) groups .....	111
Figure 8.3 $R_p$ of Ti and CoCrMo alloy tested in different synovial fluids PS, TKA (P100) and R (P32 and P88) groups.....	112
Figure 8.4 Electrical equivalent circuit of corrosion cell [113] .....	112
Figure 8.5 Galvanic corrosion rate of Ti/CoCr coupling in human synovial fluids PS, TKA (P100) and R (P32 and P88) groups .....	113
Figure 8.6 OCP, $R_p$ and polarization curves of Ti and CoCrMo alloy in simulated solutions .....	113
Figure 8.7 Galvanic corrosion rate of Ti/CoCr coupling in simulated body fluids .....	114
Figure A. 1 Schematic diagram of the crystal used in the EQCM measurements.....	118
Figure A. 2 SEM image and 3D profile of the Ti crystal surface.....	118
Figure A. 3 EQCM cell.....	118
Figure A. 4 Frequency variation of the quartz crystal by the copper plating at 37°C .....	119
Figure A. 5 Variation of frequency of quartz crystal as a function of dissipation in water/glycerol solutions with different concentrations of glycerol.....	120
Figure A. 6 OCP evolution with time for P129, P134 and P154, together with the mass changes on the Ti surfaces.....	121
Figure A. 7 Polarization curves and mass changes of Ti crystals tested in synovial fluids from P129 and P134 .....	122
Figure B. 1 The picture of the typical large cell .....	124
Figure B. 2 The polarization curves of Ti in NaCl solution tested in both cells .....	125
Figure B. 3 The polarization curves of two Ti samples in NaCl solution in the small cell ...	126

Figure C. 1 Stabilized OCP results of Ti in different simulated solutions .....	128
Figure C. 2 Comparison of $R_p$ value in different simulated solutions .....	128
Figure C. 3 Cathodic and anodic polarization curves (logarithmic scale of the absolute current density) of Ti in simulated solutions .....	131
Figure C. 4 Nyquist and Bode plot of Ti in simulated solutions .....	134
Figure C. 5 Cathodic and anodic polarization curves (logarithmic scale of the absolute current density) of Ti-1200 in simulated solutions .....	136
Figure C. 6 Nyquist and Bode plot of Ti-1200 in simulated solutions .....	139
Figure C. 7 OCP variation of Ti for NaCl and NaCl + BSA (30g/L) solutions, together with the mass changes on the surfaces .....	140
Figure C. 8 Polarization curves and mass changes of Ti crystals tested in NaCl and NaCl + BSA (30g/L) solutions .....	141
Figure C. 9 $R_p$ measurements of Ti in NaCl solution with different scan rates .....	142
Figure C. 10 Stabilized OCP results of CoCrMo alloy in different simulated solutions .....	143
Figure C. 11 Comparison of $R_p$ value of CoCrMo in simulated solutions .....	143
Figure C. 12 Cathodic and anodic polarization curves (logarithmic scale of the absolute current density) of CoCrMo alloy in simulated solutions .....	146
Figure C. 13 Nyquist and Bode plot of CoCrMo alloy in simulated solutions .....	148
 Figure D. 1 Absorption spectra of BSA and HA (str: stretching vibration, ben: bending vibration) .....	 150

# List of Tables

Table 2.1 Properties and application of three major metallic materials in joint replacements [8, 11, 13].....	6
Table 2.2 The concentration of metallic ions in human fluids released from Ti alloy and CoCrMo alloy hip and knee implants (adapted from [28]) .....	8
Table 2.3 The main chemical composition of normal synovial fluids.....	9
Table 2.4 Classification of properties based on laboratory examination [29] .....	9
Table 2.5 Factors influencing protein adsorption onto the metal surface.....	14
Table 3.1 Electrochemical measurements conducted for each patient .....	31
Table 4.1 Properties of human synovial fluid.....	37
Table 5.1 Electrochemical parameters extracted from the anodic polarization curves of Ti samples .....	51
Table 5.2 Electrochemical parameters obtained from the anodic polarization curves of CoCrMo alloys .....	56
Table 5.3 Electrochemical parameters extracted from EIS measurement of Ti samples .....	60
Table 5.4 Electrochemical parameters extracted from EIS measurements of CoCrMo alloy .....	62
Table 6.1 Interpretation of spectral position in terms of absorption peaks.....	76
Table 6.2 The sum peak intensity of representative functional groups detected on the sample surface.....	78
Table 6.3 The spectral interpretation of in-vivo CoCrMo samples .....	87
Table 7.1 Electrochemical parameters extracted from anodic polarization curves for Ti and Ti-1200 samples in different synovial fluids.....	100
Table 7.2 Electrochemical parameters extracted from EIS measurements of Ti-1200 .....	103
Table B. 1 Electrochemical parameters extracted from polarization curves .....	126
Table C. 1 Composition of NaCl based simulated solutions .....	127
Table C. 2 Composition of PBS based simulated solutions.....	127
Table C. 3 Electrochemical parameters extracted from the anodic polarization curves of Ti samples .....	132
Table C. 4 Electrochemical parameters extracted from EIS measurements of Ti.....	135
Table C. 5 Electrochemical parameters extracted from anodic polarization curves of Ti-1200 samples .....	137
Table C. 6 Electrochemical parameters extracted from EIS measurements of Ti-1200.....	139
Table C. 7 Electrochemical parameters extracted from anodic polarization curves of CoCrMo samples .....	146

Table C. 8 Electrochemical parameters extracted from EIS measurement of CoCrMo sample .....	149
---	-----

## List of Acronyms & Symbols

EIS	Electrochemical Impedance Spectroscopy
EQCM	Electrochemical Quartz Crystal Microbalance
FTIR	Fourier Transform Infrared Spectroscopy
SEM	Scanning Electron Microscopy
EDS	Energy Dispersive X-Ray Spectrometry
AES	Auger Electron Spectroscopy
PS	Primary surgery
TKA	Total knee arthroplasty
R	Revisions
RE	Reference electrode
WE	Working electrode
CE	Counter electrode
OCP	Open circuit potential
BSA	Bovine serum albumin
HA	Hyaluronic acid
ROS	Reactive oxygen species
STDEV	Standard deviation
R <sub>p</sub>	Polarization resistance
R <sub>s</sub>	Solution resistance
$\Delta m$	Mass change (g/cm <sup>2</sup> /Hz)
$\Delta f_m$	Mass loading (Hz)
$\Delta f_v$	Viscous loading (Hz)
$\theta$	Coverage of adsorbed protein on the surface
B <sub>ADS</sub>	Affinity of the protein molecules toward the surface (cm <sup>3</sup> /mol)
C	Concentration of protein in the bulk solution (mol/L)
$i_{O_2}$	Cathodic current density (A/cm <sup>2</sup> )
n	Charge number
K	Constant
F	Faraday constant (C/mol)
C <sub>O<sub>2</sub></sub>	Concentration of dissolved oxygen in the human synovial fluids (mol/L)
E	Applied potential (V)
$\beta_c$	Tafel coefficient (V)



# Chapter 1 Introduction

## 1.1 Motivation

Along with the rapid modern medical development, the application of biomedical devices has been continuously increasing in recent years. By 2030, the number of knee joint arthroplasty in the USA is estimated to be about 3,000,000 [1]. Metallic implant materials, mainly Ti and its alloys, CoCrMo alloy and stainless steel, are widely used in bone and articular surface replacement due to their excellent mechanical properties, corrosion resistance and biocompatibility. Despite their excellent performance, corrosion of the metallic implants in human liquids remains a critical issue that leads to harmful metal ions released into blood, urine and kidneys [2–4]. This can result in materials degradation and cell inflammation, which is detrimental to the human body. So far, corrosion of biomedical alloys was mainly investigated in simulated body fluids supposed to mimic real in-vivo conditions. These studies allowed ranking of alloys, understanding of mechanisms and of the role of synovial fluid components but their relevance for in-vivo situations remains unclear. Indeed, different surface responses were obtained on the materials tested in simulated fluids compared to the retrieved prosthesis. Only three papers [5–7] investigated the corrosion behavior of biomedical alloys in synovial fluids. These studies were carried out either in animal experiments or on a rather limited number of patients. They demonstrated the feasibility of in-vivo electrochemical measurements but did not provide real insights into the governing mechanisms or crucial parameters.

It is therefore necessary to investigate the corrosion behavior of metal directly in human synovial fluids to determine the actual reaction behavior and understand the corresponding reaction mechanisms. The latter can provide orientation for tailoring implant materials and improve the patients' quality of life.

## 1.2 Challenges

A sound corrosion study requires controlling the nature and properties of the exposed material and of the chemical composition of the corrosive environment as well as the physical conditions. This is necessary for appraising the possible involved reactions. Thus, the first challenge of an in-vivo study is to determine the composition of human synovial fluids. It arises from different aspects. Firstly, it is impossible to conduct a fully composition analysis of synovial fluids due to their complex composition. Secondly, although the composition analysis of specific organics or ions in synovial fluids can be performed, the desired components that control the in-vivo corrosion behavior are unknown. Thus, research was carried out in

this thesis by investigating the corrosion behavior of metals directly in human synovial fluids (within 5 minutes right after the fluid extraction from the body) from numerous patients. The results are then compared with in-vitro ones to understand the corrosion behavior and the involved synovial fluids components. The acquired results will in turn provide a guidance for a tailored composition analysis of synovial fluids.

The second challenge is the volume of synovial fluids, which is relatively small, about 2 - 6 ml in most cases. As a consequence, an electrochemical cell with a small volume (2 ml), instead of typical large cell, has to be developed. Besides, the measurements for a single patient cannot be repeated due to the small volume of synovial fluids.

As third challenge, the synovial fluids denature after leaving the human body for a long time. In absence of a specific set-up maintaining the biological integrity of the synovial fluid, the electrochemical experiments must be completed in a short time (typically within few hours).

Finally, the synovial fluids are susceptible to contamination by contact with air. For instance, the pH of synovial fluids could change in contact with air due to the reaction with CO<sub>2</sub>. The dissolved oxygen in synovial fluids could be influenced by exposure to air. Additionally, synovial fluids could denature by reacting with the bacteria in contact with air. To avoid that, the measurements must be carried out in a sealed cell.

### 1.3 Thesis Structure

The thesis consists of 9 chapters, including the introduction of the thesis (present Chapter), where the motivation of the thesis, challenges and thesis structure is presented.

In Chapter 2, a state of art will show the basic information on the metallic implants and their degradation in human body. To understand the degradation mechanisms, research on the metallic implants conducted in simulated human fluids will be presented. In addition, the comparison between in-vivo and in-vitro results will be discussed to show the necessity of the thesis. Consequently, the objective of the thesis will be introduced at the end of the chapter.

To achieve the goal, an experimental protocol has been designed and described in Chapter 3, where the detailed experimental approach will be presented.

Following the experimental protocol, the properties of extracted human synovial fluids, including appearance, pH and consistency, will be presented in Chapter 4.

Afterwards, the corrosion behavior of Ti and CoCrMo alloy in synovial fluids will be displayed in Chapter 5 using OCP, potentiodynamic polarization and EIS. In addition, in-vivo results will be compared with in-vitro ones to understand the reaction behavior.

Besides, ex-situ surface analysis through FTIR, SEM/EDS and AES have been carried out to help to investigate the corrosion behavior of Ti and CoCrMo alloy and are presented in Chapter 6.

Additionally, the effect of surface roughness on the corrosion behavior of Ti will be described in Chapter 7 through electrochemical measurements, including OCP, polarization curves and EIS. To understand the reaction behavior, the influence factors will be discussed, and the results will be compared with in-vitro ones.

A general discussion on the experimental protocol, sterilization procedures, the corrosion mechanisms and the risks of galvanic corrosion in-vivo will be present in Chapter 8.

Eventually, the conclusion of the thesis will be drawn in Chapter 9.

Additionally, an in-situ investigation of the corrosion behavior of Ti in synovial fluids will be conducted by EQCM in Appendix A. By using EQCM, the electrochemical response of the surface will be obtained simultaneously with the mass change on the surface. Based on the real-time mass change on the Ti surface, the reaction mechanisms will be discussed.

Aside from the in-vivo studies, the validation of the new designed electrochemical cell and the related in-vitro results will be present in Appendix B/C/D.

## Chapter 2 State of the art

### 2.1 Metallic Implants

Normal synovial joints consist of articular cartilage and synovial fluids, as shown in Figure 2.1. The former serves as a load-bearing tissue that covers the bones, and the latter acts as a biological lubricant and nutrient within the joints [8]. They can operate efficiently, however, they are susceptible to degenerative and inflammatory illnesses, for instance, osteoarthritis and rheumatoid arthritis, which cause inflammation of synovium and cartilage/bone loss [8, 9], as shown in Figure 2.1. In this arthritis cases, a replacement of degraded joints is often needed to relieve pain and ensure the patients' mobility.

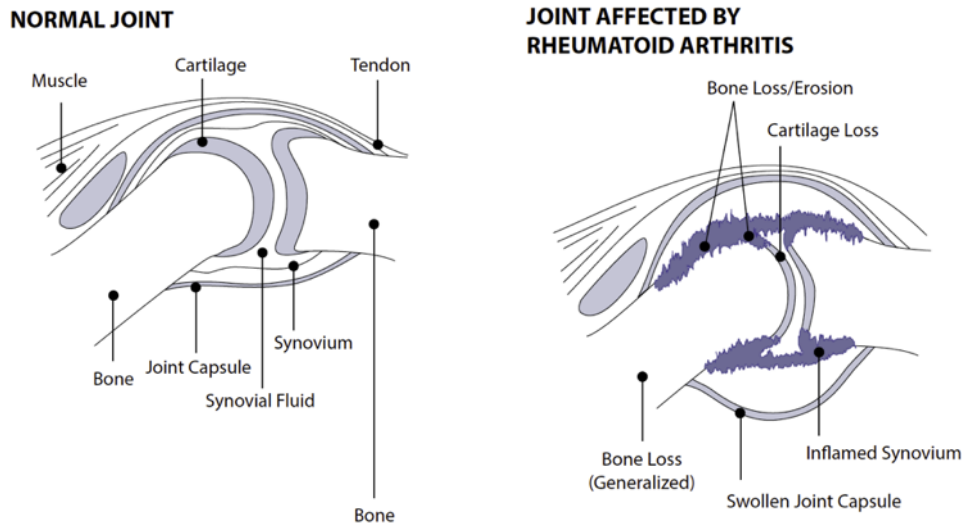


Figure 2.1 Normal and rheumatoid arthritis joint [9]

According to the degradation conditions of joints, joint replacement is divided into total joint replacement implants and resurfacing replacement. Figure 2.2 (a) displays an example of joint replacement, which usually consists of a femoral stem, a femoral head and an acetabular cup. The latter, if cementless, is combined with a metallic shell for bony growth. Resurfacing joint replacement comprises only of an acetabular cup and a femoral head. The implant materials (metal, plastic and ceramic) are selected due to their outstanding biocompatibility, high corrosion and wear resistance, good mechanical properties and osseointegration [10, 11]. The acetabular cup and femoral head are bearing surfaces, and their coupling can be classified into two groups according to the medical application, namely soft on hard (low friction) and hard on hard (low wear) material couplings, as shown in Figure 2.2 (b).

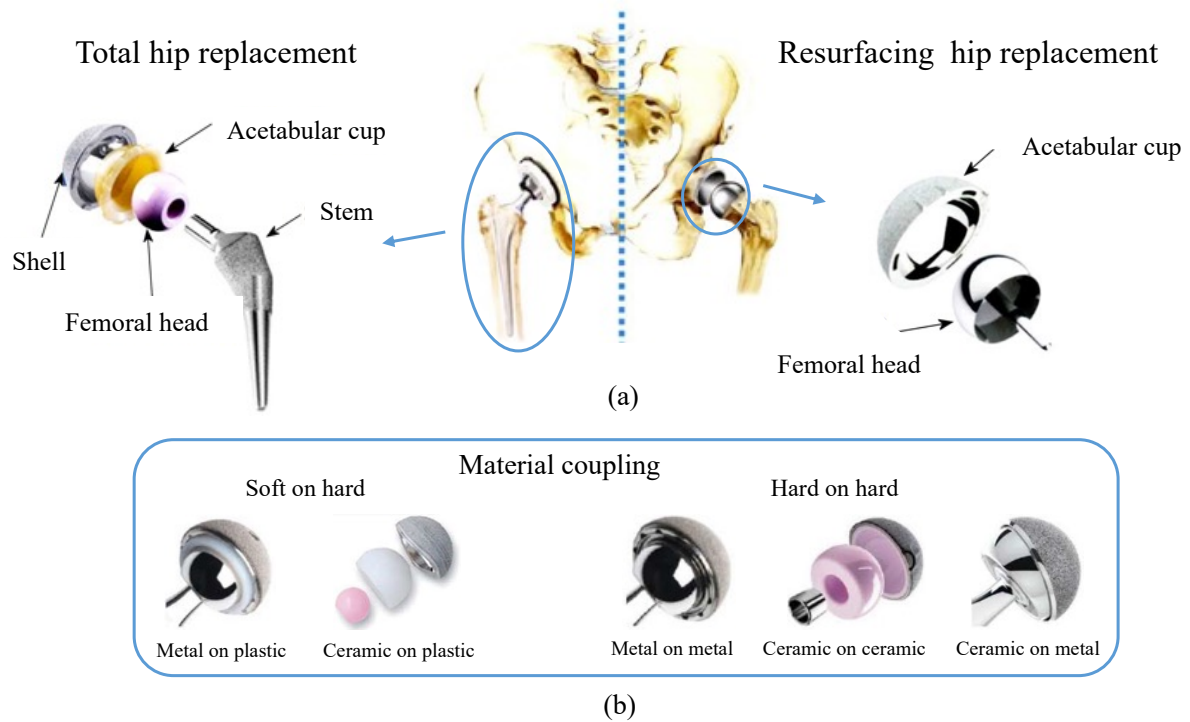


Figure 2.2 (a) hip replacements and (b) materials couplings for the cup on head in implants  
(adapted from [10])

Compared with ceramic and plastic, metallic implants possess better mechanical properties, in terms of elasticity and toughness, and were successfully introduced in the 20th century [12]. The commonly used metallic implants are made of Ti and its alloys, Cobalt-Chromium alloys and 316L type stainless steel (DIN 1.4472/ASTM F1586/ISO150 5832-9), and their typical properties and application in joint implants are summarized in Table 2.1 [8, 11, 13]. In particular, Ti and its alloys as well as CoCrMo alloy are widely used in biomedical devices thanks to their excellent corrosion resistance and biocompatibility obtained through the spontaneous formation of a passive film on the metal surfaces. The biocompatibility of these materials highly depends on the stability of the passive film, which closely relates to the environmental conditions, such as the composition of the solution and pH [14, 15].

Table 2.1 Properties and application of three major metallic materials in joint replacements [8, 11, 13]

Materials	Advantage	Disadvantage	Joint implant components
Ti and its alloys	Biocompatibility		
	Corrosion resistance	Poor wear resistance	Femoral stem, Acetabular shell
	Minimum modulus	Low shear strength	
	Fatigue strength		
	Low density		
Cobalt-Chromium alloys	Wear resistance		
	Corrosion resistance	High modulus	Femoral stem, Acetabular cup, femoral head
	Fatigue strength		
	Biocompatibility		
Stainless steel	Cost and availability	Lower corrosion resistance	Femoral stem, femoral head, Acetabular cup
	processing	High modulus	

Ti and its alloys exhibit the lowest density and strength compared to CoCrMo alloys and stainless steel, thus they are usually used as the femoral stem. They possess the highest corrosion resistance and biocompatibility by spontaneously forming a high stability  $\text{TiO}_2$  passive film [16–18], which is thermodynamically stable in the pH range of 2 - 12, and only dissolves in the presence of specific species, for example concentrated  $\text{H}_2\text{SO}_4$  and HF [16]. Commercially pure Ti and Ti6Al4V alloy are the most widely used in orthopedic. Pure Ti possesses better corrosion behavior but worse mechanical properties than Ti6Al4V alloys [19].

CoCrMo alloys possess the highest elastic modulus, mechanical strength, and wear resistance. Therefore, they are widely used in load-bearing surfaces, such as acetabular cup and femoral head. They exhibit better corrosion resistance than stainless steel due to the formation of a stabler passive film, particularly in the presence of chloride ions [20].

Stainless steel materials are used in joint implant components due to their low cost and outstanding manufacturing properties. They possess acceptable corrosion resistance and biocompatibility due to the presence of Cr. Their application for implants is restricted because of their low wear resistance and pitting corrosion susceptibility in presence of  $\text{Cl}^-$  ions.

## 2.2 Degradation of metallic Implants

Despite the excellent properties of metallic implant materials, corrosion of the metallic implants remains a critical issue that leads to the degradation of implants and the release of metal ions into human body that, above a critical threshold, become harmful to the body [2–4]. Besides corrosion, wear of joint surfaces occurs due to the applied load and the human mo-

tion. The removal of the passive film and the repassivation result in the joint actions of wear and corrosion, namely tribocorrosion. Under tribocorrosion conditions, the corrosion of implant materials is enhanced by several orders of magnitude [21]. This phenomenon is called wear-accelerated corrosion and critically depends on the ability of the alloy to reform the passive layer between consecutive loading cycles. In addition to corrosion, wear-accelerated corrosion was identified as one of the leading causes of metal-on-metal implant degradation in a hip simulator [22].

### 2.2.1 Retrieved Implants Analysis

Numerous research on the retrieved metal-on-metal implants has been carried out, and most of implant failure occurs within the taper junction between the femoral head and stem [23]. The degradation mechanisms in the taper junction are reported mainly to be fretting corrosion, crevice corrosion and galvanic corrosion [24–26].

Hydrogen embrittlement is proposed as a degradation mechanism for Ti tapers during crevice corrosion [24]. This is due to the high affinity of Ti alloys with hydrogen atoms, generated in the crevice of taper, leading to the embrittlement of the Ti surface. No such degradation mechanism is reported for CoCrMo alloys.

These reactions result in the generation of metallic debris (fretting corrosion) and metallic ions (fretting, crevice and galvanic corrosion). The release of metallic debris is associated with the aseptic loosening of articular implants [24], and the generation of corrosion products is attributed to adverse local tissue reactions (ALTRs) due to the immune response. Aseptic loosening and ALTRs are reported to be the dominant reasons for revision surgery [25]. In addition, metallic implants can also have poor osseointegration and osteoconductivity after implantation, together with aseptic loosening and metal ion release, leading to an implant rejection [13].

### 2.2.2 Metallic Ions Release in the Human Body

Because of the wear and corrosion of implants, metallic ions are detected in the human body, such as in blood, serum and urine. A large amount of released metallic ions can be toxic and could induce immune response of the human body, facilitating osteolysis and aseptic loosening [27]. They are harmful to the human body and can result in the failure of the implants. The amount of released metal ions in urine, blood, hair and serum were quantified in various research with different techniques, for instance, atomic adsorption spectrometry, optical emission spectrometry, mass spectroscopy and inductively coupled plasma [28]. The concentration of metallic ions released from Ti alloy and CoCrMo alloy implants in different clinical fluids are summarized in Table 2.2 from a review research. The results show the concentra-

tion of metallic ions for different patients varies significantly between different research, with the value of several orders of magnitude differences. This could be associated with the different implant components (stem or head), implantation time and clinical states of patients.

Table 2.2 The concentration of metallic ions in human fluids released from Ti alloy and CoCrMo alloy hip and knee implants (adapted from [28])

Type of implants	Human fluids	Metallic ions	Concentration / $\mu\text{g}\text{L}^{-1}$
CoCrMo alloy	Synovial fluid	Co	0.2 – 152
		Cr	0.2 - 238
	Serum	Co	0.02 - 25.8
		Cr	0.05 - 23.1
		Mo	0.4 - 2.1
	Blood	Co	0.16 - 116.1
		Cr	0.004 - 108.1
		Mo	0.4 - 58.6
	Urine	Co	0.004 - 205.6
		Cr	0.004 - 42.8
		Mo	0.26 - 37
	Hair	Co	147.4
		Cr	185.3
		Mo	39.3
Ti6Al4V alloy	Synovial fluids	Ti	0.1 - 194
		V	0 - 2
	Serum	Ti	0.7 - 536.8
		Al	1.36 - 16.31
	Blood	Ti	0.6 - 319.6
		V	0.04 - 0.18
	Urine	Ti	0.004 - 650
		V	0.002 - 0.004

## 2.3 Human Synovial Fluids

Normal synovial fluid is a viscous, clear and yellowish fluid in the cavities of synovial joints, which acts as a biological lubricant to reduce the friction of the joints and provide nutrition for the articular cartilage [29]. It mainly consists of ions, such as  $\text{Na}^+$ ,  $\text{Cl}^-$ ,  $\text{K}^+$ ,  $\text{HPO}_4^{2-}$ ,  $\text{Ca}^{2+}$  and  $\text{Mg}^{2+}$  [30, 31], serum proteins, lipids, hyaluronan, glucose and cells [29, 32, 33]. The main composition of synovial fluids is summarized in Table 2.3. However, the exact composition of synovial fluid is much more complex, and it varies with many factors, such as age [29] and diet [34] of patients. The pH of synovial fluids was reported to be within 7 - 8 due to the buffering capacity of the human body [35], even though some results claim that it could



vary from 7 to 10 under different clinical states [5]. Typically, the temperature of human fluids remains at around 37 °C [36], and the partial pressure of oxygen in synovial fluids is about 48 mmHg ( $0.82 \times 10^{-4}$  mol/L) [37].

Table 2.3 The main chemical composition of normal synovial fluids

Compound	Ions						Organics			
	Na	Cl	P	Ca	K	Mg	protein	lipid	hyaluronan	glucose
Concentration / gL <sup>-1</sup>	1-3	3-4	0.01-0.05	0.01-0.1	0.1-0.3	0.01-0.02	10-30	2-4	1-4	0.6-0.9

It is worth noting that both the appearance and the composition of synovial fluids are significantly dependent on clinical states [29, 38]. Based on the synovial fluid analysis, the joint diseases can be divided into non-inflammatory, inflammatory, septic and traumatic. A rough comparison for synovial fluids is listed in Table 2.4. For example, the synovial fluids become liquid, turbid and greyish-reddish in an inflammatory, septic and traumatic joint [29]. The concentration of Na<sup>+</sup>, K<sup>+</sup> and Ca<sup>2+</sup> ions in the osteoarthritis joints increases at least two times compared with normal joints [30]. The hyaluronan concentration in inflamed synovial joints decreases to 0.7 - 1.5 g/L, while the amount of phospholipid increases from 0.1 g/L to 1.5 - 3.7 g/L in rheumatoid arthritis joints [33]. Also, the partial pressure of oxygen in synovial fluids decreases in patients with rheumatoid arthritis, which can be close to 0 mmHg in some cases [39].

Table 2.4 Classification of properties based on laboratory examination [29]

Parameter	Type of effusion			
	Noninflammatory	Inflammatory	Septic	Traumatic
Volume	> 3.5 mL	> 3.5 mL	> 3.5 mL	> 3.5 mL
Color	Yellow	Yellow-greyish	Green-greyish	Red-yellow-brown
Clarity	Slight turbid	Turbid	Turbid, purulent	Clear or turbid
Viscosity	High	Low	Low	Decreased
Spontaneous clot formation	No	Yes	Yes	Yes
Protein	10-30 g/L	> 40 g/L	30-60 g/L	10-30 g/L
Glucose	0.6 - 0.9	Decreased	Decreased	0.6 - 0.9
Associated diseases	Osteoarthritis Osteochondritis Traumatic arthritis	Crystal synovitis	Infective arthritis	Trauma
		Rheumatoid arthritis		Haemophilia
		Systemic lupus erythematosus		Anticoagulant therapy
				Malignant disease

In addition, the composition of synovial fluids varies with the implantation time due to the metallic ions release and wear debris, as introduced in the last section.

## 2.4 Interfacial Reactions of Metallic Implants in Simulated Human Fluids

To understand the electrochemical reactions of the metallic prosthesis in human synovial fluids, simulated body fluids including isotonic sodium chloride (NaCl), phosphate buffers (PBS) and the more complex Ringer's and Hank's solutions, are designed to study the reaction mechanisms. Bovine serum albumin (BSA) and hyaluronic acid is sometimes added to simulate the effect of organics. The relevant test temperature is 37 °C. Attempts to simulate inflammations have been made by adding hydrogen peroxide ( $H_2O_2$ ). The main reactions of metal in a bioenvironment are summarized in Figure 2.3. The different types of interactions can be rationalized as follows.

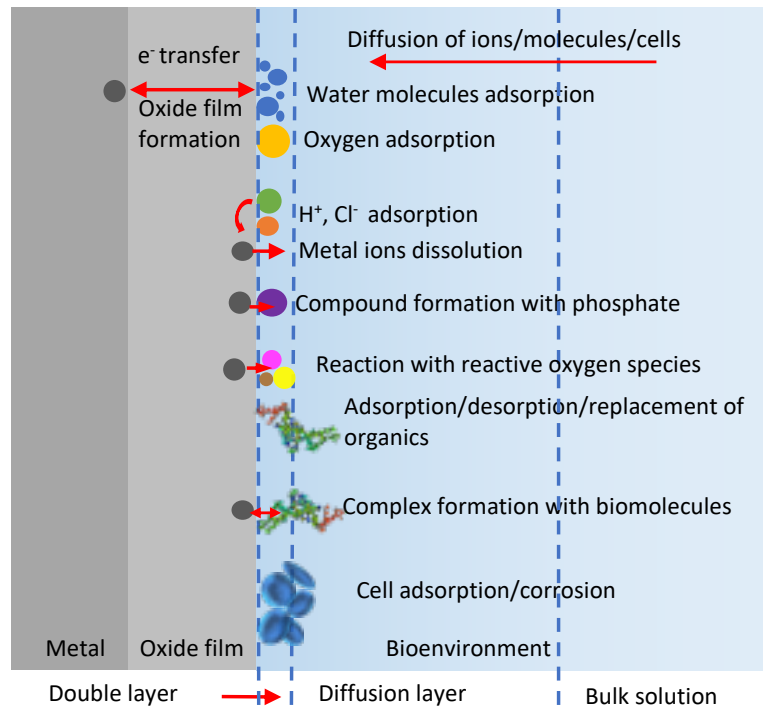
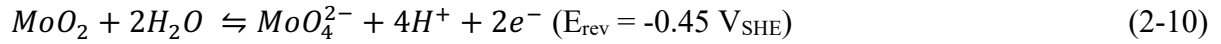
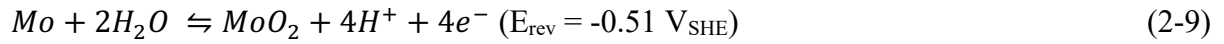
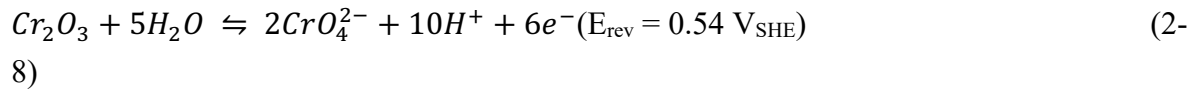
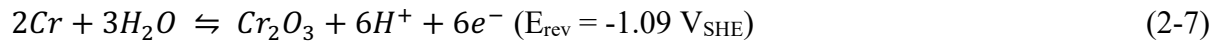
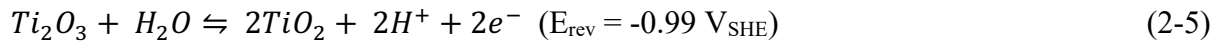
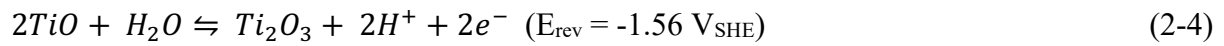
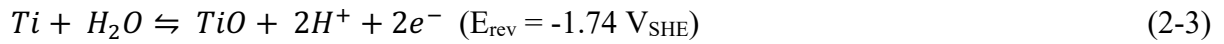
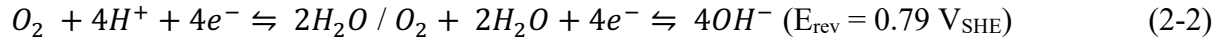
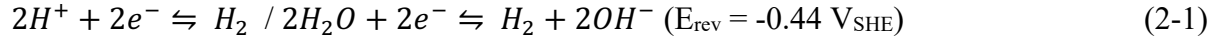


Figure 2.3 Interfacial reactions of metal immersed in bioenvironment [40]

### 2.4.1 Reactions between Metals and Water/Dissolved Oxygen

Corrosion reactions occur when metal is in contact with oxidizing agents in the environment; in this case, they are dissolved oxygen and water. When a metal surface is immersed in the fluids, water molecules adsorb onto the metal surface within nanoseconds, forming an electric double layer at the nanoscale [41], followed by dissolved oxygen adsorption. In conse-

quence, the reduction reactions occur, as shown in equations (2-1) and (2-2), accompanied by oxidation of the metal. Note that the dissolved oxygen concentration in pure water at 25°C and 1 atm is  $2.56 \times 10^{-4}$  mol/L, and it decreases at higher composition of electrolyte and higher temperature [42]. The reversible potentials indicated in the equations are obtained from the Nernst equation at the following conditions:  $P_{H_2/O_2} = 1.03$  atm,  $T = 310$  K,  $pH = 7.4$  and  $C_{\text{soluble ions}} = 10^{-6}$  mol/L.



For Ti and CoCrMo alloys, oxide films are spontaneously formed because of the high reactivity identified by low reversible potential for electrochemical reactions between metals and water at 37 °C, as presented in equations (2-3) - (2-10).

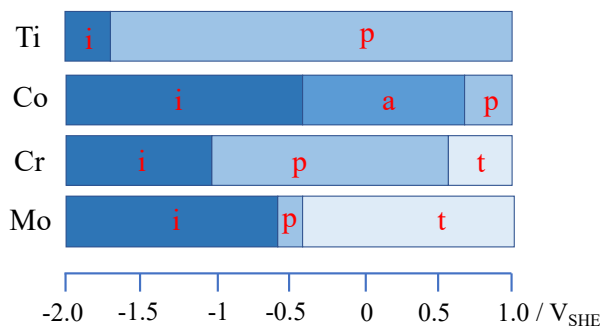


Figure 2.4 Typical equilibrium potential ranges of Ti, Co, Cr and Mo in H<sub>2</sub>O at 25 °C and pH 7.4 (physiological conditions) extracted from Pourbaix diagrams in different domains: immunity (i), active dissolution (a), passivity (p) and transpassivity (t) [43]

The typical potential range of the corrosion reaction for Ti, Co, Cr and Mo in H<sub>2</sub>O at 37 °C and pH 7.4 (physiological conditions) is extracted from Pourbaix diagrams, and is presented in Figure 2.4. The equilibrium lines for different domains are obtained by considering the concentration of soluble ions of 10<sup>-6</sup> mol/L as well. This figure is a graphical representation of the equations above. The Pourbaix diagrams only help to predict the corrosion susceptibility of a metal as a function of potential and pH, but do not offer any information on the reaction rate.

The OCP of CoCrMo alloy in body simulated solutions is around -0.2 V<sub>SHE</sub> to -0.1 V<sub>SHE</sub> [40], indicating passive film, mainly Cr<sub>2</sub>O<sub>3</sub>, is formed on the surface. The stability and thickness of passive film depend on the applied potential, oxygen availability and the media's composition. The thickness of the passive film increases with the temperature [15] and potential [44, 45], and passive film can be quickly regenerated in the presence of oxygen owing to the higher equilibrium potential of the reduction reaction [17, 18]. However, when the potential is higher than 0.4 V<sub>SHE</sub>, Cr<sub>2</sub>O<sub>3</sub> will be dissolved by forming Cr<sup>6+</sup> soluble cations [15].

#### 2.4.2 Reactions between Metals and Ions

Besides water and dissolved oxygen, ions in the human synovial fluids are also reported to react with metallic surfaces. Cl<sup>-</sup>, the most abundant ions in synovial fluids, is not discussed in this chapter since it has little effect on Ti and CoCrMo alloy due to the stable passive film formed on the surface [16], [20]. Although there are various kinds of ions in human fluids, phosphate and calcium ions are the only ions interacting with the metal surface [46–48]. Numerous research has been conducted to investigate the influence of phosphate on the corrosion behavior of metal in simulated solutions. The results indicate that reactions between metal and phosphate depend on pH [49], the composition of the solution [50–52] and the applied potential [40, 45, 50, 53]. The corresponding mechanisms can be categorized as chemisorption (ion exchange and electrostatic attraction) and Lewis acid-base interactions, as presented in Figure 2.5. The former is the most prevalent mechanism, which mainly depends on pH. A detailed introduction on the mechanisms is present below:

- Electrostatic force: The surface is positively charged when the pH is lower than the isoelectric point of the metal surface, leading to the electrostatic attraction between the metal surface and phosphate ions. When the pH is higher than the isoelectric point of the metal surface, electrostatic repulsion will be favorable, which increases with pH [54]. Previous research reported that phosphate ions diminish the anodic current of CoCrMo alloy [40, 50] and Ti alloy [53] by adsorbing onto the metal surface. At the same time, they have little influence on the cathodic reaction. The potential-dependent behavior is probably due to the electrostatic

force, where electrostatic repulsion and electrostatic attraction between the metal surface and phosphate ions occur under cathodic and anodic potential, respectively.

- **Ion exchange:** Phosphate ions could react with metal oxide/hydroxide by replacing  $\text{OH}^-$  ions, namely ligand exchange reaction. When the surface is positively charged, phosphate adsorption is attributed to the ion exchange reaction [55]. The phosphate-metal reaction was detected on Ti and CoCrMo alloy through XPS analysis and potentiodynamic techniques. A phosphate-Ti complex was identified by XPS analysis on a Ti6Al4V surface after polarizing under different anodic potentials in Hank's solution [45]. A current increase at the potential of around  $0.6 \text{ V}_{\text{Ag}/\text{AgCl}}$  was observed for CoCoMo alloy in PBS solution compared with NaCl solution, which is probably associated with the phosphate-chromium reaction [50].

- **Lewis acid-base interaction:** At a pH lower than the isoelectric point of the metal, the active sites on the metal surface are protonated and act as a weak acid, while phosphate ions ( $\text{H}_2\text{PO}_4^{2-}$ ) become a weak base. At a pH higher than the isoelectric point, metal active sites are deprotonated and behave like a weak base, and phosphate ions become a weak acid. In this interaction, metal active sites react with oxygen atoms in the phosphate anion, forming M-O bonds [56].

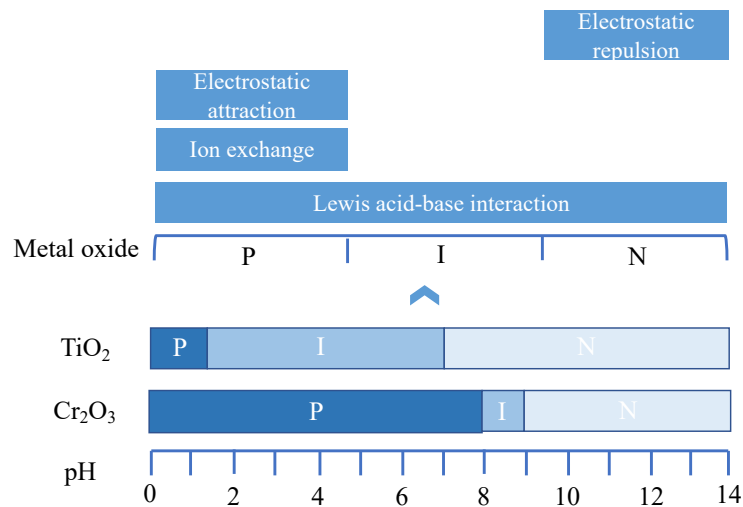


Figure 2.5 Interaction mechanisms between phosphate ions and the metallic surface under different pH (P: positive charge; I: isoelectric point; N: negative charge)

The study of the reaction between metal and calcium ions is relatively poorly documented. Like phosphate, calcium ions can slightly inhibit the passive corrosion by adsorbing onto metal surfaces due to the electrostatic attraction [57, 58]. In addition, calcium and phosphate ions react with each other and form a precipitation layer on the metal surface after immersing

in calcium and phosphate containing solutions [59, 60]. This precipitation layer significantly reduces the corrosion rate of metal in the tested solutions.

### 2.4.3 Reactions between Metals and Organic Molecules

After the adsorption of ions, organics reach the metal surface. Proteins, the main organic molecules in synovial fluids, are widely studied in the reactions with the metal surface. Proteins are prone to bind to a metal surface, and the interfacial reactions depend on many factors, which are summarized in Table 2.5.

Table 2.5 Factors influencing protein adsorption onto the metal surface

Protein properties	Size [61, 62], structural stability [63], charge [61, 62]
Surface properties of metal	Surface energy [64, 65], charge [62, 66], chemical composition [65, 67], morphology [62, 68]
External parameters	pH [62, 66], electrode potential [44, 69, 70], temperature [62, 71], composition of solution [72]

- Protein properties: Proteins are complex biopolymers mainly consisting of amino acids. The adsorption of proteins is usually a result of transportation, adsorption and repulsion processes. Small proteins are prone to adsorb on metal surfaces at the early stages thanks to their high diffusion velocity, while they will be replaced by the large ones over time, which have stronger binding force owing to the larger contact area [61]. For example, a more significant amount of adsorption on the ZnS surface is observed for BSA, which has higher conformational flexibility than the lactoglobulin [63].

- Surface properties: Generally, proteins are more prone to adsorb on hydrophobic surfaces than on hydrophilic surfaces, due to the hydrophobic groups present in proteins [67, 68]. Besides, the surface energy and chemistry are also responsible for the protein adsorption. For instance, less BSA is adsorbed on the CoCrMo alloy surface with the increase of the surface energy due to the increase of Cr<sub>2</sub>O<sub>3</sub> content [64]. BSA adsorption decreases from Ti/Cr oxide to Ta, Ni and Al oxide, and Fibrinogen adsorption increases from Al oxide to Cr/Ti, Ta and Ni oxide [65]. Additionally, the amount of protein adsorption increases with the roughness owing to the larger surface area of the metal [68].

- External factors: The adsorption of proteins, with various sizes and isoelectric points, depends on the solution pH due to the corresponding change in the surface charge of both protein and metal surface. This behavior was reported on Ti particles, where the protein adsorption is most irreversible at the pH from 3 to 8, while most reversible in the pH range of 8.5 - 9.4 [61]. It also highly depends on the temperature since proteins will denature above 50 °C [73]. Besides, protein adsorption is also related to the applied potential on the metal surface.

It was reported that albumin adsorption on CoCrMo alloy surface increases with an applied passive potential [69]. At the same time, it is also increased under cathodic potential (below  $-0.6 \text{ V}_{\text{Ag/AgCl}}$ ), supposedly due to the albumin reduction [70]. In addition, protein adsorption is affected by the presence of ions in the solution. The amount of protein adsorption on the CoCrMo surface immersed in PBS solution decreases compared to the one in 0.14 M NaCl solution due to the competitive adsorption between phosphate and albumin [50]. Contrary to phosphate, calcium ions are suggested to promote BSA adsorption on CoCrMo alloy in acidic artificial saliva due to the electrostatic force with negative charged BSA [74].

### Human Serum Albumin (HSA)

HSA, about 60% of the total protein in plasma, mainly contributes to the colloid osmotic pressure [75]. Because of the high concentration, serum albumin arrives on the metallic surface first according to the law of mass transport. HSA is quite similar to bovine serum albumin (BSA), and the main difference between them is the number of tryptophan amino acids, as shown in Figure 2.6. Thus, BSA is widely used as an alternative for HSA in in-vitro studies.

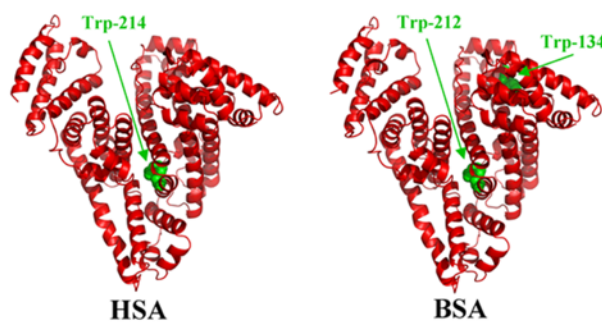


Figure 2.6 3D structures of HAS and BSA with tryptophan residues [76]

BSA is a polypeptide chain composed of 585 amino acids, with a molar weight of 66 KDa [77] and a dimensions of  $4 \text{ nm} \times 4 \text{ nm} \times 14 \text{ nm}$  [78]. It is a soft protein with an unstable structure that can deform when it adsorbs on a metal surface. The isoelectric point of BSA is around 4.7 - 4.9 in water at  $25^\circ\text{C}$  [79]. Previous research has shown that BSA can inhibit the reduction reactions by adsorbing onto the metal surfaces [61, 80–83]. However, depending on the concentration, protein can either accelerate the corrosion rate of metals by forming soluble complexes with metal ions [81, 84, 85] or inhibit corrosion by acting as a physical barrier [81, 82, 86]. As illustrated in Figure 2.7, the anodic current density of Ti6Al4V in PBS solution increases first with the addition of BSA, while it decreases when the concentration of BSA is 4 g/L. In contrast, both the cathodic and passive current density decrease after adding BSA with the same concentrations. It is worth noticing that different results are reported in other works. The cathodic current density significantly decreases with adding 1 g/L of BSA

[80], and the anodic current rate increases after adding 0.5 g/L of BSA in PBS solution [50]. These contradictory results could be due to the different experimental conditions, such as sample preparation and experimental procedure.

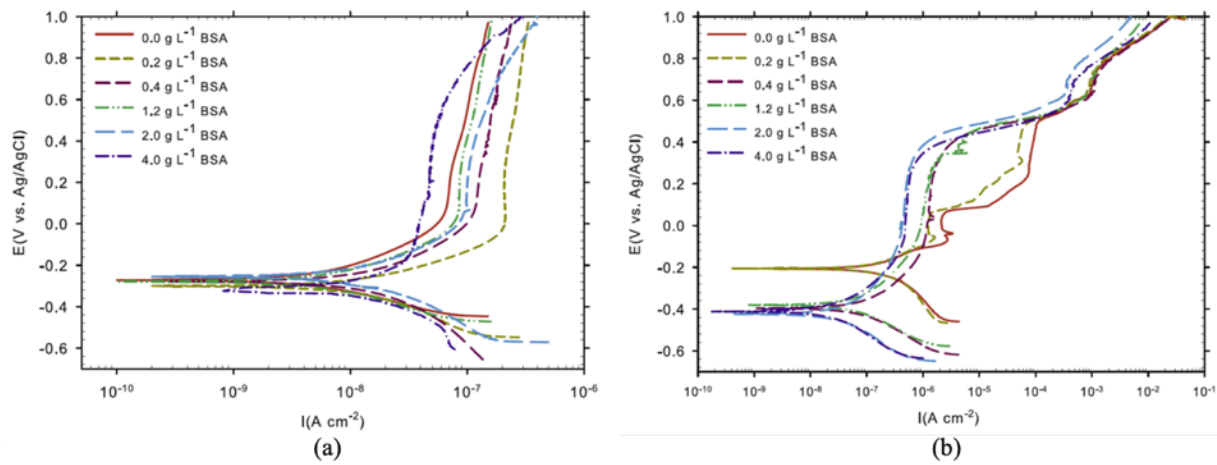


Figure 2.7 Polarization curves of Ti6Al4V (a) and CoCrMo alloy (b) in PBS solution at different concentrations of BSA with a scan rate of 0.167 mV/s at 37°C [81]

The driving force for BSA adsorption is reported to be entropy gain [62], surface energy [62, 64, 65, 71, 87], surface charge [62, 65, 71] or electron conductivity [65]. The former could be the dominant due to the conformational entropy [88]. The BSA adsorption onto metallic surface varies with the surface charge of the protein and metal surface, the chemical composition of metallic surface and solution, as well as the concentration. As a consequence, the adsorption reaction varies during the dynamic process, which makes it very complicated to separate the influence factors. Besides adsorption, BSA is also reported to bind and precipitate on the metallic surface, and the reaction behavior depends on the applied potential [89], as presented in Figure 2.8. BSA is reported to bind on Ti [90], Cr [91], Co [92] and Mo [90] ions, enhancing the dissolution rate of metal ions. At cathodic potential lower than  $-0.6 \text{ V}_{\text{Ag/AgCl}}$ , 3 or 4 disulfide bonds in BSA molecule are reduced quickly, and the products remain adsorbed on the metal surface [93]. In the transpassive domain, the protein starts to precipitate on the metal surface due to a large amount of protein-ions complex formation.



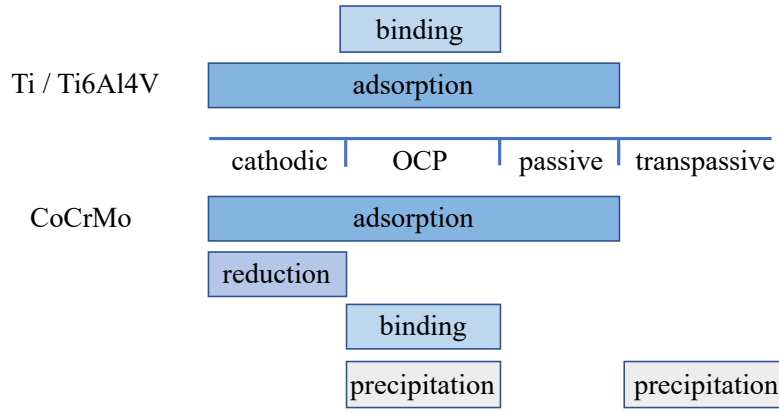


Figure 2.8 Interfacial reactions between protein and metallic surface with different applied potential, adapted from [89]

Many kinetic models for protein adsorption have been proposed to study the BSA adsorption mechanism, and the most commonly used is the Langmuir adsorption model due to the simple mathematical format:

$$\Gamma = \frac{B_{ADS} \Gamma_{max} C}{1 + B_{ADS} C} \quad (2-11)$$

Where  $\Gamma$  is the amount of adsorbed protein ( $\text{mol}/\text{cm}^2$ );  $B_{ADS}$  is the affinity of the protein molecules toward the surface ( $\text{cm}^3/\text{mol}$ );  $\Gamma_{max}$  is the maximum value of  $\Gamma$  ( $\text{mol}/\text{cm}^2$ ); and  $C$  is the concentration of protein in the bulk solution. In this model, a monolayer of protein homogeneously adsorbed on the sample surface is assumed. However, the Langmuir isotherm is a first approximation of the real adsorption phenomena. More accurate and complex models have been proposed in the literature [62].

### Hyaluronic Acid (HA)

HA, the other main component in synovial fluids, is a large linear hydrophilic polymer, with a molar mass of around 4 MDa, acting as a lubricant in the joint and being responsible for the viscosity of the synovial fluids [94]. The chemical structure is illustrated in Figure 2.9. Its concentration significantly decreases in osteoarthritis joints. Thus it is used as a treatment for patients suffering from osteoarthritis [95, 96]. The influence of HA on the lubrication of the joints is widely studied [97–99], while the study of its effect on corrosion is relatively limited. The impact of HA on the corrosion behavior of Ti [100] and CoCrMo alloy [83] is limited compared with BSA due to its hydrophilic property and large size that lead to less adsorption on metal surface.

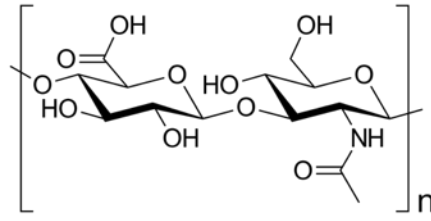
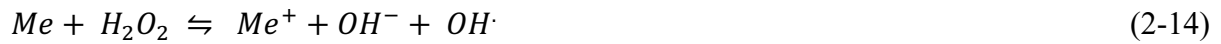


Figure 2.9 Chemical structure of HA

Although there are plenty of studies on the protein adsorption (mainly albumin and calf serum) onto metal surfaces in ideal in-vitro environments, their relevance with complex solutions such as human synovial fluids has not been proved due to the variety of reaction species as well as the possible interactions between the reaction species.

#### 2.4.4 Reactions between Metals and Reactive Oxygen Species

Reactive oxygen species (ROS) are defined as free radicals containing oxygen molecules, including hydrogen peroxide ( $H_2O_2$ ), superoxide anion ( $O_2^-$ ) and nitric oxide (NO). They are unstable and highly reactive [101], and could be produced by mitochondria [102] in general and by cells under host-defense response [103]. To study the influence of ROS on the performance of artificial joints,  $H_2O_2$  is added to the simulated solutions to conduct the electrochemical measurements on metals. The results show that  $H_2O_2$  significantly increases the corrosion rate of the metal [85, 104–106] owing to the unpaired electrons in the valence shell. They can further oxidize the metal surfaces by forming oxygen and hydroxyl radicals ( $OH^\cdot$ ) [104], as presented in equations (2-12) - (2-17). Figure 2.10 illustrates that the corrosion rate of Ti6Al4V alloy significantly increases with  $H_2O_2$ , where the difference can be more than one order of magnitude. Similar results are also obtained on Ti grade 2 in Hartmann's solution [107] and CoCrMo alloy in PBS based solutions [105]. The exact interactions of ROS with metal surfaces in a bioenvironment and the influencing factors are still unclear.



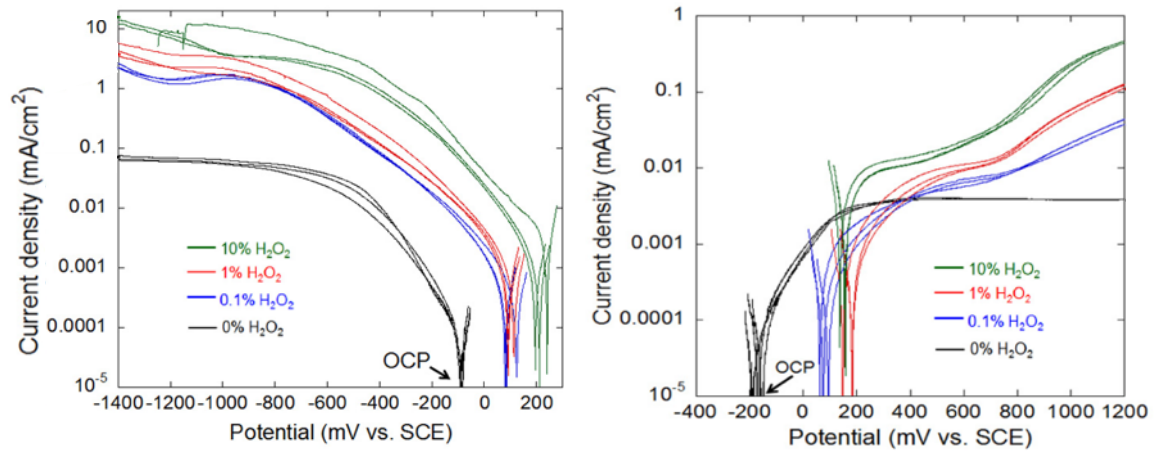


Figure 2.10 Cathodic and anodic polarization curves of Ti6Al4V in 0.5M NaCl solution at various amount of  $\text{H}_2\text{O}_2$  [103]

### 2.4.5 Reactions between Metals and Cells

Cells can adsorb on metal surfaces acting as a physical barrier hindering the diffusion of oxidant species from the solution to the metal surfaces and thus decreasing the metal dissolution rate [108, 109]. The presence of cells on metals may also induce high local corrosion susceptibility on the metal surface by generating occluded areas beneath cells and establishing different local chemistries [110]. For example, the reactive oxygen species generated by inflammation cells can accelerate the metal dissolution. From the response time perspective, it usually takes several minutes or hours for cells to adsorb onto the metal surface, which is already covered by organic molecules [111]. The response time after implantation of a metallic implant is displayed in Figure 2.11. To avoid degradation of synovial fluids out of the human body, the reactions between cells and the metallic surfaces will not be investigated in this thesis.

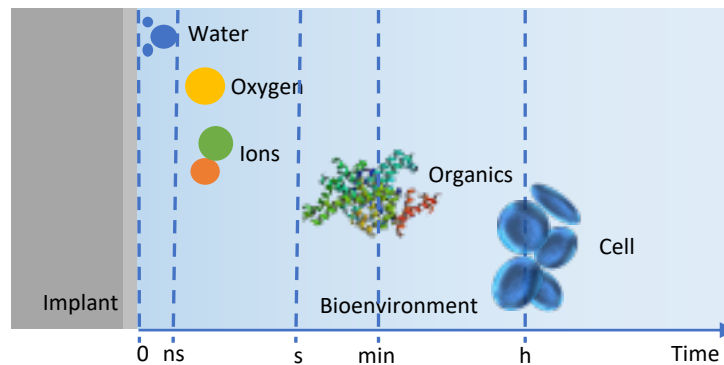


Figure 2.11 Scheme of the time response after implantation of a metallic implant [112, 113]

## 2.5 Comparison Between In-Vivo and In-Vitro Results

The study of electrochemical reactions of metal directly in human synovial fluids is quite limited [5–7]. Munoz et al. [5] investigated the electrochemical behavior of a CoCrMo alloy in different synovial fluids, which were directly extracted from 17 patients with different clinical states. The results show that the electrochemical behavior of the alloy varied significantly with the different synovial fluids, as shown in Figure 2.12. Typical reactions that occurred in simulated human fluids were also encountered in in-vivo tests, such as water reduction, mass transport limited oxygen reduction, passivation of metal, and transpassivity. Additionally, it was reported that the electrochemical behavior of the alloy depends not only on the material reactivity but also on the human synovial fluid components, mainly of the reactive oxygen species. In some patients, such as patient 2, the latter could determine the whole electrochemical reactions. The OCP values were found to be well correlated with the inflammation level of patients. However, the corresponding reaction mechanisms are not fully understood.

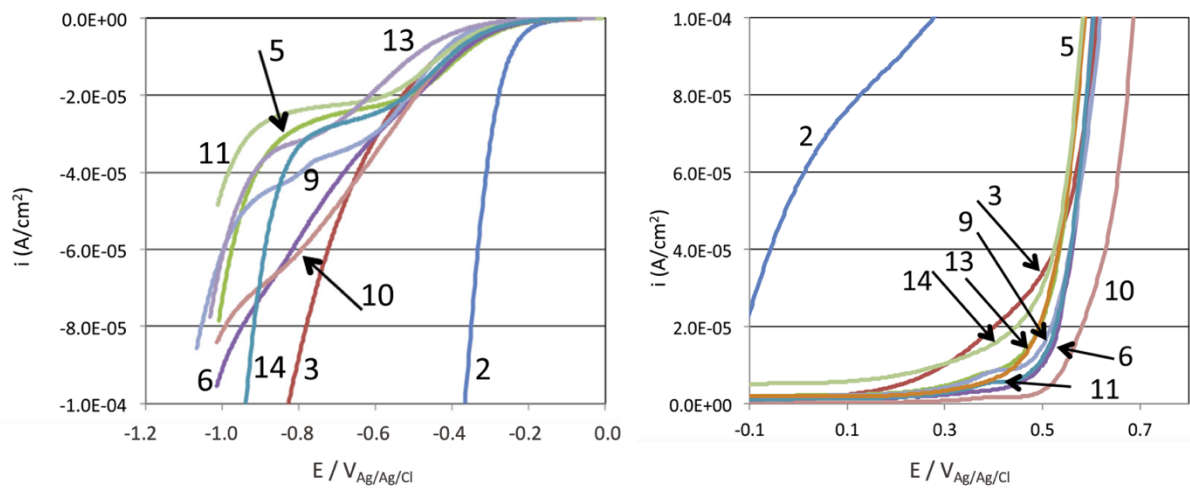


Figure 2.12 The (a) cathodic and (b) anodic polarization curves of CoCrMo alloy in synovial fluids from different patients [5]

The representative polarization curve of CoCrMo in synovial fluids is compared with that in bovine calf serum (BCS). Figure 2.13 shows a significant difference between in-vivo and in-vitro corrosion behavior. The difference is probably due to the complex composition of synovial fluids, indicating that in-vitro experiments are not adequate to predict the in-vivo behavior.

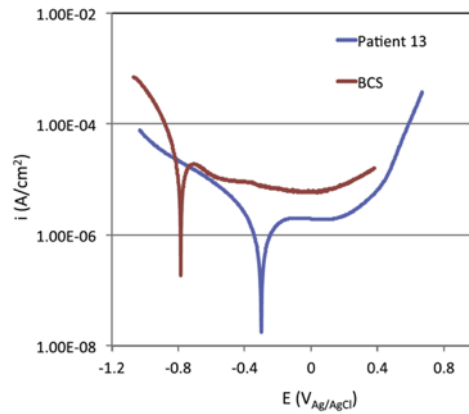


Figure 2.13 The polarization curves of CoCrMo alloy in synovial fluid from patient 13 and in BCS (30 g/L) at a pH of 7.6 [5]

Besides electrochemical research, retrieved prostheses are investigated to study the actual reaction behavior of metal in synovial fluids. A wide variety of surface layers, from oxide film to organic or even graphitic film, are found on retrieved implant load-bearing surfaces [114–116]. The schematic view of the surface films is summarized in Figure 2.14 [117].

The first case was reported by Wimmer et al. [116] who analyzed 42 retrieved hip implants made of CoCr alloys, where a thick oxide film (around 100 nm) containing organic compounds and calcium phosphate was detected on an articulating surface. The thick oxide layer cannot be explained by classical chemical mechanisms, including high electric field and ion transportation through the oxide field [117]. For instance, an electrode potential of 100 V is required to generate a 100 nm oxide film with a typical growth rate of 1 nm/V. The second case is observed on a sample from the same set of retrieved implants. The absence of oxide film could be due to the exposure of the bare metal by abrasion and faster organic adsorption than repassivation. The occurrence of the last case from a hip joint simulator [115] could be because of the high potential on the surface with the presence of ROS when thicker oxide film and a large amount of adsorbed organics are obtained on the metal surface.

Interesting, only the case three is reported in in-vitro researches [118–120]. This mismatch between in-vivo and in-vitro results is caused by the complex composition of human synovial fluids, which is patient-dependent, as is proved by Munoz et al. [5].

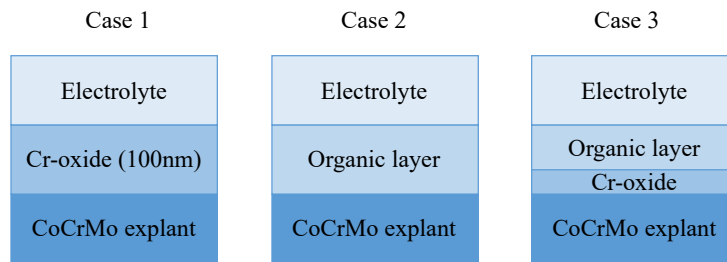


Figure 2.14 Schematic view of the surface composition on retrieved prosthesis [117]

## 2.6 Statement of the Problem

Corrosion is a crucial factor that induces the degradation of the implants. To understand the corrosion reactions, numerous studies on the electrochemical reactions of metal in simulated body fluids have been conducted. These studies reveal that the corrosion reaction between metals and human synovial fluids depend on a large number of complex phenomena. However, the effect of each phenomenon was only studied independently and their application to the complex human body fluids has not been well validated. Indeed, the only in-vivo study in a limited number of human synovial fluids shows that the simulated body fluids do not represent the synovial fluids. Besides, the corrosion behavior of metal in human synovial fluids varies significantly with patients, and the corresponding reaction mechanisms are not fully understood. The discrepancies between in-vivo and in-vitro results and the patient dependent corrosion behavior can be associated with the complex composition of human liquids, which depends on the patients. Therefore, there is a need to investigate the electrochemical reactions of metal directly in human synovial fluids to obtain the data relevant to implant conditions in the human body.

## 2.7 Objectives of the Thesis

Considering the existing problems with the prediction of corrosion in-vivo, the goal of this thesis is to design and validate an optimal experiment protocol to determine the electrochemical behavior of pure Ti and CoCrMo alloy in human synovial fluids and understand the reaction behavior as a function of the clinical state (i.e. before, during and after implantation).

To achieve this, electrochemical techniques, including Open Circuit Potential (OCP) and potentiodynamic tests, are selected to investigate the electrochemical reactions of metals in human synovial fluids. Electrochemical tests will be combined with impedance microscopy (EIS) and Quartz Crystal Microbalance (EQCM) to obtain information on the organic adsorption and mass variation simultaneously with the electrochemical behavior of metal surfaces in synovial fluids.

In addition, ex-vivo surface characterization using various techniques (SEM/EDS, FTIR and AES) will be used to characterize the surface topography and chemistry to better understand the surface composition and chemical states and underlying electrochemical mechanisms of metal in human synovial fluids. Also, a large number (~150) of synovial fluids from patients with well-defined clinical states (primary surgery, total knee arthroplasty and revision) will be tested to obtain reliable statistics and understand the electrochemical behavior.

This PhD project will contribute to a better understanding of the electrochemical behavior of metals in actual body conditions. It will therefore provide a useful guidance for in-vitro scientific research in simulated human fluids. Besides, it will help better tailor implant materials to patients to reduce the corrosion risks. Note that for legal reasons no access to clinical information concerning the patients was granted to nonmedical staff. This prevented me to assess possible correlations between electrochemical behavior and patient clinical states.

## Chapter 3      Experimental Setup and Protocol

To achieve the goals, an experimental protocol was developed and validated to systematically investigate the electrochemical reactions of metal surfaces in contact with human synovial fluids. To do that, synovial fluids were extracted from patients at the beginning of the surgery using a syringe which was transferred to the electrochemical lab within 5 minutes. The synovial fluids in the syringe were directly injected in the sterilized electrochemical cell that was immediately sealed so to prevent the contact of the fluid with air. The electrochemical measurements in this work can be then considered as in-vivo study. No clinical states of the patients can be obtained due to the patient privacy.

Besides, a multi-electrode electrochemical cell was designed and validated to meet the measurement requirements introduced in the challenges. The synovial fluids were inserted in the newly designed cell right after the characterization. Afterward, the OCP, potentiodynamic polarization, EIS and EQCM measurements were conducted at the hospital to obtain the corrosion behavior of metal surfaces in human synovial fluids. Subsequently, ex-situ surface analysis was performed using SEM to observe the surface morphology, and EDS, FTIR and AES to characterize surface chemistry. Ultimately, in-vivo electrochemical results and surface analysis data were compared with in-vitro results to understand the electrochemical behavior. The scheme for the research programs is present in Figure 3.1, and the detailed measurements are described in the following sections.



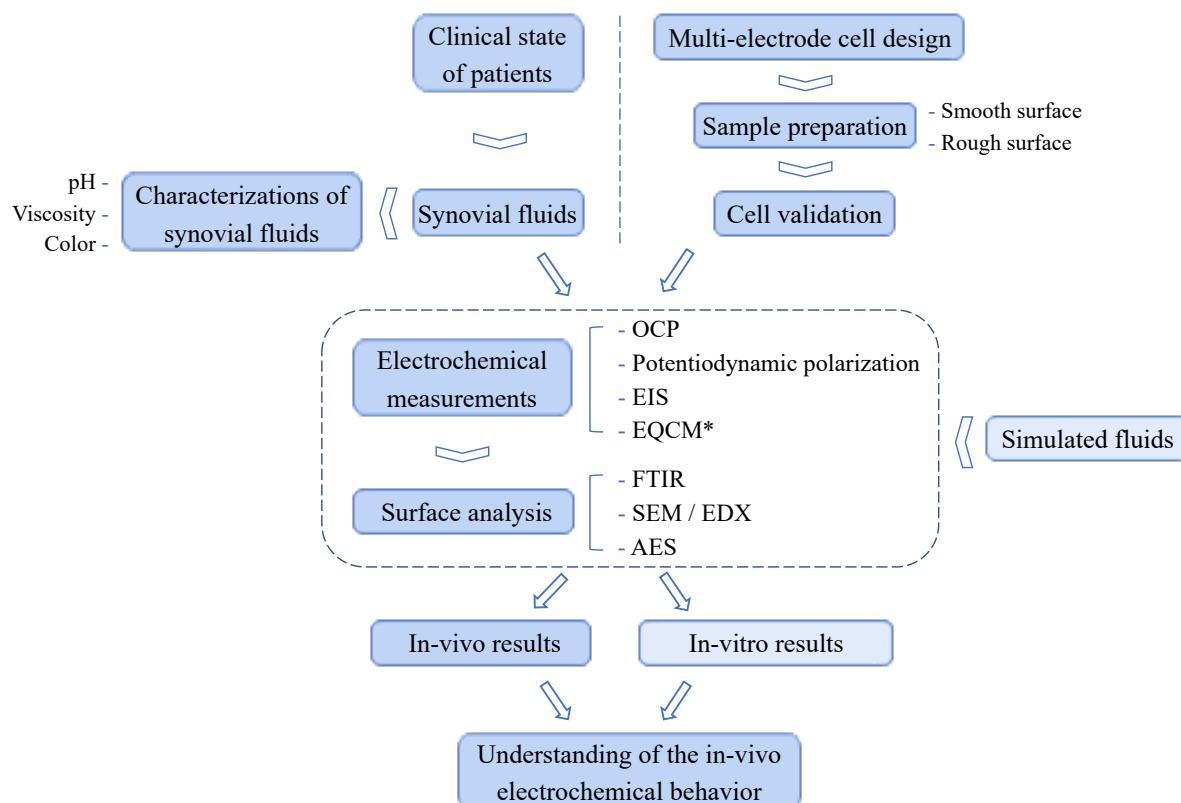


Figure 3.1 Scheme for the research programs (\*EQCM measurements were conducted in EQCM cell on a rough crystal)

### 3.1 Characterization of Human Synovial Fluids

Three kinds of patients were selected, and their synovial fluids were extracted by a skilled surgeon in the surgery room:

- Group 1, Primary surgery patients (PS): patients who do not have an implant but exhibit different grades of knee inflammation and clinical states.
- Group 2, Total Knee Arthroplasty (TKA): patients with a Total Knee Arthroplasty implant.
- Group 3, Revisions (R): patients who will go for revision surgery due to a failure, rejection, or problem with the implant.

Synovial fluids were extracted during surgery (group 1 and 3) and puncture (group 2). For group 1 and 3, synovial fluids were extracted at the beginning of the arthrotomy, right after the skin incision. It was extracted with a 10 mL syringe through a small hole, and maintained as it is after sealed with a syringe cap. For group 2, the synovial fluids were aspirated through a needle located at the supero-lateral recessus of the knee capsule following the disinfection of the skin. All care was taken by the surgeon to avoid contamination of the synovial fluid by blood or other components. The overall protocol of this study (protocol 208/13) was ap-

proved on 28 May 2013 by the ethics committee for human being studies of the local government (Commission cantonale (VD) d'éthique de la recherche sur l'être humain) according to the ICH GCP guidelines.

The synovial fluids were directly transferred from the surgery room to electrochemical laboratory in the hospital within 5 min. The picture of synovial fluid in the syringe was taken right after transfer from the surgery room. Same position for taking picture was guaranteed to eliminate the influence of illumination condition. The pH of the fluid was then measured with pH paper (sensitivity is 0.3 pH units) by depositing a drop from the syringe onto the paper. The pH test after the electrochemical measurements was also conducted. The liquids were also subjectively categorized during the injection into the electrochemical cell according to their consistency in sticky (similar to glycerol) or liquid (similar to vegetable oil). Quantitative color analysis of the fluids was conducted on the picture with a digital color meter (CIELAB color space) after finishing the electrochemical measurements.

### 3.2 Design of the Multi-electrode Electrochemical Cell

A multi-electrode electrochemical cell with 2 mL volume was designed to meet the small amount of synovial fluid (normally around 2 - 7 mL) extracted from patients. The cell is made of PMMA, a transparent material, to visually check the contact between fluids and electrodes. The diagram and the picture of the cell are presented in Figure 3.2. For each test, two Ti and two CoCrMo samples were inserted in different positions to test the electrochemical reactions. The cell included an Ag/AgCl (3 M NaCl) reference electrode (RE), purchased from ALS, UK, and 12 platinum (Pt) rods as counter electrode (CE), which were evenly distributed in the vessel cover. The potential of the reference electrode is 0.198 V relative to the standard hydrogen electrode. To check the homogeneity of synovial fluids, the OCP of each Pt rod was measured at the beginning of the immersion. After that, all the Pt rods were short circuited to serve as the CE. Prior to any experiment, the CE was polished using diamond paste and subsequently cleaned and sterilized in 70% ethanol. The RE were cleaned and sterilized in 70% ethanol before and after experiments. The injection and evacuation holes were closed with silicone caps right after injection to avoid contamination from the air. The cell was placed in an aluminum block to maintain the temperature at  $37 \pm 1$  °C. The whole set-up was installed in a Faraday cage to avoid electrostatic interferences.

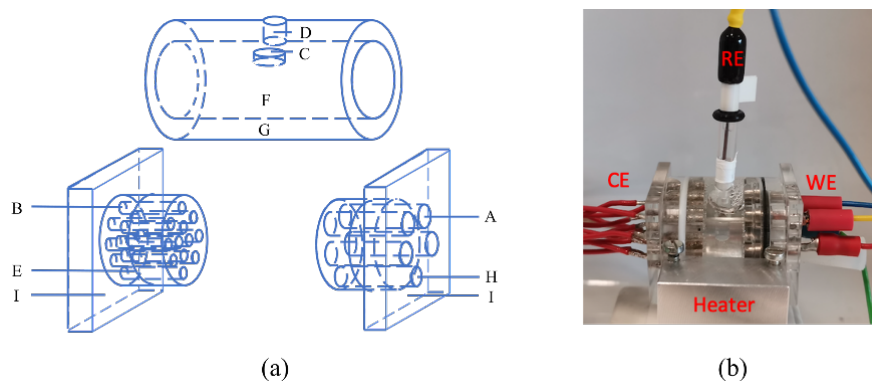


Figure 3.2 (a) Schematic diagram of the multi-electrode cell. A: working electrode, B: counter electrode, C: reference electrode, D: air evacuation hole, E: sealing O-ring, F: tested synovial fluid, G: vessel, H: injection hole, I: vessel cover. (b) The picture of the cell

The small volume of the cell may introduce artefacts due to significant modification of the chemistry of the electrolyte, possibly induced by the polarization. For example, hydrogen and oxygen generated at the CE during anodic or cathodic polarization may diffuse in the small cell towards the working electrodes, thus disturbing the electrochemical measurement. Moreover, pH changes due to electrolysis may have a significant effect because of the small volume of the cell. To check for such possible artefacts, the small cell was validated by comparison with a standard size corrosion cell. The results are shown in the Appendix (Figures A.1 - A.3, Table A.1). The results show that no obvious artefacts occurred in this small volume cell used here.

### 3.3 Sample Preparation

Complete control of the tested surface is needed for a better understanding of the electrochemical reactions of metals in human synovial fluids.

A Ti rod (grade 2: Ti  $\geq$  98.9 wt.%, Fe  $\leq$  0.30 wt.%, O  $\leq$  0.25 wt.%, C  $\leq$  0.08 wt.%) and a low carbon CoCrMo alloy rod (Co: 65.95 wt.%, Cr: 28 wt.%, Mo: 6 wt.%, C: 0.05 wt.%) supplied by Goodfellow were used in this study. Samples with 4 mm diameter and 6 mm thickness were cut from bulk rods. The samples were polished with SiC emery paper of 1200, 2400, and 4000 grit in water. To get a mirror-like surface, final polishing was carried out on a polish tissue with an ethanol-based suspension dispersed with diamond particles (0.25  $\mu$ m in diameter). The final surface roughness (Ra) was measured by a laser scanning confocal microscope (KEYENCE VK-X200) with a 20X magnification. The Ra value of Ti and CoCrMo alloy was  $15 \pm 3$  nm and  $10 \pm 1$  nm, respectively. The Ra value of CoCrMo alloy is the typical surface roughness for artificial joints. Afterwards, the samples were cleaned in an ultra-

sonic bath with acetone for 5 min and subsequently sterilized in 70% ethanol with ultrasonics for 5 min and then dried with oil-free compressed air.

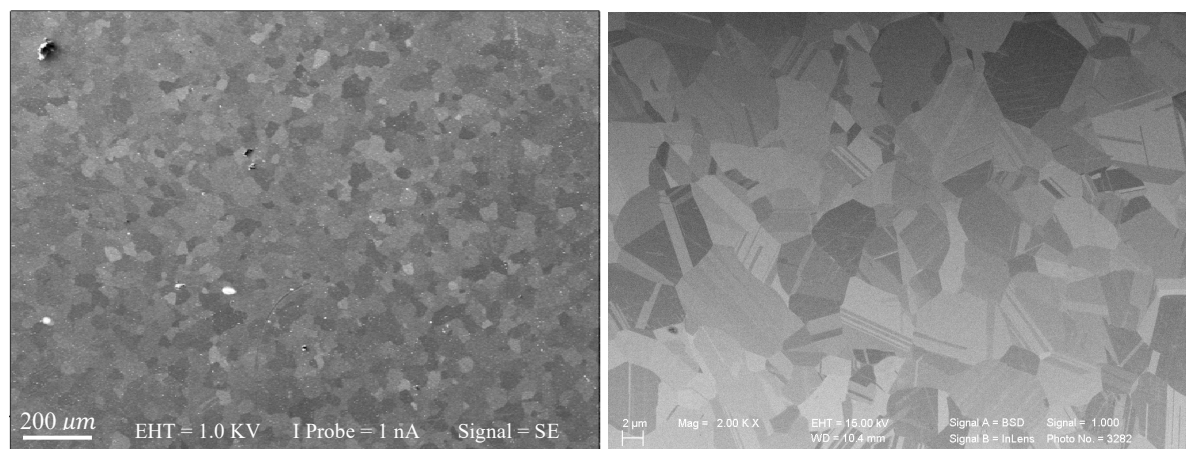


Figure 3.3 SEM images of microstructure for Ti (left) and CoCrMo alloy (right)

The microstructure of Ti was revealed using AES sputter depth profiling analysis with the ion gun of 2 KV. After sputtering, SEM image of the microstructure was taken, as shown in Figure 3.3. The detailed setting of the AES analysis is presented in Chapter 3.5.3. The microstructure of CoCrMo alloy is provided by Dajana Valenta (UDE, Germany).

### 3.4 In-vivo Electrochemical Measurements

To systemically study the electrochemical reactions between metal surfaces and human synovial fluids, experiments in terms of OCP, potentiodynamic polarization, EIS and EQCM were carried out.

#### 3.4.1 OCP and Potentiodynamic Polarization

OCP and potentiodynamic polarization measurements were conducted in the multi-electrode cell. The OCP between the working electrodes and the reference electrode varying with time was measured to represent the equilibria between the metallic oxidation and the human fluid reduction. Potentiodynamic polarization measurement was adopted to acquire the current variation as a function of applied potential. Based on the results, the electrochemical behavior of metallic surfaces in human synovial fluids and the corresponding reaction rates were obtained. EIS was tested to measure the electrical response to a potential modulation at different frequencies. The solution resistances ( $R_s$ ) of various human synovial fluids were obtained, which relates to the concentration and the conductivity of the present ions.

Different electrochemical measurements were carried out sequentially on the samples with an IVIUM potentiostat.

- OCP between each Pt rod and the RE was measured in sequence every 10 s, and the whole measurement for 12 Pt rods lasted for 100 s.
- OCP between working electrodes and the reference electrode was continuously recorded for 20 minutes. The measurement consists of four loops, and different samples were tested in each loop.
- Polarization resistance ( $R_p$ ) of one Ti and one CoCrMo sample was measured at the end of each OCP loop by scanning the potential from -20 to 20 mV with respect to OCP with a scan rate of 2 mV/s.
- EIS was tested on the same Ti and CoCrMo sample at the OCP. The applied potential amplitude was  $\pm 10$  mV and the frequencies ranged from  $10^5$  to 1 Hz.
- Potentiodynamic scan was performed on the same Ti and CoCrMo sample by scanning the potential from the OCP towards the cathodic direction to -1  $V_{Ag/AgCl}$  and reversing towards anodic direction up to 1  $V_{Ag/AgCl}$  with a scan rate of 2 mV/s.
- EIS was conducted on Ti and CoCrMo samples after the polarization scan.

The whole experiment procedure is shown in Figure 3.4.

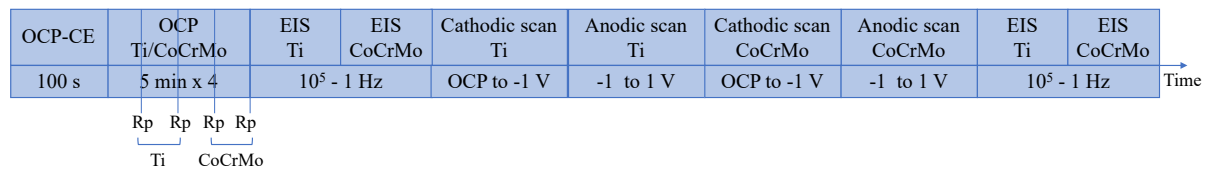


Figure 3.4 Experimental sequence 1

### 3.4.2 EIS

EIS enables the detection of a characteristic response of the electrode/electrolyte interface to a sinusoidal potential of small amplitude (typically 5 - 10 mV) in a certain frequency domain. EIS is a nondestructive sensitive technique that allows obtaining many parameters at a solid/liquid interface, such as solution resistance, double layer capacity, charge transfer resistance of the electrode and mass transport [121].

Before EIS experiments, the OCP of two Ti and CoCrMo alloy was measured for 20 minutes. Consequently, EIS experiments were carried out on one Ti and CoCrMo alloy under OCP condition. The applied potential amplitude was  $\pm 10$  mV, and the frequencies ranged from  $10^5$  to 0.005 Hz. The experiment procedure is displayed in Figure 3.5. Both OCP and EIS measurements were performed with a BioLogic potentiostat. Based on the EIS spectrum, the information on solution resistance, protein adsorption and the passive film thickness were obtained.

OCP-CE	OCP Ti/CoCrMo	EIS Ti	EIS CoCrMo	Time
100 s	5 min x 4	$10^5 - 0.005$ Hz	$10^5 - 0.005$ Hz	

Figure 3.5 Experimental sequence 2

### 3.4.3 EQCM

EQCM is a powerful technique which combines electrochemistry and quartz crystal microbalance. The latter can measure the shift in the frequency of the quartz crystal resonator, which is influenced by the mass change on its surface. Based on that, the mass variation of the surface can be obtained through the frequency shift. By using EQCM, the corrosion behavior of sample simultaneously with the mass change can be acquired. Therefore, the information on protein adsorption, passive film formation on the sample surface can be obtained.

The measurements were conducted with a EQCM (AWSensor, Spain) together with a Bio-Logic SP200 potentiostat. The EQCM is a X1 system, with the operating frequency of 4 - 160 MHz, and the frequency and mass resolution of 0.1 Hz and 0.6 ng/cm<sup>2</sup>, respectively. All measurements were performed under a temperature of 37 °C and the measurements were controlled with a AWS Suite Mirage 4.0.7.3.

A smooth Ti film on quartz crystal (QuartzPro, Sweden), with a frequency of 5 MHz and diameter of 14 mm, was used to perform the OCP measurement for 20 min. The same Ag/AgCl RE and a platinum spiral wire CE were used in the EQCM cell. The measurement consists of four loops, and  $R_p$  was measured at the end of each OCP loop by scanning the potential from -20 to 20 mV with respect to OCP with a scan rate of 2 mV/s. Afterwards, potentiodynamic scan was performed on the Ti crystal by scanning the potential from the OCP towards the cathodic direction to -1 V<sub>Ag/AgCl</sub> and reversing towards anodic direction up to 1 V<sub>Ag/AgCl</sub> with a scan rate of 2 mV/s. The experiment procedure is presented in Figure 3.6.

OCP Ti	Cthodic scan Ti	Anodic scan Ti	Time
5 min x 4	OCP to -1 V	-1 to 1 V	
Rp Rp Rp Rp			

Figure 3.6 Experimental sequence 3

Before the electrochemical experiments, the crystals were cleaned in an ultrasonic bath with acetone for 5 min and subsequently sterilized in 70% ethanol for 5 min and then dried with oil-free compressed air. After the measurement, the crystals were immersed in 70% ethanol

until arriving in the laboratory at the university. Afterward, they were cleaned in an ultrasonic bath with 70% ethanol for 2 min and blow-dried with oil-free compressed air.

For the sake of the clarity, the detailed electrochemical measurements conducted for each patient are summarized in Table 3.1.

Table 3.1 Electrochemical measurements conducted for each patient

Patient	Group	Protocol	Metals	OCP	R <sub>p</sub>	R <sub>s</sub>	Cathodic/anodic polarization	EIS
2	PS	1	Ti/CoCrMo	Yes	Yes	Yes	Yes	-
3		1	Ti/CoCrMo	Yes	Yes	Yes	Yes	-
4		1	Ti/CoCrMo	Yes	Yes	Yes	Yes	-
5		1	Ti/CoCrMo	Yes	Yes	Yes	Yes	-
11		1	Ti/CoCrMo	Yes	Yes	Yes	Yes	-
13		1	Ti/CoCrMo	Yes	Yes	Yes	Yes	-
14		1	Ti/CoCrMo	Yes	Yes	Yes	Yes	-
15		1	Ti/CoCrMo	Yes	Yes	Yes	Yes	-
16		1	Ti/CoCrMo	Yes	Yes	Yes	Yes	-
20		1	Ti/CoCrMo	Yes	Yes	Yes	Yes	-
21		1	Ti/CoCrMo	Yes	Yes	Yes	Yes	-
22		1	Ti/CoCrMo	Yes	Yes	Yes	Yes	-
23		1	Ti/CoCrMo	Yes	Yes	Yes	Yes	-
26		1	Ti/CoCrMo	Yes	Yes	Yes	Yes	-
28		1	Ti/CoCrMo	Yes	Yes	Yes	Yes	-
31		1	Ti/CoCrMo	Yes	Yes	Yes	Yes	-
35		1	Ti/CoCrMo	Yes	Yes	Yes	Yes	-
36		1	Ti/CoCrMo	Yes	Yes	Yes	Yes	-
39		1	Ti/CoCrMo	Yes	Yes	Yes	Yes	-
43		1	Ti/CoCrMo	Yes	Yes	Yes	Yes	-
46		1	Ti/CoCrMo	Yes	Yes	Yes	Yes	-
48		1	Ti/CoCrMo	Yes	Yes	Yes	Yes	-
53		1	Ti/CoCrMo	Yes	Yes	Yes	Yes	-
59		1	Ti/CoCrMo	Yes	Yes	Yes	Yes	-
67		1	Ti/Ti-1200	Yes	Yes	Yes	Yes	-
71		1	Ti/CoCrMo	Yes	Yes	Yes	Yes	-
73		1	Ti/CoCrMo	Yes	Yes	Yes	Yes	-
75		1	Ti/CoCrMo	Yes	Yes	Yes	Yes	-
76		1	Ti/CoCrMo	Yes	Yes	Yes	Yes	-
78		1	Ti/CoCrMo	Yes	Yes	Yes	Yes	-
79		1	Ti	Yes	Yes	Yes	Yes	-
83		1	Ti/CoCrMo	Yes	Yes	Yes	Yes	-
85		1	CoCrMo	Yes	Yes	Yes	Yes	-
86		1	Ti/CoCrMo	Yes	Yes	Yes	Yes	-

92		1	Ti/CoCrMo	Yes	Yes	Yes	Yes	-
95		2	Ti/CoCrMo	Yes	-	Yes	-	Yes
99		2	Ti/CoCrMo	Yes	-	Yes	-	Yes
102		2	Ti/CoCrMo	Yes	-	Yes	-	Yes
103		2	Ti/CoCrMo	Yes	-	Yes	-	Yes
106		1/2	Ti/Ti-1200	Yes	-	Yes	Yes	Yes
111		1/2	Ti/Ti-1200	Yes	-	Yes	Yes	Yes
112		1/2	Ti/Ti-1200	Yes	-	Yes	Yes	Yes
113		2	Ti/Ti-1200	Yes	-	Yes	-	Yes
114		1/2	Ti/Ti-1200	Yes	-	Yes	Yes	Yes
115		1/2	Ti/Ti-1200	Yes	-	Yes	Yes	-
116		1/2	Ti/Ti-1200	Yes	-	Yes	Yes	-
118		2	Ti/Ti-1200	Yes	-	Yes	-	Yes
119		1/2	Ti/Ti-1200	Yes	-	Yes	Yes	Yes
121		2	Ti/Ti-1200	Yes	-	Yes	-	Yes
122		1/2	Ti/Ti-1200	Yes	-	Yes	Yes	Yes
123		1/2	Ti/Ti-1200	Yes	-	Yes	Yes	Yes
124		2	Ti/Ti-1200	Yes	-	Yes	-	Yes
125		1/2	Ti/Ti-1200	Yes	-	Yes	Yes	Yes
129		3	Ti	Yes	Yes	-	Yes	-
134		3	Ti	Yes	Yes	-	Yes	-
154		3	Ti	Yes	Yes	-	-	-
17		1	Ti	Yes	Yes	Yes	Yes	-
100 (left knee)	TKA	1/2	Ti/CoCrMo	Yes	Yes	Yes	Yes	Yes
100 (right knee)		1	Ti/CoCrMo	Yes	Yes	Yes	Yes	-
6		1	Ti/CoCrMo	Yes	Yes	Yes	Yes	-
32		1	Ti/CoCrMo	Yes	Yes	Yes	Yes	-
68		1	Ti/Ti-1200	Yes	Yes	Yes	Yes	-
88	R	1	Ti/CoCrMo	Yes	Yes	Yes	Yes	-
104		2	Ti/CoCrMo	Yes	-	Yes	-	Yes
108		1/2	Ti/Ti-1200	Yes	-	Yes	Yes	Yes
109		1/2	Ti/Ti-1200	Yes	-	Yes	Yes	Yes

### 3.5 Ex-situ Surface Characterization

Characterization of the surface after being immersed in human synovial fluids and sterilized in 70% ethanol was carried out to better understand the corrosion behavior obtained from in-vivo electrochemical measurements. FTIR was adopted to quantify the amount of organic adsorption or precipitation through the intensity of the absorption spectrum, and to qualitatively determine the type of organic molecules. Microscopy techniques (SEM, EDS) were used to characterize the surface morphology and the chemical composition of the surfaces.



AES was applied to characterize the chemical composition and thickness of oxide film on the surface through sputter depth profiling analysis.

### 3.5.1 FTIR

FTIR technique measures how much light a sample absorbs when a broadband light beam incidents on it. When an infrared radiation passes through a sample, a molecular covalent bond will selectively absorb the radiation at specific wavelengths, resulting in the stretching or bending vibration of molecular bonds. The type of vibration depends on the atoms involved in the molecular bond. Since different bonds absorb different frequencies, the spectra are therefore different for different molecules.

A Bruker Vertex 80V interferometer, equipped with a global IR source and a KBr beam splitter ( $600$  to  $5\,000\text{ cm}^{-1}$ ), combined with a Hyperion 3000 IR microscope, was used for the FTIR measurements. The highest lateral resolution of this setup is  $1.1\text{ }\mu\text{m}$ . For complete image analysis, the area covered was  $700 \times 700\text{ }\mu\text{m}$ . The study was performed in the mid-infrared range, using a  $6\text{ mm}$  aperture and a resolution of  $4\text{ cm}^{-1}$ . Reference measurements on a polished Ti and CoCrMo sample served as background. Depending on the amount of organics, 2 to 10 sites were selected for each sample.

Absorption spectra for all samples were obtained by normalizing to a logarithmic intensity  $I_{\text{abs}} = -\lg(S/S_0)$ , where  $I_{\text{abs}}$  is the absorbed intensity,  $S$  is the acquired spectrum and  $S_0$  is the spectrum obtained with the same settings from a clean reference surface.

### 3.5.2 SEM/EDS

SEM creates sample images by scanning the sample surface with an electron beam. The electrons interact with the sample atoms, generating different types of signals which are detected by the detector. The generated signals include secondary electrons, backscattered electrons, characteristic X-rays amongst many others. The second electrons ejected from the sample surface at low energies, possessing a high lateral resolution signal. Thus, the qualitative topography of the sample surface can be obtained by detecting secondary electron signals. The ejected characteristic X-ray possesses a distinct energy related to the target atoms, carrying the composition information on the sample.

The sample surface morphology was measured by a Zeiss Merlin SEM combined with EDS. The EDS detector was manufactured by Oxford Instruments and quantification was performed using the algorithms from the manufacturer. Images were recorded using the SE-detector with a beam voltage of  $2\text{ kV}$  and a probe current of  $200\text{ pA}$ . The EDS spectra were acquired using a primary electron beam voltage of  $9\text{ kV}$  at a beam current of  $1\text{ nA}$ . The ele-

ment detection limit with this setup is around 0.5 at.% with a lateral resolution  $< 1\ \mu\text{m}$  and a detection depth in the scanned region of 0.3 to  $3\ \mu\text{m}$ .

### 3.5.3 AES

AES is a commonly used technique for surface analysis of the chemical composition. For this technique, an electron beam is focused on the sample surface, ejecting Auger electron from a higher shell. The mean free path of Auger electrons is within a few nanometers, thus AES analysis is more surface sensitive than EDS. In addition, depth analysis can be conducted through an ion beam sputtering on the sample surface. AES is more suited for the metallic sample analysis, and it possesses a much higher lateral resolution compared to XPS.

The surface composition and film thickness of the Ti samples were analyzed using a PHI 680 scanning Auger microscope (Physical Electronics, Eden Prairie, USA) equipped with a scanning electron microscope and an argon ion gun. Before the analysis, the samples were stored in the desiccator for at least 2 weeks. The measurements were done at a voltage of 10 kV and a current of 10 nA for the electron gun. Two settings were used for the ion gun: 1 kV, using a  $1\times 1\ \text{mm}$  raster, giving a sputter rate of 0.6 nm/min and a 2 kV and  $1\times 1$  raster, with a resulting sputter rate of 1.9 nm/min. The analysis was conducted with the samples tilted at  $30^\circ$  with respect to the incident electron beam and  $45^\circ$  with respect to the incident ion beam. The quantification was performed using sensitivity factors obtained from the PHI Auger Handbook (C: 0.2815, N: 0.6003, O: 0.7878, Ti: 0.7017/1.1032). The passive film thickness was obtained by correcting the influence of electron escape depth, which was reported by Hofmann and Sanz [122] and applied by Mischler et al [123].

## Chapter 4      Characterization of Synovial Fluids

The properties of synovial fluids are reported to depend on the patients' clinical states, as discussed in chapter 2.3. Amongst the properties, color and consistency are the basic ones to assess the patients' clinical states. Additionally, the consistency of the synovial fluids is proportional to the concentration of hyaluronic acid [94], which significantly enhances the lubrication of the human joints [97–99]. The pH of the synovial fluids influences the cathodic reaction of metals in synovial fluids due to the hydrogen reduction reaction.

Thus, color, consistency and pH of synovial fluids were measured in this chapter, instead of analyzing the composition. In addition, the correlation between color and consistency was conducted and compared with the literature.

### 4.1      Color of Human Synovial Fluids

A sufficient amount of liquid could be extracted only from certain patients. Over 154 patients, liquids can be found only in 73 patients. The pictures of the extracted synovial fluids inside the syringe are present in Figure 4.1. For patient 100, the synovial fluids from both the left and right knees were extracted. The pictures show that the color of synovial fluids can be yellow or red, depending on the patients. It is worth noting that blood is observed in some liquids, including P15, P20, P78, P108, P112, P116, P123 and P149.

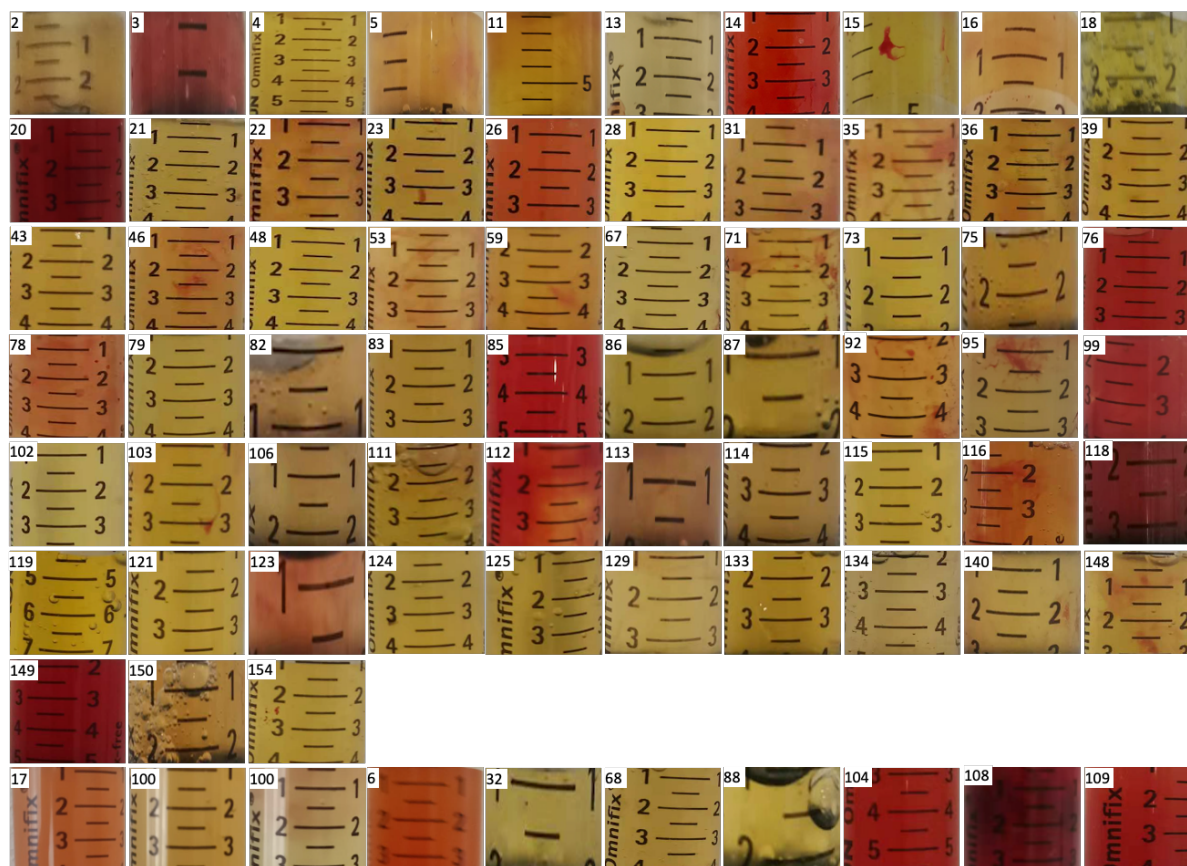


Figure 4.1 Pictures of human synovial fluids inside the syringe (PS, TKA: P17 and P100, R: P6, P32, P68, P88, P104, P108 and P109)

To quantify the color of the synovial fluids, a digital color meter, CIELAB color space, was used. CIELAB color space expresses color with three coordinates,  $L^*a^*b^*$ .  $L^*$  represents perceptual lightness,  $a^*$  represents red (positive value) and green (negative value) and  $b^*$  represents yellow (positive value) and blue (negative value). CIELAB color space is independent of the measurement device. Thus, the measurement values are comparable among different laboratories.

The color of the synovial fluids was obtained from several spots in the picture and the average values are displayed in Figure 4.2. The graph shows that the color of most human synovial fluids is in the area of  $a^*$  (0-20) and  $b^*$  (35-55). The color difference among the synovial fluids is more pronounced in the  $a^*$  coordinate, with the value of up to 60 different.

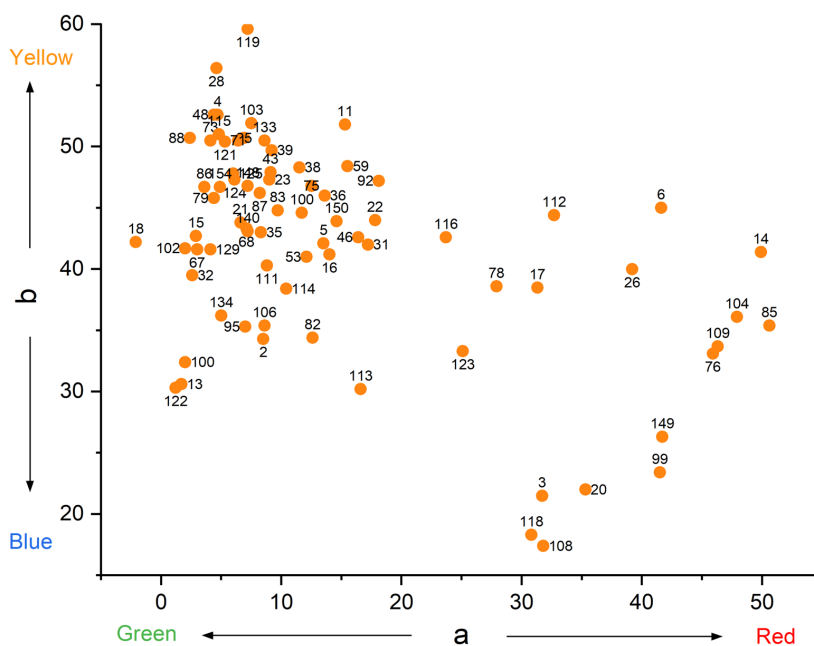


Figure 4.2 The color of synovial fluids obtained through CIELAB color space

## 4.2 Volume and pH of Human Synovial Fluids

The information on tested synovial fluids is listed in Figure 4.1. The results show that the volume of extracted human synovial fluids varies from 1 to 11 ml, the majority of which is within 2 - 8 ml. The pH of most extracted synovia is around 7 - 7.4, while the pH can reach to slightly acid of 6.5 and alkaline of 8.2, such as P76 and P20, respectively. No significant difference in pH values of the synovial fluids is observed at the end of the experiment. As shown in Table 4.1, the consistency of the synovial liquids varies with the patient, being either sticky (similar to glycerol) or liquid (similar to vegetable oil).

Table 4.1 Properties of human synovial fluid

Patient	Group	Volume/ml	pH	Observation
2	PS	6	7.4	Sticky
3		2.5	7.4	Sticky
4		5.5	7.4	Sticky
5		4	7.7	Sticky
11		7	7.4	Very sticky
13		11	7.0	Little sticky
14		8	7.4	Liquid
15		5	7.4	Sticky
16		1.5	7.9	Liquid
18		1	7.3	Sticky
20		6	8.2	Sticky
21		6	7.9	Sticky

22	6	7.9	Sticky
23	7	7.6	Sticky
25	1	7.3	Sticky
26	4	7.9	Little sticky
28	6	7.6	Little sticky
31	4	7.9	Sticky
35	6	7.6	Little sticky
36	6	7.6	Liquid
38	1	7.6	Sticky
39	8	7.3	Liquid
43	7	7.3	Sticky
46	8	7.3	Liquid
48	10	7.0	Sticky
53	6	7.3	Liquid
59	5	7.6	Sticky
67	6	7.3	Sticky
71	8	7.3	Little sticky
73	3	7.3	Little sticky
75	2	8.0	Little sticky
76	5	6.5	Liquid
78	6	7.3	Liquid
79	5	7.3	Liquid
82	1.5	7.5	Sticky
83	6	7.0	Sticky
85	8	6.5	Little sticky
86	2		Sticky
87	1.5	8.0	Sticky
92	6	7.3	Sticky
95	6	7.3	Sticky
99	3	7.3	Liquid
102	10	7.4	Sticky
103	7	7.4	Sticky
106	1.5	8.1	Sticky
111	4	7.4	Very sticky
112	4	7.1	Sticky
113	1.5	7.9	Sticky
114	2	7.7	Sticky
115	5	7.4	Sticky
116	4	7.4	Sticky
118	1.5	7.9	Sticky
119	5	7.4	Sticky
121	8	7.4	Sticky
122	4	7.1	Little sticky
123	3	7.4	Little sticky

124		9	7.0	Little sticky
125		6	7.4	Little sticky
129		3	7.4	Liquid
133		2	8.1	Sticky
134		3	7.7	Little sticky
140		2	7.7	Sticky
148		9	7.1	Little sticky
149		4	7.4	Liquid
150		2	7.4	Sticky
154		6	7.7	Sticky
17		11	7.3	Liquid
100 (left knee)	TKA	6	7.0	Sticky
100 (right knee)		5	7.0	Sticky
6		6	6.8	Liquid
32		5	7.6	Liquid
68		5	7.3	Sticky
88	R	1.5	7.3	Sticky
104		6	7.4	Liquid
108		5	7.4	Sticky
109		8	7.4	Liquid

### 4.3 Homogeneity of Human Synovial Fluids

The OCP of the twelve Pt wires was used for assessing the degree of homogeneity of the liquid at the mm scale. An example of the OCP measurement for P2 is displayed in Figure 4.3. The graph shows the OCP value varies with different Pt electrodes. Note that the OCP of electrodes is subject to variations depending on details in sample preparation (polishing, cleaning).

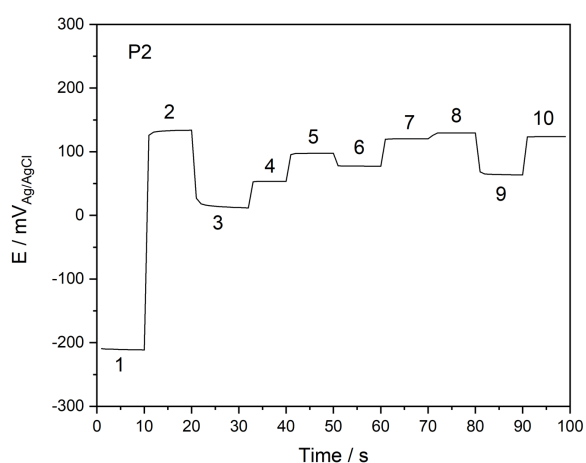


Figure 4.3 OCP measurement of Pt electrodes in synovial fluid from P2

To take this into account, the standard deviation (STDEV) of OCP of the Pt electrodes was used as an indicator. The STDEV values of OCP for Pt electrodes in synovial fluids are summarized in Figure 4.4. For reference, the STDEV value measured in 0.8% NaCl solution, taken here as a reference for a homogeneous solution, was 32 mV. This value varied depending on the patient, between a minimum of 12 mV and a maximum of 73 mV. These values are close to what is found for the NaCl reference solution, and it may, therefore, be concluded that the synovial liquids are homogeneous, at least at the mm scale.

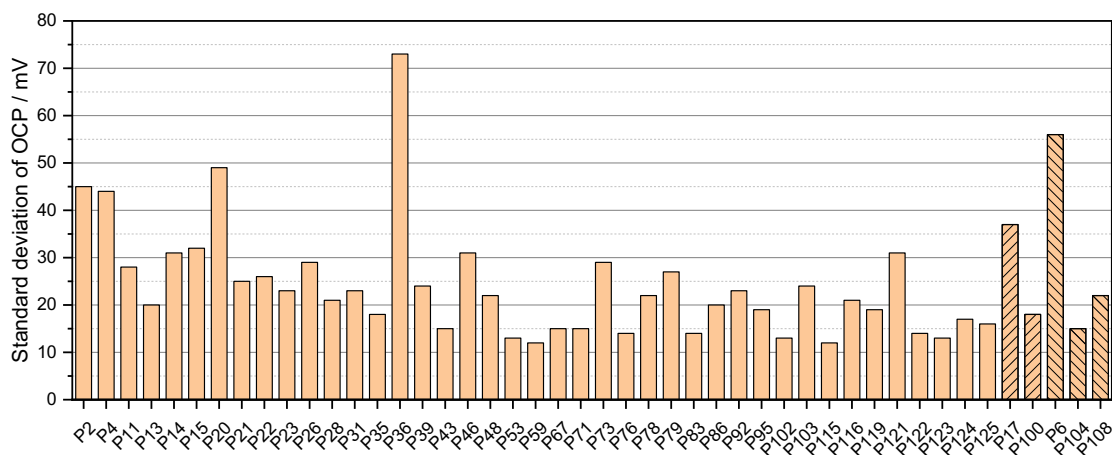


Figure 4.4 Standard deviation of OCP results of Pt rods immersed in different synovial fluids from PS, TKA (P17 and P100) and R (P6, P104 and P108) group

#### 4.4 Correlation between Color and Consistency of Synovial Fluids

The color of the extracted synovial fluids together with the information on consistency is presented in Figure 4.5. The graph indicates that the synovial fluids with the red color are mostly liquid-like, as shown in the liquid region. For the synovial fluids from P20, P108, P112, P116 and P123, the red color is probably due to blood contamination. In the sticky region, most of the synovial fluids are yellow. For synovial fluids which color is located in the regions, the correlation between color and synovial fluid consistency is in agreement with the literature [29]. In this research, the yellowish synovial fluids reported possess a high viscosity for non-inflammatory joints, while the viscosity decreased for reddish fluids for traumatic joints. The agreement between the extracted synovial fluids and that reported in the literature indicates little contamination is introduced in the synovial fluids during the extraction. Note that outliers are obtained for certain patients. However, no obvious correlation between the properties of the synovial fluids and the patient groups, PS, TKA and R, of the patients could be obtained.





## Chapter 5      Electrochemical Behaviour of Ti and CoCrMo Alloy in Human Synovial Fluids

In this chapter, some content is reproduced with the permission from Bao, Yueyue, Anna Igual Muñoz, Claes-Olof A. Olsson, Brigitte M. Jolles, and Stefano Mischler. "The Electrochemical Behavior of Ti in Human Synovial Fluids." *Materials* 15, no. 5 (2022): 1726.

### The Electrochemical Behavior of Ti in Human Synovial Fluids

Yueyue Bao, Anna Igual Muñoz, Claes-Olof A. Olsson, Brigitte M. Jolles and Stefano Mischler

Contribution of the doctoral candidate: conceptualization, methodology, investigation, writing-original draft preparation, writing-review and editing

The corrosion behavior of the Ti and CoCrMo alloy samples in human synovial fluids were studied through electrochemical techniques, such as OCP, potentiodynamic polarization and EIS, and surface characterization, including FTIR, SEM/EDS and AES. By using these techniques, the electrochemical behavior of Ti and CoCrMo alloy in synovial fluids under steady state (OCP and EIS) and polarized ( $R_p$  and polarization curves) conditions can be obtained. Additionally, the in-vivo results were compared with those obtained in simulated solutions to better understand the corrosion behavior of Ti and CoCrMo alloy in synovial fluids.

It is worth noting that a sufficient amount of liquid could be extracted only from certain patients. Over 154 patients, only 66 patients yielded enough liquid ( $\geq 2$  ml). Synovial fluids with a volume less than 2 ml were not investigated due to the contamination of the air in the unfulfilled electrochemical cell.

### 5.1      Electrochemical Results of Ti and CoCrMo Alloy in Human Synovial Fluids

#### 5.1.1 OCP of Ti and CoCrMo Alloy

The OCP of the Ti and CoCrMo alloy electrodes was measured in sequence every 5 min. An example of OCP measurement of Ti and CoCrMo alloy for P23 is present in Figure 5.1. The OCP values measured on two Ti and CoCrMo samples are indicated as Ti-1, Ti-2, CoCrMo-1 and CoCrMo-2 in the graph. Another example of OCP evolution with time for P2, P3, and P4 is displayed in Figure 5.1. The OCP value slightly varies during immersion time (variation

less than 2.5 mV/min). Interestingly, it can either increase with time (P2 and P4) or decrease (P3). Similar trends of OCP are also observed in other tested synovial fluids.

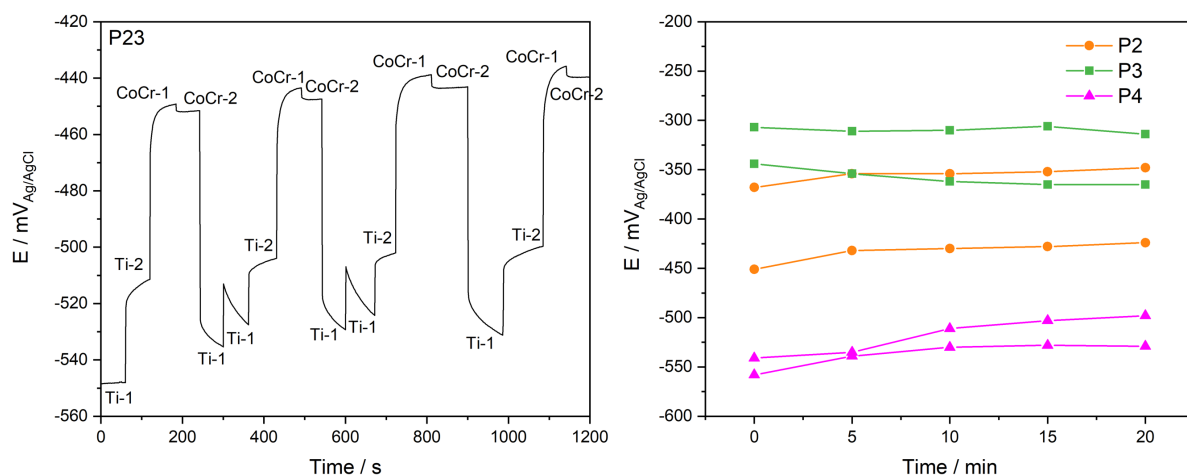


Figure 5.1 OCP measurement of Ti and CoCrMo samples for P23, and OCP evolution of Ti with time for P2, P3, and P4

The comparison of the stabilized OCP values measured after 20 minutes' immersion in tested synovial fluids is presented in Figure 5.2. The stabilized OCP varies among patients between a maximum of  $-151 \text{ mV}_{\text{Ag/AgCl}}$  and a minimum of  $-560 \text{ mV}_{\text{Ag/AgCl}}$ . In some cases (P11, P13, and P14), the two Ti electrodes immersed in the same synovial fluid differ significantly in their OCP value (difference larger than 50 mV). This can be due to slight, uncontrolled differences in sample preparation or contamination during sample storage before the experiment.

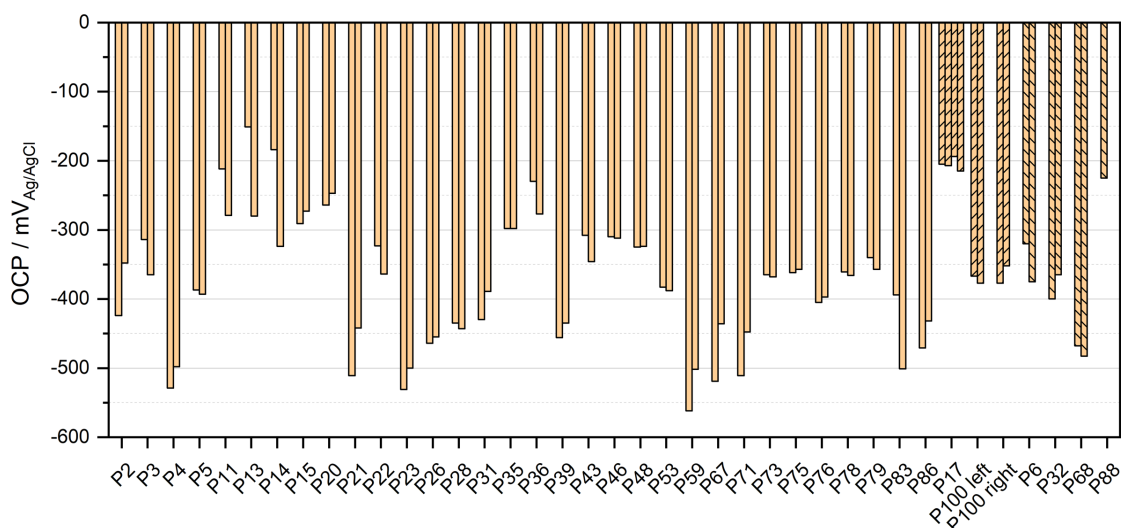


Figure 5.2 Stabilized OCP results of Ti after 20 minutes' immersion in different synovial fluids from PS, TKA (P17 and P100), and R (P6, P32, P68 and P88) group

The stabilized OCP values for CoCrMo samples in contact with synovial fluids are displayed in Figure 5.3. The stabilized OCP varies with patients, being a maximum of  $-300 \text{ mV}_{\text{Ag/AgCl}}$  and a minimum of  $-500 \text{ mV}_{\text{Ag/AgCl}}$ . The OCP values of the two CoCrMo electrodes are quite close, except for in cases P22 and P48, where the values can be more than 50 mV different. This is due to the easier control of the the CoCrMo surface during polishing. Thus, the different OCP values are probably due to contamination during sample storage before the experiment.

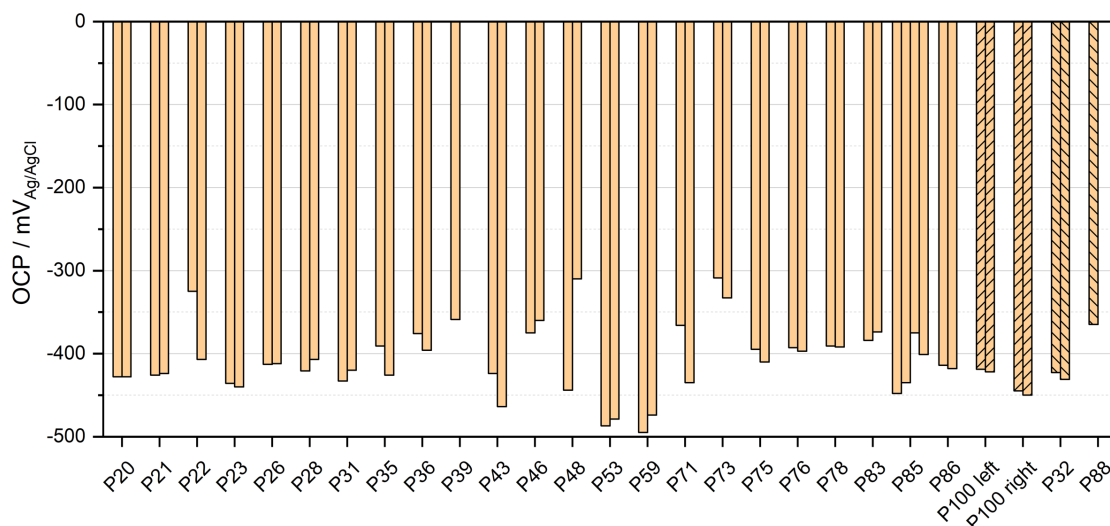


Figure 5.3 Stabilized OCP results of CoCrMo after 20 minutes' immersion in different synovial fluids from PS, TKA (P100) and R (P32 and P88) groups

### 5.1.2 $R_p$ of Ti and CoCrMo Alloy

$R_p$  of one Ti and one CoCrMo alloy was conducted during OCP measurement, and the result of Ti and CoCrMo alloy in synovia from patient 23 is displayed in Figure 5.4 as an example. A linear relationship between current and potential is observed only in the anodic current domain. Different from Ti, a linear relationship between the current and the potential is observed in both cathodic and anodic current domains, indicating that the current is determined by the charge transfer reactions.  $R_p$  was determined as the reciprocal of the slope of the linear part section, as shown in Figure 5.4.

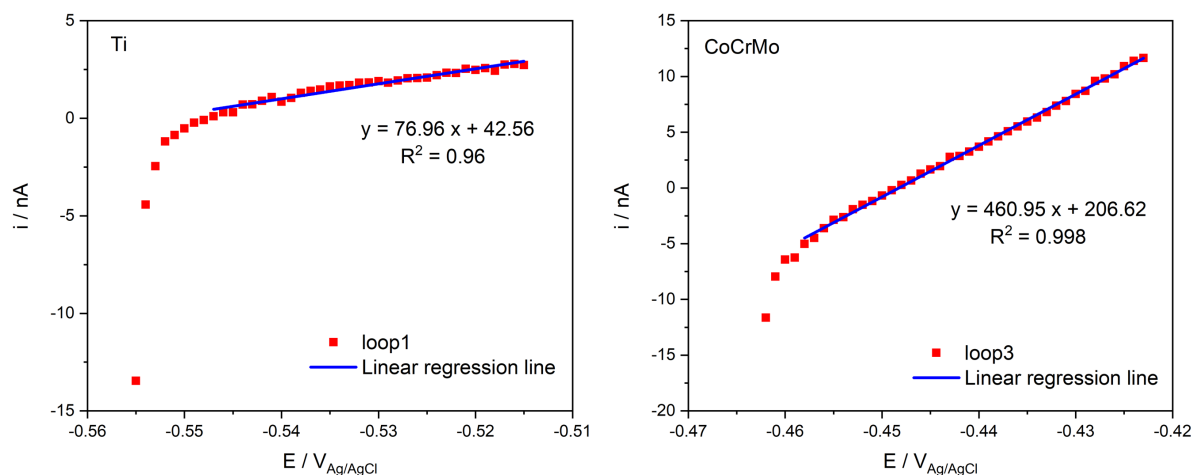


Figure 5.4 Rp measurement of Ti for P6

The obtained Rp values of Ti for all patients are plotted in Figure 5.5. These results indicate that Rp varies significantly with patients, P48 being the highest and P14 the lowest. The difference can be more than 1 order of magnitude. Note that the polarization resistance response differs from an ideal behavior (linear variation of current across the zero-current point) where the current is determined only by the charge transfer reaction kinetics [113]. Only in this ideal case, the reciprocal of the resistance is proportional to the corrosion current density. This is not the case in the present measurements where a linear behavior is only observed in the anodic domain. To interpret the present results, other effects must be considered, such as capacitive effects potentially induced by the presence of the passive film and adsorbed organic molecules. These points will be discussed in Section 5.2.2.

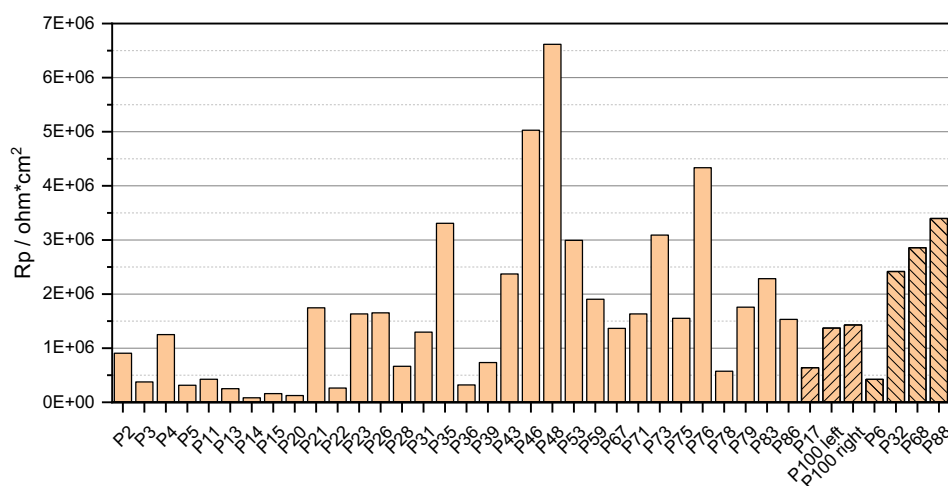


Figure 5.5 Comparison of Rp value of Ti in all synovial fluids from PS, TKA (P17 and P100), and R (P6, P32, P68 and P88) group

The obtained  $R_p$  values for CoCrMo alloy in tested patients are also present in Figure 5.6. Likewise,  $R_p$  of CoCrMo alloy varies significantly with patients, being the highest for P46 and the lowest for P20. The difference can be more than one order of magnitude.

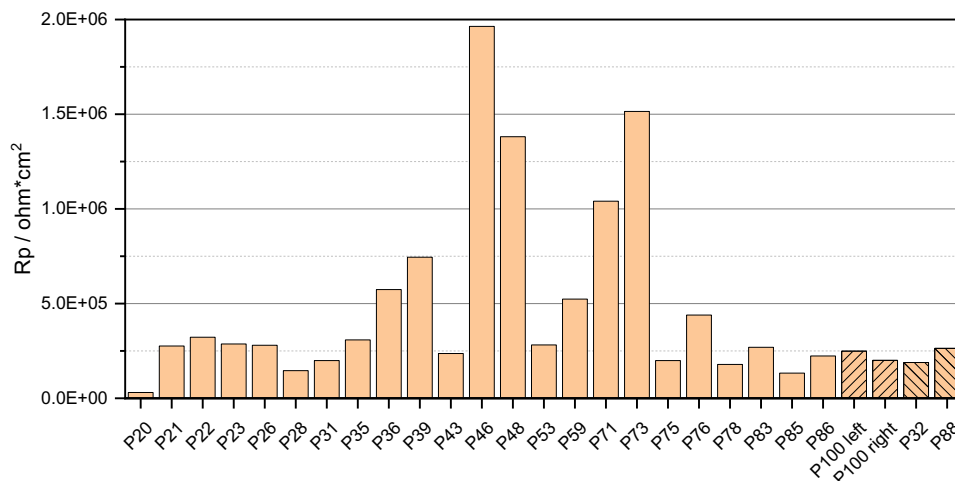


Figure 5.6 Comparison of  $R_p$  values of CoCrMo alloy in tested synovial fluids from PS, TKA (P100) and R (P32 and P88) groups

### 5.1.3 $R_s$ of Synovial Fluids

The electrical resistance of the synovial fluids was extracted from the impedance spectra measured before potentiodynamic polarization and after all measurements were completed, and this is for checking possible changes of the synovial fluids chemistry induced by the polarization and resulting reactions. A typical Bode plot is presented in Figure 5.7. The resistance at a frequency of  $10^5$  Hz is considered as representative of the ohmic resistance of the synovial fluids. They are plotted in Figure 5.8 for the different patients. Clearly, synovial fluids are conductive and present a resistance similar to a simple 0.8% NaCl solution (9 Ohm\*cm<sup>2</sup>). Moreover, no significant difference in the solution resistance tested before and after potentiodynamic scan is obtained.

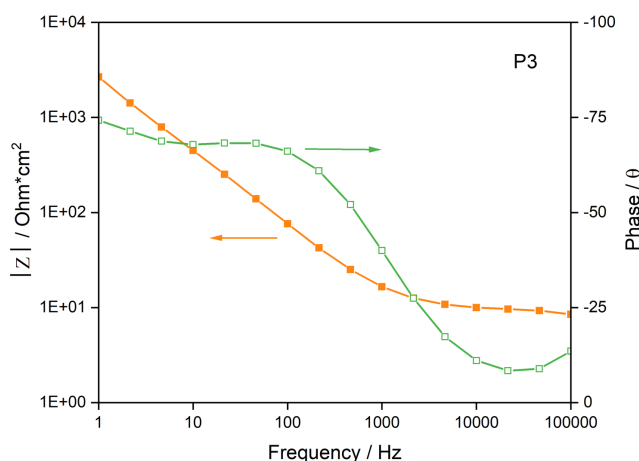


Figure 5.7 Bode plot of Ti in synovial fluid from P3

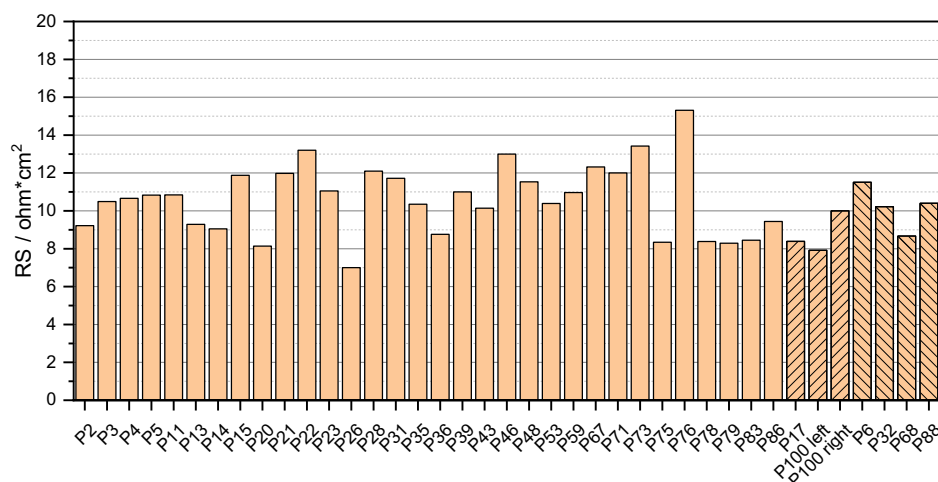
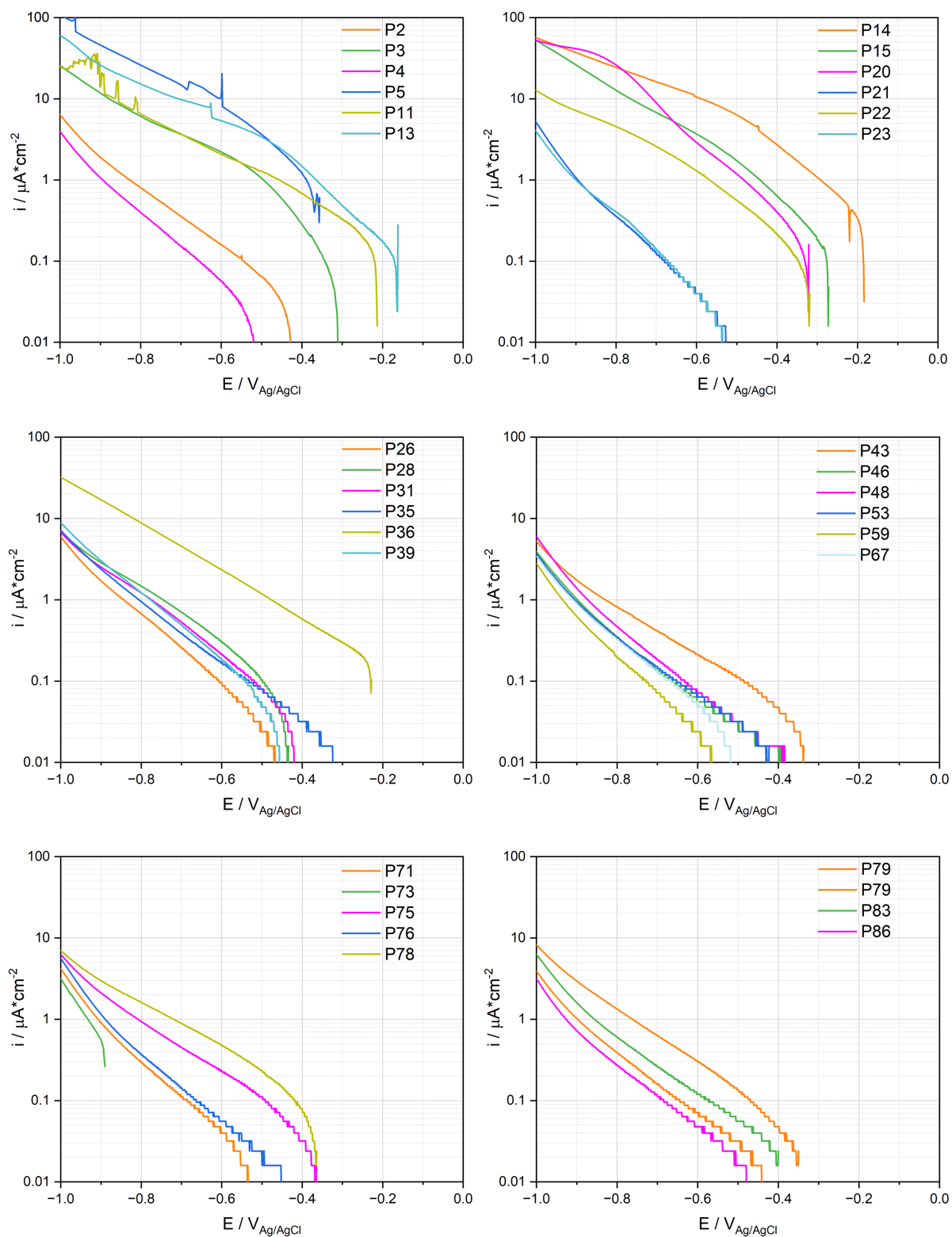


Figure 5.8 Rs of synovial fluids from different patients from PS, TKA (P17 and P100), and R (P6, P32, P68 and P88) group

#### 5.1.4 Potentiodynamic Polarization Curve of Ti and CoCrMo alloy

Potentiodynamic polarization was measured by first cathodically polarizing the samples and reversing the scan to the anodic direction when a potential of  $-1 \text{ V}_{\text{Ag/Ag/Cl}}$  was reached. Figure 5.9 shows the measured cathodic scans on Ti samples. The current density varies significantly depending on the patients. Particularly high current densities are found in the case of P3, P5, P11, P20 and P36. All curves except P5 and P13 exhibit a linear part approximately 100 - 200 mV below the OCP. P3, P11, P15 and P17 exhibit a second linear part at higher polarization with a slightly different slope. This indicates that the cathodic kinetics is under charge transfer control and could involve the reduction of oxygen, protons and/or water. In addition, a linear part with a higher slope at the applied potential lower than  $-0.9 \text{ V}_{\text{Ag/Ag/Cl}}$  is observed for most of the patients, except for P5, P11, P14, P17, P20, P22, P28, P36, P73, P75 and P78.

The different slopes suggest different reaction kinetics under different applied potentials. This behavior will be discussed in the discussion section.





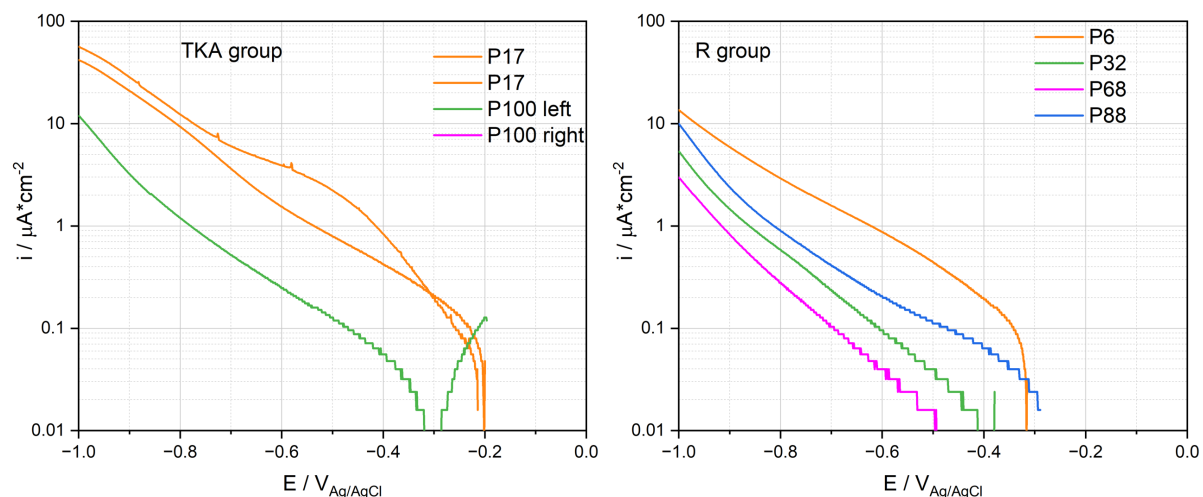
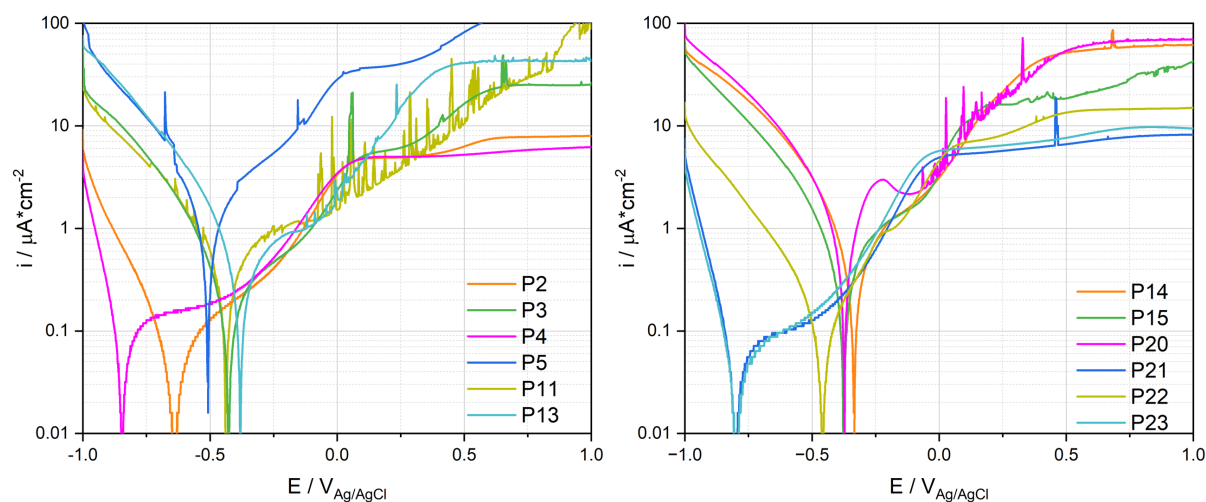


Figure 5.9 Cathodic polarization curves (logarithmic scale of the absolute current density) of Ti tested in synovial fluids from PS, TKA and R group

Anodic polarization curves of Ti for the PS, TKA and R groups are displayed in Figure 5.10. Three reaction domains are observed in polarization curves: the cathodic domain below the corrosion potential ( $E_{\text{cor}}$ ) where the current density is mainly determined by the reduction reaction, the cathodic/anodic transition at  $E_{\text{cor}}$  and the anodic domain at higher potentials. This domain is typically characterized by an initial steady increase in current followed by a plateau. Only P11 does not show any plateau in the investigated potential range.



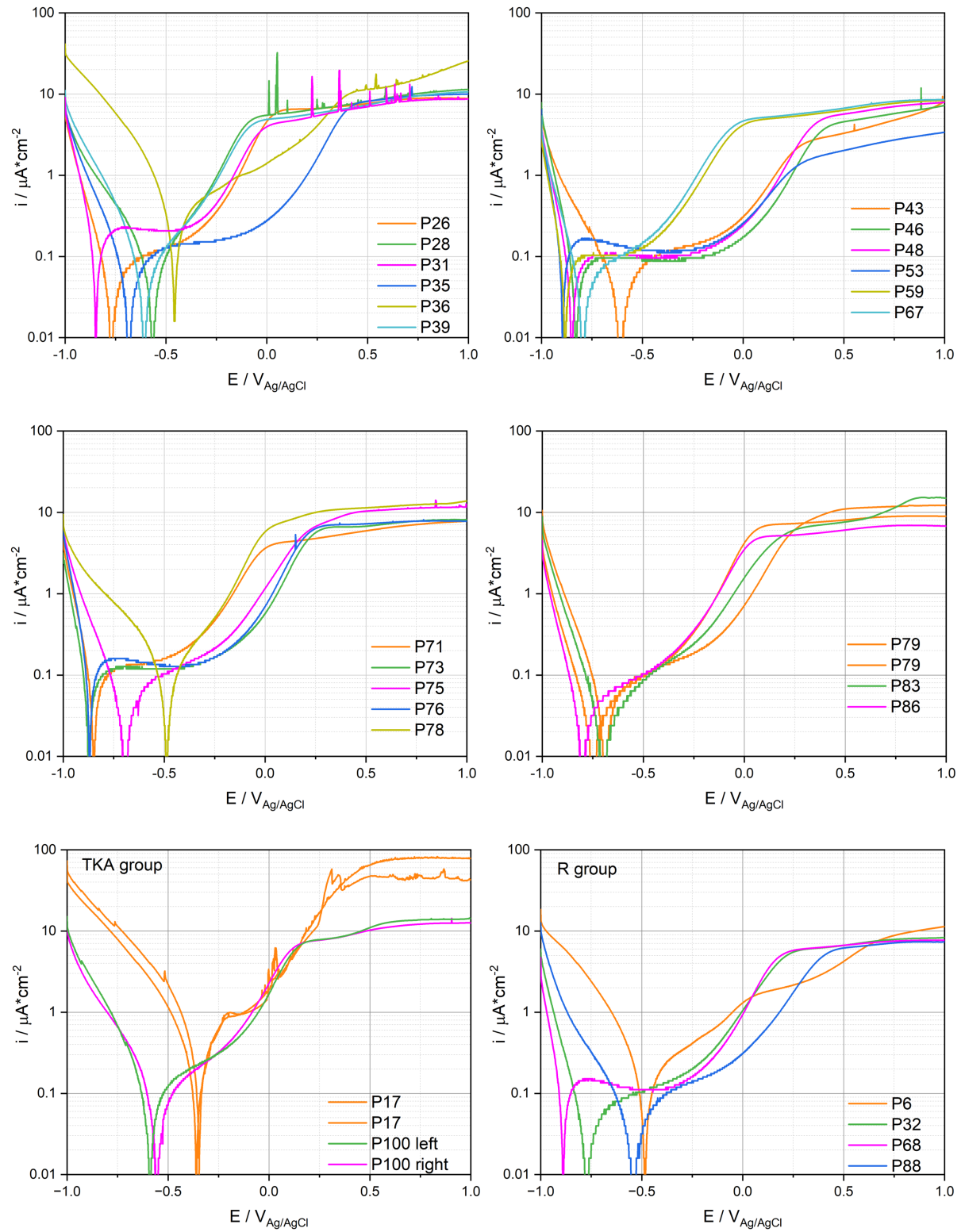


Figure 5.10 Anodic polarization curves (logarithmic scale of the absolute current density) of Ti tested in synovial fluids from PS, TKA and R group

The anodic branch of the polarization curves of P11 and P17 exhibit a sudden current oscillation, for which the origin is not clear. The two polarization curves measured on two Ti sam-

ples in the same fluid from P17 and P79 exhibit very similar behavior in the anodic polarization curves (Figure 5.10), while in the cathodic polarization curves (Figure 5.9), some small differences appear between the two measurements. This good repeatability confirms the pertinence of electrochemical measurements in synovial fluids. Not surprisingly, Figure 5.10 also exhibits large differences in results among patients, as already observed in the cathodic polarization curves.

To quantitatively assess this scatter, characteristic parameters such as the cathodic current density  $i_c$  measured at a potential of  $-0.9 \text{ V}_{\text{Ag/AgCl}}$  in the anodic scan, the corrosion potential  $E_{\text{cor}}$ , and the anodic current density  $i_{\text{pp}}$  measured in the passive range at a potential of 0 and  $0.5 \text{ V}_{\text{Ag/AgCl}}$  were extracted from Figure 5.10 and listed in Table 5.1. Also, the Tafel coefficient  $\beta_c$  was obtained as the reciprocal of the slope of the linear part of the cathodic branch at the potential around 100 mV lower than  $E_{\text{cor}}$ , and converted to the logarithm scale by dividing by 2.303. No linear part of the cathodic current can be found for some patients (P6, 11, 14, 17 and 20), thus the values are not listed in the table.

The  $E_{\text{cor}}$  value ranges between a maximum of  $-0.334 \text{ V}_{\text{Ag/AgCl}}$  to a minimum of  $-0.892 \text{ V}_{\text{Ag/AgCl}}$ . The cathodic current densities listed in Table 5.1 may vary among patients by three orders of magnitude while the anodic values exhibit less variation (one or two orders of magnitude). The  $\beta_c$  value varies from a minimum of 29 mV to a maximum of 167 mV, with the most values located within the range of 30 - 80 mV.

Table 5.1 Electrochemical parameters extracted from the anodic polarization curves of Ti samples

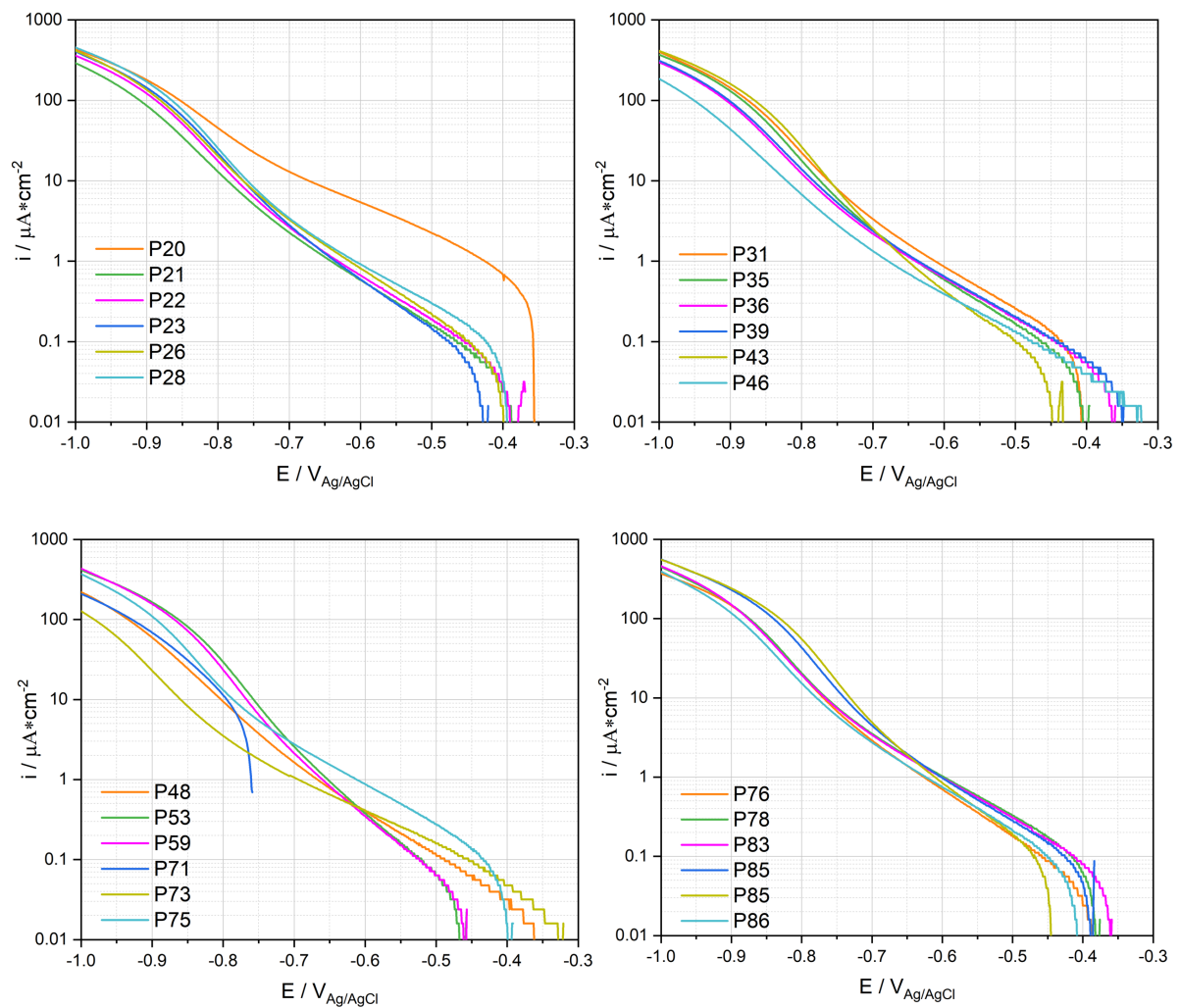
Patient	Anodic Curve				
	$i_c (-0.9\text{V})$ / $\mu\text{A}/\text{cm}^2$	$\beta_c$ / mV	$E_{\text{cor}}$ / $\text{V}_{\text{Ag/AgCl}}$	$i_{\text{pp}} (0\text{V})$ / $\mu\text{A}/\text{cm}^2$	$i_{\text{pp}} (0.5\text{V})$ / $\mu\text{A}/\text{cm}^2$
2	-1.2	84	-0.636	3.32	6.29
3	-13.3	136	-0.425	2.32	16.41
4	-0.2	38	-0.843	3.44	5.23
5	-31.8	149	-0.508	28.23	81.91
11	-10.3		-0.439	1.51	10.46
13	-34.6	139	-0.378	2.21	40.91
14	-35.1		-0.334	3.12	52.16
PS 15	-26.8	158	-0.377	3.62	18.47
20	-43.88		-0.372	7.87	53.85
21	-0.46	42	-0.802	3.29	6.63
22	-4.84	132	-0.458	4.91	13.48
23	-0.36	44	-0.799	4.56	7.65
26	-0.56	48	-0.770	5.56	7.65
28	-1.58	120	-0.567	4.58	8.11
31	-0.45	38	-0.848	5.5	6.99

	35	-1.14	73	-0.679	1.05	8.20
	36	-16.09	149	-0.458	0.28	11.49
	39	-2.30	94	-0.608	0.76	7.36
	43	-0.86	97	-0.610	4.87	3.29
	46	-0.38	38	-0.829	0.32	4.57
	48	-0.21	37	-0.846	0.18	5.68
	53	-0.02	29	-0.892	0.25	2.02
	59	-0.06	31	-0.887	4.15	6.33
	67	-0.33	48	-0.791	4.65	6.70
	71	-0.25	37	-0.852	3.60	5.39
	73	-0.10	32	-0.868	0.57	6.76
	75	-0.80	64	-0.687	1.16	10.36
	76	-0.21	31	-0.869	0.69	7.24
	78	-2.01	167	-0.495	5.75	11.38
	79	-1.15	65	-0.690	0.72	11.01
	79	-0.36	46	-0.685	4.18	8.06
	83	-1.73	56	-0.697	1.57	7.62
	86	-0.22	40	-0.799	3.48	6.07
TKA	17	-25.8	148	-0.346	2.71	47.06
	17	-20.10		-0.357	1.89	64.90
	100 left	-3.22	121	-0.592	1.68	11.02
	100 right	-2.33	94	-0.551	2.27	10.25
R	6	-6.7		-0.487	1.30	4.22
	32	-0.45	45	-0.767	3.96	6.65
	68	-0.05	31	-0.887	0.94	6.67
	88	-1.50	113	-0.537	0.31	6.18
Average		-3.02	74	-0.704	3.33	14.27
STDEV		8.41	47	-0.155	4.57	17.26
Error		7.26	0.93	0.37	4.17	2.83

Note that in the Figure 5.2 and Table 5.1, OCP values differ from  $E_{\text{cor}}$  values. This is not surprising, since they are obtained under different experimental conditions. OCP is measured in absence of any imposed external current. The  $E_{\text{cor}}$  corresponds to the potential in the polarization curves when the current changes its sign, typically at the cathodic to anodic transition. Thus,  $E_{\text{cor}}$  depends on experimental parameters, such as scan rate, current sensitivity, and feedback loop of the potentiostat, that do not affect OCP measurement. From an electrochemical point of view, OCP is the potential spontaneously attained by the electrode immersed in the solution. Note that OCP may change with time due to possible variation of electrolyte, electrode surface and interface (double layer). During measurement of  $E_{\text{cor}}$ , the electrode has already experienced polarization typically at cathodic potential, changing the original electrode state established at OCP. For example, cathodic polarization may modify the passive film and/or adsorbed layers. Thus, during measurement of  $E_{\text{cor}}$ , the electrode is experiencing

the dynamic situation imposed by the potentiostat and the associated test parameters. This electrochemical situation is very different from the OCP measurement conditions. The difference between OCP,  $E_{\text{cor}}$ , and other potentials is extensively discussed in the reference [124].

The cathodic polarization curves of CoCrMo alloy are plotted in Figure 5.11. Contrary to Ti, the current density of CoCrMo alloy varies slightly between the patients. Similarly, all curves exhibit two linear parts: around the region from -0.4 to -0.7  $V_{\text{Ag/AgCl}}$  and from -0.85 to -1  $V_{\text{Ag/AgCl}}$ . The linear curves indicate that the cathodic kinetics is under charge transfer control and could involve the reduction of oxygen, protons and/or water. Also, the different slopes indicate different reaction kinetics take place under different applied potentials. This behavior will be discussed in Chapter 5.2.



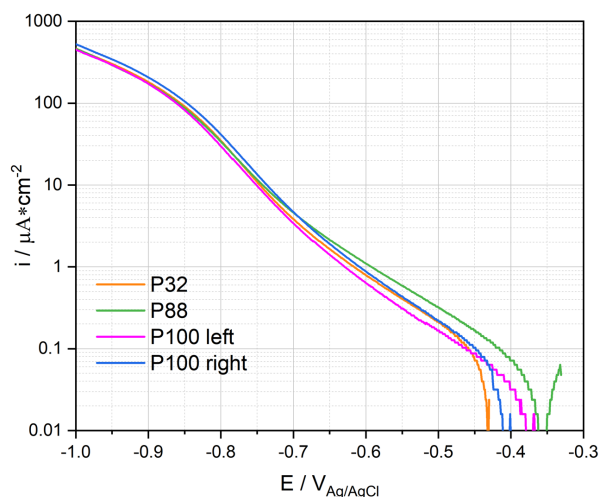
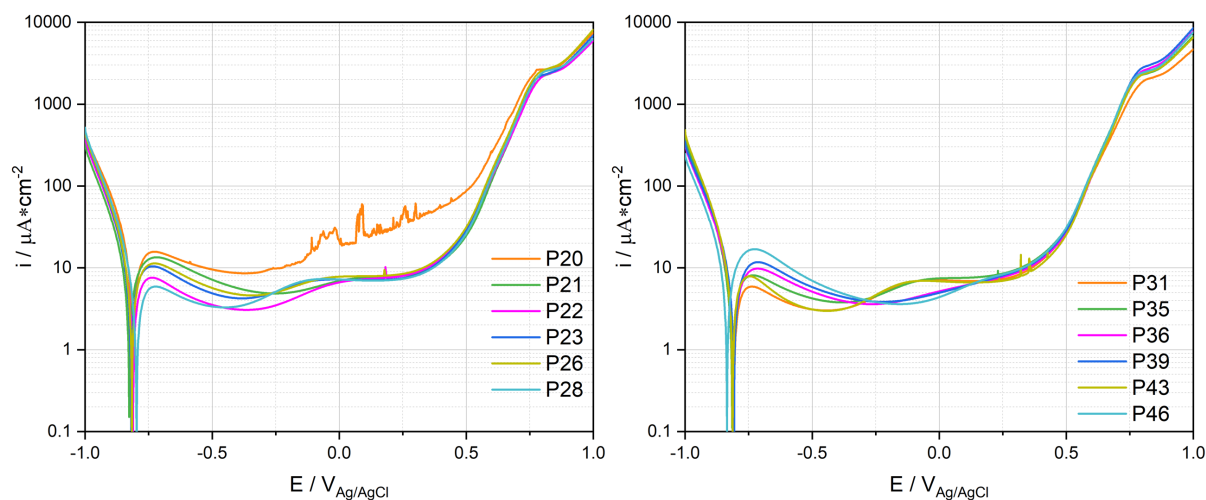


Figure 5.11 Cathodic polarization curves (logarithmic scale of the absolute current density) of CoCrMo tested in synovial fluids from PS, TKA (P100) and R (P32 and P88) groups

Anodic polarization curves of CoCrMo alloy for the synovial fluids obtained from various patients are plotted in Figure 5.12. Four reaction domains are observed in polarization curves: the cathodic domain below the corrosion potential ( $E_{cor}$ ), the cathodic/anodic transition at  $E_{cor}$ , the passive domain within the current plateau and the transpassive domain where the current increase with potential. Likewise, the anodic polarization curves exhibit slight difference among patients.



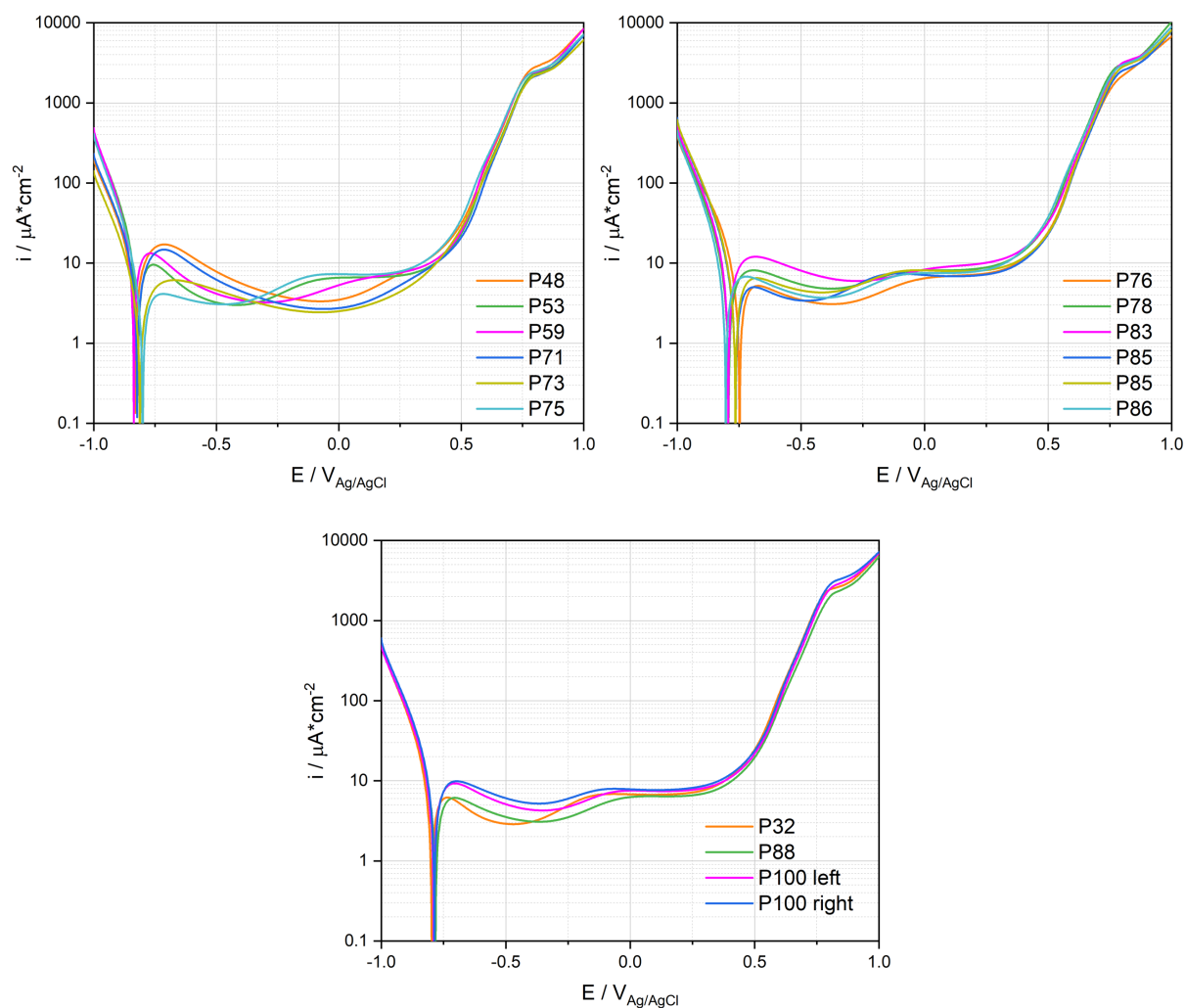


Figure 5.12 Anodic polarization curves (logarithmic scale of the absolute current density) of CoCrMo tested in synovial fluids from PS, TKA (P100) and R (P32 and P88) groups

To quantitatively assess these polarization curves, characteristic parameters such as the cathodic current density  $i_c$  measured at a potential of  $-0.9 \text{ V}_{\text{Ag/AgCl}}$ , the  $E_{\text{cor}}$ , the  $i_{\text{pp}}$  measured at a potential of  $0 \text{ V}_{\text{Ag/AgCl}}$  and the transpassive current density at a potential of  $0.75 \text{ V}_{\text{Ag/AgCl}}$  are extracted from Figure 5.12 and listed in Table 5.2. The  $E_{\text{cor}}$  varies little among the patients, with the STDEV value of 20 mV. The current densities vary among patients by no more than twice of the average, especially the transpassive current density, where the error is only 0.38.

Table 5.2 Electrochemical parameters obtained from the anodic polarization curves of CoCrMo alloys

		Anodic Curve			
Patient		$i_c (-0.9V)$ / $\mu A/cm^2$	$E_{cor}$ / $V_{Ag/Ag/Cl}$	$i_{pp} (0V)$ / $\mu A/cm^2$	$i_t (0.75V)$ / $\mu A/cm^2$
PS	20	-80.19	-0.812	21.26	2032
	21	-42.05	-0.827	6.92	1369
	22	-52.69	-0.812	6.64	1331
	23	-56.36	-0.819	7.22	1615
	26	-59.53	-0.816	7.80	1717
	28	-67.36	-0.798	7.24	1505
	31	-56.36	-0.809	7.07	1171
	35	-51.46	-0.815	7.45	1604
	36	-48.65	-0.809	5.17	1635
	39	-54.03	-0.808	4.96	1767
	43	-60.88	-0.813	6.86	1530
	46	-35.17	-0.835	4.38	1723
	48	-33.32	-0.824	3.49	1928
	53	-61.73	-0.815	6.58	1589
	59	-55.13	-0.836	5.31	1864
	71	-36.71	-0.824	2.74	1488
	73	-22.43	-0.813	2.51	1467
	75	-49.75	-0.802	7.31	1847
	76	-88.14	-0.749	6.46	1445
	78	-70.17	-0.793	8.13	2251
	83	-80.56	-0.805	8.30	1960
	85	-98.16	-0.766	7.12	1623
	85	-103.30	-0.766	8.15	1780
	86	-59.05	-0.805	7.53	2061
TKA	100 left	-79.94	-0.788	7.56	1306
	100 right	-93.03	-0.788	7.85	1493
R	32	-74.45	-0.799	6.79	1524
	88	-79.58	-0.788	6.28	1025
Average		-62.51	-0.805	6.97	1630
STDEV		20.25	0.020	3.21	277
Error		0.65	0.05	1.35	0.38

### 5.1.5 EIS Measurements on Ti and CoCrMo Alloy

Since the polarization curves of Ti and CoCrMo alloy were obtained under polarized conditions, it is important to study the electrochemical behavior under steady state condition. To do this, EIS measurements were carried out on Ti and CoCrMo surfaces in synovial fluids from different patients. Note that the tested patients in this section are different from those for potentiodynamic measurements.



The OCP values of Ti sample after 20 minute's immersion in synovial fluids from P95 to P125 are summarized in Figure 5.13. The values vary from  $-547 \text{ mV}_{\text{Ag/AgCl}}$  to  $-297 \text{ mV}_{\text{Ag/AgCl}}$ , with the variation within the range for P2 to P100 (from  $\text{mV}_{\text{Ag/AgCl}}$   $-560$  to  $-151$ ).

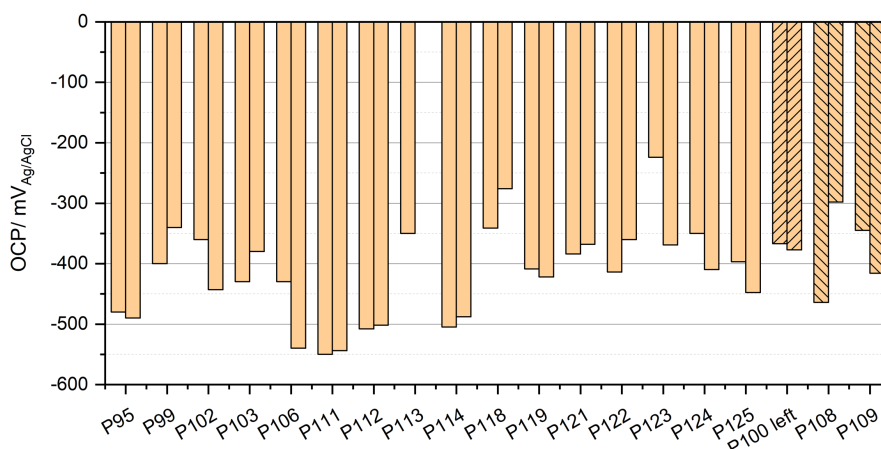


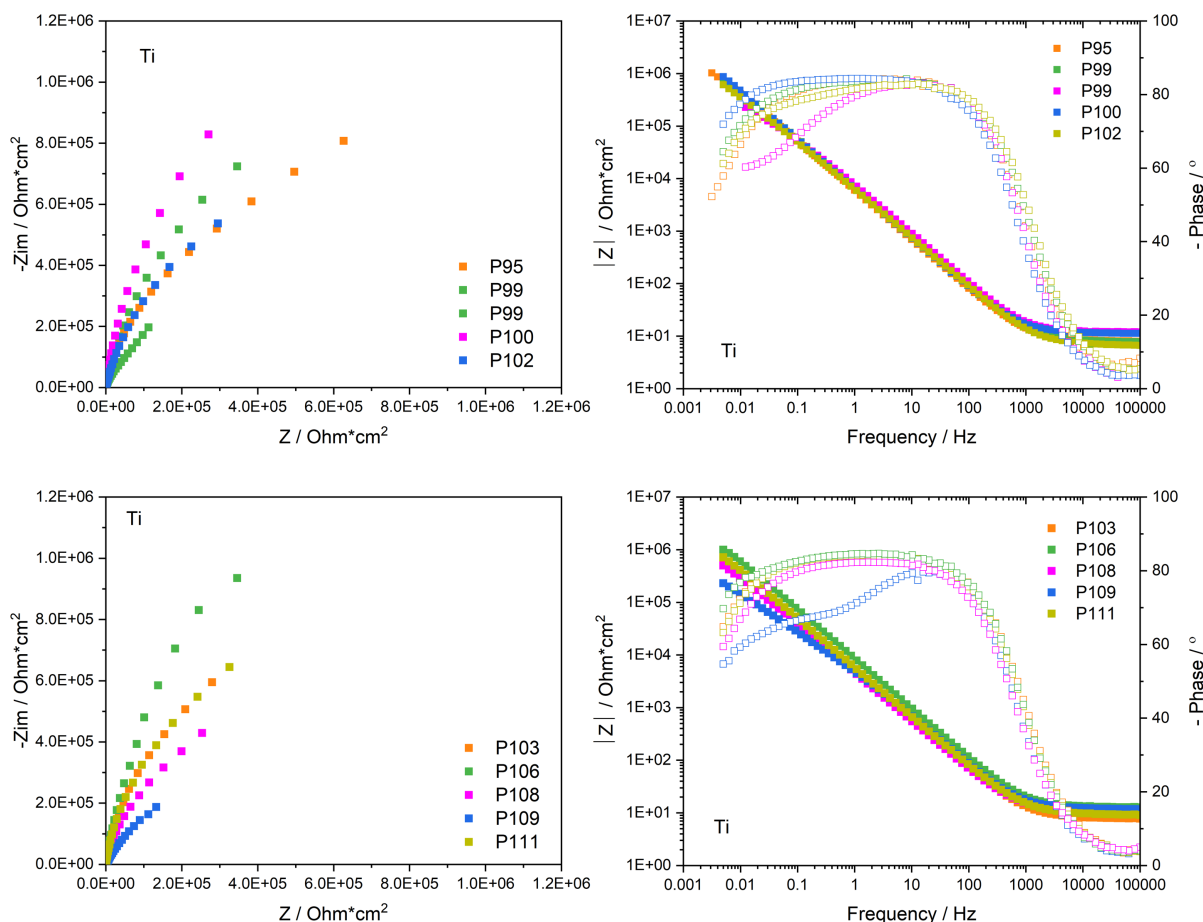
Figure 5.13 Stabilized OCP results of Ti after immersion in different synovial fluids from PS, TKA (P100), and R (P108 and P109) group

The impedance results are plotted in both Nyquist and Bode diagrams, and present in Figure 5.14. The Nyquist plot represents the impedance with the real part  $Z_{\text{re}}$  and the imaginary part  $Z_{\text{im}}$  at different frequencies. The Bode plot represents the modulus  $|Z|$  and the phase shift  $\varphi$  as a function of frequency, where  $|Z|^2 = Z_{\text{re}}^2 + Z_{\text{im}}^2$ . The Bode plot is recommended as a standard impedance plot due to the presence of all parameters, especially phase shift which is sensitive to surface changes [121].

As shown in the figure, all the Nyquist plots exhibit circular arcs with different arc lengths and angles depending on the patients. The arc length relates to the charge transfer resistance, being the shortest for P123 and the longest for P119. The arc angle relates to the property of the oxide film and adsorption layer, being the smallest for P109 and the largest for P119.

In the Bode plots, two distinctive parts depending on frequency are obtained. In the high frequency region, the modulus is almost independent of frequency, where the phase angle is close to  $0^\circ$ . This is a typical behavior of a resistance, and it corresponds to the solution resistance of the synovial fluids between the Ti sample and the RE. In the lower frequency region, the modulus increases linearly with the decrease of frequency, with the slope of -1 and the phase angle reaching to  $-80^\circ$ . For most of the patients, a broad phase plateau is obtained while two apparent time constants are observed for P99, P109, P118 and P123. The two time constants indicating two layers are present on the electrode/electrolyte interface, most probably the organic adsorption layer and the passive film layer. The broad phase plateau suggests the overlap of the two time constants. The higher phase angle of almost  $-80^\circ$  indicates an al-

most perfect capacitor behavior without charge transfer reaction, corresponding to the organic adsorption layer. The lower phase angle obtained at the lowest frequency region reveals a relative less capacitor behavior, corresponding to the passive film layer. These interpretations are in agreement with the literature where the middle frequency and low frequency regions correspond to the organic layer and passive layer, respectively [125–128]. In the lowest frequency region, no modulus plateau is obtained for all patients and the phase angle is around  $-60 \sim -70^\circ$ , indicating the system didn't reach to the steady state condition. Thus, no polarization resistance can be acquired. In consequence, no impedance fitting was carried out.



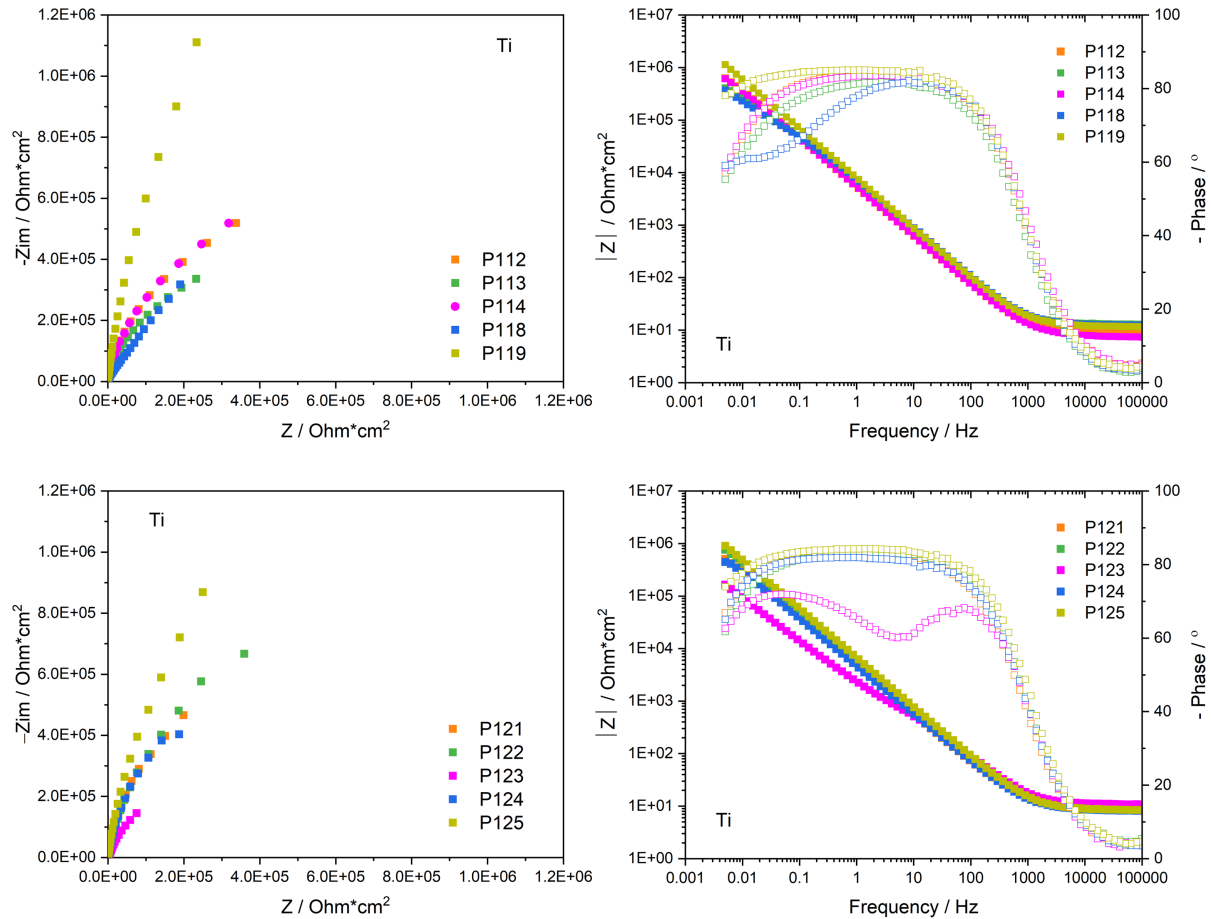


Figure 5.14 Nyquist and Bode plot of Ti in tested synovial fluids

To quantitatively analyze the EIS results, Modulus  $|Z|$  and phase angle were extracted from the Bode plot at the frequency of 0.005 Hz, and the results are summarized in Table 5.3. The  $|Z|$  is used as an alternative result of  $R_p$  to study the reaction resistance of Ti sample in different synovial fluids. Also, the  $R_s$  of the synovial fluids are extracted from Bode plot at the frequency of  $10^5$  Hz. The results show that the  $R_s$  of synovial fluids from P95 to P125 is close among the patients, with an average value of  $10 \text{ Ohm}\cdot\text{cm}^2$ . This value is similar to that for P2 - P100, indicating that all tested synovial fluids possess good and close conductivity. The  $|Z|$  varies with patient, being the highest of  $1135 \text{ KOhm}\cdot\text{cm}^2$  for P119 and the lowest of  $163 \text{ KOhm}\cdot\text{cm}^2$  for P123. The  $|Z|$  values for P95 - P125 are within the range of the  $R_p$  values for P2 - P100. Different from modulus, the phase angle varies slightly with patients, with the average value of  $68^\circ$  and the STDEV of  $7^\circ$ .

Table 5.3 Electrochemical parameters extracted from EIS measurement of Ti samples

Patient		$R_s / \text{Ohm} \cdot \text{cm}^2$	$ Z  / \text{KOhm} \cdot \text{cm}^2$	$-\text{Phase} / ^\circ$
PS	95	7.86	720	58
	99	7.69	802	70
	99	11.97	228	60
	102	6.64	612	67
	103	7.76	657	70
	106	12.65	997	75
	111	9.04	723	69
	112	8.41	620	63
	113	12.93	408	60
	114	7.35	608	64
	118	12.47	371	61
	119	11.60	1135	81
	121	8.75	506	74
	122	9.55	758	71
	123	10.68	163	68
	124	8.15	445	74
	125	8.40	904	78
TKA	100 left	7.92	872	76
R	108	9.88	498	64
	109	11.69	230	58
Average		9.59	613	68
STDEV		1.96	262	7
Error		0.33	0.79	0.34

EIS results conducted on CoCrMo sample surface are displayed in Figure 5.15. Similar to Ti results, circular arcs with different arc lengths and angles are observed depending on patients. Two distinctive parts depending on frequency are also observed in the Bode plots. The  $R_s$  of the synovial fluids between the CoCrMo sample and the RE is obtained in the high frequency region where the phase angle is close to  $0^\circ$ . The linear increase of modulus with the decrease of frequency is observed in the lower frequency region, where the phase angle reaching to  $-80^\circ$ . A broad phase plateau is obtained for all patients. No modulus plateau is observed for all patients, indicating that steady state of the electrode/electrolyte interface was not reached.

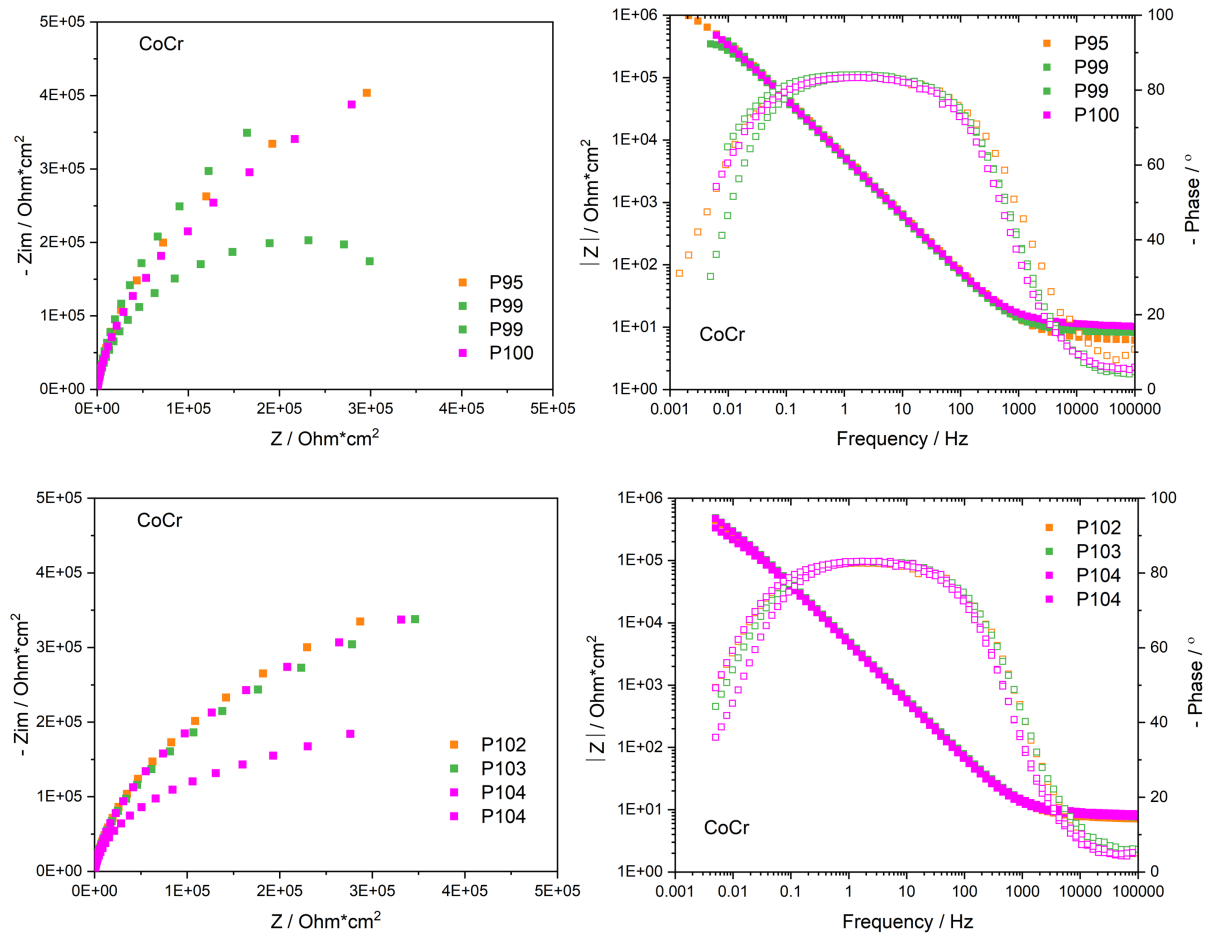


Figure 5.15 Nyquist and Bode plots of CoCrMo alloy in different synovial fluids

To quantitatively analyze the EIS results, the Modulus  $|Z|$  and phase angle were obtained from the Bode plot at the frequency of 0.005 Hz, and the  $R_s$  of the synovial fluids was extracted at the frequency of  $10^5$  Hz. All the parameters are listed in Table 5.4. The  $|Z|$  is used as an alternative result of  $R_p$  to study the reaction resistance of CoCrMo sample in different synovial fluids. The  $R_s$  value of synovial fluids from P95 to P100 varies from 6 to 9  $\text{Ohm}\cdot\text{cm}^2$ . The  $|Z|$  varied slightly with patient, being the highest of 572  $\text{KOhm}\cdot\text{cm}^2$  for P95 and the lowest of 332  $\text{KOhm}\cdot\text{cm}^2$  for P104. The  $|Z|$  values for P95 - P104 are within the range of the  $R_p$  values for P20 - P100. The phase angle varied slightly with patient, being the average value of  $45^\circ$  and the STDEV of  $8^\circ$ .

Table 5.4 Electrochemical parameters extracted from EIS measurements of CoCrMo alloy

Patient	OCP / mV <sub>Ag/AgCl</sub>	Rs / Ohm*cm <sup>2</sup>	Z  / KOhm*cm <sup>2</sup>	-Phase / °	
PS	95	-420	6.07	572	50
	99	-420	8.16	346	30
		-440	9.07	386	52
	102	-445	7.09	441	49
	103	-430	7.54	484	44
	104	-420	7.71	332	34
		-445	8.52	473	46
TKA	100	-420	9.03	478	51
Average		-430	7.90	439	45
STDEV		12	1.02	80	8
Error		0.03	0.17	0.36	0.25

## 5.2 Discussion

### 5.2.1 Electrochemical Reactions of Ti and CoCrMo Alloy in Synovial Fluids

As shown in Figure 5.9 and Figure 5.10, the electrochemical behavior of Ti is patient-dependent, especially for the cathodic reactions. According to the Nernst equation, at the pH of 7 and at 37°C, Oxygen reduction and water reduction take place at the potential lower than 0.6 V<sub>Ag/agCl</sub> and -0.6 V<sub>Ag/agCl</sub>, respectively. Thus, the cathodic current is given in principle by the reduction of water, dissolved oxygen and protons, depending on the applied potential. However, the contribution of proton reduction is estimated to be lower than 0.1  $\mu\text{A}/\text{cm}^2$  at pH 7 [70], thus proton reduction can be disregarded in the following discussion. It is reported that the oxygen tension correlates with the volume of synovial fluids, and the value is around 60 - 80 mmHg for a volume less than 20 mL [39]. Based on Henry's law, the concentration of dissolved oxygen of tested fluids is 1.03 -1.37  $\times 10^{-4}$  mol/L with the henry's constant of 1.3  $\times 10^{-3}$  mol/L atm. So, the oxygen reduction reactions are expected to significantly contribute to the electrochemical behavior in synovial fluids. The electrochemical reduction kinetics of dissolved molecular oxygen is controlled by a number of phenomena, such as the charge transfer at the electrode-solution interface and the mass transport of oxygen from the bulk solution to the interface [113]. Moreover, in body fluids, adsorption of organic molecules may also affect the oxygen reduction by acting as a barrier preventing oxygen from reaching the electrode surface [84, 86]. In conclusion, the oxygen contribution to the reduction kinetics depends on its concentration and the concentration of adsorbing organic species and can thus vary among patients depending on their clinical state. This explains the large scatter in the cathodic kinetics observed in the present study.

Corrosion studies of Ti in simulated fluids have shown that the passive film of Ti mainly consists of  $\text{Ti}_2\text{O}_3$  and  $\text{TiO}_2$ , with the  $\text{TiO}_2$  concentration increasing with potential [45]. The passive current density is determined by the rate of ion transportation through the passive film and the stability of the film against chemical dissolution.  $\text{TiO}_2$  is thermodynamically stable in the pH ranging from 2 to 12, and only dissolves in the presence of specific species, such as HF and concentrated  $\text{H}_2\text{SO}_4$  [16], thus the influence of pH on anodic reaction can be negligible. This deduction can be confirmed by the results found in the literature that the anodic current density varies little with pH from 2 to 7 [129, 130]. The variation of passive current density was observed to depend on the protein concentration [13, 79, 80, 83]. At low concentration, protein can interact with metal ions by forming soluble complexes, thus increasing the dissolution rate of metal, while at high concentration its adsorption inhibits the corrosion [81]. Dissolved ions may also influence the passive current of Ti. For example, it was reported that  $\text{Ca}^{2+}$  ions reduce the cathodic current of Ti by adsorbing onto metal surface [58, 84], while it has little influence on the anodic corrosion behavior [84]. The presence of phosphate contributes to the formation of a protective layer and thus increases the corrosion resistance of Ti [53, 58]. Silicates inhibit the corrosion of Ti in alkaline hydrogen peroxide solutions [131]. According to the AES analysis, the difference in anodic and cathodic current density seems to be determined by the formation of the organic layer on the Ti surface.

Different from Ti, the polarization curves of CoCrMo alloy in synovial fluids is similar among patients, except for P20, where higher cathodic and anodic current are obtained, as shown in Figure 5.11 and Figure 5.12. Based on the Nernst equation, the cathodic current for CoCrMo alloy is also determined by the reduction of water, dissolved oxygen and protons. As discussed for Ti, the oxygen reduction reactions are expected to significantly contribute to the electrochemical behavior in synovial fluids due to the small variation of pH value of around 7 and  $E_{\text{cor}}$  which is higher than  $-0.6 \text{ V}_{\text{Ag}/\text{AgCl}}$ . The reduction kinetics of dissolved oxygen is influenced by the charge transfer at the electrode-solution interface, the mass transport of oxygen from the bulk solution to the interface [113] and adsorption of organic molecules which acts as a barrier preventing oxygen from arriving the electrode surface [81, 82]. However, different from Ti results, the electrochemical behavior of CoCrMo alloy in synovial fluids is less dependent of organic adsorption.

Corrosion studies of CoCrMo alloy in simulated fluids revealed that the passive film of CoCrMo alloy mainly consists of  $\text{Cr}_2\text{O}_3/\text{Cr}(\text{OH})_3$  with a small amount of Co oxide/hydroxide and Mo oxide/hydroxide [15, 50, 132]. The composition and the thickness of the passive film depends on solutions and applied potential. For instance, the fraction of Co oxide/hydroxide significantly decrease with the addition of albumin in NaCl solution [50]. Also, the passive film thickness increases with the applied potential. The passive current density is determined

by the rate of ion transportation through the passive film and the stability of the film against dissolution.  $\text{Cr}_2\text{O}_3$  is thermodynamically stable even in the chloride environment [20], thus the influence of pH on anodic reaction can be negligible. The variation of passive current density was observed to depend on the protein concentration [133]. At low concentration less than 0.5 g/L, protein can interact with metal ions by forming soluble complexes, thus increasing the dissolution rate of metal, while at higher concentration (0.5 g/L) its adsorption inhibits the corrosion. Contrary results are also reported in the literature that the passive current decrease after adding 0.5 g/L BSA [50], while it increases with the addition of BSA to 4 g/L [81]. Ions from the solution may also influence the passive current of CoCrMo alloy. For example, phosphate ions adsorb on sample surface, enhancing the passive dissolution resistance [50, 134]. In the transpassive domain, the current starts to increase with applied potential due to the transformation of Co(II), Cr(III) and Mo(IV) oxide to Co(III), Cr(VI) and Mo(VI) oxide. The latter two oxides are soluble, resulting in the dissolution of passive film. The transpassive current is reported to be influenced by the presence of protein and phosphate ions, which react with metallic ions and enhance the transportation from metal surface to electrolyte [50].

It is worth to note that in a previous study, higher OCP values ranging from  $-83 \text{ mV}_{\text{Ag/AgCl}}$  to  $0 \text{ mV}_{\text{Ag/AgCl}}$  were obtained [5]. In the present study, those values lie between  $-300 \text{ mV}$  and  $-500 \text{ mV}$ . The much higher OCP obtained from that research is attributed to the higher cathodic current density compared to this thesis. However, the passive current density and the transpassive current density obtained in that study are quite close to those shown in this thesis. The different OCP values could be related to the different sterilization methods used in that study where the samples were sterilized in an autoclave under saturated steam at  $121^\circ$  for 20 minutes. Indeed, the corrosion behavior of CoCrMo alloy in NaCl solution depends on the sterilization methods [135]. The OCP of CoCrMo alloy sterilized in the autoclave is about 0.3 V higher than that sterilized with ethanol, and the cathodic current density is about two times higher. The higher OCP and cathodic current density are because of the lower passive film thickness for CoCrMo alloy sterilized in an autoclave [135]. Based on the results, the conclusion can be drawn that the much higher cathodic current density of CoCrMo alloy in synovial fluids, obtained in the study, is due to the different sterilization methods by altering the surface chemistry.

The corrosion current density  $i_{\text{cor}}$  can be obtained by extrapolating the linear part of the logarithmic plots illustrated in Figure 5.9 and Figure 5.11 to the OCP potential. Depending on the patient, the  $i_{\text{cor}}$  values of Ti range between the extremes of  $0.02$  and  $2 \mu\text{A}/\text{cm}^2$  with however most of the patients lying in the narrower range from  $0.02$  to  $0.5 \mu\text{A}/\text{cm}^2$ . Corrosion current densities of Ti measured in body simulated fluids span in a very similar range from  $0.02$  to



0.6  $\mu\text{A}/\text{cm}^2$ , but relatively high corrosion current densities observed in P5 were never been reported [84, 136]. The  $i_{\text{cor}}$  values of CoCrMo alloy for most patients are around 0.1  $\mu\text{A}/\text{cm}^2$ , except for P20, which is around 0.6  $\mu\text{A}/\text{cm}^2$ . Corrosion current densities of CoCrMo alloy measured in simulated body fluids varies in a similar range from 0.2 to 10  $\mu\text{A}/\text{cm}^2$  [40, 132].

To compare the corrosion rate with real conditions, the corrosion current density ( $\text{A}/\text{m}^2$ ) can be converted to mass loss  $m_{\text{cor}}$  ( $\text{mg}/\text{dm}^2/\text{day}^1$ ) through Faraday's law with the equation as below:

$$m_{\text{cor}} = 8640Mi_{\text{cor}}/nF \quad (5.1)$$

where  $M$  is the atomic mass: 48 g/mol (Ti), 59 g/mol (Co), 52 g/mol (Cr) and 96 g/mol (Mo),  $F$  is Faraday constant: 96,485 A s/mol, and  $n$  is its oxidation valence which is assumed to be 4 (Ti), 2 (Co), 3 (Cr) and 4 (Mo). The mass loss for each material obtained from the equation is displayed in Figure 5.16, showing that the metal ion release rates depend on the patients. The release rates of Co, Cr and Mo are calculated by assuming the amount of released metal ions is proportional to the bulk alloy composition.

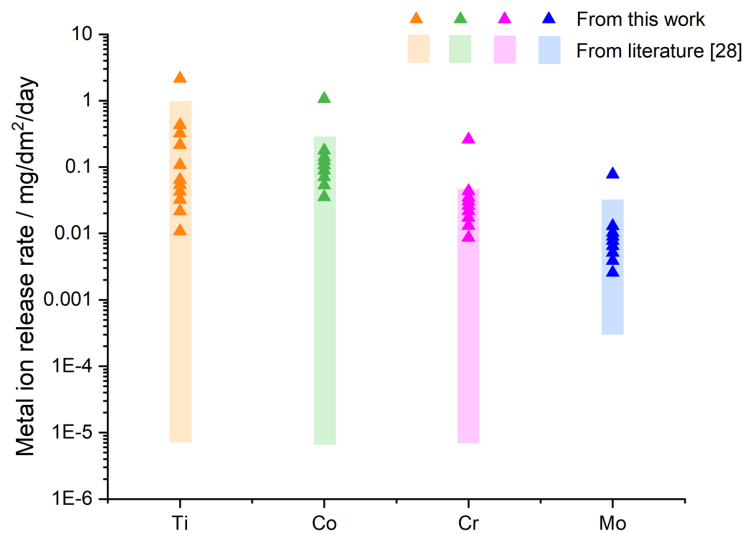


Figure 5.16 Metal ion release rates obtained from this work and from literature [28]

Although the concentrations of metallic ions in serum, plasma, whole blood, and urine are largely reported in the literature, no information on actual in-vivo corrosion rates of titanium can be found. The corrosion rate can be tentatively estimated by considering that, in case of no further ion accumulation in the body, it corresponds to the release rate of titanium through urine. This is a coarse assumption, as ions can be eliminated through other ways, such as sweat and hair growth [3]. The typical urine release rate of human bodies is approximately 1.5 l per day. Ti/Co/Cr/Mo concentration in urine for patients with hip and knee implants was reported by Matusiewicz [28], as summarized in Table 2.2. Considering an approximative

titanium or CoCrMo exposed implant surface of 1 dm<sup>2</sup>, this yields an elimination rate of Ti/Co/Cr/Mo through urine in the range  $6 \times 10^{-6}$  mg/dm<sup>2</sup>/day to 1.2 mg/dm<sup>2</sup>/day, as displayed in Figure 5.16. This range corresponds well to the corrosion rates observed here. This suggests that corrosion is an important factor responsible for the release of Ti/Co/Cr/Mo ions from metallic implants.

### 5.2.2 Comparison with Measurements in Simulated Fluids

The polarization curves measured for P4 and P5 are plotted in Figure 5.17, together with the representative polarization curves measured in simulated solutions. These patients define the envelope of all the curves measured on patients (see Figure 5.10). Interestingly the cathodic part of the curve measured in NaCl solution lies outside the envelope of the in-vivo measurements. Adding BSA and HA moves the polarization curve (cathodic part) into the in-vivo domain, especially for BSA. The addition of H<sub>2</sub>O<sub>2</sub> generates very high cathodic currents. This is not surprising as hydrogen peroxide is a strong oxidizing agent. This may indicate that the cathodic reactivity of Ti in synovial fluids is mainly determined by the presence of organics species that likely affect the reduction rate, and thus the corrosion rate, by adsorbing on the metal surface. The cathodic currents for the rest patients located in the envelope of the P4 and P5 measurements could be due to the different concentrations of organics, which reduces the cathodic current depending on the concentration. This hypothesis is supported by the polarization curves of Ti in simulated solutions with various concentrations of BSA and HA, that are displayed in Figure C. 3, shown in the Appendix.

It is worth noting that a larger current slope at the potential lower than -0.8 V<sub>Ag/AgCl</sub> is obtained in the cathodic polarization curve for P4 as well as other patients, as shown in Figure 5.9. Similar behavior is also observed for simulated solutions with the addition of BSA but not for HA, as shown in the rectangle area. This suggests that compared with HA, protein is most likely the determining factor for these patients that influences the corrosion behavior of Ti in synovial fluids. Additionally, higher adsorption intensity for FTIR measurements is obtained for the samples where larger current slope is observed. Similar results were reported on CoCrMo alloy tested in NaCl and NaCl + BSA (30 g/L) solutions [69].

Interestingly, the anodic domain is less affected by the nature of the environment than the cathodic one. The results for simulated fluids do not allow to reproduce the high anodic current densities observed in P5, even when adding a strong oxidizing agent. This indicates that the oxidative strength of the solution is not necessarily the key parameter. Possibly, the large anodic currents obtained in P5 are due to specific molecules in synovial fluid, such as protein [81, 85], that promote passive film dissolution.

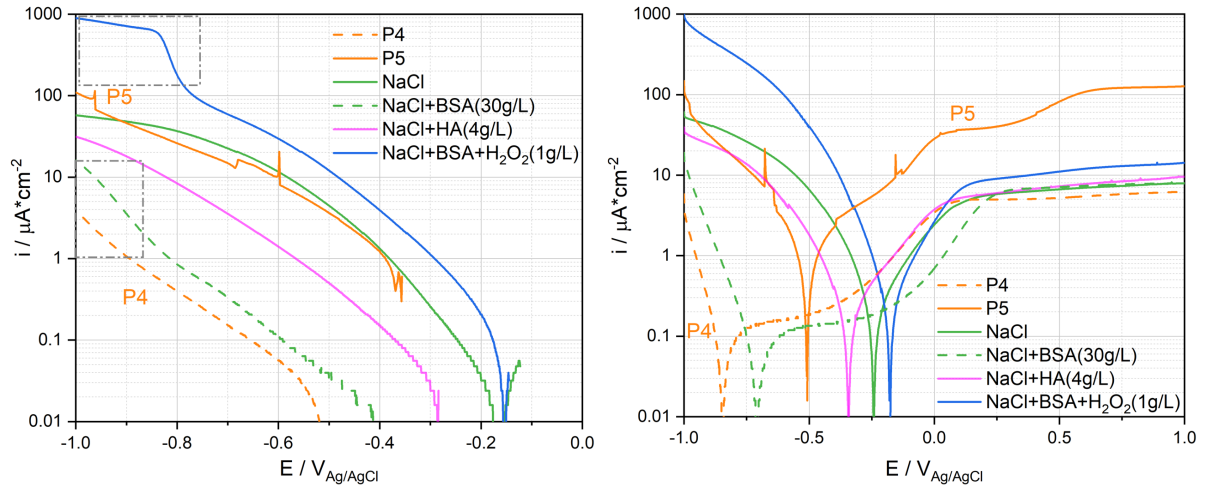
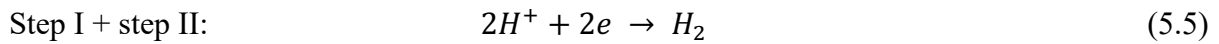
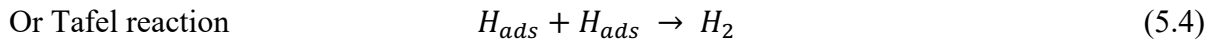
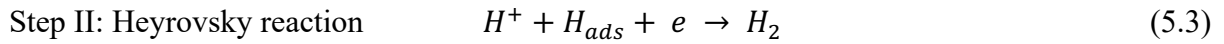
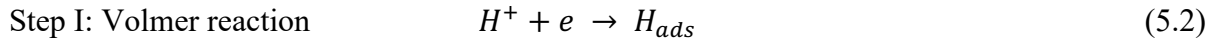


Figure 5.17 Polarization curves of Ti tested in synovial fluids and simulated solutions

In the cathodic domain, the reduction of oxygen and protons takes place at the metal oxide-electrolyte interface. For example, the proton reduction takes place in two steps. The protons are first reduced to adsorbed hydrogen atoms, followed by the formation of hydrogen molecules, either by electrochemical reaction between a proton and an adsorbed hydrogen atom or by chemical reaction between two adsorbed hydrogen atoms [113]. The detailed reactions are listed below:



If step I is the rate determining reaction, the cathodic reaction is determined by the charge transfer reaction. Then, the cathodic Tafel coefficient equals to

$$\beta_c = \frac{RT}{\alpha_c F} = 120 \text{ mV}$$

Where  $T = 25^\circ\text{C}$ , and charge transfer coefficient  $\alpha_c = 0.5$ .

If step II is the rate determining reaction, the cathodic reaction is determined by the amount of adsorbed hydrogen. This results in the cathodic Tafel coefficient

$$\beta_c = \frac{RT}{2F} = 30 \text{ mV}$$

The detailed calculation of the Tafel coefficient  $\beta_C$  at different reaction conditions is explained in [113]. The  $\beta_C$  value for the oxygen reduction mechanisms is quite close to that of hydrogen reduction [137].

The Tafel coefficients  $\beta_C$  obtained from the anodic polarization curves for P4 and P5 correspond to the above reaction mechanisms. For P4, Tafel coefficient  $\beta_C$  of 38 mV is obtained, corresponding to the low cathodic current and thick organic layer on the sample surface. For P5, Tafel coefficient  $\beta_C$  of 149 mV is obtained, where a higher cathodic current and little organic layer on the sample surface is observed. The  $\beta_C$  value extracted from the rest patients are located with the envelope of 30 - 120 mV (taking the scatter into account), suggesting different amount of organic adsorbed on sample surface, which reduces the amount of adsorbed hydrogen. This assumption is confirmed by the  $\beta_C$  values (Table B.3 in Appendix) obtained from the simulated solutions with different concentration of BSA, where the value decreases with the addition of BSA. It should be noted that the  $\beta_C$  value depends on solutions, applied potential and materials, which is widely discussed in the literature [137].

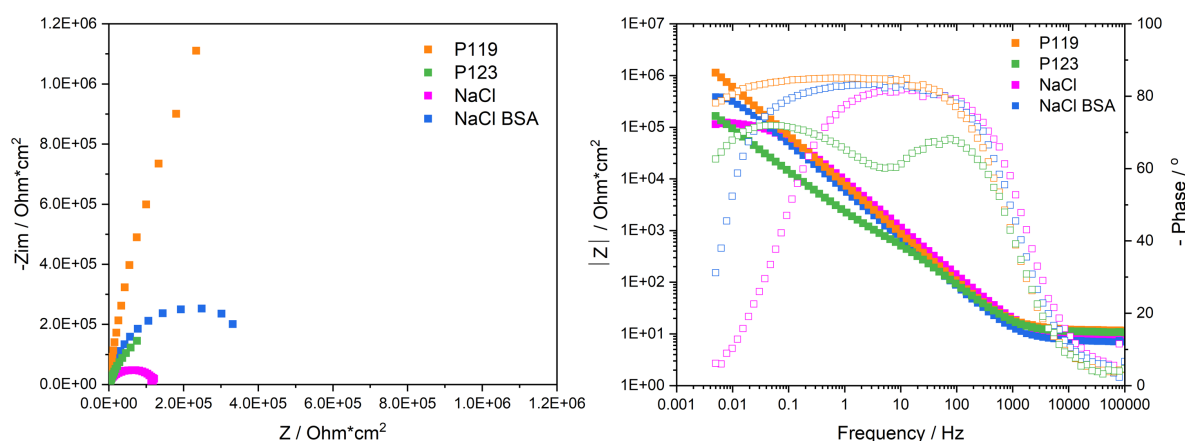
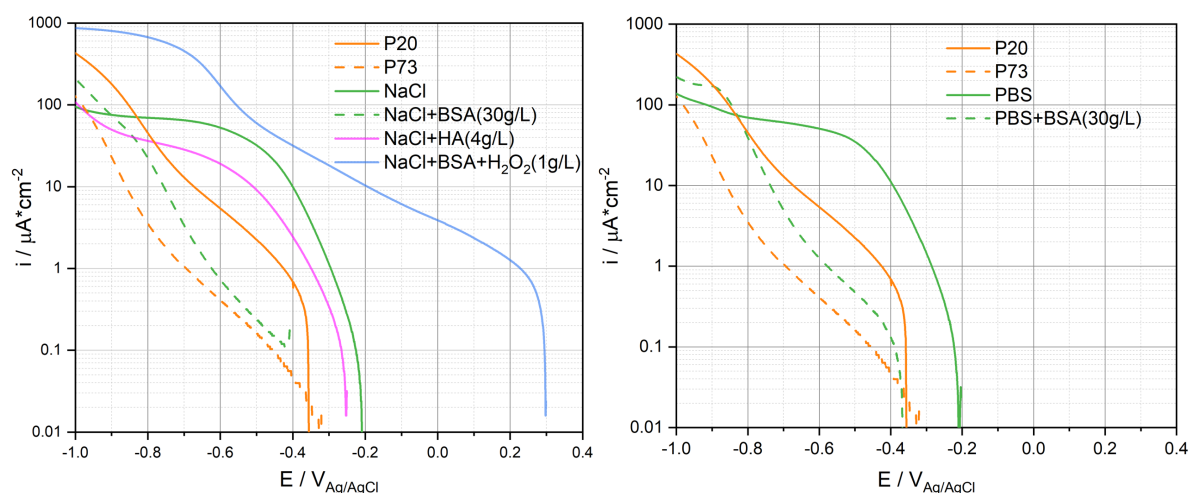


Figure 5.18 Nyquist and Bode plots of Ti in synovial fluids and simulated solutions

In addition, the extreme Nyquist and Bode plot of Ti in synovial fluids from P119 and P123 are plotted together with NaCl and NaCl + BSA (30 g/L) solutions, as presented in Figure 5.18. The modulus at the  $f = 0.005$  Hz for patients are higher than that for NaCl solution, and a broader phase shift is also observed for patients. The arc angle and arc length increase with the addition of BSA, namely the modulus is significantly enlarged. Similarly, the higher modulus for patients could be related to the organic adsorption on the sample surface. Indeed, a lower OCP value is obtained for P119 compared with that for P123, where lower modulus was obtained. The EIS results correspond well with the polarization curves, which supports the hypothesis that the different in-vivo electrochemical behavior is probably due to organic adsorption.

It is worth noting that the different modulus could also be due to the variation of potential, namely a higher anodic reaction rate was obtained with the increase of OCP according to the polarization curves presented in Figure 5.17.

The extremes polarization curves measured for P20 and P73 are displayed in Figure 5.19, together with the representative polarization curves measured in simulated solutions. The cathodic current ( $> -0.85$  V) measured in the NaCl solution is higher than the in-vivo results. Adding BSA and HA moves the polarization curve (cathodic part) close to the in-vivo domain, especially for BSA. The addition of  $H_2O_2$  generates very high cathodic currents, which is not observed in the in-vivo results. This may indicate that the cathodic reactivity of CoCrMo alloy in synovial fluids is mainly determined by the presence of organics species that adsorbed on the surface of the metal. The cathodic currents for the tested patients are quite similar to that found for BSA (5 g/L and 30 g/L) containing solutions, as shown in Appendix Figure B.12. This suggests protein plays a key role on the corrosion behavior of CoCrMo alloy in synovial fluids, and its concentration of tested synovial fluids is higher than 0.5 g/L.



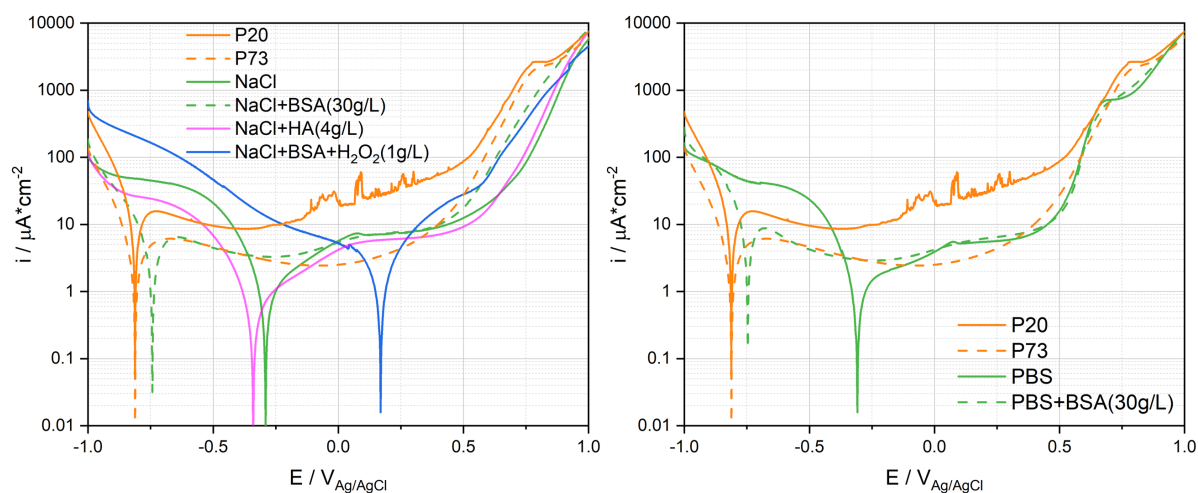


Figure 5.19 Cathodic and anodic polarization curves of CoCrMo alloy tested in synovial fluids and simulated fluids

A larger current slope at the potential lower than  $-0.8 \text{ V}_{\text{Ag/AgCl}}$  is also obtained in the cathodic polarization curve for CoCrMo samples in all patients. Similar behavior is observed for simulated solutions with the addition of BSA but HA, as shown in the cathodic polarization curves. This suggests that compared with HA, protein adsorbed and interacted with oxides is most likely the key factor for these patients that influence the corrosion behavior of CoCrMo alloy in synovial fluids. Similar results were obtained on CoCrMo alloy tested in NaCl and NaCl + BSA (30 g/L) solutions [69].

The anodic domain is less affected by the nature of the environment than the cathodic one. The addition of BSA, HA and phosphate doesn't influence the passive current density, while the transpassive current increases after adding BSA and phosphate. This is because of the reaction between metallic ions with BSA and phosphate, enhancing the dissolution of metallic ions. In addition, a current shoulder is observed for in-vivo results at the potential of 0.75 V. Similar current shoulder at the potential of 0.7 V is also obtained for PBS based solutions due to the reaction between metallic ions and phosphate [50]. The presence of current shoulder in the transpassive domain indicates that phosphate is present in synovial fluids and enhances the transpassive reaction rate of CoCrMo alloy.

The Tafel coefficients  $\beta_C$  obtained from the anodic polarization curves is about 50 - 60 mV, independent of the organic adsorption amount on sample surface. This value is close to the Tafel coefficients  $\beta_C$  (30 mV) for Tafel reaction, which is controlled by the amount of hydrogen adsorption on sample surface. The different  $\beta_C$  value could be related to different materials, as is discussed in the literature [137].

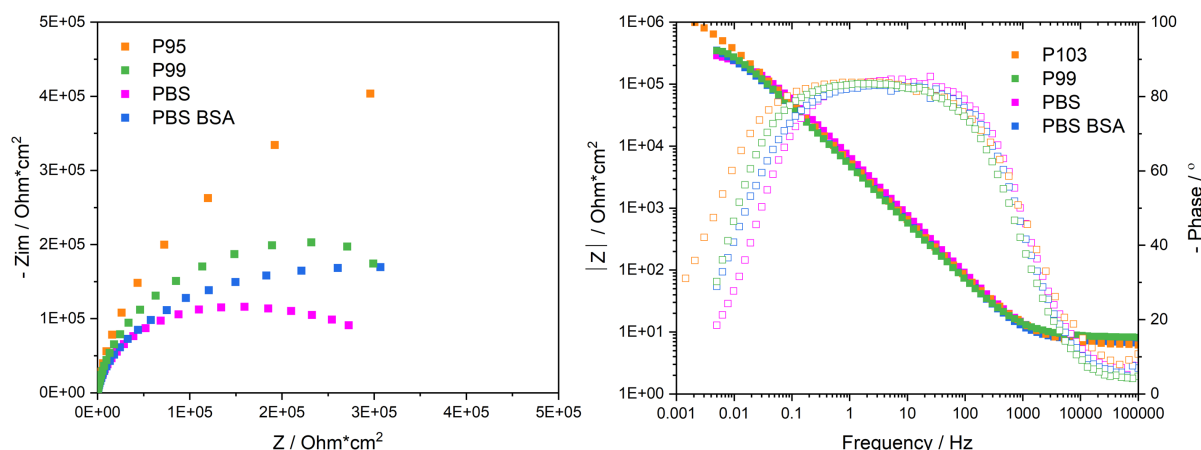


Figure 5.20 Nyquist and Bode plots of CoCrMo alloy for P95, P99 and simulated solutions

According to the in-vivo and in-vitro polarization curves, PBS and PBS + BSA (30 g/L) solutions can best simulate the in-vivo corrosion behavior of CoCrMo alloy in synovial fluids. To further understand the corrosion behavior, the EIS results for P99 and P103, the extreme cases, are plotted together with that in PBS and PBS + BSA (30 g/L) solutions, as shown in Figure 5.20. The Nyquist diagram shows that the diameter of the semicircle obtained in PBS + BSA is larger than that in PBS, indicating the polarization resistance increases with the addition of BSA. This is related to the BSA adsorption, which acts as a physical layer for the corrosion reaction. The highest diameter of the Nyquist plot obtained from P103 indicates that the corrosion rate is lower than in-vitro measurements. These results are supported by the shift phase value in the Bode plot.

The peculiar behavior observed in Figure 5.4 during the measurement of polarization resistance can also be attributed to an effect of proteins. Figure 5.21 compares the obtained results for P4 and P5 as well as the corresponding results obtained in 0.8% NaCl and in 0.8% NaCl with 30 g/L of BSA. For the sake of clarity, the polarization ( $E - E_{cor}$ ) was reported in the abscissa instead of the actual electrode potential  $E$ . In the simple NaCl inorganic solution, a well-defined linear behavior crossing the zero current is observed. Deviations from linearity are observed at the onset of polarization at the cathodic potential. This is likely related to the capacitive effects due to double layer and passive film charging. Indeed, tests carried out at a lower scan rate (0.6 mV/s) showed an identical behavior but with a much smaller deviation from linearity at the onset of polarization. Interestingly, the response of P5 is quite close to the behavior observed for NaCl solution (same slope in the anodic domain) with, however, a larger deviation from linearity in the cathodic domain possibly due to differences in open circuit potential (nearly 200 mV) and the associated differences in the double layer structure, adsorption, and passive film properties. Compared to P5, P4 shows a higher polarization resistance (reciprocal of the slope in the anodic domain). Interestingly, the same trend is found when adding BSA to the NaCl solution. This further supports the interpretation of Figure

5.17, indicating that the organic substances play a key role in the electrochemical response of titanium exposed to synovial fluids.

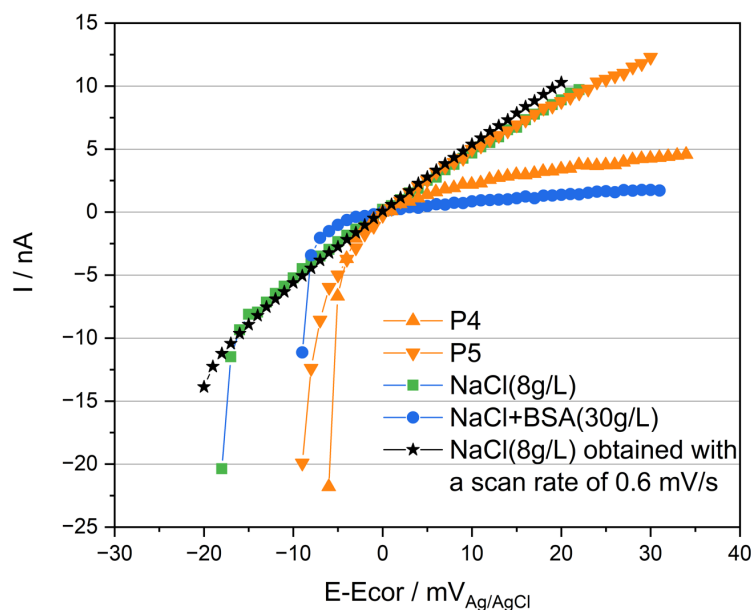


Figure 5.21 Rp measurements of Ti tested in simulated fluids and in synovial fluids with different scan rates

In addition to organics, ions, such as phosphate and calcium, are also detected in human synovial fluids [30, 31]. The presence of calcium is confirmed by the EDS analysis of the particles. To study the influence of the ions on the electrochemical behavior of Ti and CoCrMo alloy in synovial fluids, same measurements were carried out in simulated solutions, and the results are presented in Figure C. 3, Figure C. 12, Table C. 3 and Table C. 7 in Appendix. The results indicate that phosphate has little influence on the electrochemical behavior of Ti in NaCl solution, while calcium ions slightly reduce the anodic current at the potential lower than  $0.5 V_{Ag/AgCl}$ . Similar results are also reported in the literature [57, 58]. These results suggest that the different anodic current at the first initial region could be related to the adsorption of calcium ions. However, calcium ions have little influence on the electrochemical behavior of CoCrMo alloy in NaCl solution



### 5.3 Summary

This study is the first systematic investigation of the electrochemical response of Ti and CoCrMo alloy exposed to human synovial fluids extracted from various patients. It leads to following conclusions:

- The electrochemical response of Ti in both cathodic and anodic domains was found to significantly (several orders of magnitude) vary among patients. However, the electrochemical response of CoCrMo alloy varies slightly with patients.
- The calculated metal ion release rates extracted from the polarization curves depend on the patients, being from  $0.025 \mu\text{A}/\text{cm}^2$  to  $2 \mu\text{A}/\text{cm}^2$  ( $6\text{E-}6$  to  $1.2 \text{ mg dm}^{-2} \text{ day}^{-1}$ ) for Ti and from  $0.1 \mu\text{A}/\text{cm}^2$  to  $0.6 \mu\text{A}/\text{cm}^2$  ( $6\text{E-}6$  to  $0.3 \text{ mg dm}^{-2} \text{ day}^{-1}$ ) for CoCrMo alloy. These values are found to be consistent with the Ti release rate from hip and knee artificial joints implanted in humans.
- The corrosion rate of Ti and CoCrMo alloy in synovial fluids is determined by the charge transfer reaction of oxygen reduction and organic adsorption on the sample surface. The former conclusion is drawn based on the OCP values of Ti CoCrMo alloy, which are higher than the equilibrium potential of the hydrogen reduction, and the cathodic polarization curves, where no current plateau is obtained. The latter conclusion is supported by the fact that simulated body fluids containing organic molecules such as BSA and HA can better simulate the in-vivo electrochemical behavior of Ti and CoCrMo alloy than those containing oxidizing agents such as  $\text{H}_2\text{O}_2$ .

## Chapter 6      Ex-situ Surface Analysis of Ti and CoCrMo alloy in Human Synovial Fluids

As discussed in the former chapters, the corrosion behavior of Ti and CoCrMo alloy depends on patients, where the cathodic reactions are determined by oxygen reduction and organic adsorptions on sample surface. However, the anodic reaction of both materials in contact with synovial fluids cannot be predicted by tested simulated solutions. To further understand the different corrosion behavior, in this chapter, the surface qualitative morphology, chemistry and passive film thickness was investigated on Ti and CoCrMo surfaces, after exposure to synovial fluids and sterilization in ethanol, using SEM, FTIR/EDS and AES, respectively. The surface analysis results can qualitatively identify the adsorbed organics on sample surface and quantitatively characterize the chemical composition and thickness of the passive film. This information can help to understand the cathodic and anodic reaction behavior of metals, respectively.

### 6.1      Ex-situ Surface Analysis of Ti

#### 6.1.1 FTIR

FTIR spectra acquired on the Ti surfaces after exposure to synovial fluids from several patients are displayed in Figure 6.1. In each figure, the different spectra correspond to the results from different sites of the Ti surface. The dispersion, in terms of intensity and peaks, is quite significant among samples and even for the same sample on different spots. A higher absorption intensity signifies larger amounts of organics on the surface. The highest absorption with the absorption intensity of one spectrum higher than 1 is found for patient 17, while the lowest absorption intensity is obtained for patient 16, with a value of less than 0.04. More significant absorption, in which the absorption intensity is higher than 0.1, is obtained for sample 2, 3, 4, 13, 14, 17 and 18. Besides, the absorption intensity varies within one sample, and the variation can be very high (i.e., 1.2 for patient 17). In addition, different peaks are detected among samples and even among different spots on one sample, such as in P5 in which the peaks at 3000 - 3100  $\text{cm}^{-1}$  are detected only in one of the spectra.

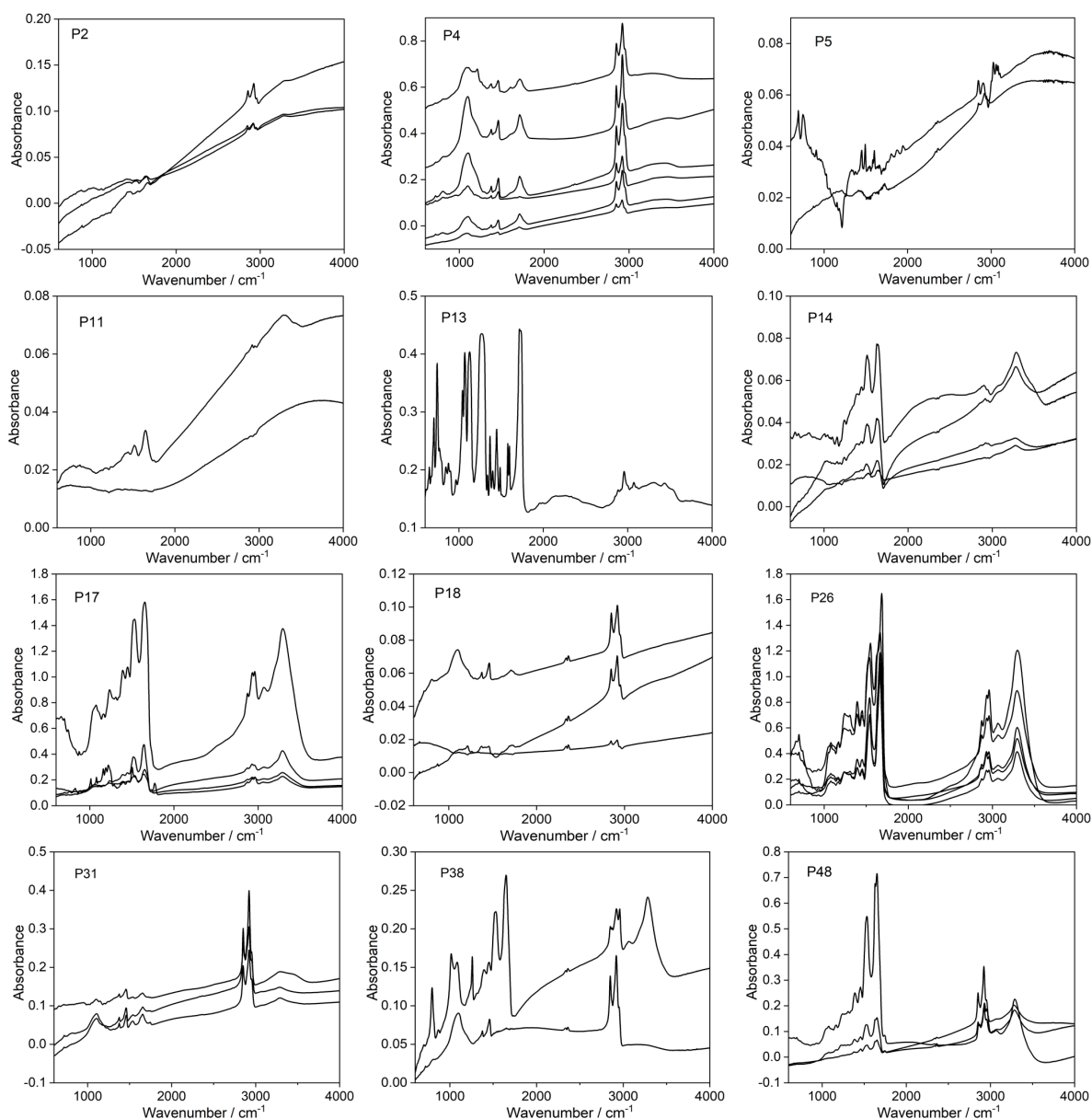


Figure 6.1 Representative absorption spectra on the Ti surface immersed in human synovia

The prominent absorption peaks were assigned using literature data, where the most important source is Movasaghi et al. [138]. Table 6.1 summarizes the main observations per patient, sorted by absorption peak. The absorption is particularly strong in the region from  $600\text{ cm}^{-1}$  to  $1800\text{ cm}^{-1}$ , which is also called the fingerprint region. As shown in the table, different peaks are obtained among patients, mainly in the fingerprint region. The stretching vibration of C-N in the amide III group and Asymmetric  $\text{CH}_3$  bending vibration is detected in most samples. Interestingly, absorption peaks at  $2840 - 2950\text{ cm}^{-1}$  are observed in all spectra, and they are identified as C-H stretching vibration. The double peaks at around  $2340\text{ cm}^{-1}$  and  $2360\text{ cm}^{-1}$  are due to  $\text{CO}_2$  in the vacuum chamber. There are also additional, non-assigned signatures in the spectra.

Table 6.1 Interpretation of spectral position in terms of absorption peaks

Peak	Patient number	Assignment
719	P3,4,22,23,31,35,39	Rotational vibrations O-H
808-813	P3,4, 18,22,35,38,39	Ring C-H deformation
966	P13	C-O stretching vibration
1006-1011	P14,17,43	C-O stretching vibration
1036-1043	P6,13,14,32	C-O stretching vibration
1070-1079	P13,17,21,26	Str C-O
1099-1107	P2,3,4,14,18,20,23,26,31,38,39,43,46,48	Stretching $\text{PO}_4^{2-}$ symmetric (phosphate II), Stretching CO/CC
1153-1170	P5,6,14,15,17,21,26,28,32,43,48	Antisymmetric stretching vibration C-O-C glycoside
1192	P17	Phosphate (P=O) bond
1207-1244	P4,5,6,14,15,16,17,18,20,21,22,23,26,32,35,36,38,48	C-N in Amide III
1275	P13	Amide III
1329-1338	P5,13	$\text{CH}_2$ wagging
1365-1369	P6,13,15	Stretching C-O, deformation C-H/ N-H/ $\text{CH}_3$
1377	P3, 4,5,16,20,22,31,36,39,43,46,48	Deformation $\text{CH}_2/\text{CH}_3$
1396	P3, 13,14,17,21,23,26,28,32,35,38	$\text{CH}_2$ bending vibration
1446-60	P3,4,5,13,14,17,15,16,18,20,21,22,23,26,28,31,32,35,36,38,39,43,46,48	Asymmetric $\text{CH}_3$ bending of the methyl groups of proteins
1490	P5, 13	Deformation C-H
1504	P17	In-plane CH bending vibration from the phenyl rings
1513-1521	P2,11,14,15,17,21,23,26,28,31,32,36,48	Amide II
1579	P13	Ring C-C stretch of phenyl
1631-1641	P2,14	Deformation of water
1658	P3,11,14,15,17,21,23,26,28,31,32,36,48	Amide I
1708-1726	P3,4,5,13,15,18	C=O
2337-2348	P3,4,5,6,14,15,16,17,18,20	$\text{CO}_2$ [139]
2362	P3,4,5,6,15,16,17,18,20	$\text{CO}_2$ [139]
2846-2950	all	Stretching C-H,
3026	P5	C-H ring
3074	P5, 13,21,22,26,28,32,36,38,48	C-H ring
3280/90	P11,13,14,15,16,17,20,21,22,23,26,28,31,32,36,38,43,46,48	Stretching O-H/N-H

Albumin is the main compound of proteins in human synovial fluids, and it is reported to have a significant influence on the interfacial reactions between Ti and electrolyte by adsorbing onto the metal surface [71, 81]. Also, BSA has a very similar structure to that of human

serum albumin [76]. The viscosity of synovial fluids is mainly given by hyaluronic acid (HA) [94], and clinical HA is injected into the joints of some patients two weeks before surgery to contribute to the lubrication of joints. Therefore, the spectra obtained from BSA and HA served as a reference for organic analysis, and the acquired spectra is in agreement with the literature [140, 141]. It is reported that the characteristic molecular bonds of proteins are amide I, amide II and amide III groups [138]. To distinguish the organic peaks, the spectra for patients with the presence of three amide groups are displayed in Figure 6.2, together with the spectrum obtained from BSA and HA.

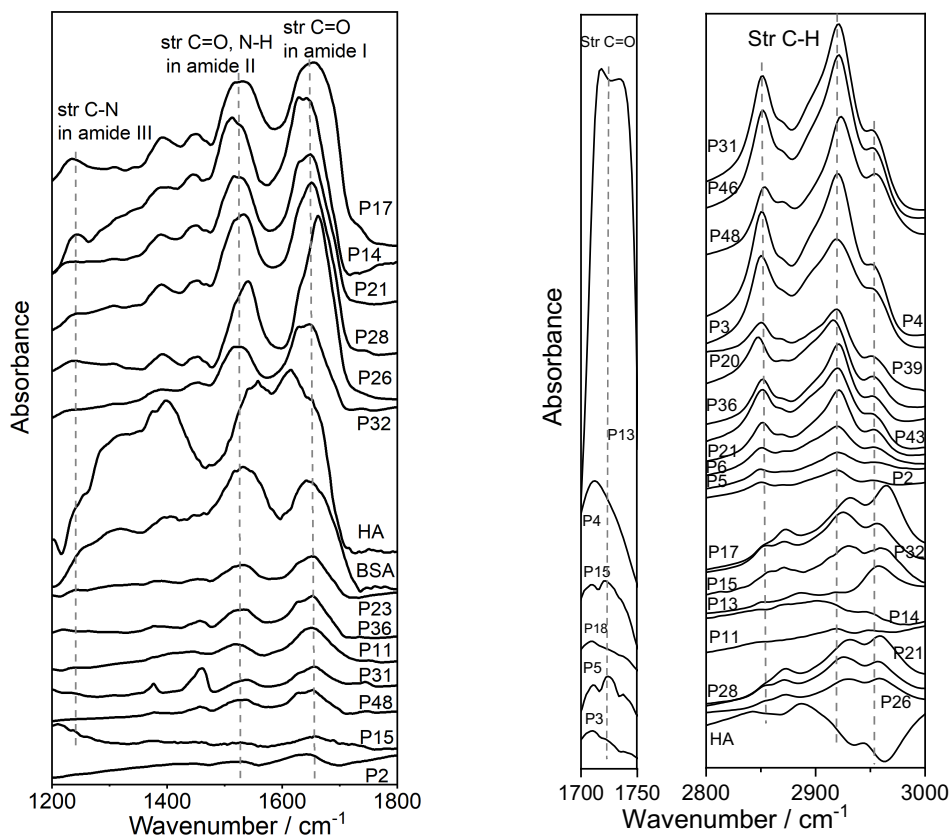


Figure 6.2 FTIR spectra of samples for patients with the presence of amide groups together with that of BSA and HA (left), and C=O as well as C-H group present in in-vivo samples and HA (right)

As shown in the graphs, amide groups are detected on samples surfaces for some of the patients, with various intensities being the highest for P17 and lowest for P11. In all spectra for patients, a strong signal is obtained from amide I and amide II groups, while the signal from amide III is weak, this is in accordance with the peaks for BSA. However, the stronger signal from amide II than amide I is contradictory to that of BSA. Amide groups are also detected in HA, while the peak positions are different from that in BSA.

Interestingly, stretching C-H groups are detected on the sample surface for most patients, as shown in Figure 6.2. These peaks are not detected in BSA while they are obtained in HA, but

the peak position and shape do not correspond to each other. It is reported that the stretching CH peaks can be used to assess lipids [138], and these peaks are typical for the fatty acid moiety. Indeed, the shape of the peaks, except for P11/13/14/15/17/21/26/28, is very similar to that of lipids from literature [142, 143]. The peak intensity varies with patients, being the highest for patient 4 and lowest for patient 11, indicating various amounts of organics are adsorbed on the sample surface. Since the peak at  $1600 - 1800 \text{ cm}^{-1}$  is reported as the fingerprint region for differentiating lipids [142], the spectra of samples in the region from  $1600$  to  $1800 \text{ cm}^{-1}$  are also plotted. The peak at  $1700 - 1800 \text{ cm}^{-1}$  can only be found on samples for P3,4,5,13,15,18.

Table 6.2 The sum peak intensity of representative functional groups detected on the sample surface

Patient	Intensity		
	C-O-C bond	Amide groups (I / II)	CH groups
P2		0.019	0.076
P3			0.177
P4			4.182
P5	0.002		0.024
P6	0.002		0.015
P11		0.018	0.003
P13			0.046
P14	0.005	0.170	0.016
P15			0.001
P16			0.004
P17	0.132	3.400	0.925
P18			0.122
P20			0.045
P21		0.410	0.137
P22			
P23		0.032	0.108
P26		8.598	5.168
P28		0.718	0.387
P31	0.009	0.089	1.113
P32	0.004	0.174	0.146
P35			0.662
P36		0.152	0.419
P38			0.139
P39			0.080
P43			0.030
P46			0.362
P48		1.464	0.977
HA	0.2	0.938	0.187

In order to quantitatively compare the amount of adsorbed/deposited organics, in terms of HA, BSA and lipids, the intensity of the peaks was acquired by calculating the height of the peaks with respect to the baseline. As a result, the peak intensity of the C-O-C bond, amide and CH groups are summarized in Table 6.2. Different amounts of organic groups are obtained among sample surfaces. For P14, 17, 31 and 32, both C-O-C bond and amide groups are detected, and the latter has a 2 - 40 times higher intensity. A detailed analysis of the FTIR results will be shown in the discussion.

### 6.1.2 SEM/EDS

Secondary electron micrographs were acquired from the Ti surface after exposure and sterilization. The appearance of the surface was quite different depending on the patients. The organic adsorption was not uniform on the surfaces and some images are shown in Figure 6.3.

The higher magnification image was taken in the rectangle area of the lower one. The samples after exposed to NaCl + BSA (30 g/L) and PBS + BSA (30 g/L) solutions were cleaned with water (a) and 70% ethanol (b), respectively.

In some cases (P2, P4, P26, P31), comparatively large regions were covered by organics, as shown in the lowest magnification images. Especially for P26, a whole organic layer is observed on the Ti surface. In addition, the morphology of the organic adsorption varied between patients. In some patients, the organic layer can be compact (P2, P4, P31) or porous (P5, P17). Also, local adsorption is observed, in a punctiform (P6, P18) or containing dried-up cells (P11). Note that different kinds of organic adsorption can be observed on the same sample, such as in patient 6 and 14, where a large area of compact organic layer is also present. Note however that the organics observed on the titanium surfaces could be caused by a deposition effect during the sterilization in 70% ethanol. This effect is confirmed by the higher amount of BSA detected on the titanium surface when cleaned with ethanol than the ones cleaned with water after immersion in NaCl/PBS + BSA solutions.



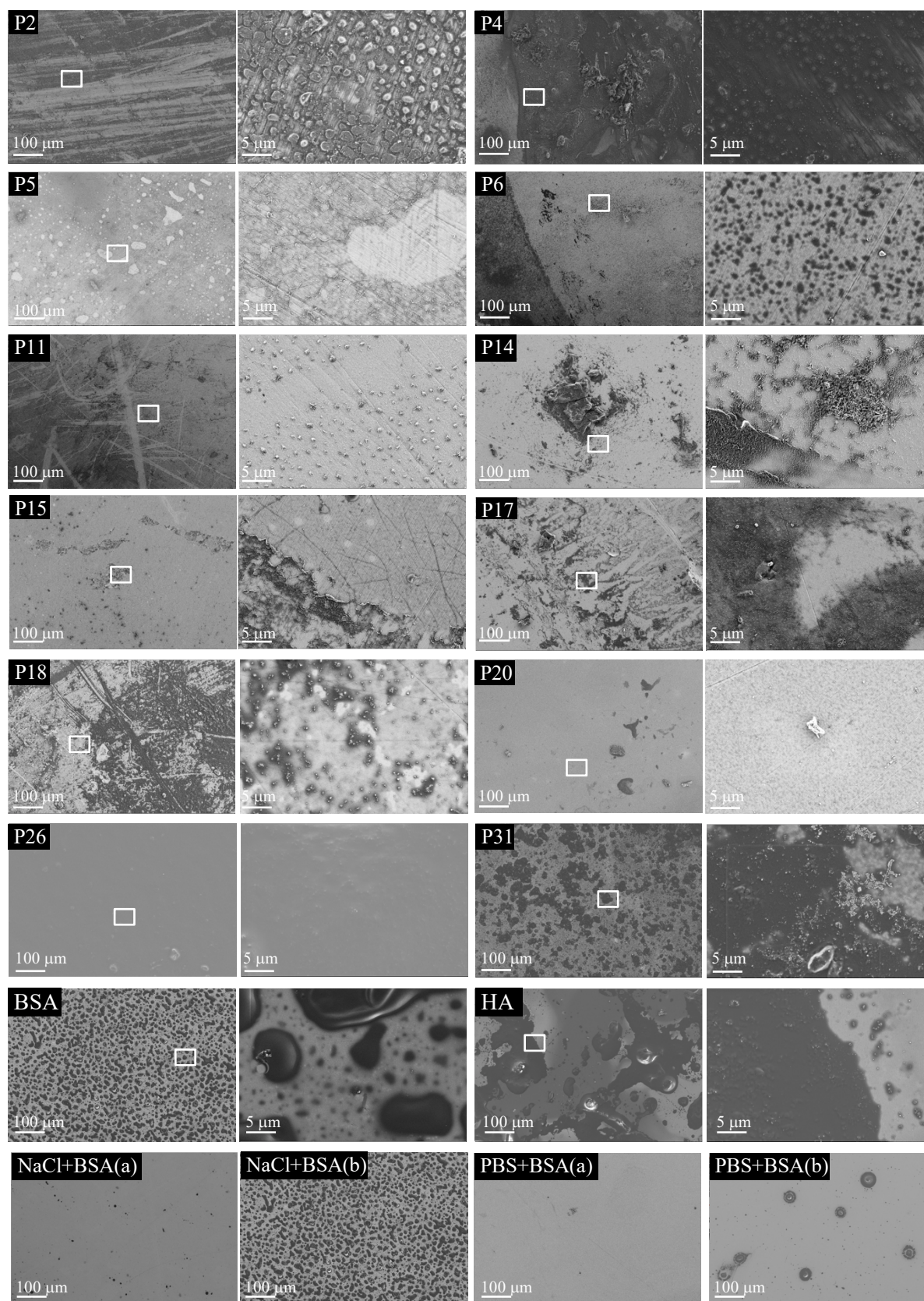


Figure 6.3 Representative SEM images of the Ti sample surface in low and high magnification for patients and simulated fluids



Titanium tested in NaCl based solutions with different BSA concentrations and cleaned with 70% ethanol were also analyzed by SEM. Some representative images are presented in Figure 6.4. The micrographs show that the deposited amount of BSA on the titanium surface increases with the albumin concentration. Based on this result, a tentative correlation between the amount of organics found on the titanium after being in contact with the human synovia and the concentration of organics in those human fluids can be established.

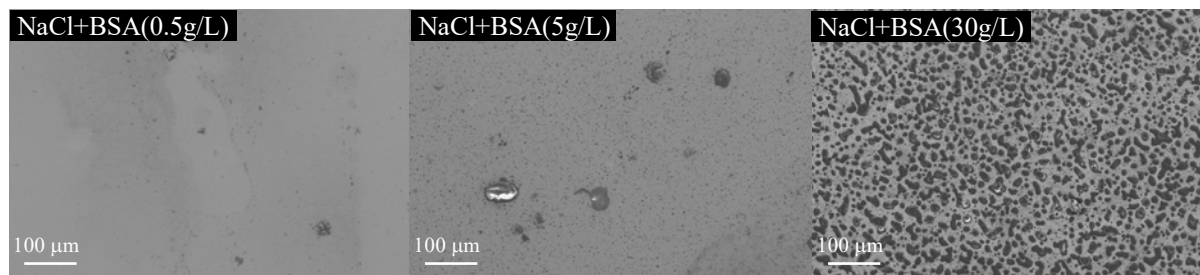


Figure 6.4 Representative SEM images of Ti sample surface after immersing in simulated fluids with different BSA concentrations

There is also a heterogeneous distribution of different types of particles over the surface for all patients, with the amount of particles varying with patients. An example of the particles observed on sample P3 and P16 are presented in Figure 6.5. Higher amount and amorphous particles with the size of around  $2\text{--}4\text{ }\mu\text{m}$  are observed in P16. The atomic concentration of the elements present in the particles was analyzed by EDS, and the summarized results are presented in Figure 6.6. All the particles contain C, O, Ca, and Ti signals with different concentrations. The atomic concentration of the four elements is very close among patients, except for P5 in which less O/Ca and higher Ti is detected. The Ti signal probably comes from the substrate due to the large reaction volume between the electron beam and the sample. The stronger Ti signal obtained for P5 could also be attributed to the small particle size. Besides, a small amount of Mg/S/K/P/Si ( $< 0.5\text{ at. }\%$ ) is detected in some particles.

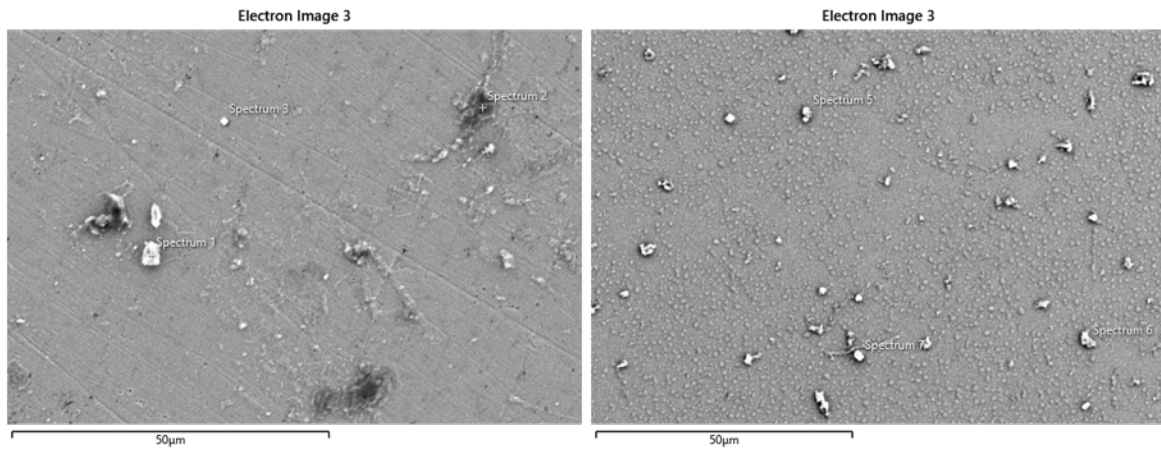


Figure 6.5 SEM images of the calcium particles for Ti exposure to synovial fluids from P3 and P16

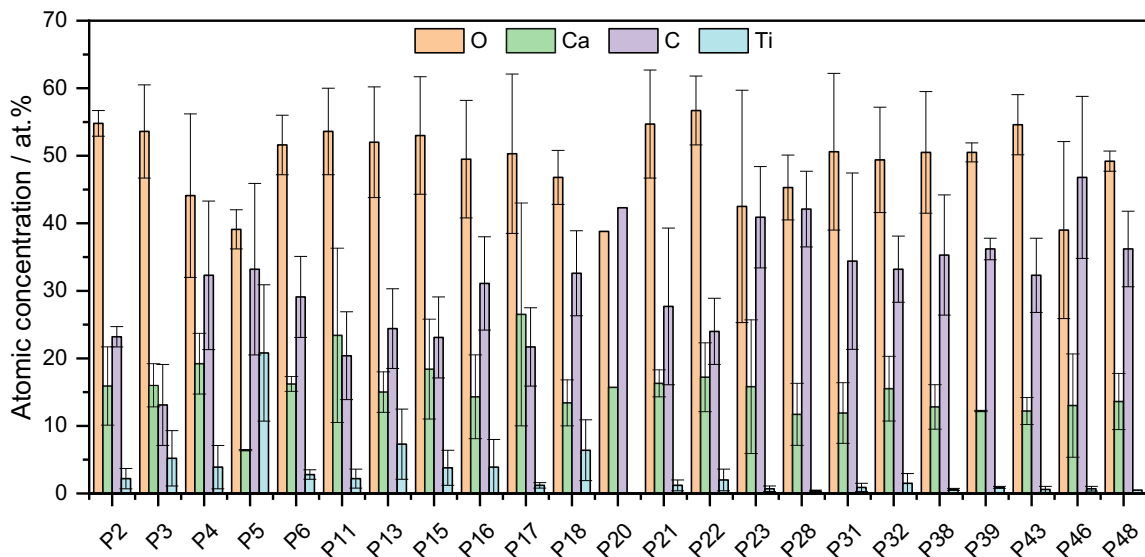
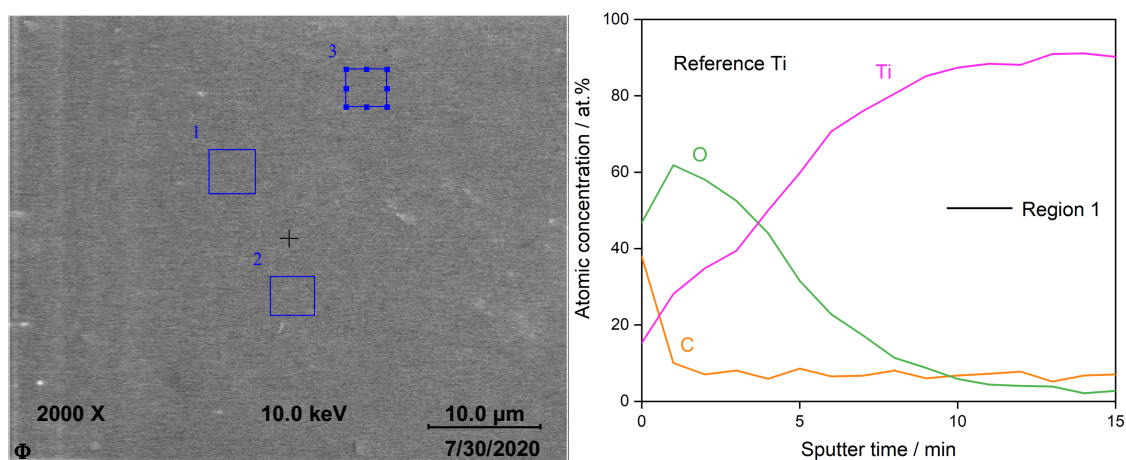


Figure 6.6 Atomic concentration of the particles observed on the Ti surface after being immersed in the synovia from several patients

### 6.1.3 AES

Auger depth profile analysis was conducted to investigate the chemical composition and passive film thickness of the samples. Figure 6.7 shows the surfaces and the corresponding depth profiles after exposure to the synovia from P4 and P5. As already observed, the organic adsorption is not homogeneous. Therefore, different AES depth profiles in different areas of the titanium samples were acquired, as illustrated in Figure 6.7. A depth profile was also carried out on a polished titanium sample before exposure to serve as a reference.

The carbon signal drops after the first sputter cycle due to the elimination of the contamination. The oxygen signal is used to estimate the surface oxide thickness by calculating the sputter time from the highest O concentration to the half of the peak, and the resulting passive film thickness lies around 3 nm. The Ti signal increases throughout the profile to reach the substrate. For patient 4, a thick carbonaceous layer of approximately 30 nm is obtained in region 4, and consequently only a small signal from O and Ti was detected throughout the sputter depth profile duration. Compared with region 4, little C signal is obtained in region 1, while a large amount of O was detected after the elimination of C. For patient 5, no thick organic layer was detected and similar profiles are obtained among the four different regions. Only in region 4 the amount of carbon is slightly higher and requires about 3 minutes of sputtering to be removed. The resulting profiles show more organic material adsorbed in the darker regions according to the slightly longer sputter time needed to make the C signal disappear. Interestingly, Si signal was detected in sample P5 in all three regions. The amount of Si decreased with the decrease of C and the increase of O, reaching the minimum at the lowest C concentration and the highest O concentration. This suggests that the Si comes from the thin carbonaceous layer. It can also be confirmed by SEM/EDS analysis, where Si was widely detected in organic depositions. These results correlate with other literature data where Si was detected in blood plasma [31] and synovial fluids [144].



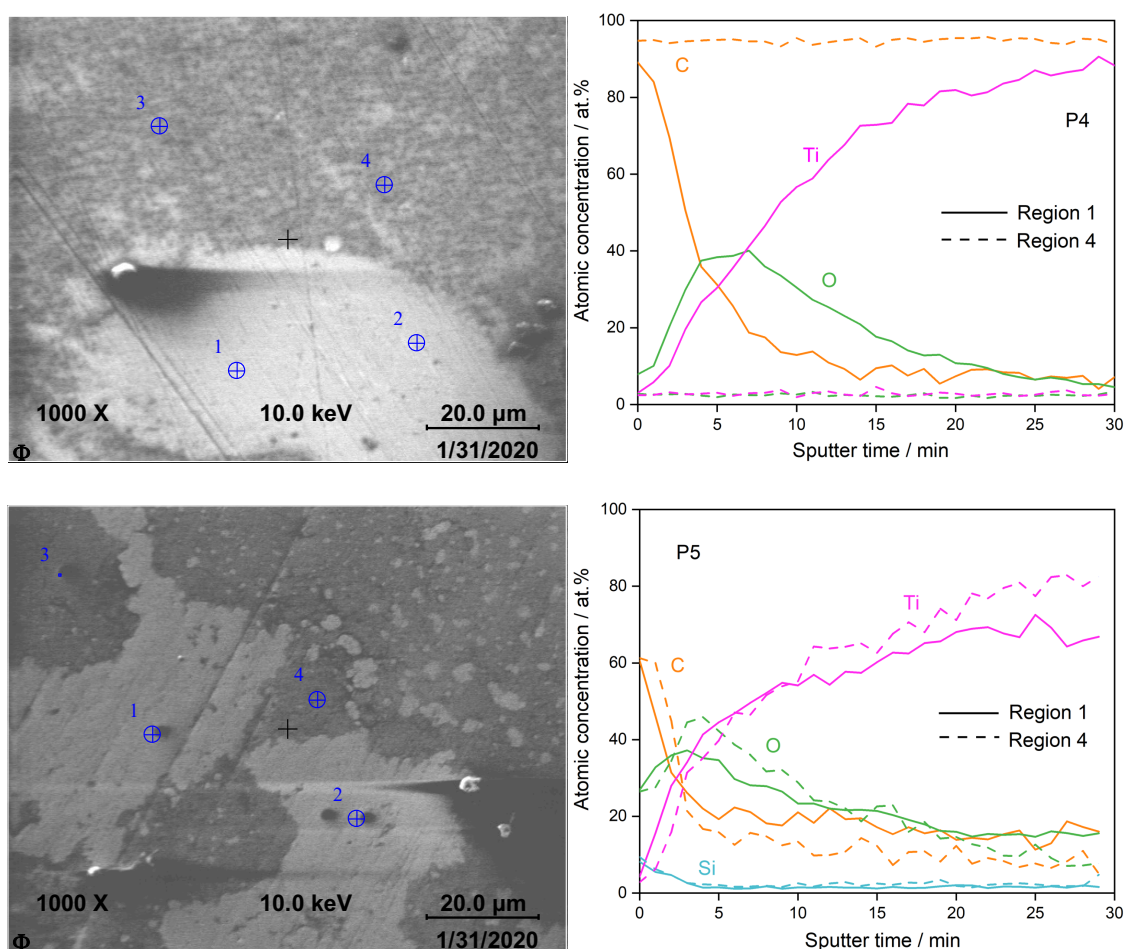


Figure 6.7 Auger sputter depth profiles from the reference sample before exposure and after contact with the synovial fluid from P4 and P5. (Sputter rate: 0.6 nm/min)

The passive film thickness of the titanium samples was calculated with the O depth profile after removing the influence of electron escape depth, and the results are displayed in Figure 6.8. Results show a similar passive film thickness, around 4-5 nm, is detected for the titanium immersed in the human synovial fluids. It is about 1-2 nm thicker than that of the reference sample. However, this 1 nm difference in the passive film thickness is within the resolution of depth analysis which decreases with the presence of an organic layer on the sample surface [145]. Given that the open circuit potential of the titanium samples in the tested synovial fluids ranges from -0.5 to -0.2 V<sub>Ag/AgCl</sub>, these results agree with in-vitro studies, where the passive film thickness of Ti alloy depends on the applied potential (increasing with an average rate of around 1 nm/V [146]).

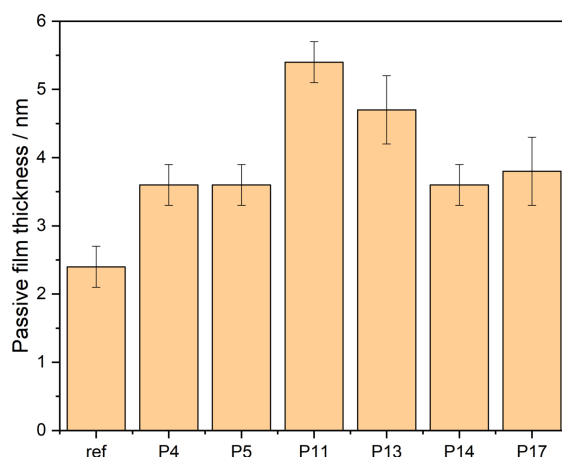


Figure 6.8 Passive film thickness of the reference Ti sample and the samples after contact with the synovial fluid from some patients

## 6.2 Ex-situ Surface Analysis of CoCrMo Alloy

### 6.2.1 FTIR

FTIR spectra acquired on the CoCrMo surfaces after exposure to several synovial fluids are present in Figure 6.9. In each figure, the different spectra correspond to the results from different sites of the CoCrMo surface. The dispersion, in terms of intensity and peaks, is significant among samples and even for the same sample on different spots. A higher absorption intensity indicates a larger amount of organics on the surface. The highest absorption with the absorption intensity of one spectrum higher than 1 is found for P31, while the lowest absorption intensity is obtained for P20, with a value of smaller than 0.05. The variation of the adsorption intensity within one sample can be up to 1 for P21. In addition, different peaks are detected among samples and among different spots on one sample. For example, the peaks at  $1000 - 1200 \text{ cm}^{-1}$  are detected only in one of the spectra in P43.

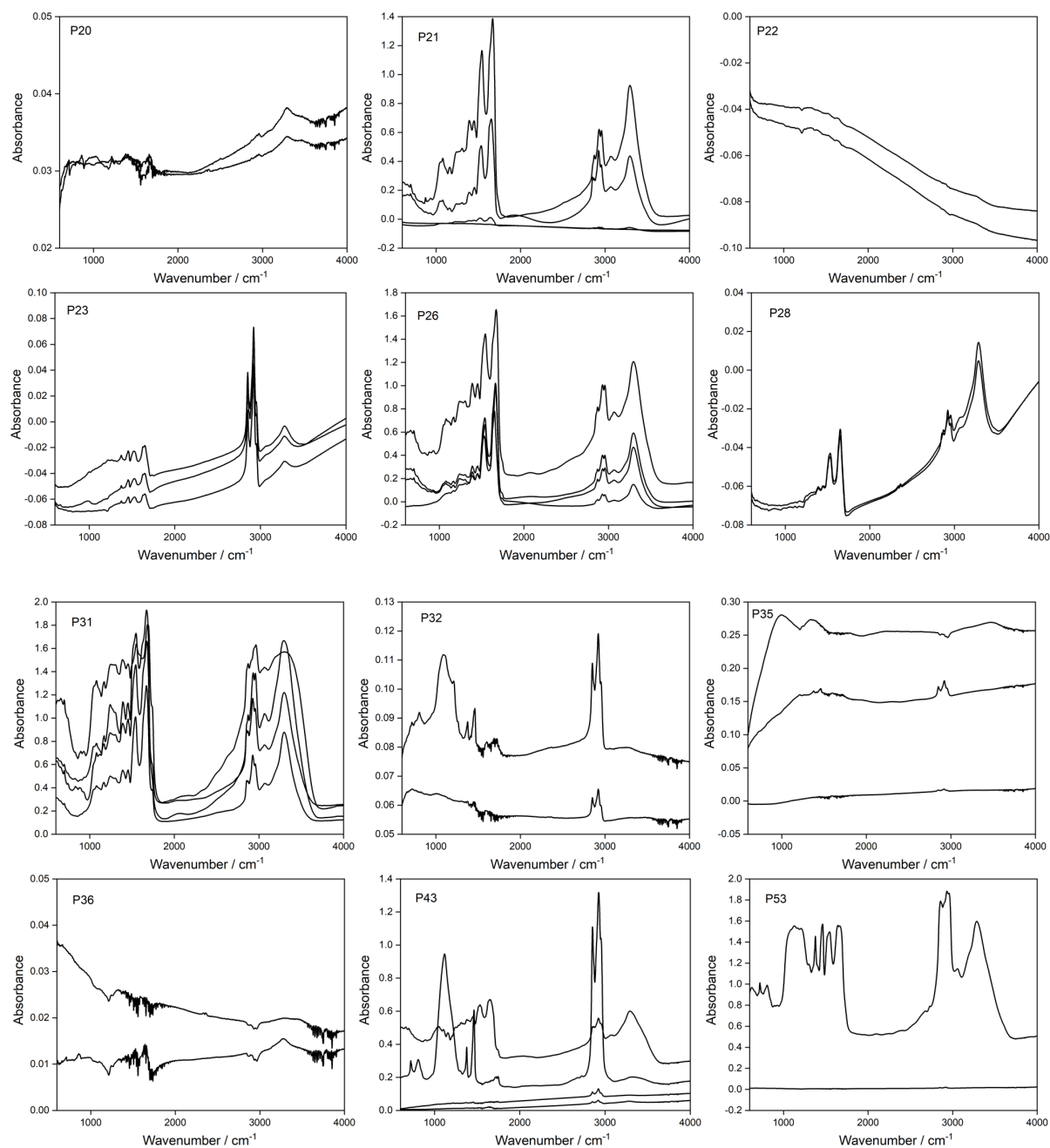


Figure 6.9 Representative absorption spectra on the CoCrMo surface immersed in the human synovial fluids from patients

The prominent absorption peaks were assigned according to the literature [138], and listed in Table 6.3. The absorption is especially strong in the region from  $600\text{ cm}^{-1}$  to  $1800\text{ cm}^{-1}$ , namely the fingerprint region. As shown in the table, different peaks are detected among patients, mainly in the fingerprint region. The amide I/II groups and asymmetric  $\text{CH}_3$  bending vibration are detected in most samples. Similarly, C-H stretching vibration peaks at  $2850 - 2960\text{ cm}^{-1}$  are observed in most spectra. The double peaks at around  $2340\text{ cm}^{-1}$  and  $2360\text{ cm}^{-1}$



are because of CO<sub>2</sub> in the vacuum chamber. Additional and non-assigned peaks are present in the spectra, and they are not listed in the Table.

Table 6.3 The spectral interpretation of in-vivo CoCrMo samples

Peak	Patient number	Assignment [138]
712-723	P20,36,44,48,53	Rotational vibrations O-H
802	P43,48,53	Ring C-H deformation
875-883	P21,26,36	C-C
1000/8	P23,	C-O, C-C, C-H
1045-1077	P21,26,43	C-O stretching vibration
1159-1168	P21,23,26	Antisymmetric stretching vibration C-O-C glycoside
1212-1242	P21,26,31,43	C-N in amide III
1307/21	P21,26	Amide III bond components of proteins Collagen, CH <sub>2</sub> wagging
1374-1394	P21,22,23,26,28,31,35,43,48,53	Deformation CH <sub>2</sub> /CH <sub>3</sub> /CH <sub>2</sub> bending vibration
1450-1461	P20,21,22,23,26,28,31,35,43,48,53	Asymmetric CH <sub>3</sub> bending of the methyl groups of proteins
1515-1544	P21,23,26,28,31,36,43,48,53	Amide II
1648-1664	P21,23,26,28,31,36,43,48,53	Amide I (C=O stretching vibration)
1710-1740	P20,31,36,43,53	C=O
2333/9	P20,28	CO <sub>2</sub> [139]
2362	P20,28	CO <sub>2</sub> [139]
2854-2958	P21,23,26,28,31,36,43,48,53	Stretching C-H
3058-3078	P21,23,26,28, 31,36,43,48,53	C-H ring
3284	P20,21,23,26,28, 31,36,43,48,53	Stretching N-H/O-H symmetric

Since protein and HA are the main compound of synovial fluids, and amide groups are the characteristic molecular bonds of protein, the spectra for patients with the presence of amide groups are displayed in Figure 6.10. As shown in the graph, amide groups are detected on samples surfaces for some patients with various intensities, being the highest for P31 and lowest for P21. The stronger signals obtained from amide I and amide II groups correspond to the peaks for BSA. However, the stronger signal from amide I than amide II is contradictory to that of BSA. Amide groups are also detected in HA, while different peak positions.

Similarly, stretching C-H groups are detected on the sample surface for most patients, as shown in Figure 6.10. These peaks are obtained only in HA, but the peak position and shape do not correspond to each other. The stretching CH peaks are reported can be used to assess lipids [138], typically the fatty acid moiety. Indeed, the shape of the peaks for P23, P48 and P53 is quite similar to that of lipids reported in the literature [142, 143]. The peak intensity varies with patients, being the highest for P48 and lowest for P36. Since the peak at 1600 -

$1800\text{ cm}^{-1}$  was reported to be the fingerprint region for differentiating lipids [133], the spectra of samples at the region of  $1600 - 1800\text{ cm}^{-1}$  are also plotted. The peak at  $1700 - 1800\text{ cm}^{-1}$  can only be detected on samples for P20, P31, P36, P43 and P53.

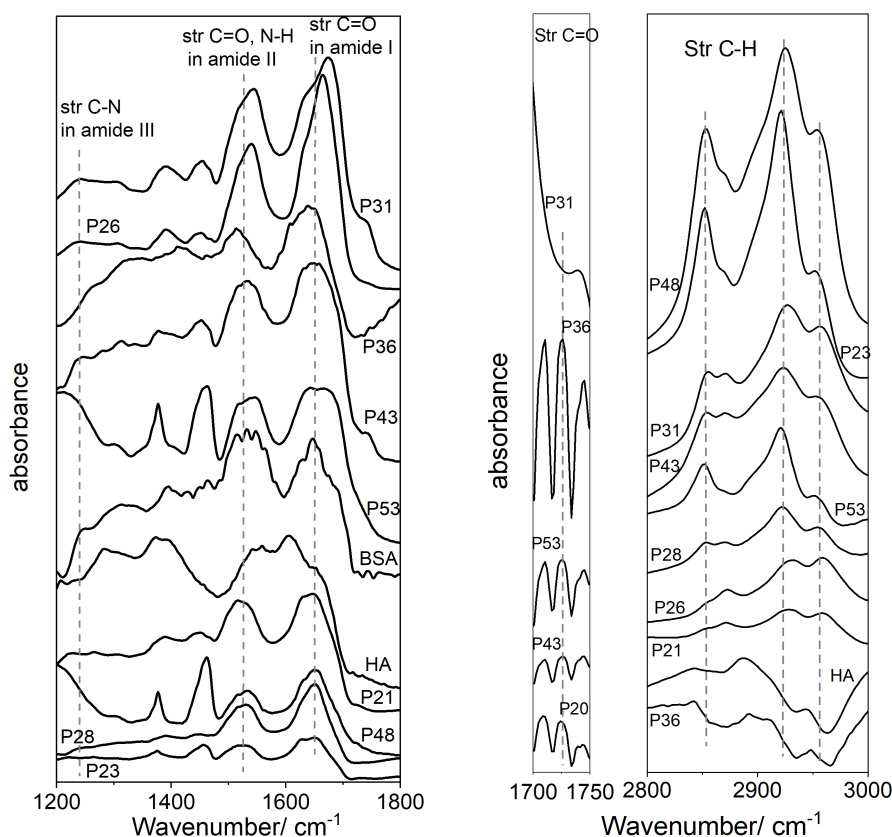


Figure 6.10 FTIR spectra of CoCrMo samples for patients with the presence of amide groups together with that of BSA and HA, and C=O as well as C-H group present in in-vivo samples and HA

### 6.2.2 SEM/EDS

Secondary electron micrographs were acquired from the CoCrMo surface after exposure and sterilization. The organic adsorption is not homogeneous on the surfaces and the representative images are present in Figure 6.11. Higher magnification images were taken in the rectangle area of the lower ones.



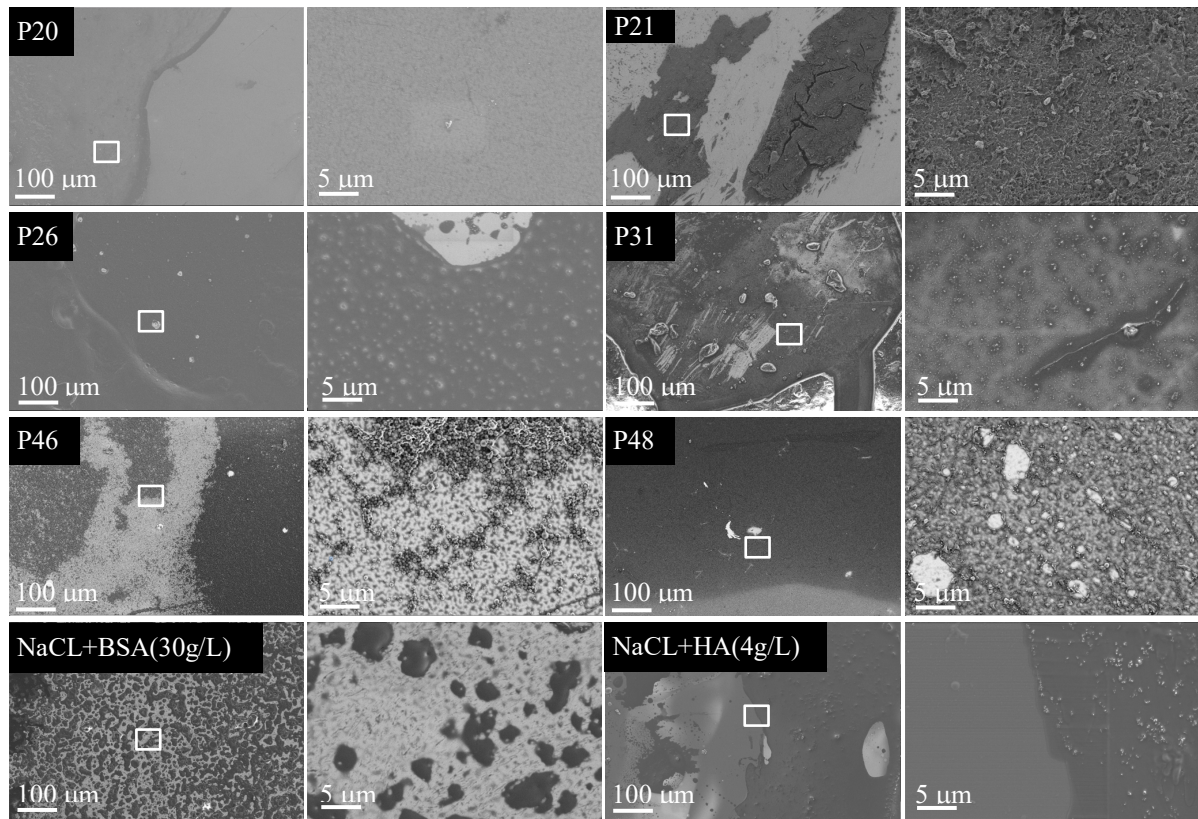


Figure 6.11 Representative SEM images of the CoCrMo sample surface in low and high magnification for patients and simulated fluids

In some cases (P26, P31), comparatively large regions are covered by organics, as shown in the lower magnification images. Same to Ti sample, a whole organic layer is observed on CoCrMo surface for P26. Additionally, the morphology of the organic adsorption varied with patients. In some patients, the organic layer can be compact (P21, P26) or porous (P46, P48). The morphology of the organics observed for patients are different from BSA and HA.

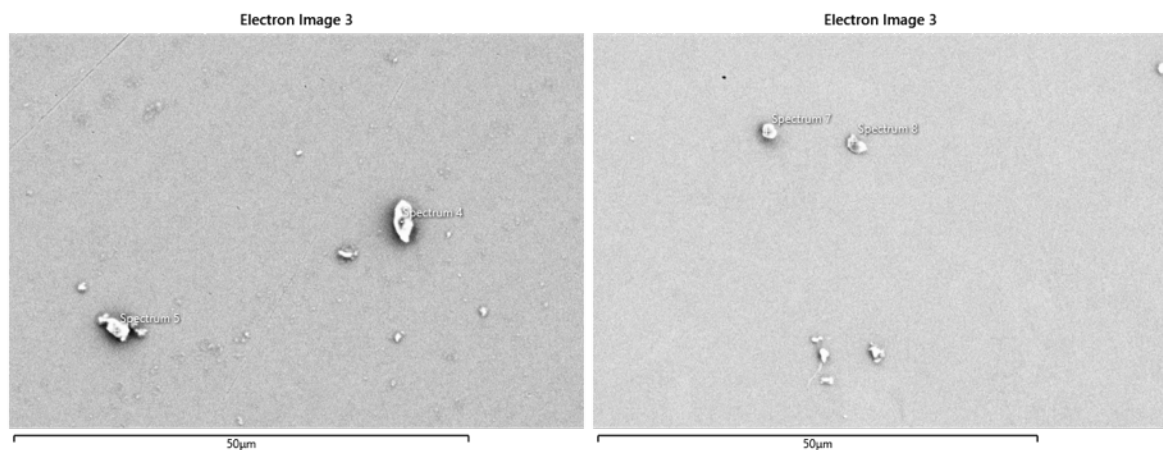


Figure 6.12 SEM image of the calcium particles on CoCrMo surface for P21 and P22

There is also a heterogeneous distribution of various types of particles over the surface for all patients, with the amount of particles depending on patients. An example of the particles observed on sample P21 and P22 are displayed in Figure 6.12. The atomic concentration of the particles was analyzed by EDS, and the summarized results are presented in Figure 6.13. All the particles contain C, O, Ca, while Co, Cr and Mo signals are only detected on several samples. The atomic concentration of C, O and Ca is very close among patients, except for P23 where higher O/Ca was detected. The Co, Cr and Mo signals probably come from the substrate due to the large reaction volume between the electron beam and the sample. The stronger Co/Cr signal obtained for P21 and P22 could also be due to the small particle size. In addition, a small amount of Mg/Si/Al/Na ( $< 0.5$  at. %) was detected in some particles.

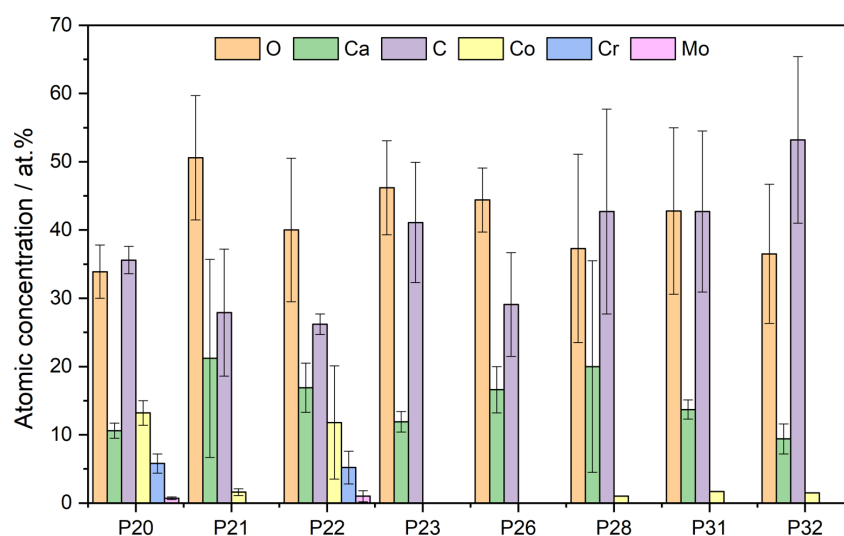


Figure 6.13 Atomic concentration of the particles observed on the CoCrMo surface after being immersed in the synovia from several patients

## 6.3 Discussion

### 6.3.1 Organic adsorption/deposition

As shown in Figure 6.2 and Figure 6.10, amide groups are identified on Ti and CoCrMo sample surfaces tested in some synovial fluids (basically the same patients for both materials), while their shapes are different from that of BSA and HA. This could be due to the presence of other organics in human synovial fluids, which influence the intensity and position of the peaks [147]. Besides, the shift of peaks is also reported to be related to different secondary structure [148] and the thickness of the organic layer [149].

Amide groups are present in both BSA and HA, while the stretching vibration of the C-O-C bond at  $1150\text{ cm}^{-1}$  is only present in HA. This peak is obtained on samples for P5, 6, 14, 17,

31 and 32, and both presence of C-O-C bond and amide groups on samples for P14, 17, 31 and 32, suggests HA is adsorbed onto Ti sample surface for these four patients. Besides, the intensity ratio of amide group/C-O-C bond for these four patients is much higher than the value for HA (As shown in Table 6.2), suggesting that proteins are present on the sample surface for these four patients. C-O-C bond and amide groups are detected on CoCrMo surface for P21, suggesting HA is adsorbed onto the sample surface for this patient. CH groups with different shapes are detected on both materials for most patients while the stretching C=O bond is only present for some ones. Since the stretching C=O bond is not present on all types of lipids, the results suggest various types and amounts of lipids are adsorbed on the sample surface. Also, lipids could be present on Ti samples for P14, 17, 31 and 32, according to the much higher CH/C-O-C intensity ratio than HA.

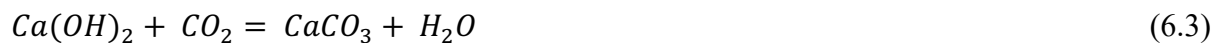
A tentative conclusion can be found that lipids are probably adsorbed on both sample surfaces for most patients, while protein and HA are only present for certain ones. The peaks did not occur in BSA and HA spectra, suggesting other organics could be adsorbed onto the metal surface, which is confirmed by the different appearance of adsorbed organics observed on in-vitro samples.

### 6.3.2 Particles containing calcium

Figure 6.5 and Figure 6.6 show the different compositions and morphology of the oxide particles (Ca, O, C, Ti, etc.) found on the titanium surfaces by SEM/EDS. Similar particles are also observed on CoCrMo surfaces, as shown in Figure 6.12 and Figure 6.13. The chemical composition of the particles on both surfaces, exposed to different synovial fluids, is very similar, with a Ca/O ratio around 0.3, corresponding well with the calcium carbonate. However, the Ca/C ratio varies with patients for both surfaces. The fluctuation of C composition could be attributed to organic adsorption and contamination. The Ti/Co/Cr/Mo signals detected by EDS probably comes from the substrate due to the small size of the particles. The small amount of S/K/Mg/P/Si found in the particles could be due to the adsorption of ions in synovial fluids [30]. The chemical composition of the particles found in the human synovia, is similar to that detected on the titanium surface immersed in NaCl + CaCl<sub>2</sub> (1 g/L) solution, indicating that the organics and other ions in synovial fluids have little influence on the particle formation.

The particle formation can be explained based on the following hypothesis: when Ti samples are exposed to synovial fluids, oxygen reduction takes place, forming OH<sup>-</sup> ions (reaction 6.1). Ca<sup>2+</sup> ions then react with the OH<sup>-</sup> ions and form Ca(OH)<sub>2</sub> on the surface (reaction 6.2). After that, CaCO<sub>3</sub> particles were formed through the reaction between Ca(OH)<sub>2</sub> and CO<sub>2</sub>,

dissolved in synovial fluids or the ambient air (section 6.3). It should be noted that the particles are probably the mixture of  $\text{Ca(OH)}_2$  and  $\text{CaCO}_3$ , at different ratios.



However, various particles are found in human synovial fluids. It was widely reported that calcium phosphate crystals are frequently found in osteoarthritis synovial fluids and deposited in articular cartilage [150–153], and define subsets of patients with inflammatory or rapidly destructive arthritis [154]. There are several kinds of calcium phosphate particles, and the basic calcium phosphate (BCP) and calcium phosphate dehydrate (CPPD) are the most common forms [155]. The BCP crystals usually are less than  $1\ \mu$  and aggregate into amorphous globular clumps, while the CPPD crystals appear like a rod or rhomboid, with the size of  $1\text{--}20\ \mu\text{m}$  [151]. Similar shape and sizes with BCP crystals are observed on our samples, while no phosphate signal was detected.

The absence of phosphate in observed particles could be due to a short immersion time. Indeed, calcium particles are first found on the Ti sample surface after immersing in Hank's solution, afterwards phosphate is detected and the concentration increases with immersion time. Finally, a layer of calcium phosphate crystals, similar to BCP, was observed on the sample surface after exposure for 7 days [58]. However, contrary results are reported that phosphate adsorption is the prerequisite of calcium phosphate formation on Ti sample surface when exposure to Hank's solution [47], and the nucleation of particles on sample surface starts within 30 mins [156]. Further research needs to be conducted to study the mechanism of particle formation.

### 6.3.3 Correlation between surface analysis and in-vivo electrochemical results

Since the amount of detected organics corresponds to the organic concentration in synovial fluid, the correlation between organic adsorption/deposition and the electrochemical behavior of Ti was investigated, and the results are displayed in Figure 6.14. Since the amount of COC bond detected on the sample surface is much lower than that of amide and CH groups, the influence of the COC bond is not taken into account. As shown in the graphs, no correlation between OCP/corrosion rate and organic adsorption/deposition is found. This does not consistent with the in-vitro results, where OCP and corrosion rate decrease with the addition of BSA. This mismatch is not surprising given that amide groups and CH groups are also present in other organics in synovial fluids, especially the CH bond.

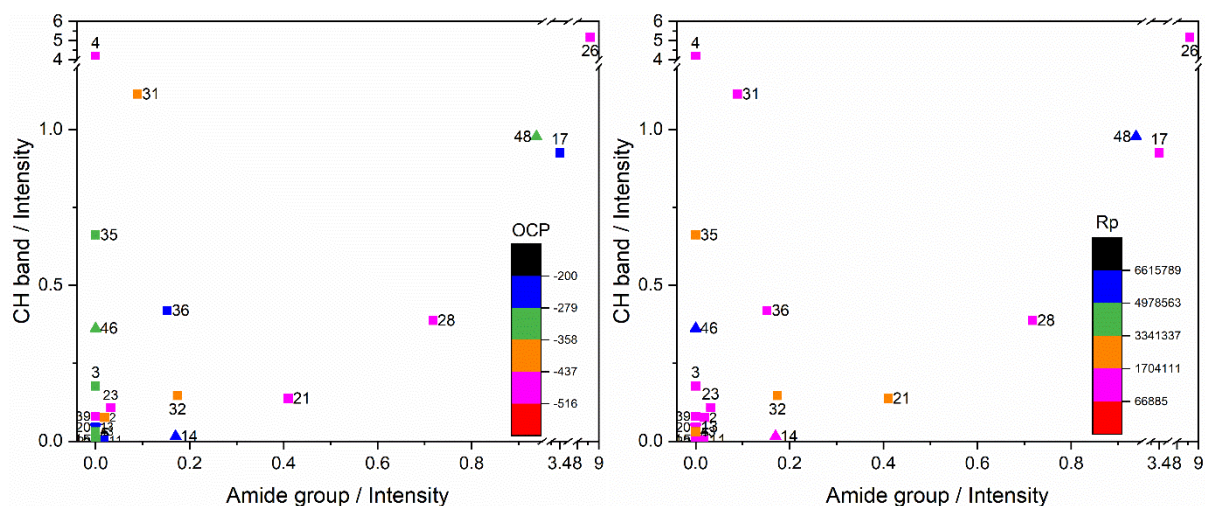


Figure 6.14 Correlation between organic adsorption/deposition and OCP as well as Rp of Ti in tested synovial fluids

To avoid the influence of cleaning on the results, the in-situ electrochemical parameters of Rp and OCP of Ti tested in synovial fluids are plotted in Figure 6.15. In the graph, the sum intensity of the FTIR spectra within the wavenumber of  $600 - 4000 \text{ cm}^{-1}$  was calculated and indicated as different colors for each patient. The larger value of the sum intensity indicates the higher amount of organic adsorption/deposition. The graph shows no straightforward correlation between Rp and OCP is found for in-vivo measurements, as well as the correlation between amount of organic adsorption. For comparison, results obtained from simulated solutions, containing BSA, HA and Ca ions, are also present in Figure 6.15. As seen in the graph, a linear correlation between OCP and Rp of Ti in BSA-containing solutions is found, namely the Rp decreases with the increase of OCP value due to organic adsorption on the Ti surface. However, little influence of HA on Rp and OCP is obtained and an increase of OCP value with the addition of Ca ions is acquired.

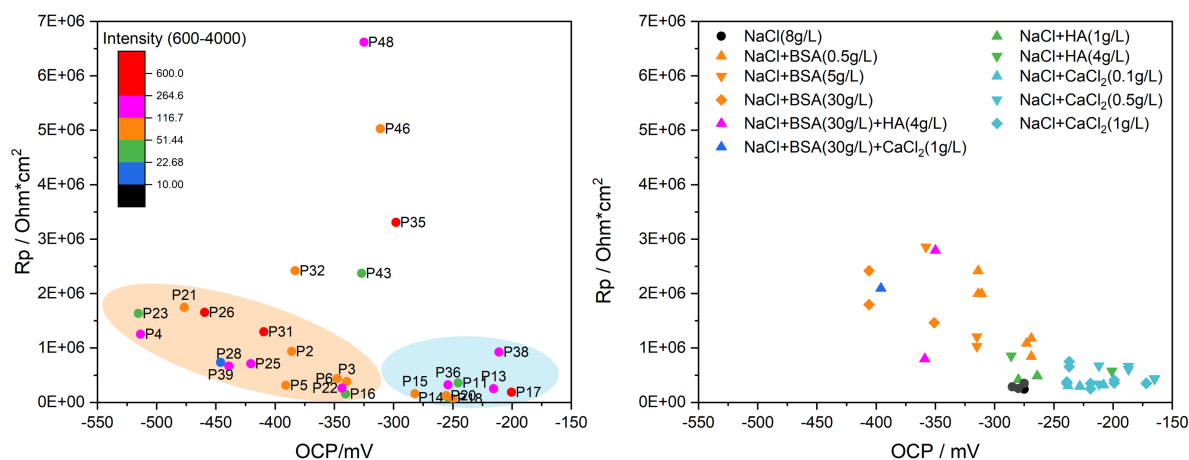


Figure 6.15 Correlation between Rp and OCP of Ti in tested synovial fluids and simulated solutions

Based on the results obtained from simulated solutions, a tentative correlation can be found for the results from synovial fluids. The linear correlation between  $R_p$  and OCP in the orange region for synovial fluids could be due to protein adsorption on the sample surface. Indeed, lower cathodic reactions and a higher amount of organic adsorption are observed on samples with higher  $R_p$  and lower OCP values. Besides, the higher OCP values in the blue region could be related to Ca ions in synovial fluids, for which the polarization curves correspond to the in-vitro results that Ca ions has little influence on the cathodic reaction. The data points located out of the two regions might be related to other organics in synovial fluids.

## 6.4 Summary

The combination of FTIR, SEM/EDS and AES techniques made it possible to obtain a certain information on organics present in synovial fluids and on the passive film formed on Ti surfaces exposed to human synovia. The obtained results indicate that:

- Protein and HA could be identified in the organic deposit on the surface after exposure to synovial fluids and sterilization in ethanol. The amount of deposit varies significantly with patients.
- Knowing that the amount of deposited organics on the surface is proportional to their concentration in the fluids, the obtained results suggest that the concentration of protein and HA varies significantly among patients.
- No relation between the corrosion behavior of both materials in synovial fluids and the organic deposit on the surfaces exposed to synovial fluids was found. This suggests that other factors than protein and HA influence the corrosion behavior. These factors could be oxygen concentration as well as other organics not deposited during the sterilization process. For example, no deposit was found when exposing the surface to a lipid emulsion and subsequent sterilization.

## Chapter 7      Influence of Surface Roughness on the Electrochemical Behavior of Ti in Human Synovial Fluids

Implants with rough surface can enhance the growth of osseous tissue on the surface due to the large surface area. The attachment of osseous tissue to implant without intervening connective tissue is defined as osseointegration [157]. To facilitate the integration of bone tissue on implant surface, several types of implant surface are available for clinical application [157].

Beside osseointegration, the surface roughness is well known to influence the wear and corrosion behavior of the implants. To investigate the effect of surface roughness on the corrosion behavior of Ti implants, several research has been conducted in saline solutions through OCP, potentiodynamic and EIS measurements [158–161]. The results show the corrosion rate of the raw Ti samples is enhanced with the increase of Ra. However, the impact of surface roughness on the corrosion behavior of Ti in organic containing solutions is still not found in the literature.

To obtain the effect of surface roughness on the corrosion behavior of Ti implants in the real reaction conditions, the electrochemical measurements, including OCP, polarization curves and EIS, were carried out on both smooth and rough surfaces in several synovial fluids. For the sake of clarity, the synovial fluids tested in this chapter were extracted from another set of patients.

### 7.1      Sample Preparation

Ti implants with different surface roughness were used in arthroplasty. To obtain the reaction behavior of Ti with various surface roughness, a rough Ti surface was prepared. The same Ti samples were polished with SiC emery paper of 1200 grit in water, with a Ra of  $290 \pm 5$  nm. Same cleaning and sterilization methods were applied for the rough surface. The SEM image and the 3D topography (taken by KEYENCE) of polish samples are displayed in Figure 7.1.

To quantitatively study the effect of surface area on the corrosion behavior, the real surface area of both surfaces was measured through KEYENCE. The measurement was performed with a magnification of 50X, with a depth resolution of  $0.1 \mu\text{m}$ . Based on the results, the surface area ratio between rough and smooth surface of 1.14 is acquired.



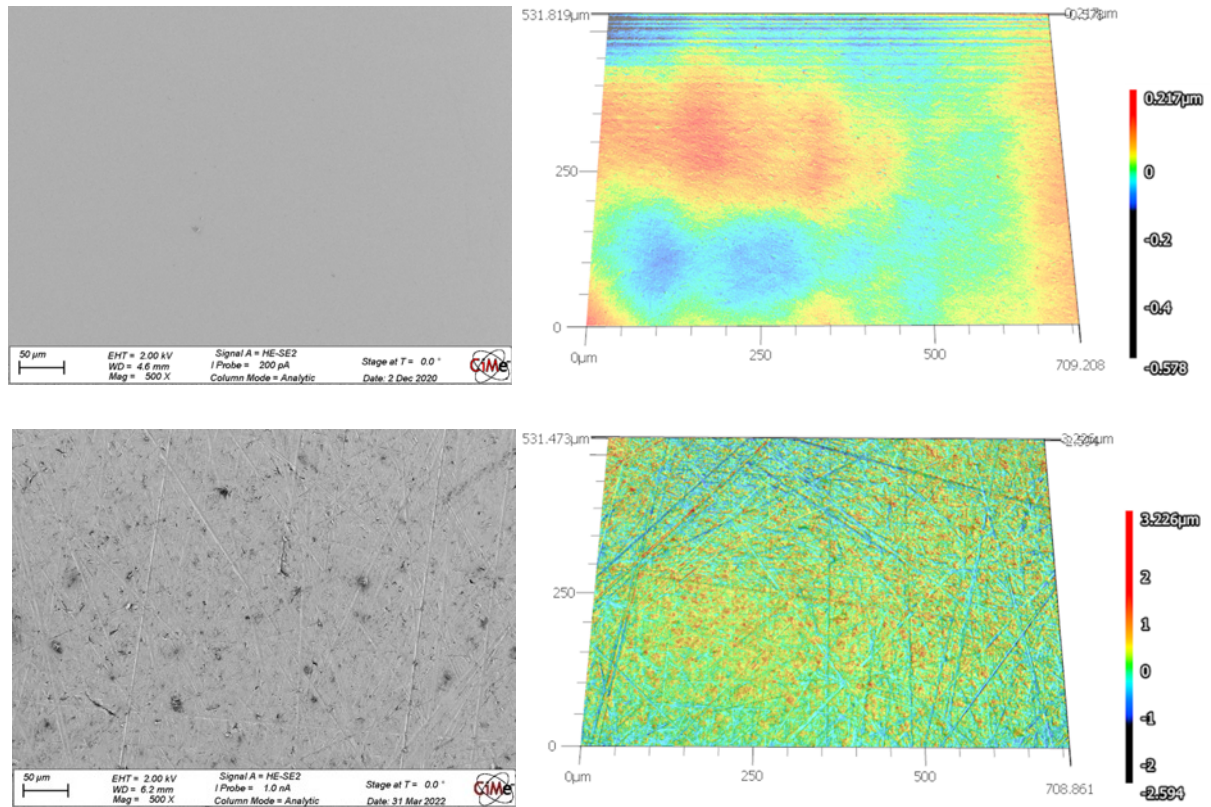


Figure 7.1 SEM and 3D images of polished smooth and rough Ti surface

## 7.2 Electrochemical Results

### 7.2.1 OCP of Ti and Ti-1200 samples

The OCP of both smooth and rough surfaces was measured in several synovial fluids for 20 minutes and the stabilized OCP values are presented in Figure 7.2. The stabilized OCP of both surfaces varies among patients, being from  $-220 \text{ mV}_{\text{Ag}/\text{AgCl}}$  to  $-550 \text{ mV}_{\text{Ag}/\text{AgCl}}$  for smooth surface and  $-200 \text{ mV}_{\text{Ag}/\text{AgCl}}$  to  $-480 \text{ mV}_{\text{Ag}/\text{AgCl}}$  for rough surface. The OCP values of both surfaces are close for most patients, except for P67, P111, P112 and P116, where obvious higher OCP values are obtained for rough surface.



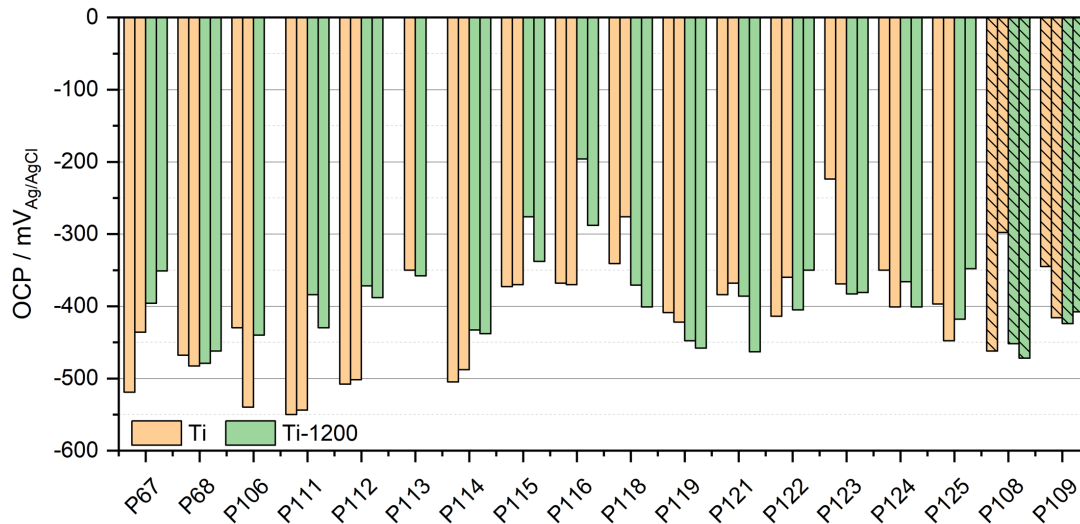


Figure 7.2 Stabilized OCP of Ti and Ti-1200 samples immersed in different synovial fluids from PS, and R (P108 and P109) groups

### 7.2.2 Potentiodynamic Polarization Curve of Ti samples

The cathodic polarization curves for both surfaces in synovial fluids are plotted in Figure 7.3. The graphs show that the current density for smooth surface slightly varies with most patients, except for P123, which is about one magnitude higher than the rest. The current density for tested synovial fluids in this chapter is within the range for P2 - P100. The current density for the rough surface varies with patient, being the lowest for P68 and the highest for P125. All curves exhibit a linear part approximately 100 - 200 mV below the OCP. This indicates that the cathodic kinetics is under charge transfer control and could involve the reduction of oxygen, protons and/or water. In addition, for smooth surface, a linear part with a higher slope at the applied potential lower than  $-0.9 \text{ V}_{\text{Ag/Ag/Cl}}$  is observed for most of the patients, but not for P123. The different slopes suggest different reaction kinetics under different applied potentials. This behavior is already discussed in Chapter 5.

In terms of the effect of  $R_a$ , higher current density is obtained for rough surface for most patients, except for P123. The difference of current density for two surfaces in synovial fluids depending on patients, being the highest for P123 and the lowest for P108.

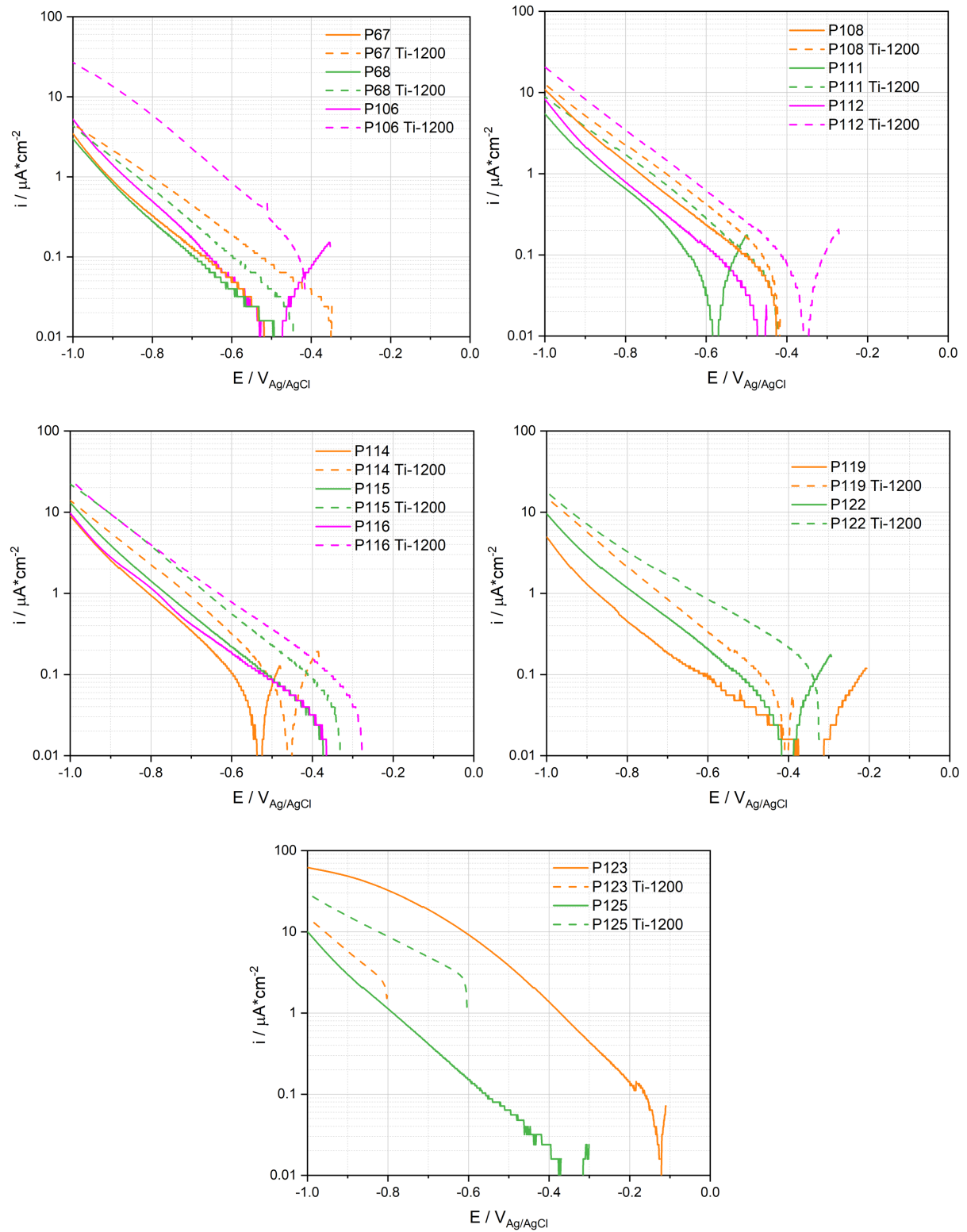
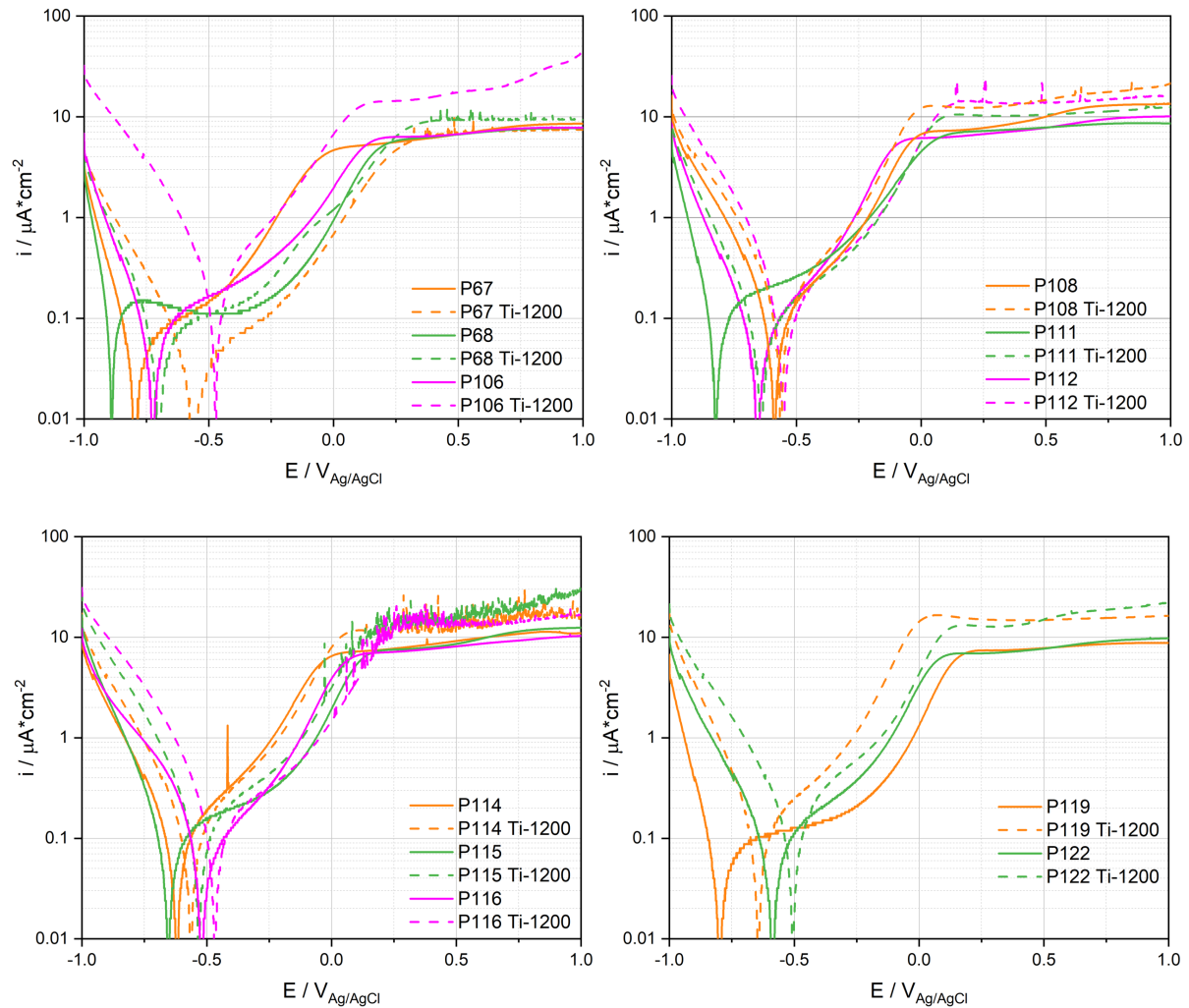


Figure 7.3 Cathodic polarization curves (logarithmic scale of the absolute current density) of Ti and Ti-1200 samples in tested synovial fluids from PS, and R (P108 and P109) groups

Anodic polarization curves of Ti and Ti-1200 are displayed in Figure 7.4. Three reaction domains are observed in polarization curves for both surfaces: the cathodic domain below the

corrosion potential ( $E_{\text{cor}}$ ), the cathodic/anodic transition at  $E_{\text{cor}}$  and the anodic domain at higher potentials. Similar with cathodic scan, the cathodic current density for rough surface is higher than that for smooth surface, except for P123. The difference in the current density can be up to one order of magnitude. Differently, the anodic current density in the lower potential region is independent of surface roughness for most patients. Exceptions are observed for P67, P106, P119 and P125, where the anodic current for rough surface can be either higher (P106, P119 and P125) or lower than that of smooth surface. Different behavior is observed for the current in the higher potential region, where the current density for the rough surface is always higher than that for smooth surface, especially for P106, P119, P122 and P125. It is worth noting that the different current at one applied potential between smooth and rough surfaces for some patients is within the scattering of the measurements, as shown in Table C. 3 and Table C. 5.



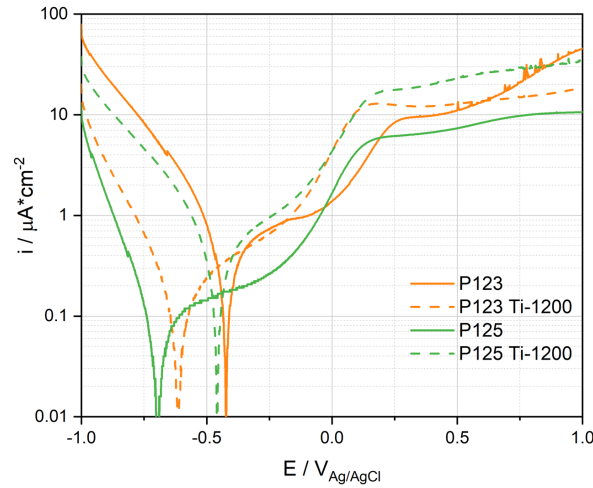


Figure 7.4 Anodic polarization curves (logarithmic scale of the absolute current density) of Ti and Ti-1200 samples in tested synovial fluids from PS, and R (P108 and P109) groups

To quantitatively assess the results, characteristic parameters such as cathodic current density  $i_c$  measured at a potential of  $-0.9 \text{ V}_{\text{Ag/AgCl}}$  in the anodic scan, the corrosion potential  $E_{\text{cor}}$ , and the anodic current density  $i_{\text{pp}}$  measured at a potential of  $-0.2 \text{ V}_{\text{Ag/AgCl}}$  and  $0.5 \text{ V}_{\text{Ag/AgCl}}$  are extracted from Figure 7.4 and listed in Table 7.1. The results show the STDEV of cathodic current density and the  $E_{\text{cor}}$  for smooth surface is higher than that of rough surface. In contrast, opposite results are obtained for the anodic current density at  $0.5 \text{ V}_{\text{Ag/AgCl}}$ .

Table 7.1 Electrochemical parameters extracted from anodic polarization curves for Ti and Ti-1200 samples in different synovial fluids

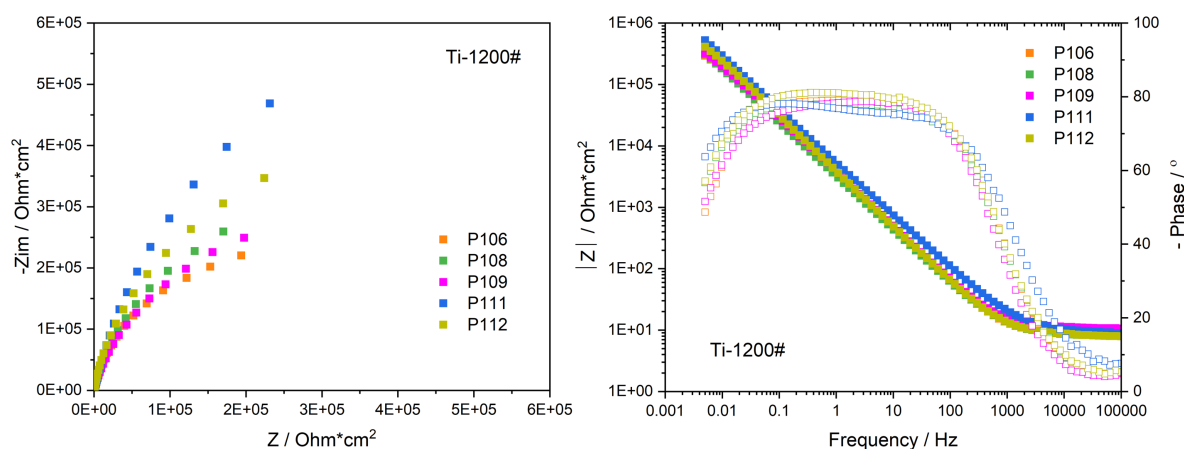
Patient		$i_c (-0.9V) / \mu A/cm^2$		$E_{cor} / V_{Ag/Ag/Cl}$		$i_{pp} (-0.2V) / \mu A/cm^2$		$i_{pp} (0.5V) / \mu A/cm^2$	
		Ti	Ti-1200	Ti	Ti-1200	Ti	Ti-1200	Ti	Ti-1200
PS	67	-0.33	-1.26	-0.79	-0.55	1.30	0.15	6.70	6.96
	68	-0.05	-0.95	-0.89	-0.70	0.20	0.35	6.67	9.90
	106	-0.79	-11.36	-0.72	-0.48	0.49	1.30	6.72	17.50
	111	-0.41	-1.96	-0.82	-0.64	1.05	0.77	7.83	10.51
	112	-1.45	-6.42	-0.66	-0.56	2.18	0.83	7.78	14.44
	114	-2.16	-4.15	-0.62	-0.57	1.38	1.10	9.18	12.47
	115	-2.60	-7.08	-0.66	-0.53	0.37	0.56	8.59	14.65
	116	-2.70	-10.26	-0.52	-0.47	0.49	0.40	8.11	13.99
	119	-0.37	-3.56	-0.79	-0.64	0.26	1.82	7.80	14.85
	122	-2.12	-5.48	-0.58	-0.51	0.51	0.77	7.71	15.03
	123	-23.82	-3.36	-0.42	-0.61	0.85	0.82	11.07	12.85
	125	-1.56	-12.19	-0.69	-0.46	0.32	1.16	7.34	23.01
R	108	-2.95	-4.07	-0.59	-0.56	1.15	1.79	10.02	14.71
Average		-3.18	-5.55	-0.67	-0.56	0.81	0.91	8.12	13.91
STDEV		6.28	3.75	0.13	0.07	0.58	0.51	1.32	3.86
Error		3.74	1.01	0.35	0.21	1.22	0.92	0.27	0.58

### 7.2.3 EIS Measurements on Ti-1200

To investigate the influence of  $R_a$  on the corrosion behavior under steady state condition, the EIS measurements on Ti-1200 in different synovial fluids were conducted under OCP condition. The results for rough surface are displayed in Figure 7.5. The results for smooth surface are already shown in Chapter 5, thus not shown here.

Similar to smooth surfaces, all the Nyquist plots for rough surface are circular arcs with different arc lengths and angles depending on the patients. The smallest and largest arc length and arc angle are obtained for P125 and P124, respectively.

Two distinctive parts depending on frequency are also observed in the Bode plots. The solution resistance of the synovial fluids between the Ti sample and the RE is obtained in the high frequency where the phase angle is close to  $0^\circ$ . The linear increase of modulus with the decrease of frequency in the lower frequency region, where the phase angle is reaching to  $-80^\circ$ . A broad phase plateau is obtained for most patients, except for P125. Two time constants are observed for P125, indicating the presence of a double layer in the higher frequency region and a passive layer on the sample surface in the low frequency region. The broad phase plateau suggests the overlap of the two time constants. No modulus plateau is obtained for all patients, indicating the steady state of the electrode/electrolyte interface is not reached.



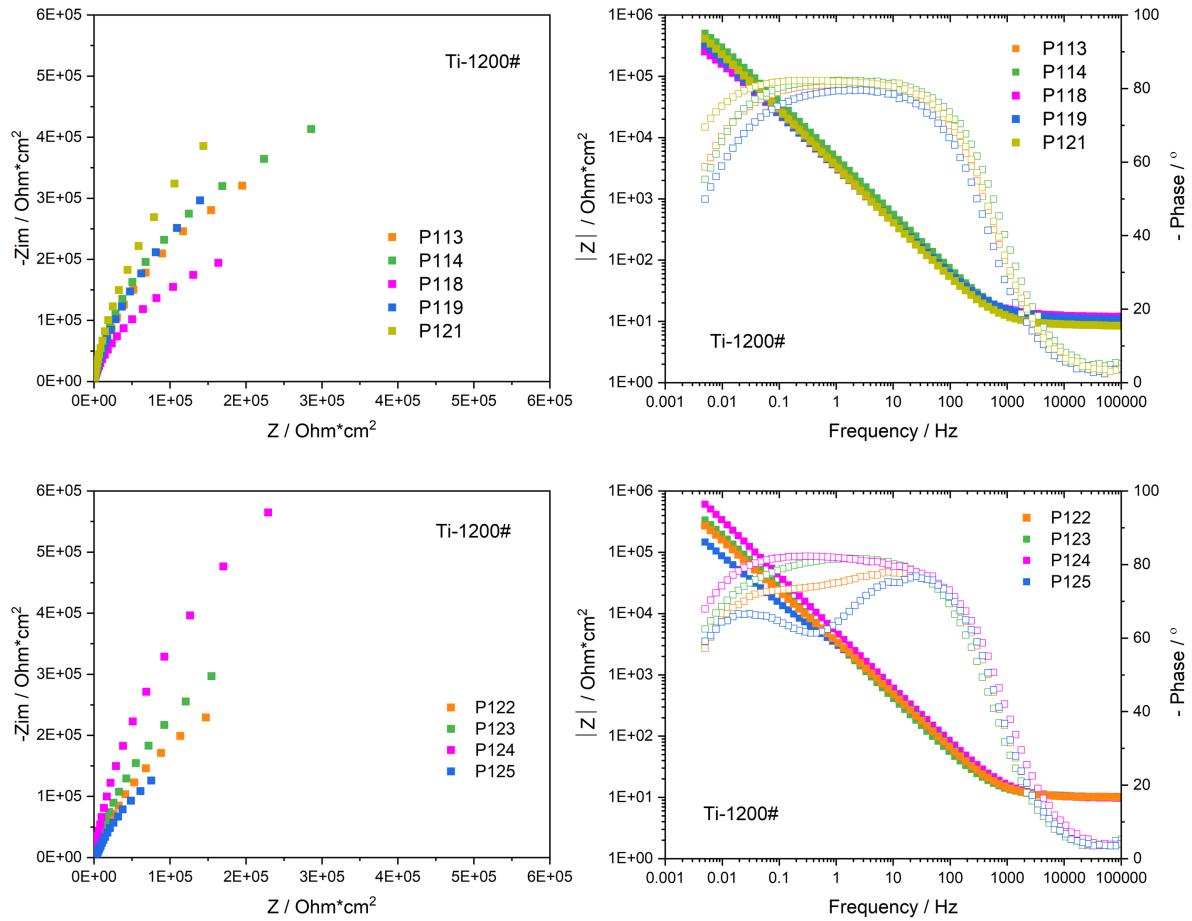


Figure 7.5 Nyquist and Bode plots of Ti-1200 in tested synovial fluids

To quantitatively analyze the EIS results, Modulus  $|Z|$  and phase angle are extracted from the Bode plot at the frequency of 0.005 Hz. The  $R_s$  of the synovial fluids are also extracted at the frequency of  $10^5$  Hz. All the parameters are listed in

Table 7.2. The  $|Z|$  is used as an alternative result of  $R_p$  to study the reaction resistance of Ti sample in different synovial fluids. The  $R_s$  values of synovial fluids from P106 to P125 are close to the results obtained on smooth surface, indicating that no influence of  $R_a$  on the  $R_s$  measurement is obtained. The  $|Z|$  varies with patient, being the highest of 610  $\text{K}\Omega\text{cm}^2$  for P124 and the lowest of 147  $\text{K}\Omega\text{cm}^2$  for P125. The phase angle varies slightly with patient, with the average value of  $58^\circ$  and the STDEV of  $7^\circ$ .

Table 7.2 Electrochemical parameters extracted from EIS measurements of Ti-1200

Patient	Rs / Ohm*cm <sup>2</sup>	Z  / KOhm*cm <sup>2</sup>	-Phase / °
PS	106	7.99	293
	111	8.71	523
	112	7.84	412
	113	11.00	375
	114	8.96	503
	118	11.94	254
	119	10.75	328
	121	8.50	411
	122	10.14	273
	123	9.95	334
	124	9.65	610
	125	10.25	147
R	108	7.99	310
	109	10.50	318
Average	9.54	255	58
STDEV	1.28	198	7
Error	0.17	0.38	0.18

Comparing the results with smooth surface listed in Table 5.2, lower modulus is obtained for rough surface in most synovial fluids, except for P109, P123 and P124. The modulus values obtain on both surfaces are in agreement with the current density in Figure 7.3 and Figure 7.4, namely higher modulus value corresponds to lower current density.

### 7.3 Discussion

It is not surprising to obtain a higher cathodic or anodic current on a rough surface in synovial fluids due to the larger real contact area of the electrode/electrolyte interface. However, the small difference in area (1.14) between rough surface and smooth surface indicates that the real surface area will not have significant impact on the different current densities. However, lower cathodic or anodic current is also obtained for some patients, such as P106 and P123. These results are contradictory to the general understanding of the influence of surface roughness except if we consider that another oxide or defects are present on the rough surface.

To understand the influence of Ra on the electrochemical behavior of Ti in synovial fluids, same measurements were carried out in several simulated solutions and the results are plotted in Figure 7.6. A lower cathodic current is obtained for rough surface in NaCl, PBS and PBS +

BSA + HA solutions, however higher cathodic current is measured for the rest of the tested solutions. Interestingly, higher anodic current, especially in the initial stage, is measured for rough surface in all tested solutions. For all tested simulated solutions, the corrosion rate of Ti increases with the surface roughness. The corresponding EIS measurements on Ti-1200 were conducted, and the results are summarized in Figure C. 5 and Table C. 5. Except for NaCl + BSA and PBS + BSA + HA solutions, the modulus corresponds well with the polarization resistance, namely lower modulus is obtained for rough surface. For NaCl + BSA and PBS + BSA + HA solutions, higher modulus is acquired on rough surface.

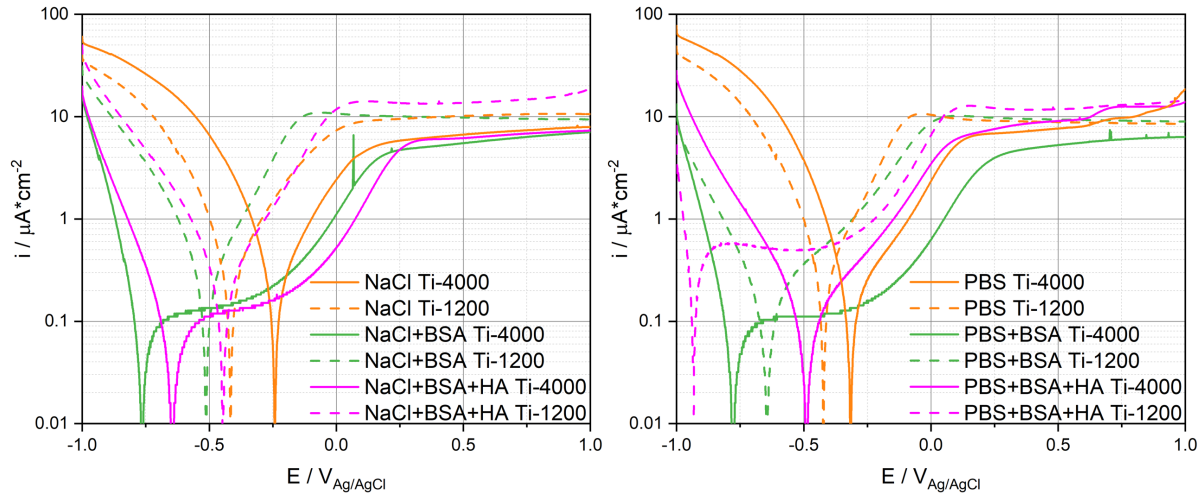


Figure 7.6 Anodic scan of the polarization curves of Ti and Ti-1200 in simulated solutions

Our results are in accordance with the results for Ti or Ti alloy in saline solutions where the corrosion rate increases with a certain roughness range [158–161]. For instance, the corrosion rate of CP Ti in Ringer's solution increases with the increase of Ra from 46 nm to 474 nm [158]. However, the study in organic containing solutions is limited. The influence of Ra on the corrosion behaviour of Ti surface in PBS with different concentration of bovine serum albumin was investigated with EQCM [162]. The results show that 15 times more organic was adsorbed on a rough surface than on smooth one. The roughness enhances the anodic current density but has little influence on the cathodic reaction. The little influence of Ra on the cathodic current obtained from the literature is contradictory to those displayed in Figure 7.6.

To understand the different corrosion behavior, EIS was used to obtain detailed information on the electrode/electrolyte interface. It is widely reported that there are two layers on sample surface after immersing in solutions, namely the inner layer of the compact passive film, and the outer layer of double layer/organic adsorption layer [125, 128] or porous passive film layer [158]. Based on the previous research, the polarization resistance consists of charge transfer resistance ( $R_c$ ) of passive film and polarization resistance ( $R_{p1}$ ) of the outer layer



[158]. The  $R_c$  was reported to decrease with  $R_a$  from 43 nm to 116 nm, and then increases with  $R_a$  from 116 nm to 474 nm. However, the opposite trend was found for  $R_{p1}$  [158]. These results indicate that the passive film thickness obtained by different polishing procedure varies with  $R_a$ .

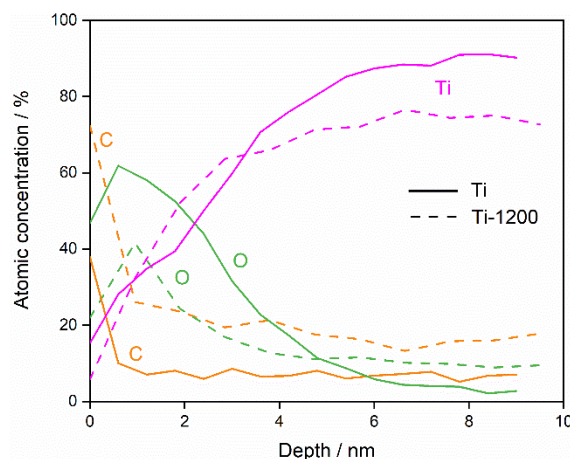


Figure 7.7 Auger depth profiles from the smooth and rough surfaces before exposure to solutions

To support the conclusion, AES depth analysis was performed on the rough surface and the profiles were displayed in Figure 7.7. For comparison, the depth profile obtained on the smooth surface is also present. The graph shows that a higher amount of carbon layer is obtained throughout the sputter duration on the rough surface than on the smooth one. Contradictory to the C signal, the O signal detected on a rough surface is about half of the atomic concentration for the smooth one. According to the O signal, a slightly thinner passive film thickness (about 1.5 nm) is detected on the rough surface compared with the smooth one (about 2.5 nm). Little difference is obtained for the Ti signal on both surfaces. These results indicate that more carbon contamination is present on the rough surface and cannot be sputtered efficiently. The slightly lower cathodic current for rough surface in NaCl and PBS solutions could be due to the carbon contamination on the surface, which decreases wettability.

In addition, Kelvin probe force microscopy was applied to measure the Voltage potential on the sample surface [163]. The results indicate that rough surface is more electrochemical active due to the more significant difference in Voltage potential between the peaks and valleys, forming a micro-galvanic corrosion [163]. The micro-galvanic corrosion could be responsible for the higher anodic current densities for the rough surface.

According to the literature, the influence of surface roughness is quite complex, let alone in human synovial fluids, which composition is too complex to be studied. Therefore, in this chapter the influence mechanisms of  $R_a$  on the electrochemical behavior of Ti in synovial

fluids was not studied. Instead, inductive analysis was carried out by comparing the in-vivo and in-vitro results.

To summarize, the increase of cathodic current with Ra in synovial fluids is similar to the results for NaCl + BSA, NaCl + BSA + HA and PBS + BSA solutions, not only the current variation with Ra, but also the current value on both surfaces. Similarly, the decrease of cathodic current density with Ra is similar to the behavior for NaCl and PBS solutions. The increase of the in-vivo anodic current for the rough surface is observed for all simulated solutions, however, the close or declined anodic current cannot be obtained for in-vitro results. Thus, a tentative conclusion can be obtained that the Ra influence on all in-vivo cathodic reaction behavior can be predicted by simulated solutions, but the anodic reaction behavior cannot.

## 7.4 Summary

In this chapter, the influence of surface roughness on the corrosion behavior of Ti in contact with human synovial fluids was carried out using OCP, potentiodynamic polarization and EIS. The results were compared with in-vitro measurements, and a conclusion can be drawn below:

- The electrochemical behavior of Ti surface exposed to synovial fluids is significantly affected by surface roughness.
- Except for 1 out of 14 patients, higher Ra implies higher cathodic and anodic current response. This effect cannot be attributed alone to the larger exposed area and to the presence of organic molecules which adsorption is known to be promoted by surface roughness. Thus, other factors play a role such as the different electrochemical reactivity of the peaks and valleys of the surface.
- These conclusions are consistent with the observations carried out in the simulated fluids.

## Chapter 8 Discussion

Based on the obtained results and outcomes, some general aspects concerning the experimental protocol, the corrosion mechanisms and the risks of galvanic corrosion in-vivo will be discussed in this chapter.

### 8.1 Improvement of the Experimental Protocol

In this thesis, a systematic experimental protocol was designed and validated. It is important since it allows to assess in a rigorous repeatable way the electrochemical behavior of Ti and CoCrMo alloy in human synovial fluids. As discussed in the previous chapter the corrosion rate determined in this study over relative shorter time correspond well with the metal release rates obtained in the patients with metallic implants. This shows that the conclusions from these electrochemical experiments can be used to describe the behavior of biomedical alloys once implanted in the patients.

However, there are several points need to be improved, as discussed below:

For example,  $R_p$  results depend on the scan rates of the measurement according to Figure C. 9. To avoid that, a lower scan rate ( $\leq 0.6$  mV/s) can be applied. In addition, a shorter scan region from -10 mV to 10 mV with respect to OCP can be applied to reduce the recovery time from the polarization to OCP condition.

EIS measurements with the frequency lower enough to obtain the modulus plateau is necessary to be performed. Meanwhile, other potentiostats with short acquisition time can be introduced to reduce the measurement duration. For example, the measurement duration for the frequency region of  $10^5$  - 0.005 Hz obtained through recently commercialized VIONIC potentiostat (24 bits A/D converter) is half of that obtained with BioLogic potentiostat (16 bits A/D converter). Additionally, the  $R_p$  test during OCP measurement can be introduced to compare the values with those acquired from EIS.

EQCM technique is a powerful technique that combines electrochemistry and mass change. It is important to understand the electrochemical behavior of a metal surface in contact with electrolytes. However, it is difficult to find a crystal that works properly. For instance, oscillation peaks are observed in the polarization curves of Ti crystal in both synovial fluids and simulated solutions. This is probably due to the limited adhesion of the deposits on the crystal, the porosity, the continuity of the coating and possible galvanic coupling between Ti and Au. All these aspects should be evaluated in order to develop robust Ti coated crystals for

optimized EQCM measurements. Moreover, it will be beneficial to combine EQCM with surface analysis for samples exposed to synovial fluids. To avoid unwanted precipitation induced by the sterilization procedure, see Chapter 7, the samples could be rinsed with water upon extraction from synovial fluids and prior to sterilization.

The protocol should further include better characterization of human synovial fluids. Indeed, according to the OCP and polarization curves of Ti and CoCrMo alloy, dissolved oxygen reduction and organic adsorption on the sample surfaces are the key factors determining the corrosion rates of both materials in human synovial fluids. Thus, the dissolved oxygen concentration in human synovial fluids should be detected in a future work. Besides, the concentration of the main organic components of synovial fluids (HSA, HA and lipids) should be determined.

## 8.2 Corrosion Mechanisms

The present study has shown that the anodic and the cathodic behavior can significantly change depending on patients. The dominating cathodic reaction at OCP is the oxygen reduction reaction. Moreover, in the cathodic domain the presence of organic species also plays a major role on the electrochemical kinetics. This can be explained by the adsorption of organics limiting the access of oxygen to the surface and thus its reduction. Thus, the electrochemical response is determined by the interaction of organics and oxygen and not simply by one of these factors taken separately.

To describe this interaction, one can assume that the adsorption of organics follows a Langmuir isotherm [62], thus the surface coverage by organics can be described by equation (8-1).

$$\theta = \frac{B_{ADS} C}{1 + B_{ADS} C} \quad (8-1)$$

Where  $\theta$  is the coverage of adsorbed protein on the surface;  $B_{ADS}$  is the affinity of the protein molecules toward the surface ( $\text{cm}^3/\text{mol}$ ); and  $C$  is the concentration of protein in the bulk solution ( $\text{mol/L}$ ).

The oxygen reduction reaction takes place on the surface areas not covered by organics and follows the Volmer-Butler equation for charge transfer control reactions.

$$i_{O_2} = -nFK(1 - \theta)C_{O_2} \exp\left(\frac{E}{\beta_c}\right) \quad (8-2)$$

Where  $i_{O_2}$  is the cathodic current density ( $\text{A}/\text{cm}^2$ );  $n$  is the charge number;  $K$  is a constant;  $F$  is Faraday constant ( $\text{C}/\text{mol}$ );  $\theta$  is the coverage of adsorbed protein on the surface;  $C_{O_2}$  is the

concentration of dissolved oxygen in human synovial fluids (mol/L);  $E$  is the applied potential (V); and  $\beta_C$  is the Tafel coefficient (V).

$$i_{O_2} = -nFK \frac{1}{1 + B_{ADS} C} C_{O_2} \exp\left(\frac{E}{\beta_C}\right) \quad (8-3)$$

By combining equation (8-1) and (8-2) one obtains equation (8-3) that describes the influence of oxygen and organic concentration on the oxygen reduction current. Note that this current at OCP corresponds to the corrosion rate. Figure 8.1 is the graphical representation of equation (8-3) and shows for example that much higher currents can occur in patients with high oxygen and low organic concentration compared to patients with low oxygen and high organic concentration.

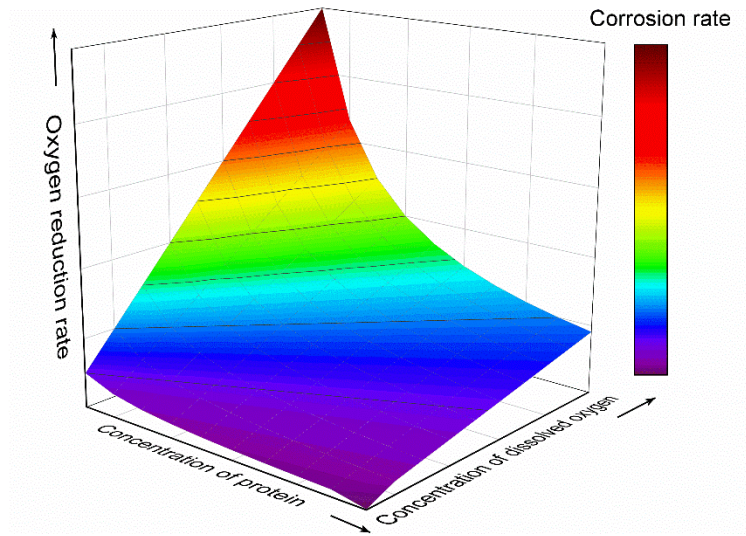


Figure 8.1 Oxygen reduction rate as a function of concentration of protein and dissolved oxygen (arbitrary units)

This simple model clearly shows that the reactivity of synovia thus the corrosion behavior is controlled by the antagonistic effect of oxygen and of adsorbing organics.

Less clear is the effect of synovial fluid of the different patients on the anodic current of titanium. No correlation was found between the in-vivo results and the invitro investigations on the effect of BSA, HA and  $H_2O_2$  on that anodic electrochemical behavior. This points out to another synovial component acting on the anodic reaction either by promoting dissolution (i.e. complexation [89]) or by inhibiting it by adsorption [89].

### 8.3 Galvanic Corrosion Between Ti and CoCrMo Alloy in Human Synovial Fluids

Ti/CoCrMo coupling is widely used in joint prostheses due to its excellent corrosion resistance and mechanical properties. However, the contact of dissimilar materials in an environment can result in galvanic corrosion attributed to the different corrosion behaviors. In the galvanic coupling, the corrosion rate of the noble material decreases while it increases for the less noble material.

To determine if galvanic corrosion occurs between Ti alloy and CoCrMo alloy, in-vivo study was conducted on retrieved prostheses with Ti/CoCrMo coupling, and contrary results were obtained from the literature [26, 164]. Corrosion is observed in 25 out of 48 retrieved hip prostheses with Ti/CoCr coupling for the stem and head through SEM analysis, while no evidence of corrosion is found in the rest 91 prostheses where the same alloy was used for stem and head [26]. It should be noted that the corrosion was reported depending on the implantation time, namely the implant was corroded only when the implantation time was longer than 40 months. However, contrary results are reported by Lucas et al. [164] that no galvanic corrosion is observed on four retrieved CoCrMo/Ti6Al4V hip implants implanted for 2-6 years. The results were verified by direct coupling experiments in 0.9% NaCl solution. The different results for the retrieved implants could be due to the different properties of the materials.

Besides, research on simulated body fluids has also been conducted [165–168]. The results indicate that the galvanic corrosion between the coupling materials depends on surface quality and solution composition. For instance, pure Ti behaves as an anode when coupled to CoCrMo alloy in saline solutions, while it has a cathodic behavior after an acid etching surface treatment due to the increase of surface roughness [165]. Also, the geometry of the galvanic couple, such as the area ratio of anodic/cathodic and insulation distance between two electrodes, is reported to significantly influence the galvanic corrosion behavior [169]. Besides, studies on the corrosion behavior of unconnected Ti6Al4V alloy and CoCrMo alloy in Ringer's solution were carried out, and the galvanic corrosion behavior between materials was acquired by the Tafel method and mix potential theory [170], [171]. Contradictory results were obtained with the galvanic current density of CoCrMo alloy being  $0.1 \mu\text{A}/\text{cm}^2$  and  $7 \mu\text{A}/\text{cm}^2$ , respectively. In the former case, galvanic corrosion is negligible.

Since contradictory results are both obtained for in-vivo and in-vitro study, and in-vitro study cannot represent the real reaction conditions. It is therefore important to study if galvanic corrosion occurs for Ti/CoCrMo coupling in real conditions. The galvanic corrosion current was simply calculated with the OCP and  $R_p$  values of both materials in tested synovial fluids.

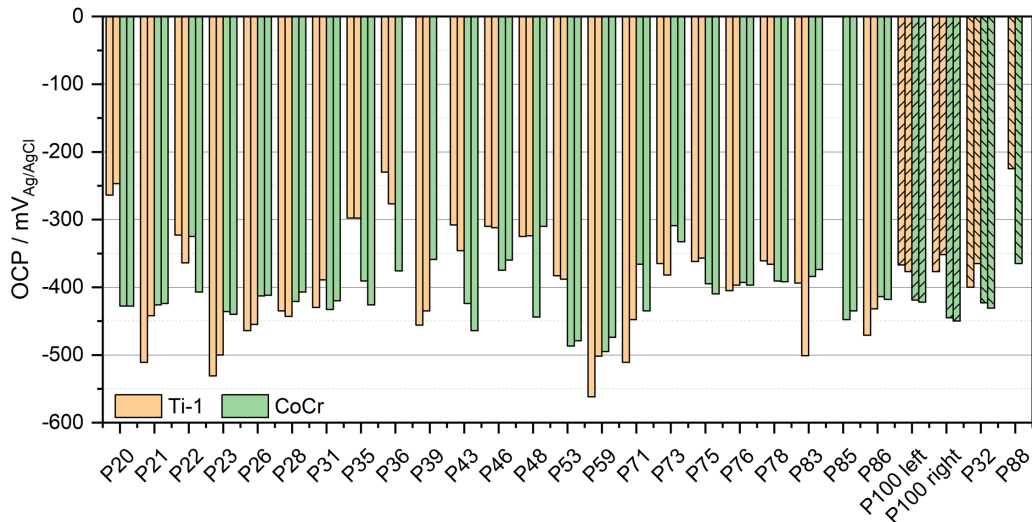


Figure 8.2 OCP of Ti and CoCrMo alloy immersed in human synovial fluids from PS, TKA (P100) and R (P32 and P88) groups

The stabilized OCP of Ti and CoCrMo alloy in tested human synovial fluids are summarized in Figure 8.2. The figure shows that the OCP value of Ti can be higher or lower than that of CoCrMo alloy, depending on the synovial fluids. The difference in OCP value between Ti and CoCrMo alloy varies from 28 mV for P28 to 164 mV for P20.

The  $R_p$  values measured during OCP measurement for Ti and CoCrMo alloy in synovial fluids are presented in Figure 8.3. The results reveal that much higher  $R_p$  values are obtained for Ti compared with CoCrMo alloy in most synovial fluids, but in P22, P36 and P39, where the  $R_p$  value of both materials are very close. The difference of  $R_p$  value between Ti and CoCrMo alloy varies from a minimum of 9.89  $\text{K}\Omega\text{cm}^2$  for P39 to a maximum of 4.65  $\text{M}\Omega\text{cm}^2$  for P48.

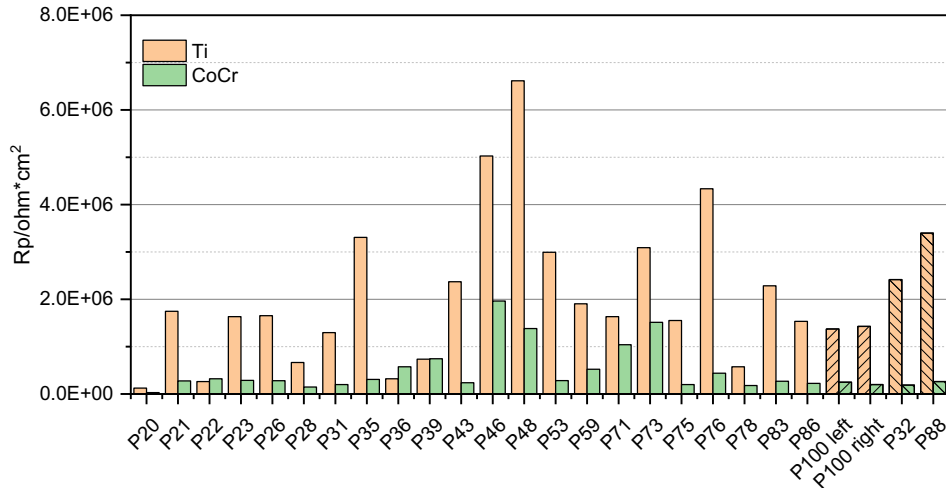


Figure 8.3 Rp of Ti and CoCrMo alloy tested in different synovial fluids PS, TKA (P100) and R (P32 and P88) groups

The corrosion cell can be represented by an electrical equivalent circuit, as shown in Figure 8.4. The voltage source  $E_{cor,I}$  and  $E_{cor,II}$  represent the OCP of the two materials. The  $R_{p,I}$  and  $R_{p,II}$  represent the polarization resistance of the two materials in the electrolytes. The  $R_{int}$  represents the solution resistance between the two materials, and  $R_{ext}$  represent the resistance of the electronic conductors.

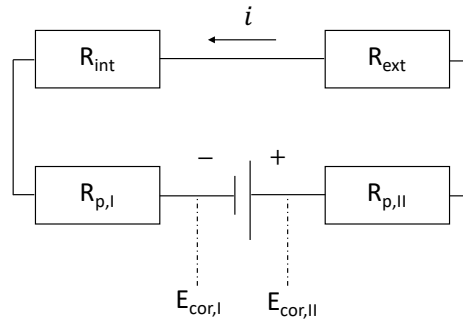


Figure 8.4 Electrical equivalent circuit of corrosion cell [113]

Then, the galvanic corrosion current  $i_G$  can be calculated through the equation (8-4):

$$i_G = \frac{E_{cor,II} - E_{cor,I}}{R_{p1} + R_{p2} + R_s} \quad (8-4)$$

Where the  $R_{ext}$  is not considered due to the negligible electrical resistance.

By putting the corresponding values, the galvanic corrosion of Ti/CoCrMo coupling for each synovial fluid can be obtained, and the results are presented in Figure 8.5. In the graph, the current with CoCrMo alloy works as anode is displayed in green. The current varies with



patients from  $\text{nA}/\text{cm}^2$  to  $\mu\text{A}/\text{cm}^2$ , being the maximum and the minimum current for P20 and P76, respectively. The  $i_G$  value is close to the corrosion current density of Ti in synovial fluids, indicating there is no significant galvanic corrosion of Ti/CoCrMo coupling in tested synovial fluids. This is probably due to the small  $\Delta\text{OCP}$  between Ti and CoCrMo alloy in synovial fluids.

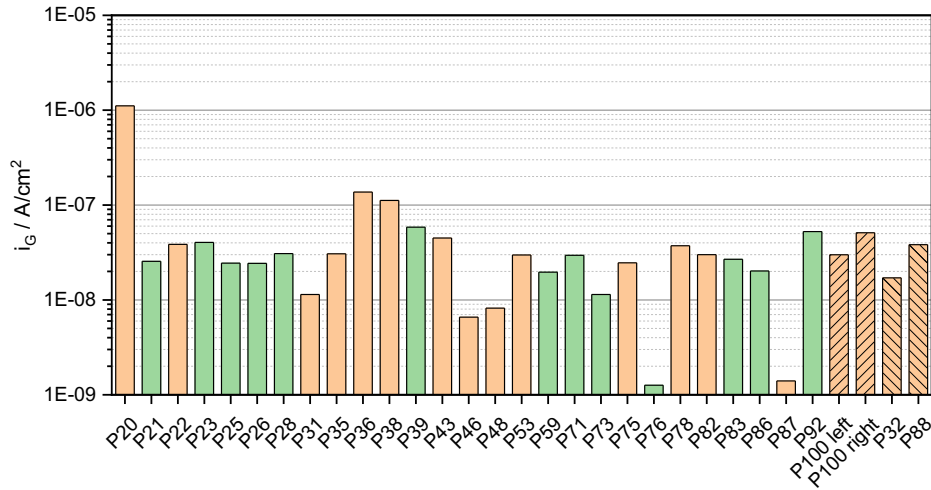


Figure 8.5 Galvanic corrosion rate of Ti/CoCr coupling in human synovial fluids PS, TKA (P100) and R (P32 and P88) groups

For comparison, the galvanic corrosion between Ti and CoCrMo alloy in simulated solutions was calculated. The OCP and  $R_p$  values and polarization curves of Ti and CoCrMo alloy in simulated solutions are displayed in Figure 8.6. The corresponding  $i_G$  values are presented in Figure 8.7. The calculated values are lower than  $0.15 \mu\text{A}/\text{cm}^2$ , and they are relatively lower than the corrosion current density of Ti in simulated fluids.

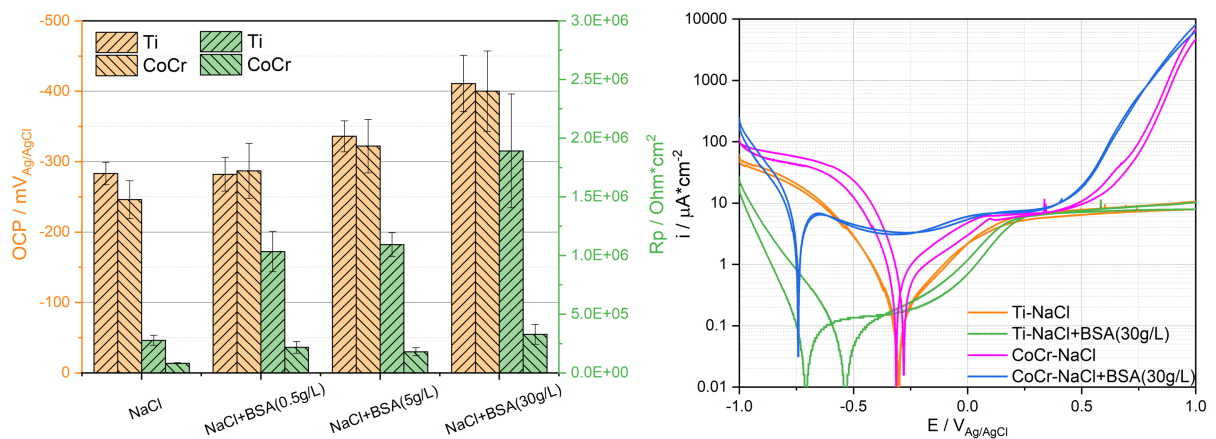


Figure 8.6 OCP,  $R_p$  and polarization curves of Ti and CoCrMo alloy in simulated solutions

The calculated values are verified by directly measuring the current between Ti and CoCrMo alloy in NaCl solution with a zero-resistance ohmmeter for 30 minutes. In this measurement, the Ti was connected to the WE cable and the CoCrMo alloy was connected to the ground cable, following the experimental protocol provided by IVIUM software. The real current density is also presented in Figure 8.7. The calculated  $i_G$  is about four times higher than the measured one, this is related to the lower  $R_p$ . As shown in Figure C. 9 in the Appendix, a higher current is obtained with a scan rate of 2 mV/s compared with that of 0.167 mV/s. Correspondingly, lower  $R_p$  is acquired, which is about four times different.

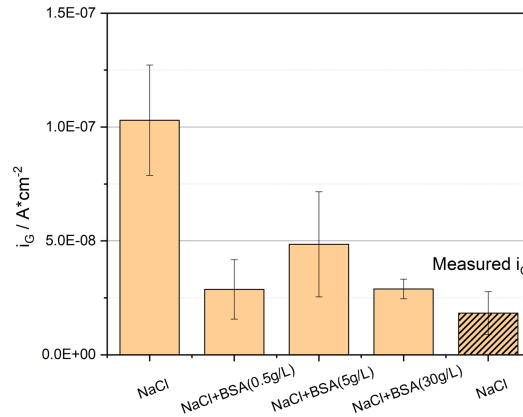


Figure 8.7 Galvanic corrosion rate of Ti/CoCr coupling in simulated body fluids

To summarize, no significantly galvanic corrosion is obtained for Ti/CoCrMo coupling in both synovial fluids and simulated solutions. It should be noted that the galvanic corrosion current in the real corrosion cell may not be uniform, depending on the system geometry, such as the area ratio between the cathode and anode [113]. It should be noted that the OCP of CoCrMo alloy, at least in the initial stage of the immersion, depends on the used sterilization procedure while Ti does not. Moreover, the OCP of Ti varies with  $R_a$ , as shown in Chapter 7.

## Chapter 9                      Conclusions

A first large-scale investigation on the electrochemical behavior of bulk Ti and CoCrMo alloy in human synovial fluids, directly extracted from patients with an ad-hoc procedure, was successfully carried out with a well-designed systematic experimental protocol, including electrochemical techniques (OCP, potentiodynamic polarization, EIS and EQCM) and surface characterization (FTIR, SEM/EDS and AES). The results were compared with those acquired in simulated solutions to understand the electrochemical reactions of both materials in synovial fluids.

The obtained results lead to the following conclusions:

- A reliable protocol for in-vivo electrochemical experiments of bulk metallic samples was successfully designed and validated. Out of 154 patients 73 yielded synovial liquid and 66 in sufficient amount for the electrochemical measurements (>2ml).
- The electrochemical behavior of Ti in human synovial fluids varies significantly with patients, being several orders of magnitude different. The electrochemical behavior of CoCrMo alloy is also patient dependent although its relative variation is sensibly less.
- The corrosion rates of Ti and CoCrMo alloy correspond well to the overall metal ion release rates into the human body found in patients with implanted hip and knee artificial joints.
- The corrosion rate of Ti and CoCrMo alloy is controlled by the combined action of charge transfer reaction of oxygen reduction and organic adsorption on the surface. Reactive oxygen species such as  $H_2O_2$  has been demonstrated not to play a crucial role in the electrochemical behavior of Ti and CoCrMo alloy. The results suggests that not only protein and HA are the organic components actively involved in the adsorption phenomena but probably also other synovial components such as lipids.
- The electrochemical behavior of Ti surface exposed to synovial fluids is significantly affected by surface roughness.
- The obtained results indicates that there is no significant risk of galvanic corrosion between Ti and CoCrMo alloy in human synovial fluids.

## Appendix A EQCM Study of Ti in Human Synovial Fluids

In the former chapters, the electrochemical behavior of Ti in human synovial fluids and the surface characterization of the reaction surface have been investigated. Although the obtained surface chemistry helps to understand the electrochemical behavior, it was influenced by the sample cleaning and sterilization. To avoid that, an in-situ technique that can measure the electrochemical responses of the sample surface to the electrolyte with the real-time mass variation is necessary. Thus, EQCM is introduced in this chapter to study the corrosion behavior of the Ti sample in contact with synovial fluids simultaneously with the mass change on the surface. To do this, OCP and potentiodynamic polarization were performed on the Ti coated crystal in several synovial fluids.

### A.1. Theory

EQCM device consists of two parts, namely, electrochemical cell and QCM. Two metal electrodes are deposited on both sides of the piezoelectric quartz crystal. The electrode that contacts with the electrolyte works as a WE, together with a RE and CE, forming the electrochemical cell. The electrode on the other side of the crystal is not in contact with the electrolyte and works as an oscillating electrode. EQCM technique is designed based on the piezoelectric effect where mechanical shear stress is generated proportional to the applied potential on the crystal. The resonate frequency of the crystal decreases or increases due to the mass increase or decrease on the electrodes [172]. Therefore, the mass variation of the surface can be obtained through the resonance frequency shift.

The relation between mass change  $\Delta m$  and frequency change  $\Delta f_m$  can be obtained from the Sauerbrey equation [173]

$$\Delta f_m = -\frac{2f_0^2}{\sqrt{\rho_q \mu_q}} \Delta m \quad (\text{A-1})$$

The frequency change is not only due to the mass loading ( $\Delta f_m$ ), but also attributed to the viscous loading ( $\Delta f_v$ ) [174].

$$\Delta f = \Delta f_m + \Delta f_v \quad (\text{A-2})$$

Where  $f_0$  is the resonance frequency of the crystal: 5MHz,  $\rho_q$  is the density of the crystal: 2.65 g/cm<sup>3</sup> and  $\mu_q$  is the shear coefficient: 2.956 · 10<sup>11</sup> g/cm/s<sup>2</sup>. These values are valid at room temperature. In that sense, Equation (A-2) can be rewritten as

$$\Delta m = -C_s \cdot \Delta f \quad (\text{A-3})$$

Where  $C_s$  is the Sauerbrey constant and it can be calculated from the equation (A-2).

The frequency change due to viscous loading has been reported by Kanazawa and Gordon [175], and it can be expressed as below

$$\Delta f_v = -f_0^{3/2} \cdot \sqrt{\frac{\rho_L \eta_L}{\pi \rho_q \mu_q}} \quad (\text{A-4})$$

Where the  $\rho_L$  is the density of the liquid g/cm<sup>3</sup> and  $\mu_L$  is the shear coefficient of the liquid g/cm/s<sup>2</sup>. For the EQCM measurements conducted in this chapter, the viscous damping of the liquids is reflected by the dissipation of the crystal.

Besides mass and viscous loading, the frequency change is also influenced by the surface roughness of the crystal, temperature, internal stress, and pressure [176]. However, these parameters are reported to be within the same Gaussian distribution of the radial sensibility [177]. Therefore, the effect of these parameters is not considered in this thesis.

## A.2. Experimental

### A.2.1. Quartz Crystal Characterization

The crystal consists of a Ti PVD coating on the top, an Au coating underneath the Ti surface and a key shape Au oscillating electrode on the back. The schematic diagram of the crystal is shown in Figure A. 1. The areas of the Ti surface and the Au oscillating surface are 1.12 cm<sup>2</sup> and 0.25 cm<sup>2</sup>, respectively. The Ra of the Ti surface was measured with KYENCE under the magnification of 20X, and the value is 18 ± 1 nm. The SEM image and the 3D profile of the Ti surface obtained through AES are displayed in Figure A. 2. The surface chemistry of the Ti electrode was conducted by through AES depth analysis [162], from which a layer of about 18 nm Ti electrode was detected.

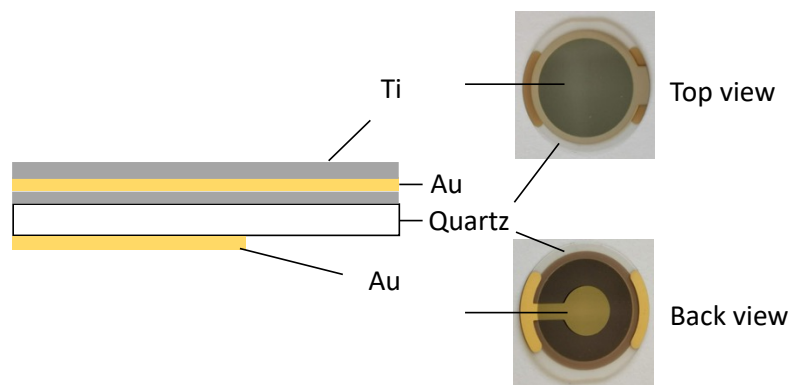


Figure A. 1 Schematic diagram of the crystal used in the EQCM measurements

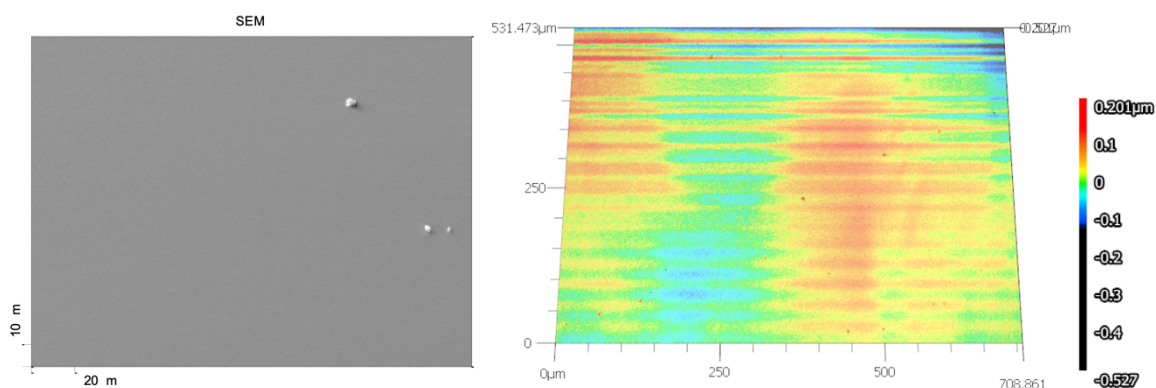


Figure A. 2 SEM image and 3D profile of the Ti crystal surface

The EQCM cell used for the electrochemical measurements is presented in Figure A. 3. As shown in the figure, the Ti coating is in contact with the tested solutions, and the Au electrode is coated on the back side of the crystal.

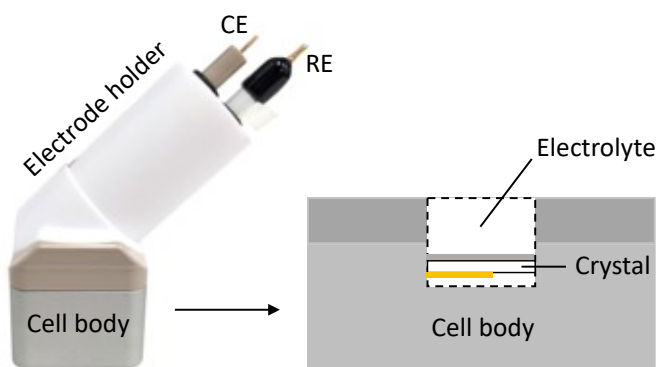


Figure A. 3 EQCM cell

### A.2.2. Calibration of the Sauerbrey Constant

Although the Sauerbrey constant  $C_s$  can be calculated from equation (A-2), the value is only valid at room temperature. To obtain the  $C_s$  value at 37°C, the calibration measurement was

conducted by electrochemical deposition of copper on a smooth Au crystal. The calibration measurements for  $C_s$  and  $C_v$  were conducted by Claes-Olof A. Olsson for an unpublished work.

The crystal (AWSensor, Spain) was coated with an Au layer on the top, with an Au area of  $1.14 \text{ cm}^2$  and an oscillating area of  $0.26 \text{ cm}^2$ . The calibration was carried out by applying  $-1 \text{ mA}$  on Au crystal in  $0.5 \text{ M CuSO}_4 + 0.5 \text{ M H}_2\text{SO}_4 + 1.1 \text{ M ethanol}$  for  $300 \text{ s}$ . Under this condition,  $100\%$  current efficiency can be obtained [178].

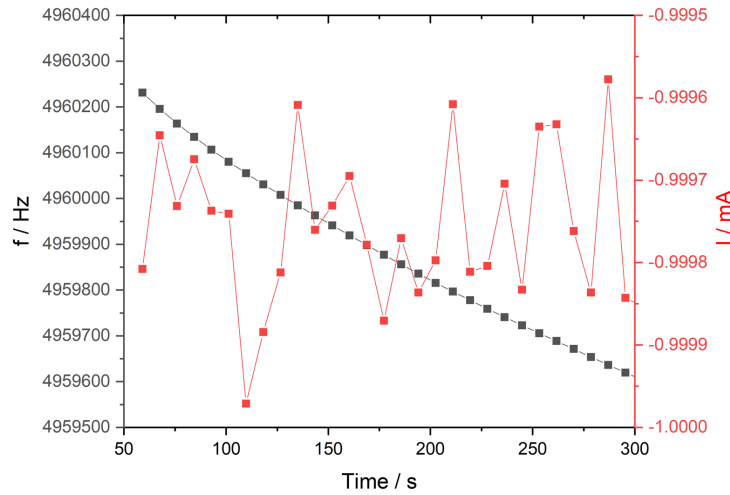


Figure A. 4 Frequency variation of the quartz crystal by the copper plating at  $37^\circ\text{C}$

The frequency variation on the crystal by copper plating is presented in Figure A. 4. Based on the result, the  $C_s$  can be calculated using Faraday's law

$$C_s = \frac{\Delta m}{\Delta f} = \frac{1}{\Delta f} \frac{M_{\text{Cu}} \int I dt}{nF} \frac{A_{\text{osc}}}{A_{\text{curr}}} \quad (9-5)$$

Where  $M_{\text{Cu}}$  is the molar mass of copper:  $63.54 \text{ g/mol}$ ,  $n$  is the charge number:  $2$ ,  $F$  is the faraday constant:  $96485 \text{ C/mol}$ ,  $A_{\text{curr}}$  is the Au surface area:  $1.14 \text{ cm}^2$  and  $A_{\text{osc}}$  is the oscillating area:  $0.26 \text{ cm}^2$ . Thus,  $C_s$  is acquired for Au crystal with the value of  $-29.25 \text{ ng/Hz}$ . Considering the  $A_{\text{osc}}$  for Ti crystal, the  $C_s$  of  $-117 \text{ ng/cm}^2/\text{Hz}$  can be calculated.

### A.2.3. Calibration of the Viscous Loading

The separation between mass loading and viscous loading was performed on the Au crystal in water/glycerol solutions. The solutions with the concentration of glycerol of  $0$ ,  $0.95 \text{ wt.}\%$ ,  $1.50 \text{ wt.}\%$  and  $3.35 \text{ wt.}\%$  were used. The measurement was carried out under OCP condition at  $37^\circ\text{C}$  for  $5 \text{ minutes}$ . The average frequency and dissipation value for each solution are plotted in Figure A. 5. As shown in Figure A. 5, a linear regression line is obtained for the data points, where the viscous constant  $C_v$  is obtained

$$C_v = \frac{\Delta f}{\Delta D} = -2.51 \cdot 10^6 \quad (9-6)$$

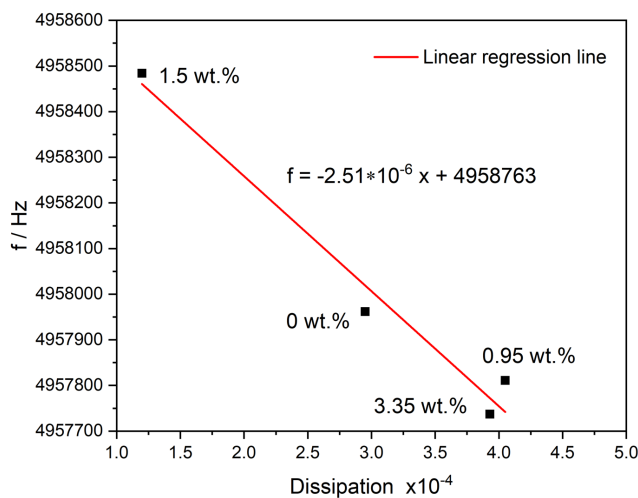
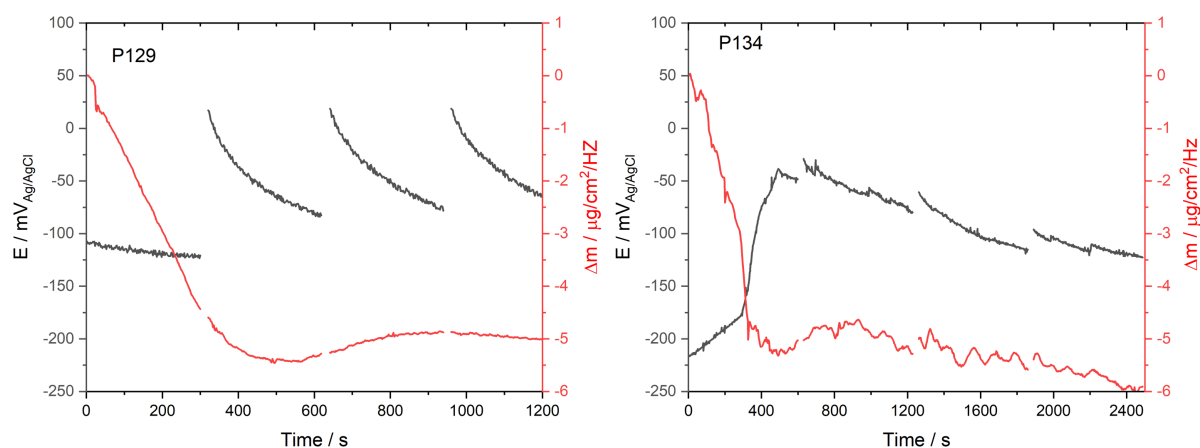


Figure A. 5 Variation of frequency of quartz crystal as a function of dissipation in water/glycerol solutions with different concentrations of glycerol

### A.3. Results

#### A.3.1. OCP of Ti Crystal

Due to the time limitation of the thesis, only three valid EQCM results are obtained. The OCP variations with time for P129, P134 and P154 are displayed in Figure A. 6. Besides, the corresponding calculated mass changes are also present in the figure. The OCP gaps in the graph are due to Rp measurements which is not shown here.





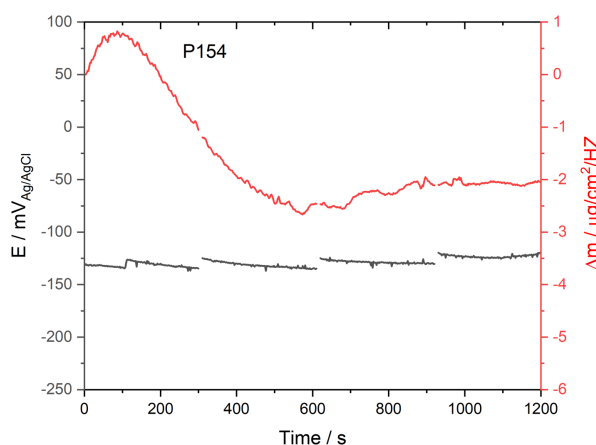


Figure A. 6 OCP evolution with time for P129, P134 and P154, together with the mass changes on the Ti surfaces

The graphs show the stabilized OCP of Ti for P129, P134 and P154 is  $-50 \text{ mV}_{\text{Ag}/\text{AgCl}}$ ,  $-125 \text{ mV}_{\text{Ag}/\text{AgCl}}$  and  $-120 \text{ mV}_{\text{Ag}/\text{AgCl}}$ , respectively. The interrupts of the curves in the graphs are due to the  $R_p$  measurement during OCP. Similarly, the decline of the OCP after the interrupts is attributed to the recovery of the steady state on the sample surface after the  $R_p$  measurement. The OCP values obtained on Ti crystal are relatively positive than those acquired on bulk materials (from  $-550 \text{ mV}_{\text{Ag}/\text{AgCl}}$  to  $-200 \text{ mV}_{\text{Ag}/\text{AgCl}}$ ). Unlike OCP results, the mass changes on the Ti surface for P129 and P134 are quite similar, abruptly decreasing about  $5 \mu\text{g}/\text{cm}^2/\text{Hz}$  by 400 s and roughly remaining stable until 1200 s. For P134, the mass change slightly decreases continuously to  $6 \mu\text{g}/\text{cm}^2/\text{Hz}$  at 2400s. Different mass change was obtained for P154, where the mass obviously increases with the immersion time to a maximum of  $1 \mu\text{g}/\text{cm}^2/\text{Hz}$  at 100s. Subsequently, the mass starts to decrease significantly until reaching the plateau of around  $-2 \mu\text{g}/\text{cm}^2/\text{Hz}$  from 600 s.

### A.3.2. Potentiodynamic Polarization Curves of Ti Crystal

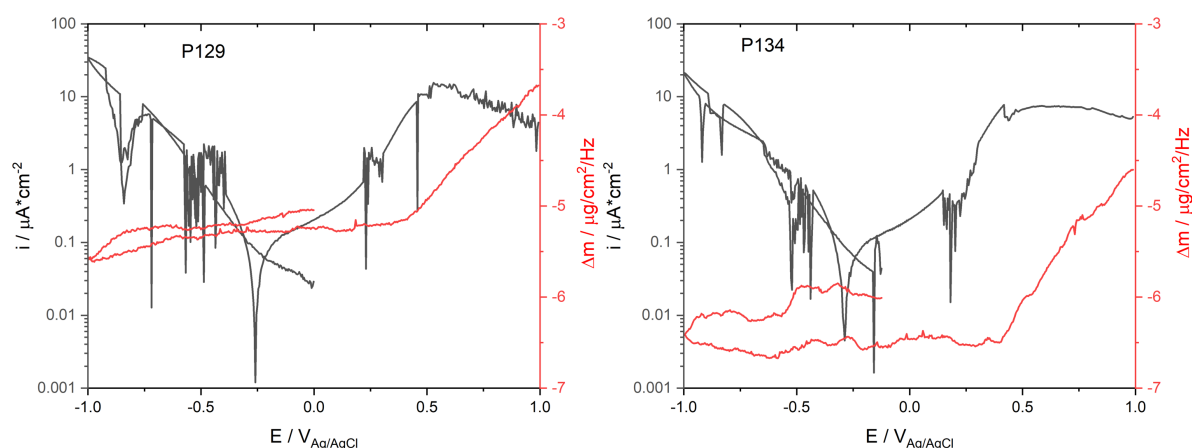


Figure A. 7 Polarization curves and mass changes of Ti crystals tested in synovial fluids from P129 and P134

The cathodic and anodic scans on Ti crystals were conducted in synovial fluids, and the obtained results are plotted in Figure A. 7. Significant oscillation in current is observed for both patients, which could be attributed to the limited adhesion of the Ti layer on the quartz crystal. Despite the oscillation, the polarization curves for both patients are quite similar. Likewise, the same trend of the mass change with applied potential is obtained, although the absolute value is about  $1 \mu\text{g}/\text{cm}^2/\text{Hz}$  different. The mass slightly decreases with the applied potential varies from OCP to  $-1 \text{ V}_{\text{Ag}/\text{AgCl}}$ . When the potential is increased in the anodic direction, the mass slightly increases until  $0.5 \text{ V}_{\text{Ag}/\text{AgCl}}$  when the current plateau starts to form. In consequence, the mass abruptly increases with the applied potential probably due to anodic oxidation. No potentiodynamic polarization was performed on the Ti crystal for P154 due to oscillation currents.

### A.4. Discussion

The increase of the OCP value with time for three patients suggests the generation of the passive film on the surface, which hinders the anodic dissolution of Ti. The generation of passive film indicates that a mass increase is expected, however, a mass decrease is observed for three patients. The mass decrease with the cathodic scan of the potential is not surprising since the electrical field decreases with the applied potential, thus reducing the passive film thickness on the Ti surface. Likewise, the mass slightly increases from cathodic potential to the anodic ones. The significant increase of mass at the potential from 0.5 to 1 is due to the generation of a compact passive film. The mass change under applied potential is in accordance with the theory but the results obtained under OCP condition cannot be easily explained.

Indeed, a mass increase on the Ti surface, after 20 minutes' immersion in NaCl solution, is obtained, as shown in Figure C. 7 in Appendix. However, the mass change on the surface decreases from  $2 \mu\text{g}/\text{cm}^2/\text{Hz}$  to  $-1 \mu\text{g}/\text{cm}^2/\text{Hz}$  with the addition of BSA. Similar results are reported in a study of the adsorption of corrosion inhibitors on an iron surface with a rotating EQCM [179]. In this study, a mass decrease on the crystal was obtained after the adsorption of organic corrosion inhibitors. The mass decrease is attributed to the replacement of the water molecules by the adsorbed corrosion inhibitors.

### A.5. Summary

The electrochemical behavior of Ti in human synovial fluids was first conducted through EQCM under OCP and potentiodynamic polarization conditions. Based on the results, a conclusion can be drawn below:

- Higher OCP values compared with bulk material, ranging from  $-125 \text{ mV}_{\text{Ag}/\text{AgCl}}$  to  $-50 \text{ mV}_{\text{Ag}/\text{AgCl}}$ , are obtained on Ti crystal immersed in several synovial fluids. During the OCP measurements, a mass decrease is observed during the immersion in the synovial fluids. This can be interpreted that water molecules are replaced by less dense organic molecules which adsorbed on the surface.
- In the polarization curves, large current oscillations are observed (their origin is not clear at present). A mass increase in the anodic domain is observed in agreement with the expected passive film thickening.

## Appendix B Validation of the Multi-electrode Electrochemical Cell

The feasibility of the small cell was investigated by conducting the corrosion behavior of Ti in NaCl (8g/L) solution in both small cell and typical large cell.

### B.1. Materials

Ti samples were used for both small cell and large cell, and the sample preparation is shown in Chapter 3.3. An Ag/AgCl (3 M KCl) and a graphite rod was served as reference electrode and counter electrode respectively in the large cell. The temperature of the large cell was maintained at  $37 \pm 1$  °C by heating the water in the interlayer of the cell container. NaCl (8g/L) solution was used, and its pH was adjusted to 7.4 with NaOH. The picture of the typical large cell is presented in Figure B. 1. For each test, one Ti sample was placed in each cell and the test was carried out for three times to guarantee the reproducibility.

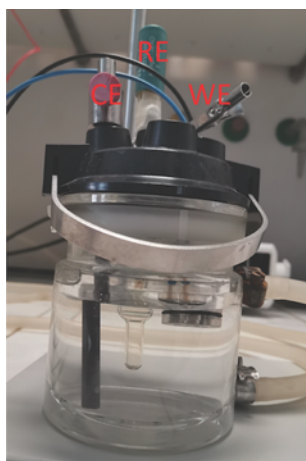


Figure B. 1 The picture of the typical large cell

### B.2. Experimental

Different electrochemical measurements were conducted sequentially on the Ti sample with a IVIUM (small cell) and NOVA potentiostat (large cell) respectively. The experimental procedure is listed as below:

- OCP, between Ti and NaCl solution, was continuously recorded for 20 min.

- Potentiodynamic scan was performed on the sample by scanning the potential from the OCP towards the cathodic direction to  $-1 \text{ V}_{\text{Ag/AgCl}}$  and reversing towards the anodic direction up to  $1 \text{ V}_{\text{Ag/AgCl}}$  with a scan rate of  $2 \text{ mV/s}$ .

### B.3. Results

The polarization curves of Ti in NaCl solution tested in both cells were presented in Figure B. 2. Results show that the polarization curves obtained from the small cell are similar with that from the large cell, the latter shows better reproducibility. The lower current for the small cell at the potential lower than  $-0.6 \text{ V}_{\text{Ag/AgCl}}$  might be due to the less amount of  $\text{H}^+$  or dissolved  $\text{O}_2$  in the electrolyte due to the small volume. The higher anodic current density acquired for small cell could also be attributed to the less amount of dissolved  $\text{O}_2$ , which promotes the generation of passive film and thus reduces the passive current density.

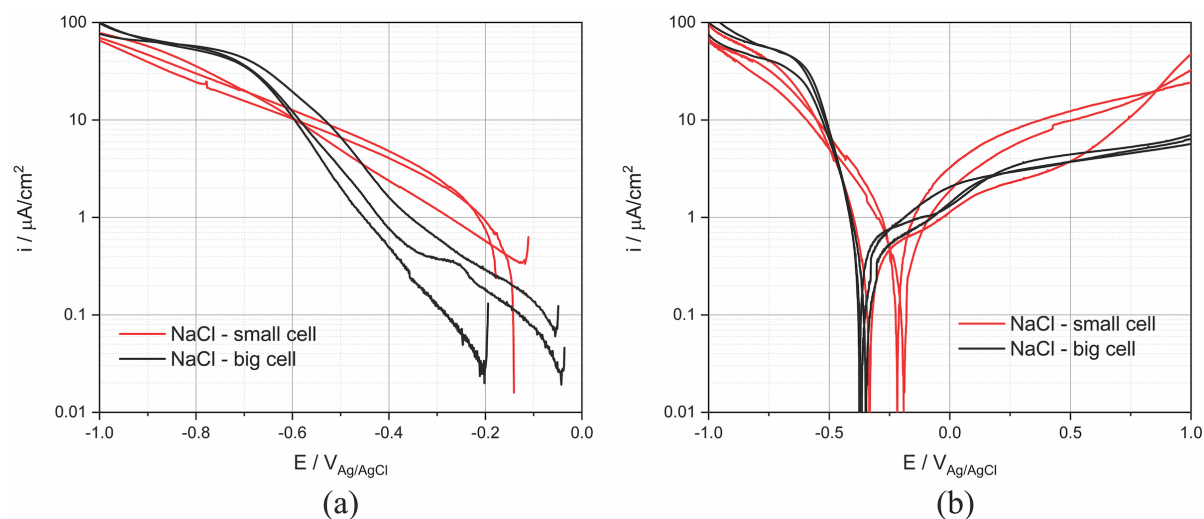


Figure B. 2 The polarization curves of Ti in NaCl solution tested in both cells

The electrochemical parameters extracted from polarization curves are presented in Table B. 1. As is shown in the table, no significant difference is obtained for the OCP value of Ti obtained from both cells. Therefore, there is little influence of the cell size on the corrosion behavior of Ti in NaCl solution.

Table B. 1 Electrochemical parameters extracted from polarization curves

			Cathodic polarization		Anodic polarization curve		
		OCP/ mV	i <sub>c</sub> (-0.8V)/ μA/cm <sup>2</sup>	i <sub>c</sub> (-0.3V)/ μA/cm <sup>2</sup>	i <sub>c</sub> (-0.8V)/ μA/cm <sup>2</sup>	E <sub>cor</sub> / mV <sub>Ag/AgCl</sub>	i <sub>p</sub> (0.5V)/ μA/cm <sup>2</sup>
Small cell	Average	-201	-27.64	-1.52	-34.26	-0.30	7.90
	STDEV	61	8.15	0.89	14.66	0.06	0.54
Large cell	Average	-184	-56.60	-0.37	-54.23	-0.36	4.13
	STDEV	60	3.99	0.25	7.35	0.01	0.51

Considering the possible effects of hydrogen and oxygen generated on Pt electrode on the corrosion behavior of Ti, two Ti samples were put in the small cell and the polarization scan was conducted on both samples in sequence after 20 minutes' immersion in NaCl solution. The experiment was conducted three times, and the results are displayed in Figure B. 3. The identical results for both samples indicate that the hydrogen and oxygen generated on Pt have no effect on the corrosion behavior of Ti in NaCl solution.

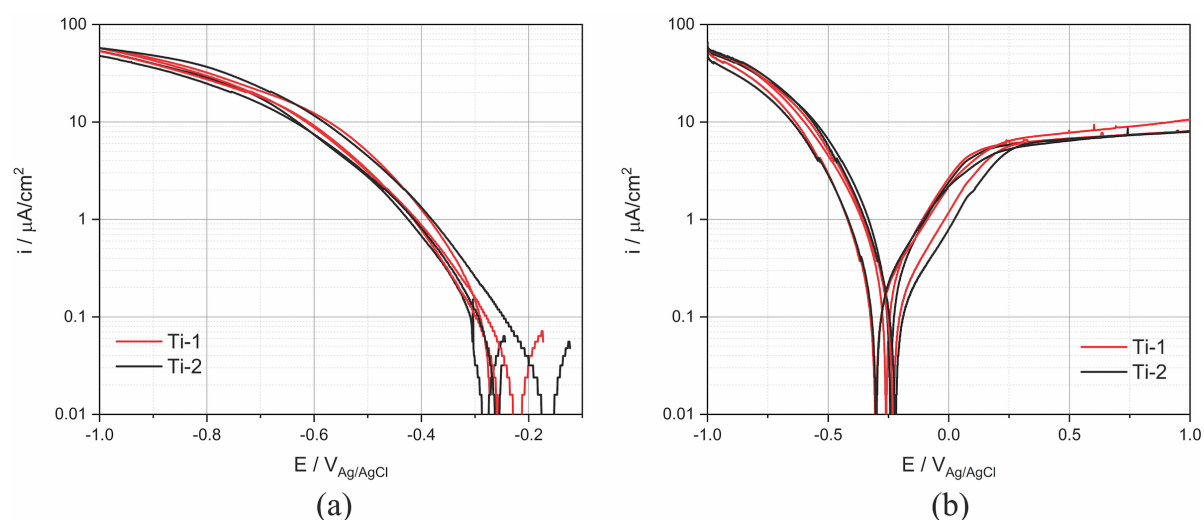


Figure B. 3 The polarization curves of two Ti samples in NaCl solution in the small cell

#### B.4. Conclusion

Based on the results, conclusions can be drawn as below:

Electrochemical experiments can be conducted by the small new cell with high reliable results based on the similar results with that from the large typical cell.

There is no influence of hydrogen and oxygen generated on Pt on the corrosion behavior of Ti tested in the small cell.

## Appendix C Electrochemical Behavior of Ti and CoCrMo Alloy in Simulated Fluids

For comparison purposes, the electrochemical behavior of Ti and CoCrMo alloy was also tested in simulated body fluids (composition is given in Table C. 1 and Table C. 2) using the same procedure and conditions applied for synovial fluids. NaCl solutions are the simplest fluid used for simulating body fluids. Incorporation of bovine serum albumin (BSA) and hyaluronic acid (HA) is widely used to assess the influence of the organic molecules contained in body fluids [78–84]. Since calcium particles were detected through EDX on sample surface after immersing in synovial fluids, CaCl<sub>2</sub> was added in to NaCl based solution to study its effect on the corrosion behavior. H<sub>2</sub>O<sub>2</sub> was added into simulated fluid to investigate the influence of reactive oxygen species (ROS) [102–104]. In addition, PBS was used to investigate the influence of phosphate on the corrosion behavior of metals. The solutions were prepared using reagents: NaCl, CaCl<sub>2</sub> (Sigma-Aldrich, Gribskov, Denmark), BSA (Fisher Scientific AG, Basel, Switzerland), HA (abcr GmbH, Germany), and H<sub>2</sub>O<sub>2</sub> (Reactolab S.A., Servion, Switzerland). The pH of NaCl based solutions was adjusted to 7.4 by using small amounts of NaOH.

Table C. 1 Composition of NaCl based simulated solutions

Solution	NaCl / (g/L)	BSA / (g/L)	HA / (g/L)	CaCl <sub>2</sub> / (g/L)	H <sub>2</sub> O <sub>2</sub> / (g/L)
NaCl	8	-	-	-	-
NaCl+BSA	8	0.5 / 5 / 30	-	-	-
NaCl+HA	8	-	1 / 4	-	-
NaCl+BSA+HA	8	30	4	-	-
NaCl+CaCl <sub>2</sub>	8	-	-	0.1 / 0.5 / 1	-
NaCl+BSA+CaCl <sub>2</sub>	8	30	-	1	-
NaCl+H <sub>2</sub> O <sub>2</sub>	8	-	-	-	1 / 5
NaCl+BSA+H <sub>2</sub> O <sub>2</sub>	8	30	-	-	1 / 5

Table C. 2 Composition of PBS based simulated solutions

Solution	Composition
PBS	NaCl (8g/L) + KCl (0.2g/L) + Na <sub>2</sub> HPO <sub>4</sub> (1.42g/L) + KHPO <sub>4</sub> (0.24g/L)
PBS+BSA	PBS + BSA (0.5/5/30 g/L)
PBS+BSA+HA	PBS + BSA (30 g/L) + HA (4g/L)

## C.1. Electrochemical Behavior of Ti in Simulated Solutions

### C.1.1 OCP and Rp Results of Ti

The electrochemical behavior of Ti was tested in different simulated body fluids listed in Table C. 1 and Table C. 2. Each measurement was repeated three times. The OCP and Rp results are present in Figure C. 1 and Figure C. 2, respectively. The results show that the OCP value decreases with the addition of BSA and HA, while it increases after adding  $H_2O_2$ . No obvious influence of phosphate and calcium ions on the OCP value is obtained. The Rp values correspond well with the OCP results that higher Rp values were acquired for samples with lower OCP values.

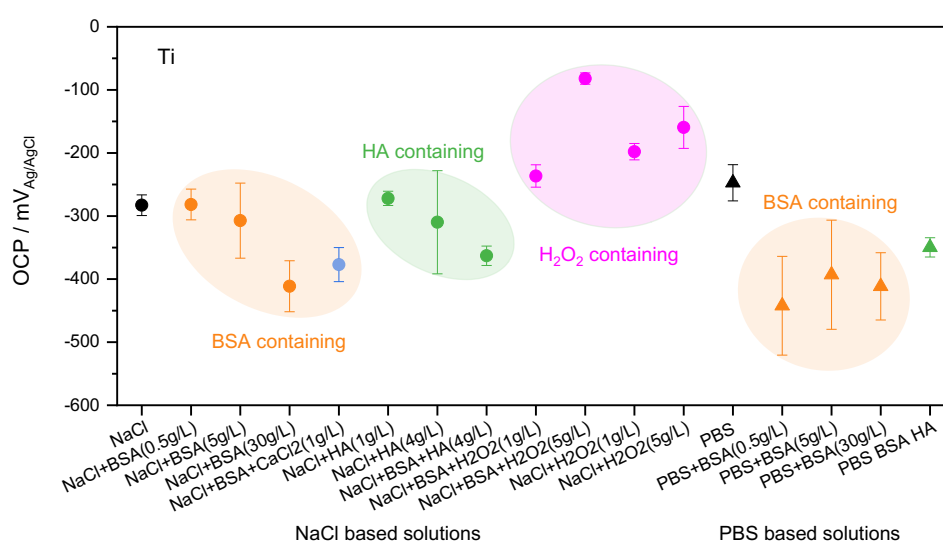


Figure C. 1 Stabilized OCP results of Ti in different simulated solutions

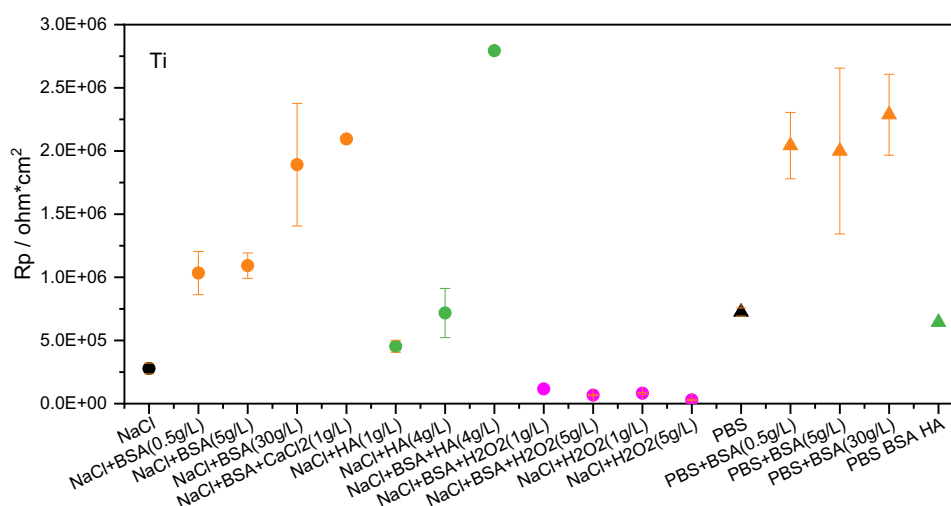


Figure C. 2 Comparison of Rp value in different simulated solutions

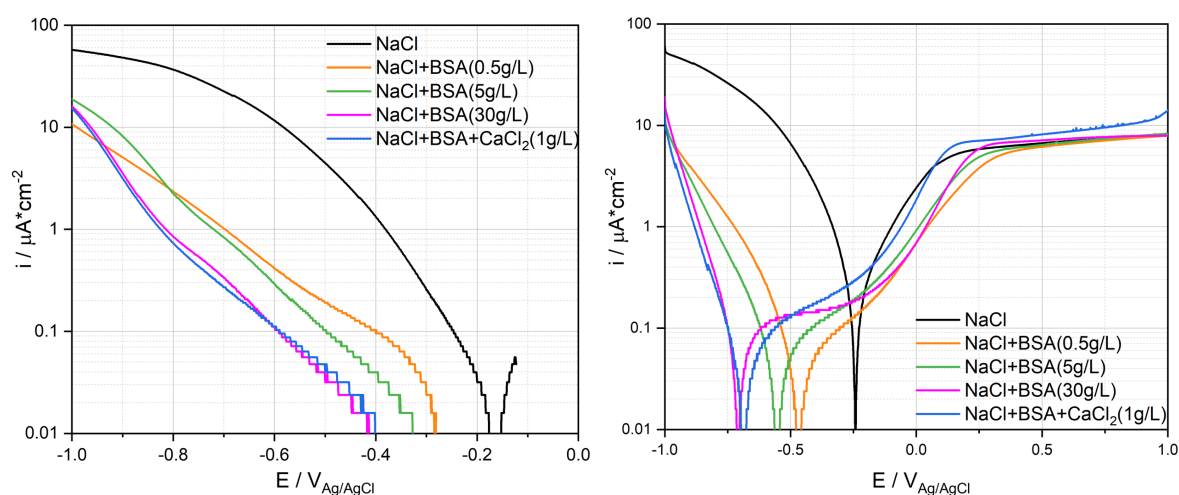


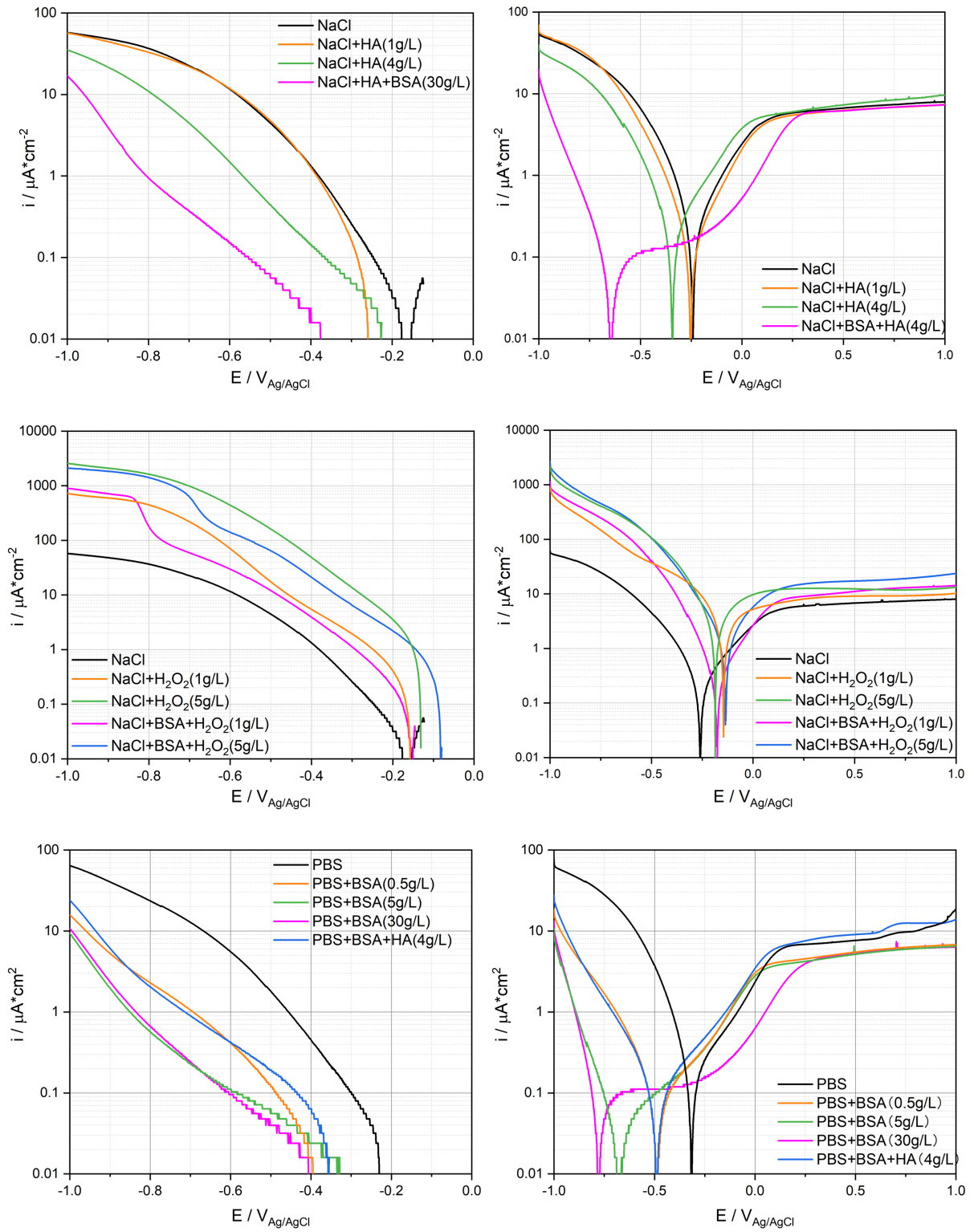
### C.1.2 Potentiodynamic Polarization Curves of Ti

The representative polarization curves of Ti in simulated solutions are presented in Figure C.3. From this figure, it appears that the solution composition mainly affects the cathodic reactivity (differences in cathodic current up to two orders of magnitude). However, the anodic behavior is less affected (current densities within the same order of magnitude).

As previously reported, albumin acts as an inhibitor of the oxygen reduction reaction [59, 78–84]. This explains the significant lowering of the cathodic current density observed in the BSA solution. Contrary to the cathodic domain, the BSA slightly lowers the anodic current density. The influence of HA on the cathodic reaction is small compared with BSA due to its less hydrophilic properties [98]. Similarly, little effect of HA on anodic current is observed. In PBS+BSA based solution, a cathodic current increase was observed after adding HA, suggesting there is a competitive adsorption between BSA and HA on the sample surface. The increase of current density in the cathodic domain by adding  $\text{H}_2\text{O}_2$  is expected because of the strong contribution of  $\text{H}_2\text{O}_2$  reduction. The slightly enhanced corrosion in the anodic domain could be attributed to the formation of thicker and porous passive film because of the large amount of  $\text{OH}^-$ , which leads to the release of Ti [83, 102, 104]. The cathodic and anodic current varies little with the addition of phosphate. Similar results were obtained for calcium ions, except for the slight decrease of the anodic current at the potential lower than 0.5  $V_{\text{Ag}/\text{AgCl}}$ . The decrease of the anodic current is independent of calcium concentration. The polarization curves correspond well with the OCP and  $R_p$  results, namely, the OCP and  $R_p$  value is mainly determined by the cathodic reaction of Ti in tested simulated solutions.

It is worth noting that a higher current slope at the potential lower than -0.8  $V_{\text{Ag}/\text{AgCl}}$  was observed in the solution with BSA concentration no less than 5 g/L. Likewise, the cathodic currents for  $\text{H}_2\text{O}_2$  containing solutions significantly increased with potential lower than -0.8  $V_{\text{Ag}/\text{AgCl}}$  to the values without BSA.





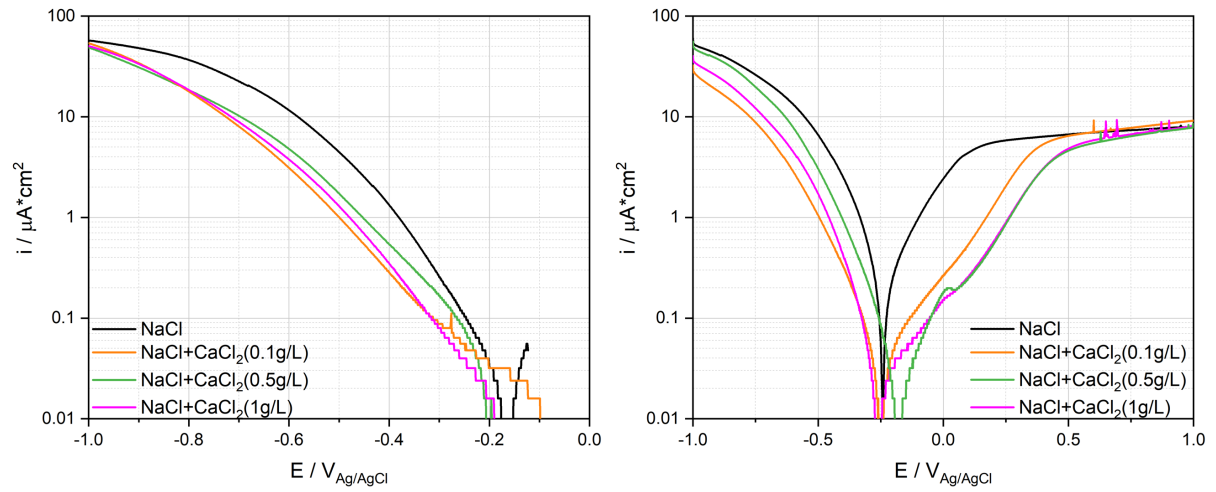


Figure C. 3 Cathodic and anodic polarization curves (logarithmic scale of the absolute current density) of Ti in simulated solutions

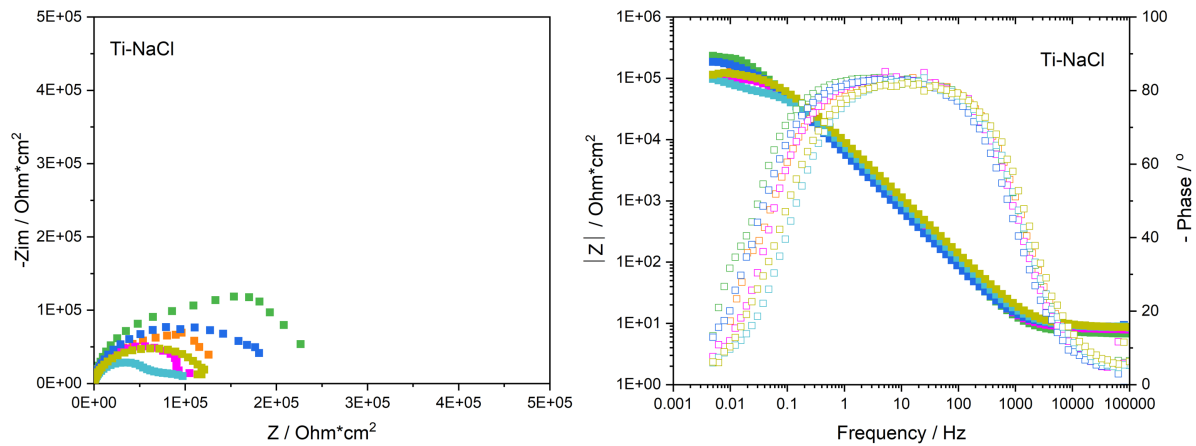
The same parameters extracted from in-vitro, were obtained from anodic polarization curves and summarized in Table C. 3. The standard deviation (STDEV) and error were calculated to assess the reproducibility of the polarization curves. As is shown in the Table, the corrosion behavior of Ti in BSA containing solution shows the best reproducibility.

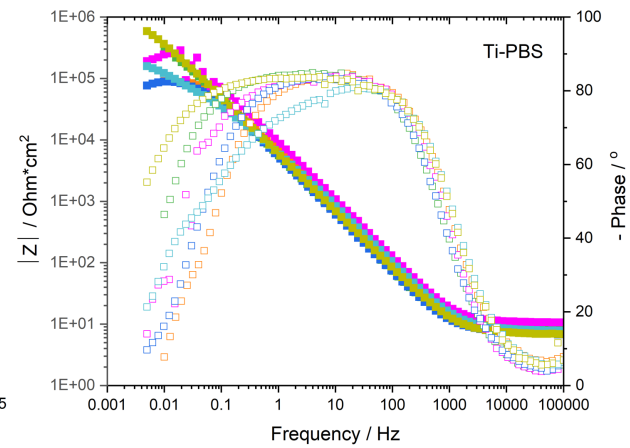
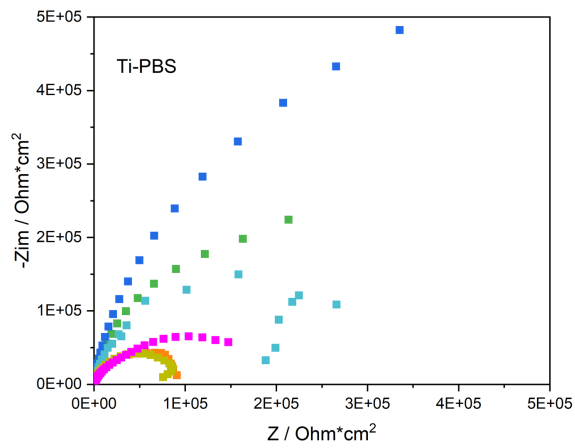
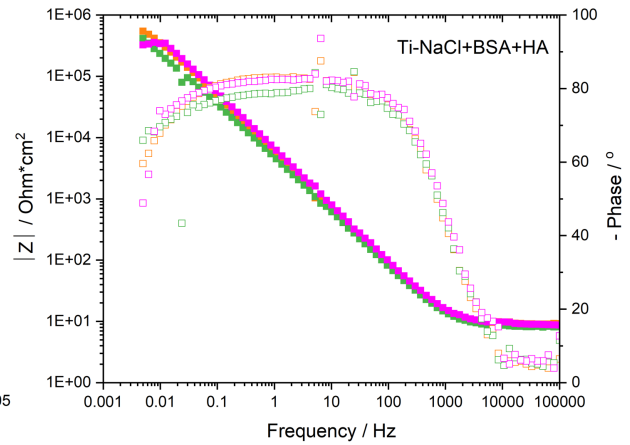
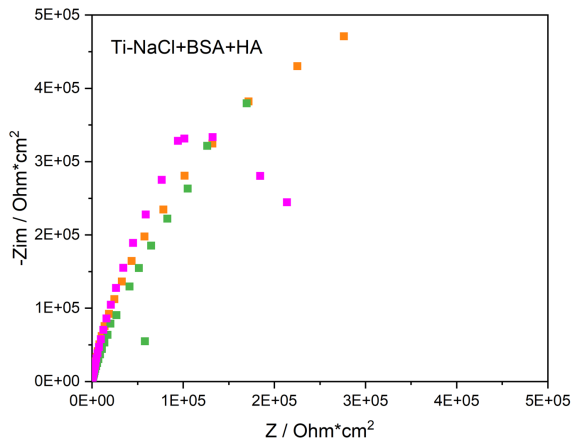
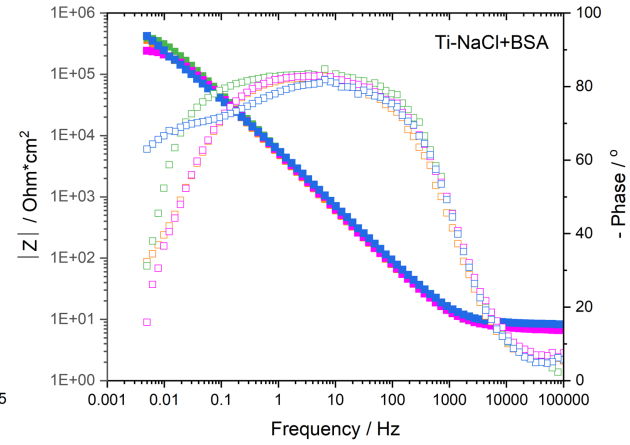
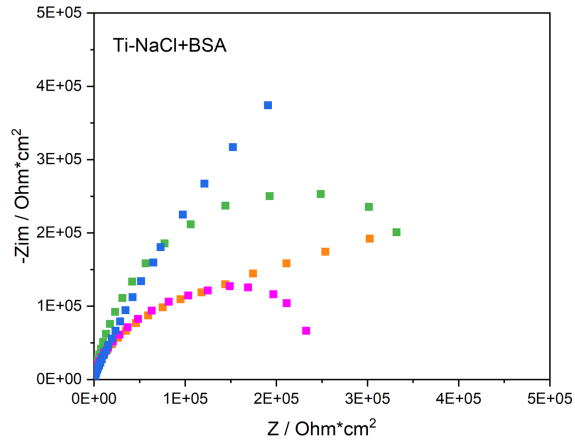
Table C. 3 Electrochemical parameters extracted from the anodic polarization curves of Ti samples

Solution	$i_c (-0.9V) / \mu A/cm^2$	$\beta_c / mV$	$E_{cor} / V_{Ag/AgCl}$	$i_{pp} (0V) / \mu A/cm^2$	$i_{pp} (0.5V) / \mu A/cm^2$
NaCl(8g/L)	$-40.85 \pm 4.90$		$-0.26 \pm 0.03$	$1.87 \pm 0.73$	$6.84 \pm 0.46$
NaCl+BSA(0.5g/L)	$-3.88 \pm 0.85$	$94 \pm 21$	$-0.52 \pm 0.07$	$0.60 \pm 0.17$	$6.05 \pm 0.86$
NaCl+BSA(5g/L)	$-4.22 \pm 0.97$	$73 \pm 23$	$-0.58 \pm 0.05$	$0.79 \pm 0.13$	$6.66 \pm 0.90$
NaCl+BSA(30g/L)	$-2.66 \pm 1.43$	$55 \pm 20$	$-0.69 \pm 0.11$	$0.99 \pm 0.21$	$6.71 \pm 1.06$
NaCl+ CaCl <sub>2</sub> (1g/L)	$-29.68 \pm 5.51$		$-0.23 \pm 0.03$	$0.16 \pm 0.02$	$4.37 \pm 2.38$
NaCl+BSA+CaCl <sub>2</sub> (1g/L)	$-1.52 \pm 0.16$		$-0.73 \pm 0.06$	$1.64 \pm 0.28$	$7.96 \pm 0.28$
NaCl +HA(1g/L)	$-42.32 \pm 2.21$		$-0.25 \pm 0.00$	$2.14 \pm 0.08$	$5.86 \pm 0.56$
NaCl +HA(4g/L)	$-21.27 \pm 3.02$		$-0.32 \pm 0.06$	$4.01 \pm 0.36$	$2.41 \pm 0.31$
NaCl+BSA+HA(4g/L)	$-2.64 \pm 0.64$	$66 \pm 5$	$-0.66 \pm 0.01$	$0.67 \pm 0.19$	$4.31 \pm 2.64$
NaCl+BSA+H <sub>2</sub> O <sub>2</sub> (1g/L)	$-492 \pm 6$		$-0.21 \pm 0.05$	$4.36 \pm 2.43$	$10.42 \pm 0.93$
NaCl+BSA+ H <sub>2</sub> O <sub>2</sub> (5g/L)	$-915 \pm 65$		$-0.15 \pm 0.02$	$6.44 \pm 1.03$	$17.02 \pm 0.28$
NaCl +H <sub>2</sub> O <sub>2</sub> (1g/L)	$-358 \pm 15$		$-0.17 \pm 0.03$	$6.03 \pm 1.07$	$9.93 \pm 1.15$
NaCl +H <sub>2</sub> O <sub>2</sub> (5g/L)	$-831 \pm 56$		$-0.09 \pm 0.14$	$5.03 \pm 6.7$	$12.06 \pm 0.43$
PBS	$-40.83 \pm 6.74$		$-0.28 \pm 0.03$	$1.24 \pm 0.94$	$4.31 \pm 1.48$
PBS+BSA(0.5g/L)	$-0.95 \pm 0.05$	$109 \pm 10$	$-0.78 \pm 0.01$	$2.61 \pm 0.46$	$5.14 \pm 0.37$
PBS+BSA(5g/L)	$-1.03 \pm 0.34$	$53 \pm 12$	$-0.73 \pm 0.06$	$1.54 \pm 1.21$	$5.19 \pm 0.65$
PBS+BSA(30g/L)	$-1.02 \pm 0.35$	$59 \pm 21$	$-0.78 \pm 0.03$	$0.76 \pm 0.35$	$5.46 \pm 0.24$
PBS+BSA+HA(4g/L)	$-6.28 \pm 0.16$	$106 \pm 6$	$-0.51 \pm 0.02$	$3.73 \pm 0.40$	$9.42 \pm 0.49$

### C.1.3 EIS Results of Ti

According to the above results, the corrosion behavior of Ti in simulated solution is mainly influenced by the presence of BSA and HA. To further study the influence of organics, the impedance measurements were carried out at OCP conditions in representative BSA and HA containing solutions. The EIS results are displayed in Nyquist and Bode plot, as shown in Figure C. 4. For each solution, the measurement was conducted at least three times to guarantee the reproducibility of the results.





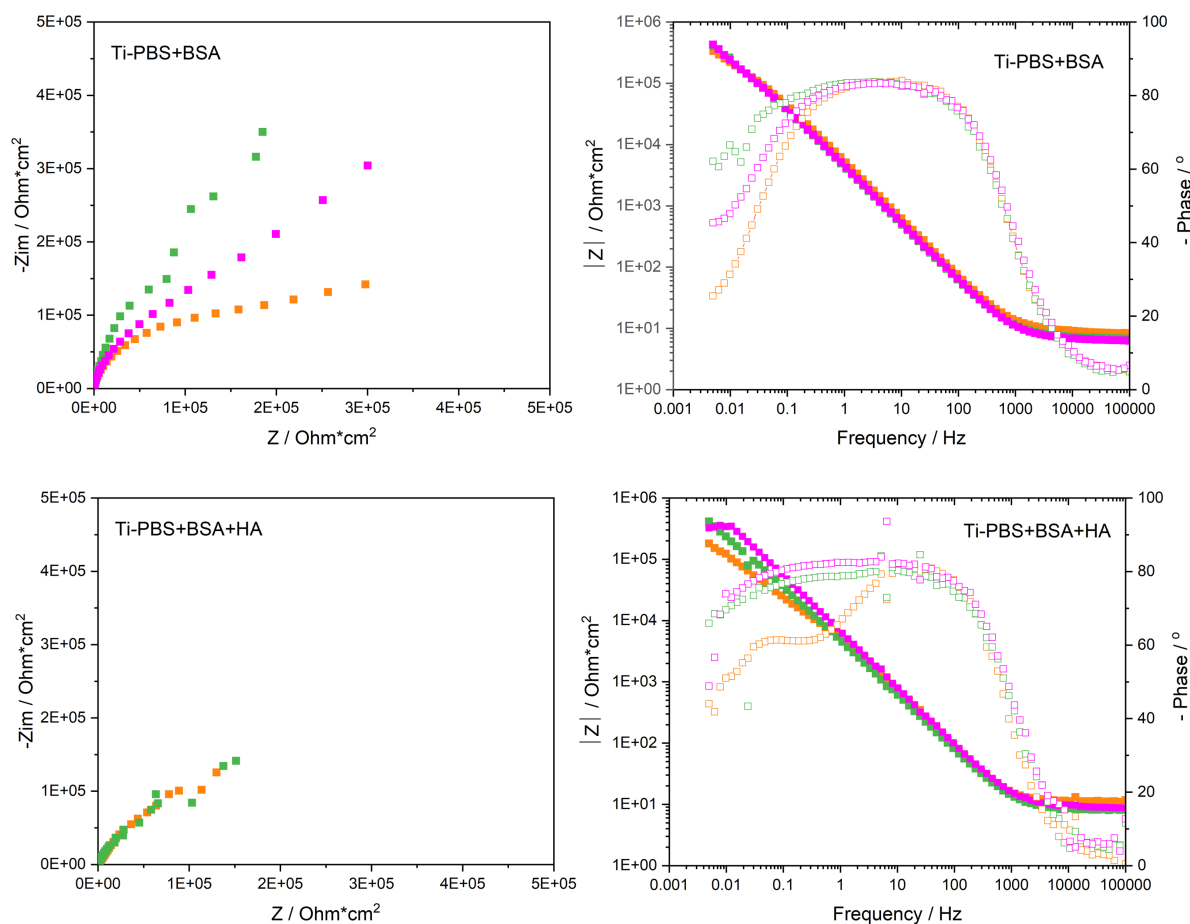


Figure C. 4 Nyquist and Bode plot of Ti in simulated solutions

In the Nyquist plots, the arc length and angle increase with the addition of BSA and HA in NaCl solution, while they decrease after adding HA in PBS+BSA solution. In the Bode plots, three distinctive sections depending on the frequency were observed in NaCl and PBS solutions. In the high frequency region, the modulus curve is almost independent of the frequency, with the phase angle value approaching  $0^\circ$ . In the medium frequency region, a linear increase of modulus with the decrease of frequency, and the phase angle reaching to  $-80^\circ$ . In the low frequency region, the modulus is independent of frequency, and the phase angle is approximately  $0^\circ$ . No modulus plateau was observed in BSA and HA-containing solutions at the low frequency region. With the addition of BSA and HA, the modulus at the low frequency region increases and the phase angle curve at the middle frequency region becomes broader. Also, the phase angle at the low frequency increases from  $0^\circ$  to about  $60^\circ$ . The higher modulus suggests that the polarization resistance of Ti increases with the addition of BSA and HA.

Table C. 4 Electrochemical parameters extracted from EIS measurements of Ti

Solution	OCP / mV <sub>Ag/AgCl</sub>	R <sub>s</sub> / Ohm*cm <sup>2</sup>	Z  / KOhm*cm <sup>2</sup>	-Phase / °
NaCl(8g/L)	-283 ± 16	8.0 ± 0.0	147 ± 59	9 ± 4
NaCl+BSA(30g/L)	-411 ± 40	7.5 ± 0.7	352 ± 78	36 ± 20
NaCl+BSA+HA(4g/L)	-363 ± 15	8.7 ± 0.7	429 ± 111	58 ± 9
PBS	-247 ± 29	7.8 ± 0.6	254 ± 228	25 ± 20
PBS+BSA(30g/L)	-411 ± 53	7.5 ± 1.3	385 ± 50	44 ± 18
PBS+BSA+HA(4g/L)	-350 ± 15	9.8 ± 2.0	194 ± 19	53 ± 11

The electrochemical parameters were extracted from EIS measurements and summarized in Table C. 4. R<sub>p</sub> value cannot be obtained since no modulus plateau was observed in the low frequency region in the Bode plot of the results. Thus, the modulus (|Z|) at the frequency of 0.005 Hz was extracted and listed in the table for the comparison of the polarization resistance of Ti in different solutions. The phase angle was extracted from the f = 0.005 Hz, and the R<sub>s</sub> was obtained at the f = 10<sup>5</sup> Hz.

As shown in the Table, the |Z| value increases with the addition of BSA and HA in NaCl solution. In contrast, the value decreases after further addition of HA in PBS+BSA solution. These results are in accordance with the polarization curves. The higher |Z| value could be due to the adsorption of BSA and HA, where lower OCP and anodic current density are obtained. A continuously increase of phase angle with the addition of BSA and HA was obtained for both NaCl and PBS based solutions. Higher |Z| and phase angle were obtained for PBS solution compared with NaCl solution, suggesting phosphate ions adsorbed on sample surface. The |Z| values correspond to the R<sub>p</sub> results acquired from the linear potentiodynamic measurements.

## C.2. Electrochemical Behavior of Ti-1200 in Simulated Solutions

### C.2.1. Potentiodynamic Polarization Curve of Ti-1200

To study the influence of Ra on the corrosion behavior of Ti in simulated solutions, the same measurements were carried out on a rough surface Ti-1200. Based on the results for mirror polished Ti, BSA and HA are the dominant factors that influence the corrosion behavior. Therefore, the same measurements on the rough surface were only conducted in BSA and HA containing solutions. The polarization curves of the rough surface in certain simulated solutions are displayed in Figure C. 1.

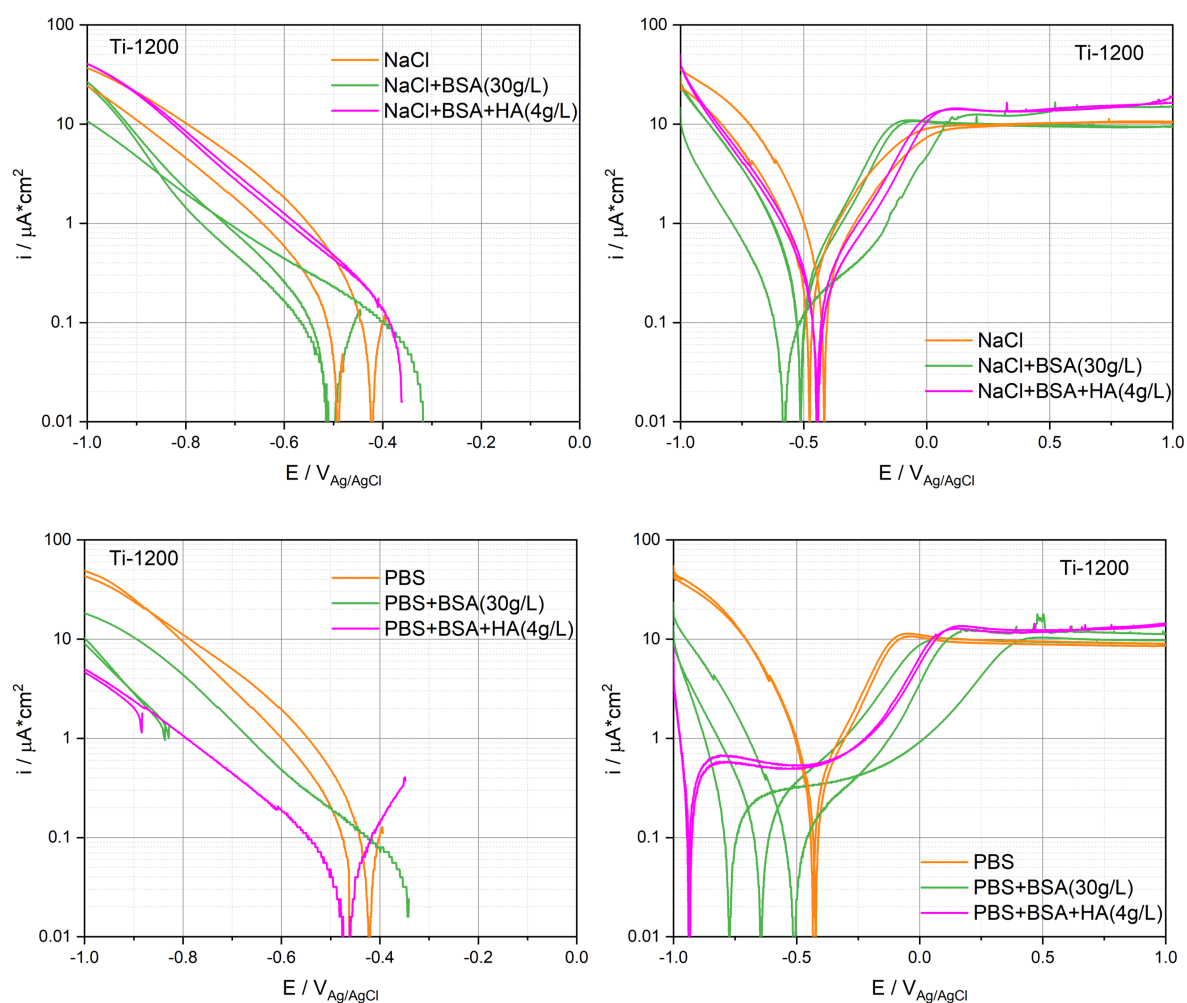


Figure C. 5 Cathodic and anodic polarization curves (logarithmic scale of the absolute current density) of Ti-1200 in simulated solutions

Contrary to the smooth surface, the current varies little with adding BSA and HA in NaCl based solutions. Differently, the cathodic current declines significantly with the addition of BSA and HA in PBS based solutions. Contrary to the cathodic region, the anodic current slightly decreases with BSA but HA.



Table C. 5 Electrochemical parameters extracted from anodic polarization curves of Ti-1200 samples

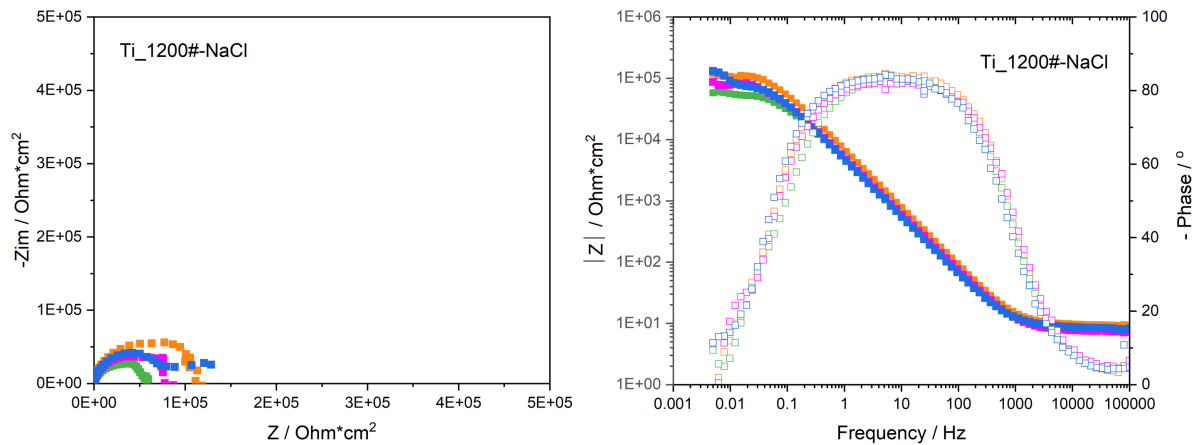
Solution	$i_c (-0.9V) / \mu A/cm^2$	$E_{cor} / V_{Ag/AgCl}$	$i_{pp} (0V) / \mu A/cm^2$	$i_{pp} (0.5V) / \mu A/cm^2$
NaCl(8g/L)	$-19.77 \pm 7.01$	$-0.45 \pm 0.04$	$8.16 \pm 1.17$	$10.23 \pm 0.05$
NaCl+BSA(30g/L)	$-8.4 \pm 4.89$	$-0.53 \pm 0.04$	$8.66 \pm 3.40$	$10.87 \pm 2.15$
NaCl+BSA+HA(4g/L)	$-14.3 \pm 0.86$	$-0.44 \pm 0.00$	$11.14 \pm 0.92$	$13.95 \pm 0.40$
PBS	$-30.88 \pm 2.31$	$-0.42 \pm 0.00$	$10.74 \pm 0.43$	$9.19 \pm 0.46$
PBS+BSA(30g/L)	$-3.64 \pm 2.82$	$-0.71 \pm 0.09$	$4.39 \pm 3.97$	$9.70 \pm 0.59$
PBS+BSA+HA(4g/L)	$-0.38 \pm 0.06$	$-0.94 \pm 0.00$	$6.06 \pm 0.68$	$12.06 \pm 0.35$

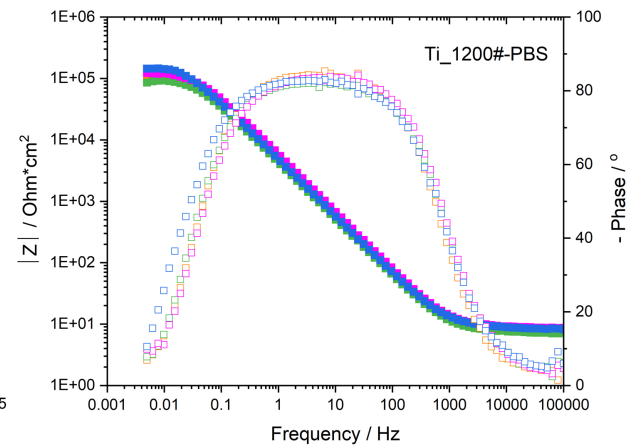
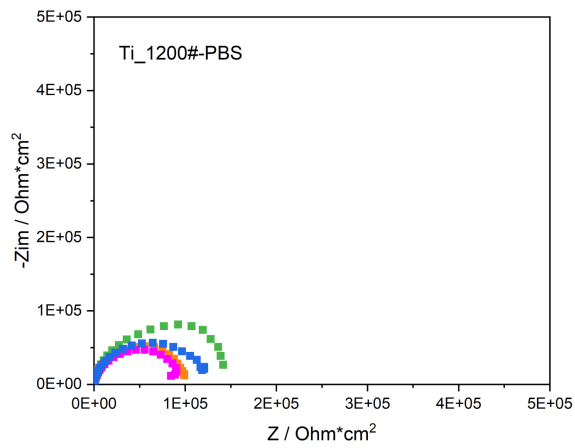
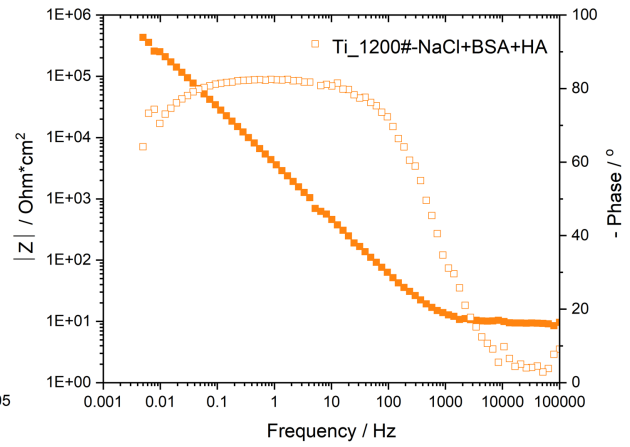
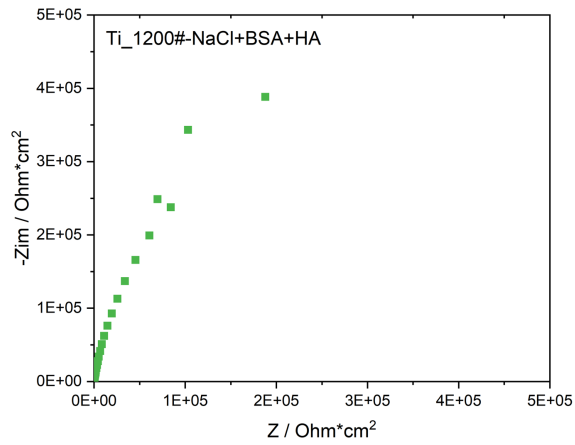
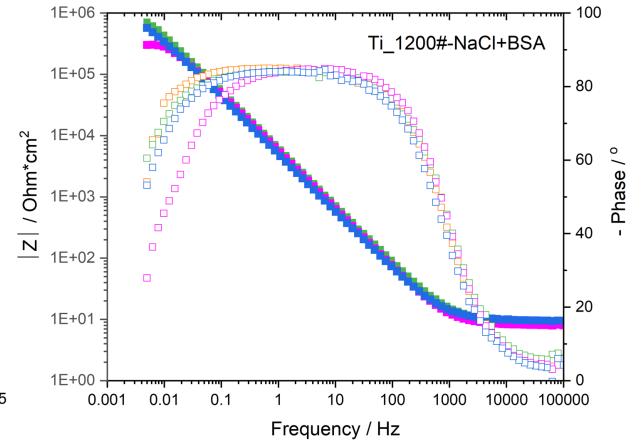
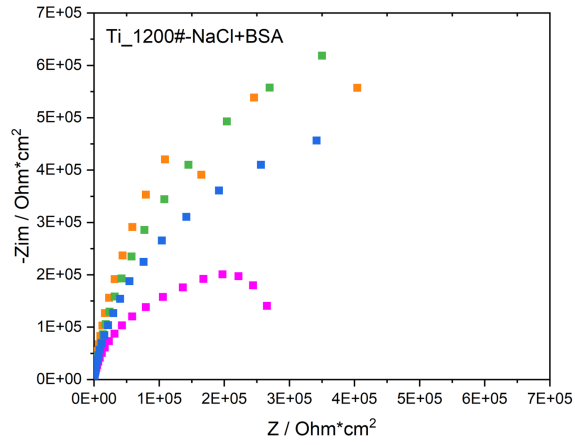
The same parameters were extracted from anodic polarization curves and summarized in Table C. 5. The standard deviation (STDEV) and error were calculated to assess the reproducibility of the polarization curves.

### C.2.2. EIS Results of Ti-1200

To further study the influence of organics, the impedance measurements were carried out at OCP conditions in BSA and HA containing solutions. The EIS results are displayed in Figure C. 6. Similar to the smooth surface, the arc length and angle increase with the addition of BSA and HA in NaCl solution, while they decrease after adding HA in PBS+BSA solution.

In the Bode plots, three distinctive segments (same with smooth surface) were observed in NaCl and PBS solutions. However, no modulus plateau was obtained at the low frequency domain in BSA and HA containing solutions. After adding BSA and HA, the modulus at  $f = 0.005$  Hz increases, and the phase angle curve at the middle frequency region extends to the lower frequency region.





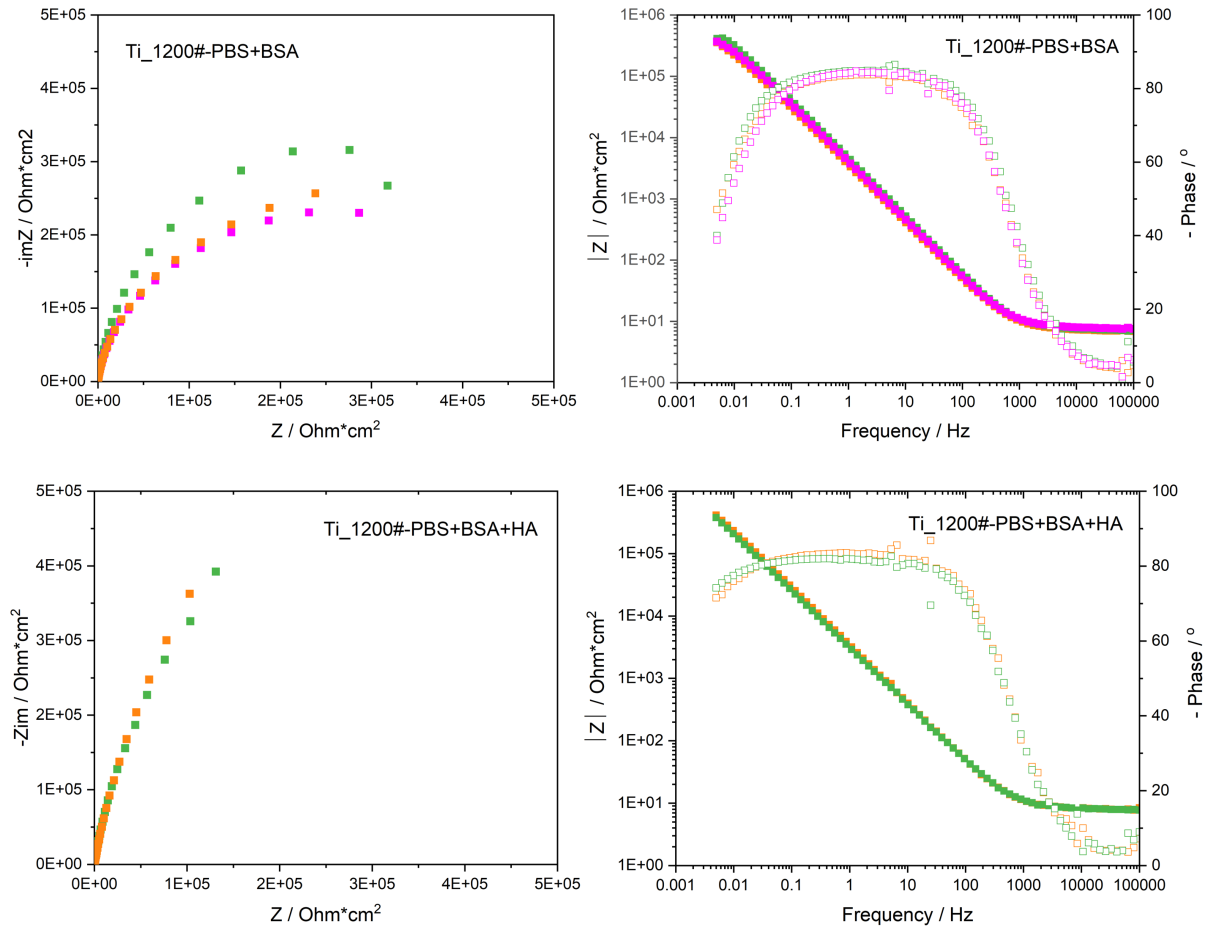


Figure C. 6 Nyquist and Bode plot of Ti-1200 in simulated solutions

The electrochemical parameters were extracted from Bode plots and summarized in Table C. 6. The modulus  $|Z|$  and phase angle were extracted at  $f = 0.005$  Hz, and the  $R_s$  was obtained at the  $f = 10^5$  Hz. As shown in the table, the  $|Z|$  value increases with the addition of BSA in NaCl solution while decreases with the further addition of HA. Increase of  $|Z|$  is also obtained after adding BSA in PBS solution, while it increases little with the further addition of HA. Contrary to modulus values, the phase angle continuously increases after adding BSA and HA. The  $|Z|$  value increases with the addition of phosphate in NaCl and NaCl + BSA + HA solution, while decreases for NaCl + BSA solution.

Table C. 6 Electrochemical parameters extracted from EIS measurements of Ti-1200

Solution	OCP / mV <sub>Ag/AgCl</sub>	$R_s$ / Ohm*cm <sup>2</sup>	$ Z $ / KOhm*cm <sup>2</sup>	-Phase / °
NaCl(8g/L)	-481 ± 19	9.30 ± 0.88	99 ± 033	5 ± 5
NaCl+BSA(30g/L)	-514 ± 4	9.55 ± 0.25	568 ± 188	49 ± 14
NaCl+BSA+HA(4g/L)	-359 ± 7	10.43 ± 1.51	217 ± 303	64
PBS	-471 ± 19	8.17 ± 0.88	113 ± 26	9 ± 2
PBS+BSA(30g/L)	-541 ± 39	7.42 ± 0.38	377 ± 34	42 ± 4
PBS+BSA+HA(4g/L)	-640 ± 28	7.92 ± 0.13	394 ± 26	72 ± 1

### C.3. EQCM Measurements of Ti

To help understand the electrochemical behavior of Ti in simulated solutions, in-vitro EQCM measurements were carried out on the same crystal in NaCl and NaCl + BSA (30g/L) solutions. The measurements were repeated twice for each solution, and the obtained OCP and mass change results are shown in Figure C. 7. The OCP gaps in the graph are due to R<sub>p</sub> measurements which is not shown here. The graphs show that the OCP value gradually decreases with the immersion time for NaCl, while it slightly increases with time for NaCl + BSA (30g/L) solution. The stabilized OCP of Ti for NaCl and NaCl + BSA (30g/L) is -20 mV<sub>Ag/AgCl</sub> and -55 mV<sub>Ag/AgCl</sub>, respectively. The OCP values obtained on Ti crystal are more positive than those acquired on bulk materials (-290 mV<sub>Ag/AgCl</sub> and -420 mV<sub>Ag/AgCl</sub>, respectively). Good reproducibility is acquired for OCP results in both solutions.

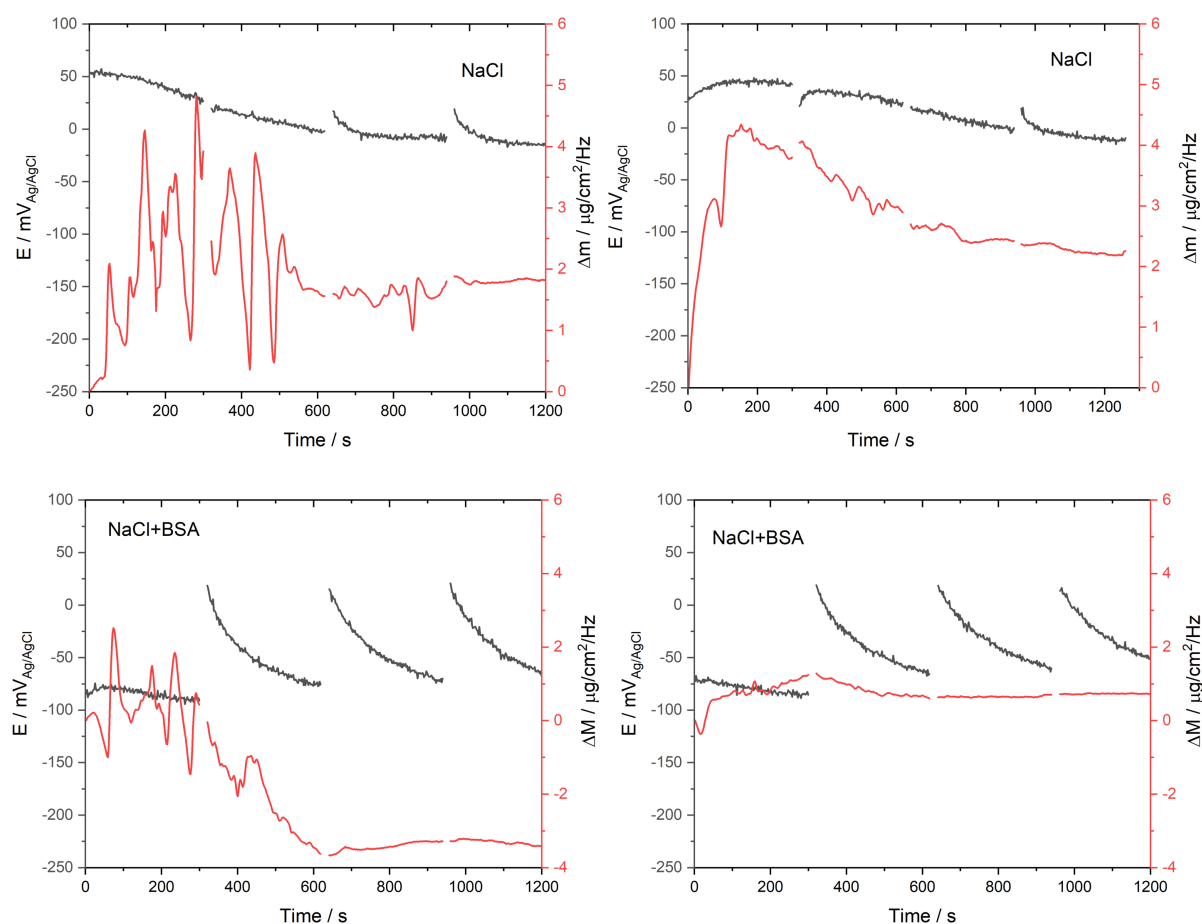


Figure C. 7 OCP variation of Ti for NaCl and NaCl + BSA (30g/L) solutions, together with the mass changes on the surfaces

Unlike OCP results, the mass changes on the Ti surface for each solution are less reproducible. Despite the oscillations, stabilized mass changes on Ti surfaces of 1.8  $\mu\text{g}/\text{cm}^2/\text{Hz}$  and 2.2

$\mu\text{g}/\text{cm}^2/\text{Hz}$  are acquired for NaCl solution. Differently, a mass decrease is obtained after adding BSA, being  $-3.4 \mu\text{g}/\text{cm}^2/\text{Hz}$  and  $0.8 \mu\text{g}/\text{cm}^2/\text{Hz}$ .

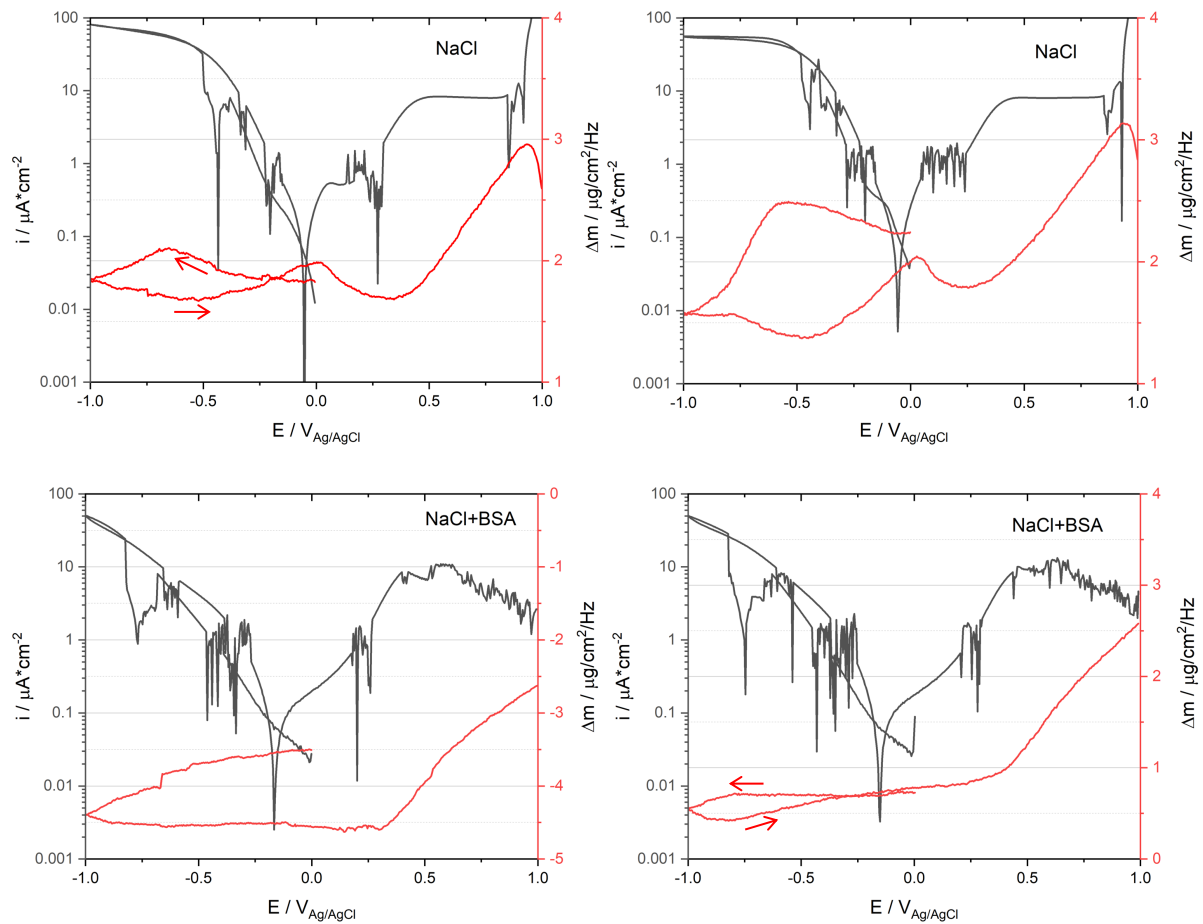


Figure C. 8 Polarization curves and mass changes of Ti crystals tested in NaCl and NaCl + BSA (30g/L) solutions

The cathodic and anodic scans on Ti crystals were conducted in synovial fluids, and the obtained results are plotted in Figure C. 8. The graphs show significant current oscillation for both simulated solutions. Despite that, good reproducibility is observed for polarization curves in both solutions. Higher cathodic current and lower anodic current at the potential lower than  $0.5 V_{\text{Ag}/\text{AgCl}}$  are obtained for the Ti crystal compared with those for bulk material. The decrease of cathodic current after adding BSA follows the trend obtained on the bulk material. For NaCl, the mass gradually increases with the cathodic scan of the potential towards around  $-0.7 V_{\text{Ag}/\text{AgCl}}$ , and subsequently decreases until the potential reaches  $-1 V_{\text{Ag}/\text{AgCl}}$ . Reverse mass change is obtained by anodically scanning the potential from  $-1 V_{\text{Ag}/\text{AgCl}}$  to  $E_{\text{cor}}$ . After that, the mass first decreases slightly and then continuously increases with the applied potential. With the addition of BSA, the mass slightly decreases with the applied potential

from OCP to  $-1 \text{ V}_{\text{Ag/AgCl}}$ , and subsequently remains stable until  $\sim 0.35 \text{ V}_{\text{Ag/AgCl}}$ , followed by a linear increase up to  $1 \text{ V}_{\text{Ag/AgCl}}$ .

#### C.4. Influence of the Scan Rate on the Rp Measurements

The scan rate is a key parameter that controls the measured current especially when diffusion plays a role. The relation between the current and the scan rate is described by Cottrell equation.

$$I = -nFA(C_B - C_S)\left(\frac{D}{\pi t}\right)^{1/2}$$

Where  $I$  is the current,  $n$  is the number of the electron transferred in the redox reaction,  $A$  is the surface area of the working electrode,  $C_B$  is the reactant concentration in the bulk solution,  $C_S$  is the reactant concentration on the electrode surface,  $D$  is the diffusion coefficient of the reactant in the electrolyte,  $t$  is the transition time, which is inversely proportional to scan rate. Namely, a higher scan rate results in the decrease of the diffusion layer thickness, consequently, higher current.

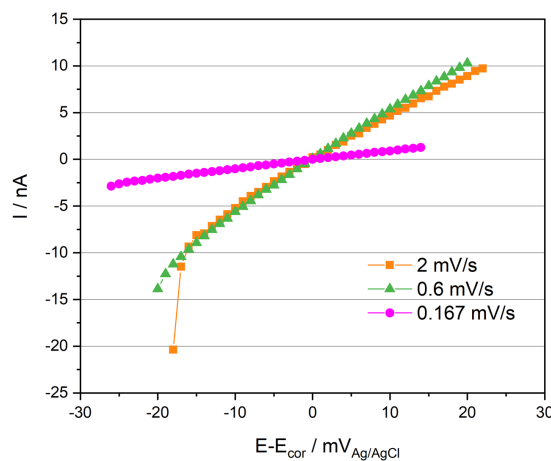


Figure C. 9 Rp measurements of Ti in NaCl solution with different scan rates

To quantitatively study the influence of scan rate on the measured current, the Rp measurements were carried out with different scan rates on Ti sample in NaCl solution. The corresponding results are plotted in Figure C. 9. The graph shows the current varies little with the scan rate decreasing from  $2 \text{ mV/s}$  to  $0.6 \text{ mV/s}$ . In comparison, it declines significantly when the scan rate is  $0.167 \text{ mV/s}$  (the recommended scan rate by ASTM standard). In consequence, the Rp value obtained for  $0.167 \text{ mV/s}$  is about four times higher than  $2 \text{ mV/s}$  and  $0.6 \text{ mV/s}$ .

## C.5. Electrochemical Behavior of CoCrMo Alloy in Simulated Solutions

### C.5.1. OCP and Rp Results of CoCrMo Alloy

The electrochemical behavior of CoCrMo alloy was tested in simulating fluids same with Ti. Each measurement was repeated three times. The OCP and Rp results are displayed in Figure C. 10 and Figure C. 11, respectively. The results show that the OCP value obviously decreases with the addition of BSA, while it increases significantly after adding  $H_2O_2$ . No obvious influence of HA, phosphate and calcium ions on the OCP value is obtained. The Rp values correspond to the OCP results that higher Rp values were obtained for samples with lower OCP values.

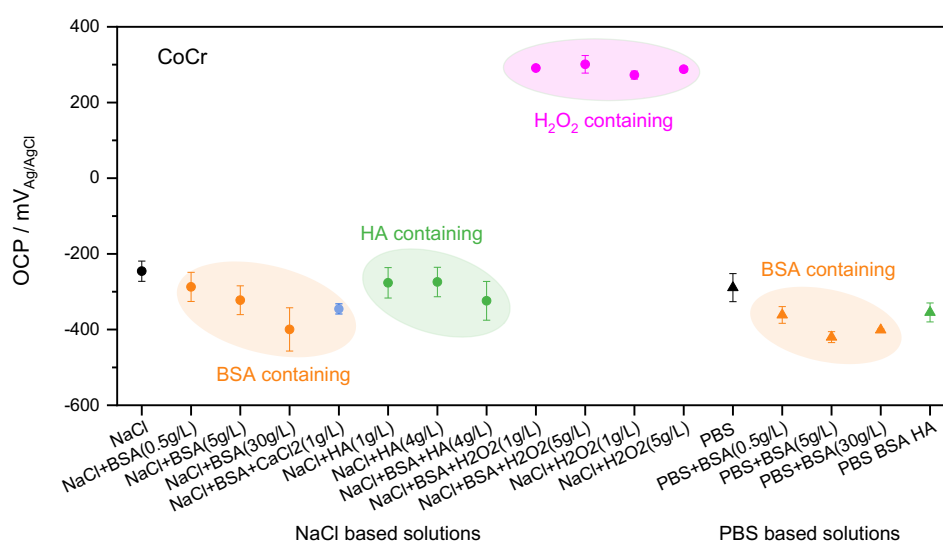


Figure C. 10 Stabilized OCP results of CoCrMo alloy in different simulated solutions

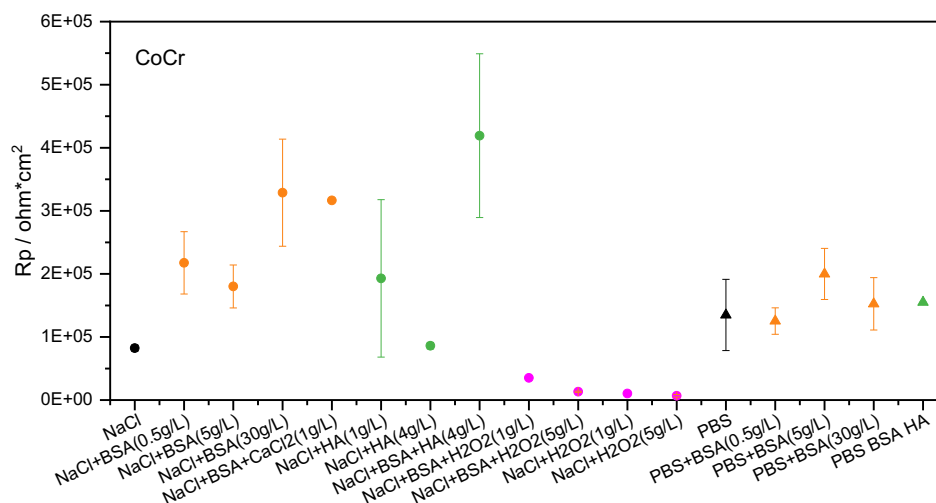
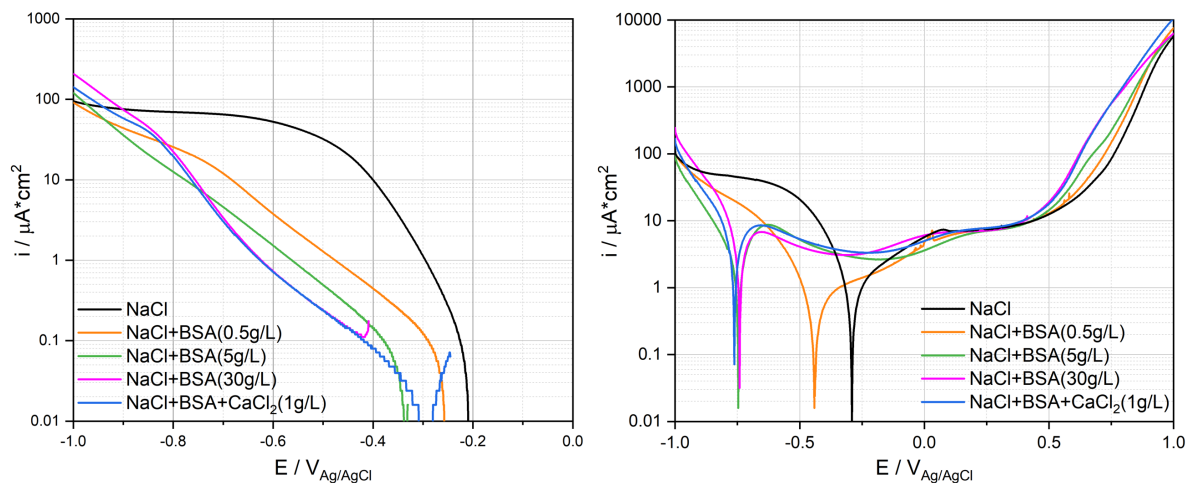


Figure C. 11 Comparison of Rp value of CoCrMo in simulated solutions

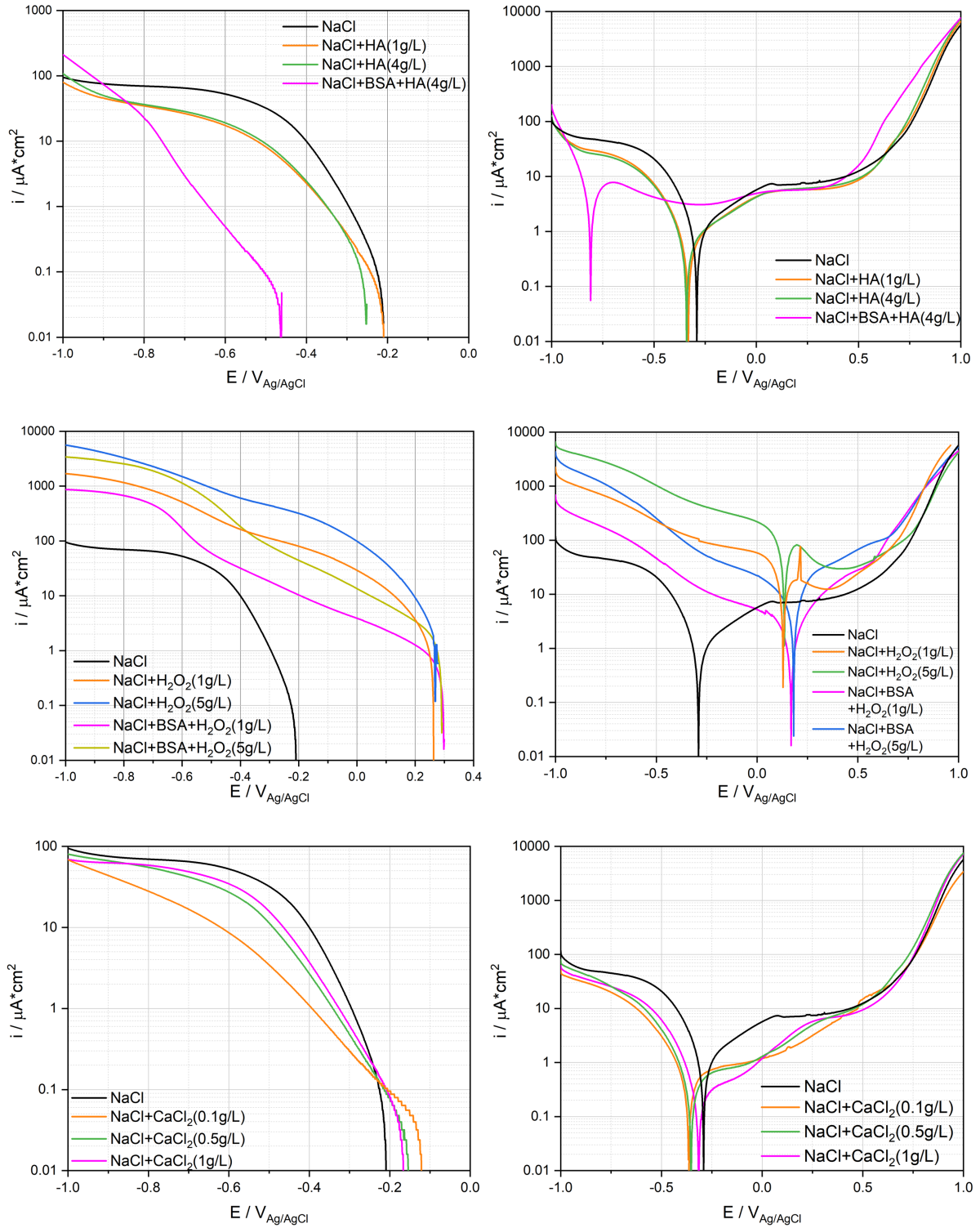
### C.5.2. Potentiodynamic Polarization Curve of CoCrMo Alloy

The representative polarization curves of CoCrMo alloy in simulated solutions are presented in Figure C. 12. In summary, the solution composition mainly influences the cathodic reaction behavior while the anodic reaction is less affected.

With the addition of BSA, the cathodic current significantly decreases. These results correspond to the literature where BSA is reported to act as an inhibitor of the oxygen reduction reaction [79-81]. Contrary to the cathodic behavior, the passive current varies little with BSA while the transpassive current slightly increases with BSA. The increase of transpassive current could be due to the reaction between BSA and Co/Cr/Mo ions, which enhances the dissolution of metallic ions [88-90]. The cathodic current is less affected by HA compared with BSA, and little variation is obtained for the anodic current after adding HA. This could be related to the hydrophilic property and the large size of HA that results in less amount of adsorption on metal surface [83]. The cathodic current is significantly enhanced with  $\text{H}_2\text{O}_2$  due to the contribution of  $\text{H}_2\text{O}_2$  reduction. The slightly increased anodic current is reported because of the formation of thicker and porous passive film because of the large amount of  $\text{OH}^-$ , which leads to the release of metal ions [103]. The cathodic and passive currents vary little with phosphate ions, while the transpassive current increased at about 0.6  $\text{V}_{\text{Ag/AgCl}}$ . This could be due to the reaction between phosphate ions and Cr ions [48]. Similar to phosphate, calcium ions have little effect on cathodic and transpassive currents, but the anodic current, which slightly decreases independent of calcium concentration. The polarization curves correspond to the OCP and  $R_p$  results, which are mainly controlled by the cathodic reaction.







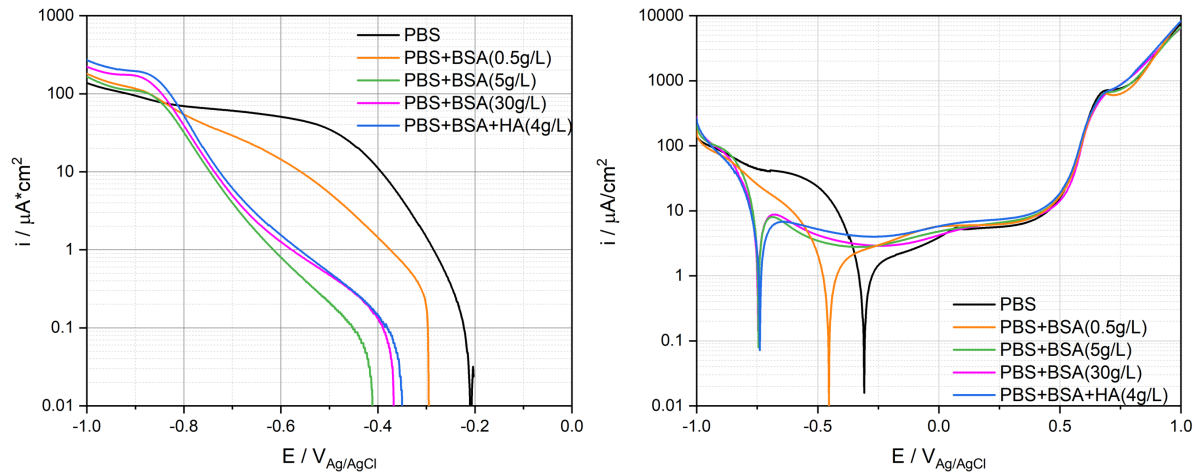


Figure C. 12 Cathodic and anodic polarization curves (logarithmic scale of the absolute current density) of CoCrMo alloy in simulated solutions

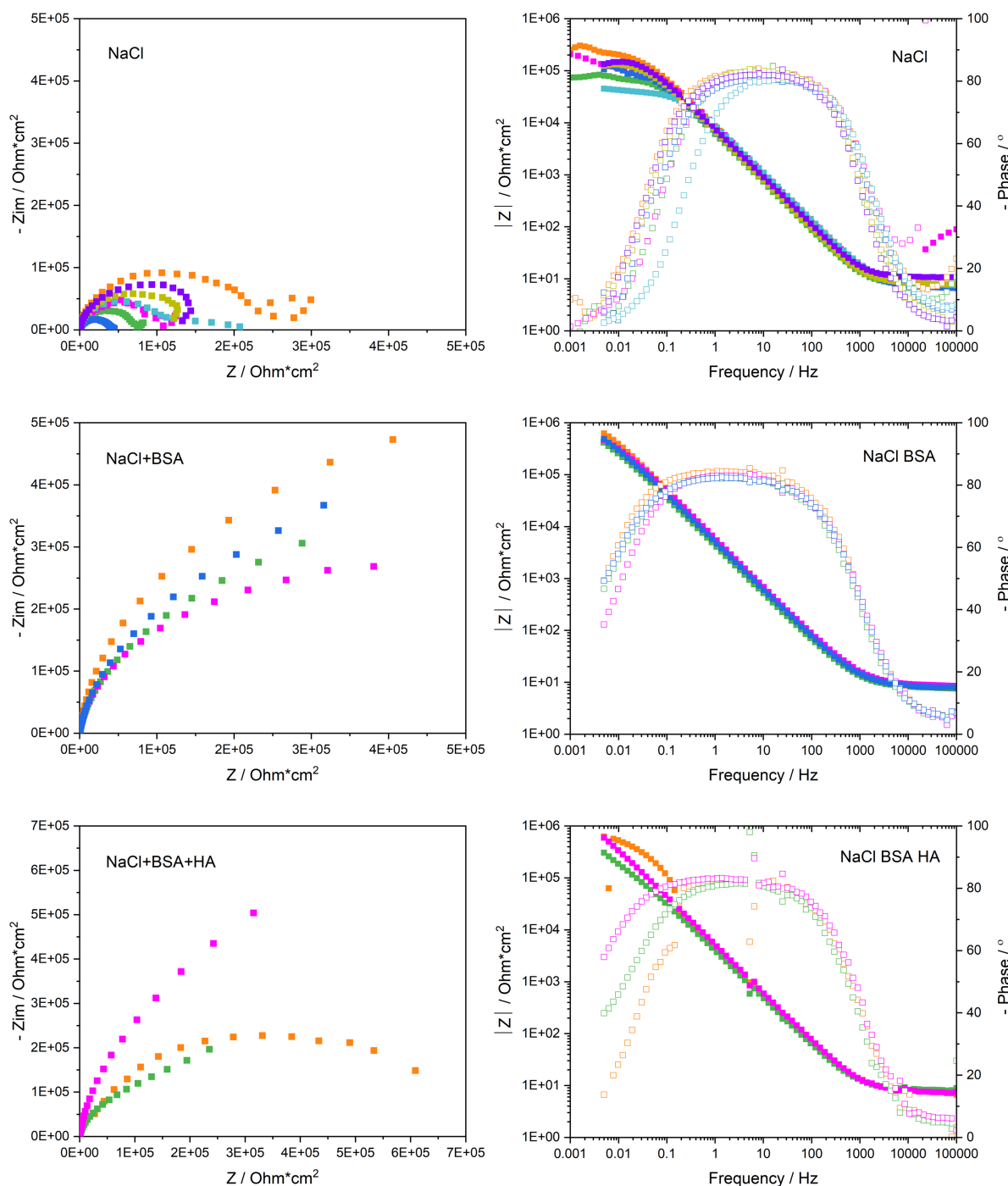
The same parameters were extracted from anodic polarization curves and summarized in Table C. 7. In PBS+BSA based solution, the cathodic current slightly increased after adding HA, suggesting a competitive adsorption between BSA and HA on sample surface.

Table C. 7 Electrochemical parameters extracted from anodic polarization curves of CoCrMo samples

Solution	$i_c (-0.9V) / \mu A/cm^2$	$E_{cor} / V_{Ag/AgCl}$	$i_{pp} (0V) / \mu A/cm^2$	$i_t (0.75V) / \mu A/cm^2$
NaCl(8g/L)	$-66.04 \pm 7.06$	$-0.3 \pm 0.02$	$4.75 \pm 1.05$	$96.72 \pm 23.37$
NaCl+BSA(0.5g/L)	$-47.94 \pm 13.34$	$-0.53 \pm 0.02$	$4.35 \pm 0.85$	$141.70 \pm 4.87$
NaCl+BSA(5g/L)	$-21.77 \pm 5.93$	$-0.74 \pm 0.03$	$3.80 \pm 1.63$	$214.96 \pm 9.10$
NaCl+BSA(30g/L)	$-46.25 \pm 8.52$	$-0.75 \pm 0.03$	$5.05 \pm 1.22$	$527.24 \pm 33.63$
NaCl+ CaCl <sub>2</sub> (1g/L)	$-39.45 \pm 8.87$	$-0.74 \pm 0.03$	$5.76 \pm 1.10$	$146.72 \pm 86.70$
NaCl+BSA+CaCl <sub>2</sub> (1g/L)	$-55.38 \pm 14.05$	$-0.31 \pm 0.01$	$1.75 \pm 1.25$	$554.00 \pm 26.88$
NaCl +HA(1g/L)	$-39.29 \pm 0.81$	$-0.33 \pm 0.02$	$3.36 \pm 1.31$	$99.64 \pm 2.37$
NaCl +HA(4g/L)	$-36.09 \pm 0.83$	$-0.31 \pm 0.04$	$3.66 \pm 0.75$	$122.95 \pm 1.99$
NaCl+BSA+HA(4g/L)	$-32.91 \pm 6.41$	$-0.78 \pm 0.04$	$4.72 \pm 0.27$	$496.72 \pm 19.71$
NaCl+BSA+H <sub>2</sub> O <sub>2</sub> (1g/L)	$-396 \pm 155$	$0.19 \pm 0.03$	$5.19 \pm 0.16$	$356.62 \pm 7.95$
NaCl+BSA+ H <sub>2</sub> O <sub>2</sub> (5g/L)	$-2371 \pm 586$	$0.21 \pm 0.06$	$28.36 \pm 8.20$	$296.82 \pm 8.39$
NaCl +H <sub>2</sub> O <sub>2</sub> (1g/L)	$-1103 \pm 93$	$0.14 \pm 0.01$	$117 \pm 83$	$167.07 \pm 60.58$
NaCl +H <sub>2</sub> O <sub>2</sub> (5g/L)	$-3525 \pm 691$	$0.16 \pm 0.04$	$264 \pm 63$	$112.83 \pm 6.51$
PBS	$-91.84 \pm 14.79$	$-0.34 \pm 0.05$	$5.16 \pm 1.82$	$814.70 \pm 51.98$
PBS+BSA(0.5g/L)	$-76.89 \pm 11$	$-0.48 \pm 0.04$	$7.46 \pm 3.53$	$646.56 \pm 35.31$
PBS+BSA(5g/L)	$-80.44 \pm 17.81$	$-0.75 \pm 0.01$	$5.81 \pm 1.41$	$730.41 \pm 6.82$
PBS+BSA(30g/L)	$-87.28 \pm 1.73$	$-0.76 \pm 0.02$	$6.26 \pm 2.88$	$952.27 \pm 117.66$
PBS+BSA+HA(4g/L)	$-70.48 \pm 0.78$	$-0.74 \pm 0.00$	$6.56 \pm 1.08$	$895.14 \pm 42.01$

### C.5.3. EIS Results of CoCrMo Alloy

Based on the above results, the BSA and HA are the key parameters that influence the corrosion behavior of CoCrMo alloy in simulated solutions. To further study the impact of organics, the impedance measurements were conducted under OCP conditions in representative BSA and HA containing solutions. The EIS results are plotted in Figure C. 13. For each solution, the measurement was conducted at least three times to guarantee the reproducibility.



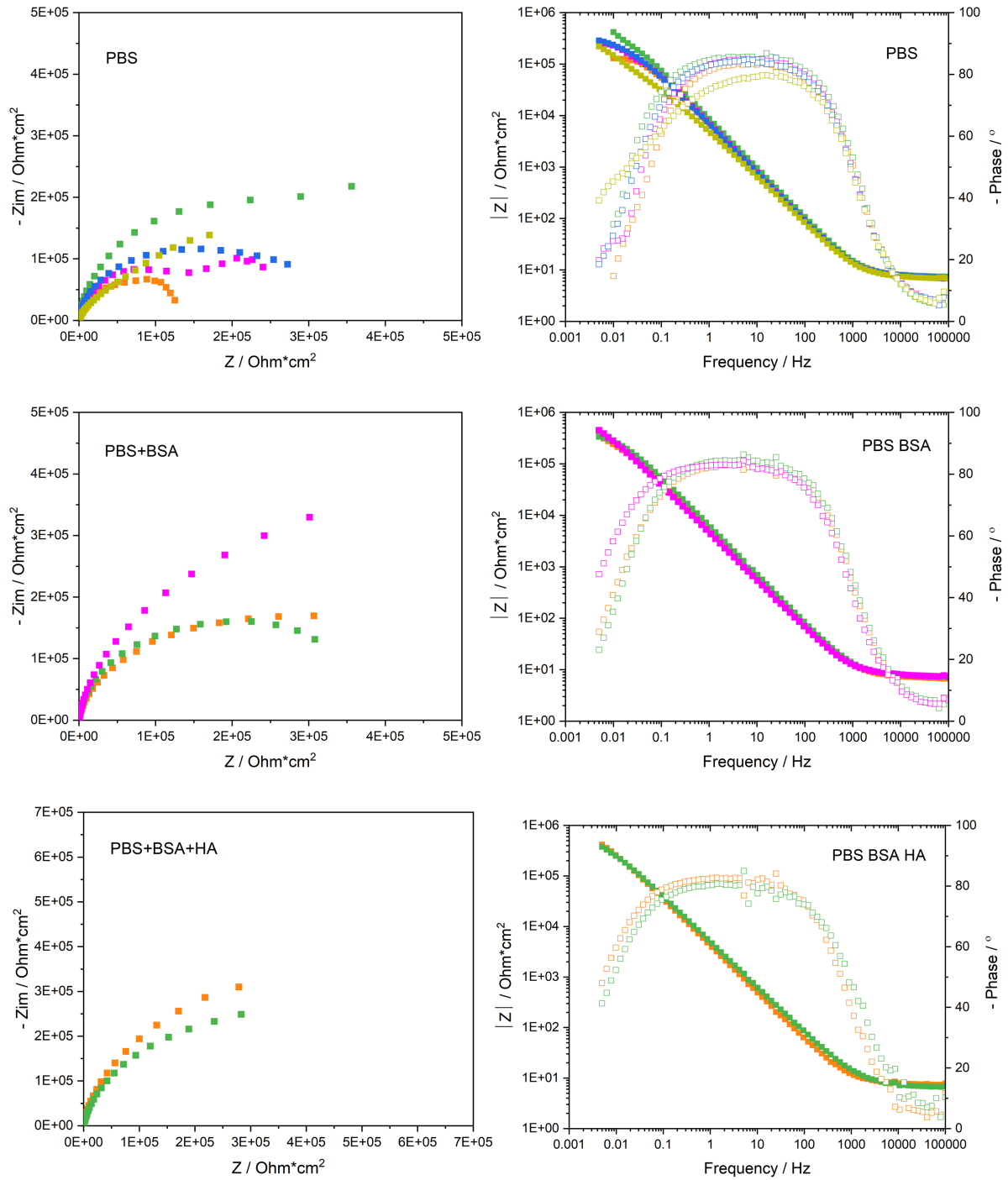


Figure C. 13 Nyquist and Bode plot of CoCrMo alloy in simulated solutions

In the Nyquist plots, the arc length and angle increased with the addition of BSA and HA, while they decreased after adding HA. Three distinctive sections,  $R_s$ , capacitive behavior and  $R_p$ , were obtained in the Bode plot for NaCl solution. However, no modulus plateau was observed in the rest solutions at the low frequency region. The modulus at the low frequency region increases and the phase angle curve at the middle frequency region extends with the

addition of phosphate, BSA and HA. The higher modulus indicates that the polarization resistance of CoCrMo alloy increases with the addition of phosphate, BSA and HA.

Table C. 8 Electrochemical parameters extracted from EIS measurement of CoCrMo sample

Solution	OCP / mV <sub>Ag/AgCl</sub>	R <sub>s</sub> / Ohm*cm <sup>2</sup>	Z  / KOhm*cm <sup>2</sup>	-Phase / °
NaCl(8g/L)	-146 ± 27	7.9 ± 1.4	121 ± 55	8 ± 4
NaCl+BSA(30g/L)	-400 ± 57	8.3 ± 0.4	499 ± 88	45 ± 7
NaCl+BSA+HA(4g/L)	-324 ± 51	7.9 ± 0.5	509 ± 176	37 ± 22
PBS	-289 ± 37	7.5 ± 0.5	254 ± 34	26 ± 12
PBS+BSA(30g/L)	-401 ± 2	7.4 ± 0.4	377 ± 60	33 ± 13
PBS+BSA+HA(4g/L)	-355 ± 25	7.2 ± 0.5	397 ± 28	45 ± 5

The same electrochemical parameters were extracted from EIS measurements and summarized in Table C. 8. As shown in the Table, the |Z| value increase with the addition of BSA and HA in NaCl and PBS solution. The higher |Z| value could be due to the adsorption of BSA and HA. Continuous increase of phase angle with the addition of BSA and HA was obtained for both NaCl and PBS based solutions. Higher |Z| and phase angle were obtained for PBS solution compared with NaCl solution, suggesting phosphate ions adsorbed on the sample surface. The |Z| values correspond to the R<sub>p</sub> results acquired from the linear potentiodynamic measurements polarization curves.

## Appendix D Fourier Transform Infrared Spectroscopy of BSA and HA

To study the adsorbed organics on the sample surface after immersing in synovial fluids, FTIR measurements on BSA and HA were conducted. The obtained spectra correspond well with the literature [136, 137], and they are shown in Figure D. 1. The prominent adsorption peaks were assigned in the graph according to the literature.

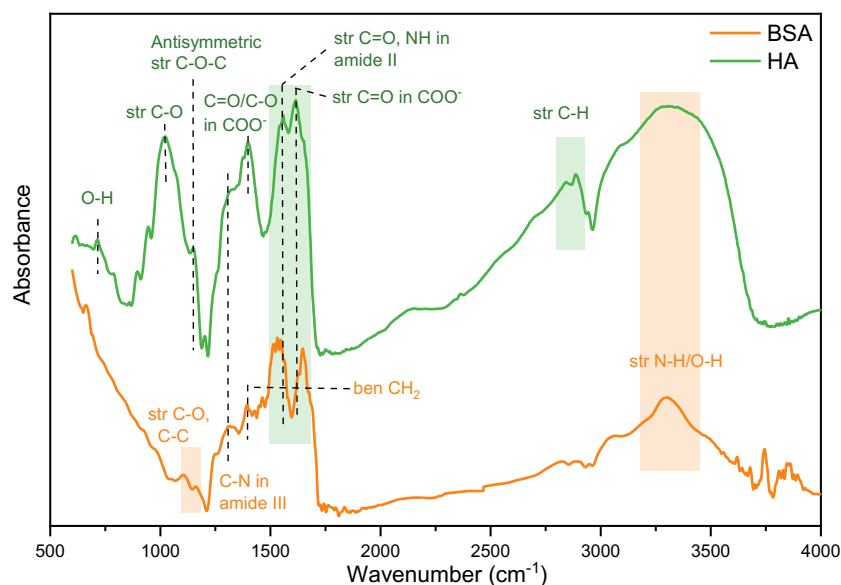


Figure D. 1 Absorption spectra of BSA and HA (str: stretching vibration, ben: bending vibration)

As is shown in the graph, common bands were detected on both organics, such as stretching vibration of C=O, C-O, C-H, N-H and O-H bonds, despite the different peak positions. However, the stretching vibration of C-O-C is only observed in the HA spectrum, corresponding well with the HA structure. Amide groups are the characteristic molecular bands of proteins [134], and they are present in both BSA and HA.

## References

- [1] Bashinskaya, B., Zimmerman, R.M., Walcott, B.P., Antoci, V., Arthroplasty Utilization in the United States is Predicted by Age-Specific Population Groups. *ISRN Orthopedics* 2012, 2012, 1–8.
- [2] Lons, A., Putman, S., Pasquier, G., Migaud, H., et al., Metallic ion release after knee prosthesis implantation: a prospective study. *International Orthopaedics (SICOT)* 2017, 41, 2503–2508.
- [3] Rodríguez de la Flor, M., Hernández-Vaquero, D., Fernández-Carreira, J.M., Metal presence in hair after metal-on-metal resurfacing arthroplasty: METAL PRESENCE IN HAIR AFTER METAL-ON-METAL. *J. Orthop. Res.* 2013, 31, 2025–2031.
- [4] Forsthoefel, C.W., Brown, N.M., Barba, M.L., Comparison of metal ion levels in patients with hip resurfacing versus total hip arthroplasty. *Journal of Orthopaedics* 2017, 14, 561–564.
- [5] Igual Munoz, A., Schwiesau, J., Jolles, B.M., Mischler, S., In vivo electrochemical corrosion study of a CoCrMo biomedical alloy in human synovial fluids. *Acta Biomaterialia* 2015, 21, 228–236.
- [6] S.G. Steinemann, Corrosion of Surgical Implants-in vivo and in vitro Tests, in evaluation of biomaterials. *Advances in Biomaterials* 1980, 1–34.
- [7] Lewis, A.C., Kilburn, M.R., Papageorgiou, I., Allen, G.C., et al., Effect of synovial fluid, phosphate-buffered saline solution, and water on the dissolution and corrosion properties of CoCrMo alloys as used in orthopedic implants. *J. Biomed. Mater. Res.* 2005, 73A, 456–467.
- [8] Long, M., Rack, H.J., Titanium alloys in total joint replacement—a materials science perspective. *Biomaterials* 1998, 19, 1621–1639.
- [9] Tamer, T.M., Hyaluronan and synovial joint: function, distribution and healing. *Interdisciplinary Toxicology* 2013, 6, 111–125.
- [10] Puccio, F.D., Biotribology of artificial hip joints. *WJO* 2015, 6, 77.
- [11] Asri, R.I.M., Harun, W.S.W., Samykano, M., Lah, N.A.C., et al., Corrosion and surface modification on biocompatible metals: A review. *Materials Science and Engineering: C* 2017, 77, 1261–1274.
- [12] Murphy, W., Black, J., Hastings, G. (Eds.), *Handbook of Biomaterial Properties*, Springer New York, New York, NY 2016.
- [13] Manam, N.S., Harun, W.S.W., Shri, D.N.A., Ghani, S.A.C., et al., Study of corrosion in biocompatible metals for implants: A review. *Journal of Alloys and Compounds* 2017, 701, 698–715.

- [14] Hodgson, A.W.E., Kurz, S., Virtanen, S., Fervel, V., et al., Passive and transpassive behaviour of CoCrMo in simulated biological solutions. *Electrochimica Acta* 2004, 49, 2167–2178.
- [15] Vidal, C.V., Muñoz, A.I., Olsson, C.-O.A., Mischler, S., Passivation of a CoCrMo PVD Alloy with Biomedical Composition under Simulated Physiological Conditions Studied by EQCM and XPS. *J. Electrochem. Soc.* 2012, 159, C233–C243.
- [16] Textor, M., Sittig, C., Frauchiger, V., Tosatti, S., et al., Properties and Biological Significance of Natural Oxide Films on Titanium and Its Alloys, in: *Titanium in Medicine*, Springer Berlin Heidelberg, Berlin, Heidelberg 2001, pp. 171–230.
- [17] Assis, S.L. de, Wolynec, S., Costa, I., Corrosion characterization of titanium alloys by electrochemical techniques. *Electrochimica Acta* 2006, 51, 1815–1819.
- [18] Mouhyi, J., Dohan Ehrenfest, D.M., Albrektsson, T., The Peri-Implantitis: Implant Surfaces, Microstructure, and Physicochemical Aspects: The Peri-Implantitis. *Clinical Implant Dentistry and Related Research* 2012, 14, 170–183.
- [19] Khan, M.A., Williams, R.L., Williams, D.F., In-vitro corrosion and wear of titanium alloys in the biological environment. *Biomaterials* 1996, 17, 2117–2126.
- [20] Vidal, C.V., Muñoz, A.I., Effect of thermal treatment and applied potential on the electrochemical behaviour of CoCrMo biomedical alloy. *Electrochimica Acta* 2009, 54, 1798–1809.
- [21] Mischler, S., Sliding Tribo-Corrosion of Passive Metals: Mechanisms and Modeling, in: Blau, P.J., Celis, J.-P., Drees, D. (Eds.), *Tribo-Corrosion: Research, Testing, and Applications*, ASTM International, 100 Barr Harbor Drive, PO Box C700, West Conshohocken, PA 19428-2959 2013, pp. 1–18.
- [22] Mischler, S., Muñoz, A.I., Wear of CoCrMo alloys used in metal-on-metal hip joints: A tribocorrosion appraisal. *Wear* 2013, 297, 1081–1094.
- [23] Jacobs, J.J., Cooper, H.J., Urban, R.M., Wixson, R.L., et al., What Do We Know About Taper Corrosion in Total Hip Arthroplasty? *The Journal of Arthroplasty* 2014, 29, 668–669.
- [24] Rodrigues, D.C., Urban, R.M., Jacobs, J.J., Gilbert, J.L., *In vivo* severe corrosion and hydrogen embrittlement of retrieved modular body titanium alloy hip-implants. *J. Biomed. Mater. Res.* 2009, 88B, 206–219.
- [25] Hall, D.J., Pourzal, R., Lundberg, H.J., Mathew, M.T., et al., Mechanical, chemical and biological damage modes within head-neck tapers of CoCrMo and Ti6Al4V contemporary hip replacements: DAMAGE MODES IN THR MODULAR JUNCTIONS. *J. Biomed. Mater. Res.* 2018, 106, 1672–1685.



- [26] Collier, J., Surprenant, V., Jensen, R., Mayor, M., et al., Corrosion between the components of modular femoral hip prostheses. *The Journal of Bone and Joint Surgery. British Volume* 1992, 74-B, 511–517.
- [27] Magone, K., Luckenbill, D., Goswami, T., Metal ions as inflammatory initiators of osteolysis. *Arch Orthop Trauma Surg* 2015, 135, 683–695.
- [28] Matusiewicz, H., Potential release of in vivo trace metals from metallic medical implants in the human body: From ions to nanoparticles – A systematic analytical review. *Acta Biomaterialia* 2014, 10, 2379–2403.
- [29] Terčič, D., Božič, B., The Basis of the Synovial Fluid Analysis. *Clinical Chemistry and Laboratory Medicine* 2001, 39.
- [30] Bertram, K.L., Banderali, U., Taylor, P., Krawetz, R.J., Ion channel expression and function in normal and osteoarthritic human synovial fluid progenitor cells. *Channels* 2016, 10, 148–157.
- [31] Krebs, H.A., Chemical Composition of Blood Plasma and Serum. *Annu. Rev. Biochem.* 1950, 19, 409–430.
- [32] Noble P, Collin B, Lecomte-Beckers J, Magnée A, Denoix JM, Serteyn D. L’articulation synoviale: un système tribologique parfait. In *Annales de Médecine Vétérinaire* 2010 (Vol. 154, No. 2, pp. 83-93). Université de Liège. n.d.
- [33] Mazzucco, D., Scott, R., Spector, M., Composition of joint fluid in patients undergoing total knee replacement and revision arthroplasty: correlation with flow properties. *Biomaterials* 2004, 25, 4433–4445.
- [34] Davidson, R., Gardner, S., Jupp, O., Bullough, A., et al., Isothiocyanates are detected in human synovial fluid following broccoli consumption and can affect the tissues of the knee joint. *Sci Rep* 2017, 7, 3398.
- [35] Milošev, I., Levašič, V., Vidmar, J., Kovač, S., et al., pH and metal concentration of synovial fluid of osteoarthritic joints and joints with metal replacements: OSTEOARTHRITIC JOINTS AND JOINTS WITH METAL REPLACEMENTS. *J. Biomed. Mater. Res.* 2017, 105, 2507–2515.
- [36] Geneva, I.I., Cuzzo, B., Fazili, T., Javaid, W., Normal Body Temperature: A Systematic Review. *Open Forum Infectious Diseases* 2019, 6, ofz032.
- [37] Ortiz-Prado, E., Dunn, J.F., Vasconez, J., Castillo, D., et al., Partial pressure of oxygen in the human body: a general review. n.d., 14.
- [38] Regan, E.A., Bowler, R.P., Crapo, J.D., Joint fluid antioxidants are decreased in osteoarthritic joints compared to joints with macroscopically intact cartilage and subacute injury. *Osteoarthritis and Cartilage* 2008, 16, 515–521.
- [39] Richman, A.I., Su, E.Y., Ho, G., Reciprocal relationship of synovial fluid volume and Oxygen tension. *Arthritis & Rheumatism* 1981, 24, 701–705.

- [40] Valero Vidal, C., Study of the degradation mechanisms of the CoCrMo biomedical alloy in physiological media by electrochemical techniques and surface analysis, Universitat Politècnica de València, 2012.
- [41] Kang, Y., Li, X., Tu, Y., Wang, Q., et al., On the Mechanism of Protein Adsorption onto Hydroxylated and Nonhydroxylated TiO<sub>2</sub> Surfaces. *J. Phys. Chem. C* 2010, *114*, 14496–14502.
- [42] Xing, W., Yin, M., Lv, Q., Hu, Y., et al., Oxygen Solubility, Diffusion Coefficient, and Solution Viscosity, in: *Rotating Electrode Methods and Oxygen Reduction Electrocatalysts*, Elsevier, 2014, pp. 1–31.
- [43] Parsons, R., Atlas of electrochemical equilibria in aqueous solutions. *Journal of Electroanalytical Chemistry and Interfacial Electrochemistry* 1967, *13*, 471.
- [44] Ithurbide, A., Frateur, I., Galtayries, A., Marcus, P., XPS and flow-cell EQCM study of albumin adsorption on passivated chromium surfaces: Influence of potential and pH. *Electrochimica Acta* 2007, *53*, 1336–1345.
- [45] Milošev, I., Metikoš-Huković, M., Strehblow, H.-H., Passive film on orthopaedic TiAlV alloy formed in physiological solution investigated by X-ray photoelectron spectroscopy. *Biomaterials* 2000, *21*, 2103–2113.
- [46] Milošev, I., The effect of biomolecules on the behaviour of CoCrMo alloy in various simulated physiological solutions. *Electrochimica Acta* 2012, *78*, 259–273.
- [47] Hanawa, T., Ota, M., Calcium phosphate naturally formed on titanium in electrolyte solution. *Biomaterials* 1991, *12*, 767–774.
- [48] Hodgson, A.W.E., Mueller, Y., Forster, D., Virtanen, S., Electrochemical characterisation of passive films on Ti alloys under simulated biological conditions. *Electrochimica Acta* 2002, *47*, 1913–1923.
- [49] Valero Vidal, C., Igual Muñoz, A., Effect of physico-chemical properties of simulated body fluids on the electrochemical behaviour of CoCrMo alloy. *Electrochimica Acta* 2011, *56*, 8239–8248.
- [50] Muñoz, A.I., Mischler, S., Interactive Effects of Albumin and Phosphate Ions on the Corrosion of CoCrMo Implant Alloy. *J. Electrochem. Soc.* 2007, *154*, C562.
- [51] Ouerd, A., Alemany-Dumont, C., Berthomé, G., Normand, B., et al., Reactivity of Titanium in Physiological Medium. *J. Electrochem. Soc.* 2007, *154*, C593.
- [52] Chubar, N.I., Kanibolotsky, V.A., Strelko, V.V., Gallios, G.G., et al., Adsorption of phosphate ions on novel inorganic ion exchangers. *Colloids and Surfaces A: Physicochemical and Engineering Aspects* 2005, *255*, 55–63.
- [53] Rahimi, E., Offoiaich, R., Baert, K., Terryn, H., et al., Role of phosphate, calcium species and hydrogen peroxide on albumin protein adsorption on surface oxide of Ti6Al4V alloy. *Materialia* 2021, *15*, 100988.

- [54] Li, M., Liu, J., Xu, Y., Qian, G., Phosphate adsorption on metal oxides and metal hydroxides: A comparative review. *Environ. Rev.* 2016, 24, 319–332.
- [55] Liu, J., Wan, L., Zhang, L., Zhou, Q., Effect of pH, ionic strength, and temperature on the phosphate adsorption onto lanthanum-doped activated carbon fiber. *Journal of Colloid and Interface Science* 2011, 364, 490–496.
- [56] Acelas, N.Y., Martin, B.D., López, D., Jefferson, B., Selective removal of phosphate from wastewater using hydrated metal oxides dispersed within anionic exchange media. *Chemosphere* 2015, 119, 1353–1360.
- [57] Szymanek, K., Charnas, R., Piasecki, W., A study on the mechanism of  $\text{Ca}^{2+}$  adsorption on  $\text{TiO}_2$  and  $\text{Fe}_2\text{O}_3$  with the usage of calcium ion-selective electrode. *Chemosphere* 2020, 242, 125162.
- [58] Tsutsumi, Y., Nishisaka, T., Doi, H., Ashida, M., et al., Reaction of calcium and phosphate ions with titanium, zirconium, niobium, and tantalum: Reaction of calcium and phosphate ions with metals. *Surf. Interface Anal.* 2015, 47, 1148–1154.
- [59] Yang, B.C., Weng, J., Li, X.D., Zhang, X.D., The order of calcium and phosphate ion deposition on chemically treated titanium surfaces soaked in aqueous solution. n.d., 7.
- [60] Tamilselvi, S., Raman, V., Rajendran, N., Corrosion behaviour of Ti–6Al–7Nb and Ti–6Al–4V ELI alloys in the simulated body fluid solution by electrochemical impedance spectroscopy. *Electrochimica Acta* 2006, 52, 839–846.
- [61] Imamura, K., Shimomura, M., Nagai, S., Akamatsu, M., et al., Adsorption characteristics of various proteins to a titanium surface. *Journal of Bioscience and Bioengineering* 2008, 106, 273–278.
- [62] Rabe, M., Verdes, D., Seeger, S., Understanding protein adsorption phenomena at solid surfaces. *Advances in Colloid and Interface Science* 2011, 162, 87–106.
- [63] Saikia, J., Saha, B., Das, G., Interpreting the adsorption of serum albumin and lactoglobulin onto ZnS nanoparticles: Effect of conformational rigidity of the proteins. *Journal of Colloid and Interface Science* 2014, 416, 235–242.
- [64] Zhou, K., Chen, J., Wang, T., Su, Y., et al., Effect of surface energy on protein adsorption behaviours of treated CoCrMo alloy surfaces. *Applied Surface Science* 2020, 520, 146354.
- [65] Silva-Bermudez, P., Rodil, S.E., An overview of protein adsorption on metal oxide coatings for biomedical implants. *Surface and Coatings Technology* 2013, 233, 147–158.
- [66] Yan, Y., Yang, H., Su, Y., Qiao, L., Albumin adsorption on CoCrMo alloy surfaces. *Sci Rep* 2016, 5, 18403.
- [67] Mücksch, C., Urbassek, H.M., Accelerated Molecular Dynamics Study of the Effects of Surface Hydrophilicity on Protein Adsorption. *Langmuir* 2016, 32, 9156–9162.

- [68] Rechendorff, K., Hovgaard, M.B., Foss, M., Zhdanov, V.P., et al., Enhancement of Protein Adsorption Induced by Surface Roughness. *Langmuir* 2006, 22, 10885–10888.
- [69] Valero-Vidal, C., Igual-Muñoz, A., Olsson, C.-O.A., Mischler, S., Adsorption of BSA on Passivated CoCrMo PVD Alloy: An EQCM and XPS Investigation. *J. Electrochem. Soc.* 2014, 161, C294–C301.
- [70] Muñoz, A.I., Mischler, S., Electrochemical Quartz Crystal Microbalance and X-Ray Photoelectron Spectroscopy study of cathodic reactions in Bovine Serum Albumin containing solutions on a Physical Vapour Deposition-CoCrMo biomedical alloy. *Electrochimica Acta* 2015, 180, 96–103.
- [71] Talha, M., Ma, Y., Kumar, P., Lin, Y., et al., Role of protein adsorption in the bio corrosion of metallic implants – A review. *Colloids and Surfaces B: Biointerfaces* 2019, 176, 494–506.
- [72] Meissner, J., Prause, A., Bharti, B., Findenegg, G.H., Characterization of protein adsorption onto silica nanoparticles: influence of pH and ionic strength. *Colloid Polym Sci* 2015, 293, 3381–3391.
- [73] Teilum, K., Olsen, J.G., Kragelund, B.B., Protein stability, flexibility and function. *Biochimica et Biophysica Acta (BBA) - Proteins and Proteomics* 2011, 1814, 969–976.
- [74] Yang, L., Zhu, Q., Xie, X., Cao, X., et al., Electrochemical behavior of CoCrMo alloy for dental applications in acidic artificial saliva containing albumin. *Colloids and Surfaces B: Biointerfaces* 2019, 184, 110492.
- [75] Guizado, T.R.C., Analysis of the structure and dynamics of human serum albumin. *J Mol Model* 2014, 20, 2450.
- [76] Belatik, A., Hotchandani, S., Carpentier, R., Tajmir-Riahi, H.-A., Locating the Binding Sites of Pb(II) Ion with Human and Bovine Serum Albumins. *PLoS ONE* 2012, 7, e36723.
- [77] Roche, M., Rondeau, P., Singh, N.R., Tarnus, E., et al., The antioxidant properties of serum albumin. *FEBS Letters* 2008, 582, 1783–1787.
- [78] Klinger, A., Steinberg, D., Kohavi, D., Sela, M.N., Mechanism of adsorption of human albumin to titanium in vitro. *J. Biomed. Mater. Res.* 1997, 36, 387–392.
- [79] Righetti, P.G., Caravaggio, T., Isoelectric points and molecular weights of proteins. *Journal of Chromatography A* 1976, 127, 1–28.
- [80] Liamas, E., Thomas, O.R.T., Muñoz, A.I., Zhang, Z.J., Effect of the electrochemical characteristics of titanium on the adsorption kinetics of albumin. *RSC Adv.* 2019, 9, 34265–34273.
- [81] Karimi, S., Nickchi, T., Alfantazi, A., Effects of bovine serum albumin on the corrosion behaviour of AISI 316L, Co–28Cr–6Mo, and Ti–6Al–4V alloys in phosphate buffered saline solutions. *Corrosion Science* 2011, 53, 3262–3272.

- [82] Karimi, S., Alfantazi, A.M., Electrochemical Corrosion Behavior of Orthopedic Biomaterials in Presence of Human Serum Albumin. *J. Electrochem. Soc.* 2013, 160, C206–C214.
- [83] Milošev, I., Hmeljak, J., Cör, A., Hyaluronic acid stimulates the formation of calcium phosphate on CoCrMo alloy in simulated physiological solution. *J Mater Sci: Mater Med* 2013, 24, 555–571.
- [84] Cheng, X., Roscoe, S.G., Corrosion behavior of titanium in the presence of calcium phosphate and serum proteins. *Biomaterials* 2005, 26, 7350–7356.
- [85] Berbel, L.O., Banczek, E. do P., Karousis, I.K., Kotsakis, G.A., et al., Determinants of corrosion resistance of Ti-6Al-4V alloy dental implants in an In Vitro model of peri-implant inflammation. *PLoS ONE* 2019, 14, e0210530.
- [86] Contu, F., Elsener, B., Böhni, H., Serum effect on the electrochemical behaviour of titanium, Ti6Al4V and Ti6Al7Nb alloys in sulphuric acid and sodium hydroxide. *Corrosion Science* 2004, 46, 2241–2254.
- [87] Khosa, M.A., Ullah, A., Mechanistic insight into protein supported biosorption complemented by kinetic and thermodynamics perspectives. *Advances in Colloid and Interface Science* 2018, 261, 28–40.
- [88] Norde, W., Driving forces for protein adsorption at solid surfaces. *Macromol. Symp.* 1996, 103, 5–18.
- [89] Klok, O., Igual Munoz, A., Mischler, S., An Overview of Serum Albumin Interactions with Biomedical Alloys. *Materials* 2020, 13, 4858.
- [90] Karimi, S., Nickchi, T., Alfantazi, A.M., Long-term corrosion investigation of AISI 316L, Co–28Cr–6Mo, and Ti–6Al–4V alloys in simulated body solutions. *Applied Surface Science* 2012, 258, 6087–6096.
- [91] Hedberg, Y., Lundin, M., Jacksén, J., Emmer, Å., et al., Chromium–protein complexation studies by adsorptive cathodic stripping voltammetry and MALDI-TOF-MS. *J Appl Electrochem* 2012, 42, 349–358.
- [92] Hedberg, Y., Karlsson, M.-E., Wei, Z., Žnidaršič, M., et al., Interaction of Albumin and Fibrinogen with Stainless Steel: Influence of Sequential Exposure and Protein Aggregation on Metal Release and Corrosion Resistance. *CORROSION* 2017, 73, 1423–1436.
- [93] Stankovich, M.T., Bard, A.J., The electrochemistry of proteins and related substances part III. Bovine serum albumin. *Journal of Electroanalytical Chemistry and Interfacial Electrochemistry* 1978, 86, 189–199.
- [94] Necas, J., Bartosikova, L., Brauner, P., Kolar, J., Hyaluronic acid (hyaluronan): a review. *Veterinarni Medicina* 2008, 53, 397–411.

- [95] Hui, A.Y., McCarty, W.J., Masuda, K., Firestein, G.S., et al., A systems biology approach to synovial joint lubrication in health, injury, and disease. *WIREs Mechanisms of Disease* 2012, 4, 15–37.
- [96] Zhang, Y., Jordan, J.M., Epidemiology of Osteoarthritis. *Clinics in Geriatric Medicine* 2010, 26, 355–369.
- [97] Kawai, N., Tanaka, E., Takata, T., Miyauchi, M., et al., Influence of additive hyaluronic acid on the lubricating ability in the temporomandibular joint. *J. Biomed. Mater. Res.* 2004, 70A, 149–153.
- [98] Bell, C.J., Ingham, E., Fisher, J., Influence of hyaluronic acid on the time-dependent friction response of articular cartilage under different conditions. *Proc Inst Mech Eng H* 2006, 220, 23–31.
- [99] Forsey, R., Fisher, J., Thompson, J., Stone, M., et al., The effect of hyaluronic acid and phospholipid based lubricants on friction within a human cartilage damage model. *Biomaterials* 2006, 27, 4581–4590.
- [100] More, N.S., Paul, S.N., Roy, M., Electrochemical Corrosion Behaviour of Ti–29Nb–13Ta–4.6Zr Alloy in Physiological Solution Containing Various Synovial Joint Lubricants. *J Bio Tribo Corros* 2018, 4, 42.
- [101] Adam-Vizi, V., Chinopoulos, C., Bioenergetics and the formation of mitochondrial reactive oxygen species. *Trends in Pharmacological Sciences* 2006, 27, 639–645.
- [102] Turrens, J.F., Mitochondrial formation of reactive oxygen species. *The Journal of Physiology* 2003, 552, 335–344.
- [103] Mittal, M., Siddiqui, M.R., Tran, K., Reddy, S.P., et al., Reactive Oxygen Species in Inflammation and Tissue Injury. *Antioxidants & Redox Signaling* 2014, 20, 1126–1167.
- [104] Höhn, S., Virtanen, S., Effect of inflammatory conditions and H<sub>2</sub>O<sub>2</sub> on bare and coated Ti–6Al–4V surfaces: Corrosion behavior, metal ion release and Ca-P formation under long-term immersion in DMEM. *Applied Surface Science* 2015, 357, 101–111.
- [105] Liu, Y., Gilbert, J.L., The effect of simulated inflammatory conditions and Fenton chemistry on the electrochemistry of CoCrMo alloy: THE EFFECT OF SIMULATED INFLAMMATORY CONDITIONS AND FENTON CHEMISTRY. *J. Biomed. Mater. Res.* 2018, 106, 209–220.
- [106] Yu, F., Addison, O., Davenport, A.J., A synergistic effect of albumin and H<sub>2</sub>O<sub>2</sub> accelerates corrosion of Ti6Al4V. *Acta Biomaterialia* 2015, 26, 355–365.
- [107] Fonseca-García, A., Pérez-Alvarez, J., Barrera, C.C., Medina, J.C., et al., The effect of simulated inflammatory conditions on the surface properties of titanium and stainless steel and their importance as biomaterials. *Materials Science and Engineering: C* 2016, 66, 119–129.

- [108] Impergre, A., Ter-Ovanessian, B., Der Loughian, C., Normand, B., Systemic strategy for biocompatibility assessments of metallic biomaterials: Representativeness of cell culture medium. *Electrochimica Acta* 2018, 283, 1017–1027.
- [109] Tang, Y.-C., Katsuma, S., Fujimoto, S., Hiromoto, S., Electrochemical study of Type 304 and 316L stainless steels in simulated body fluids and cell cultures. *Acta Biomaterialia* 2006, 2, 709–715.
- [110] Tsaryk, R., Peters, K., Barth, S., Unger, R.E., et al., The role of oxidative stress in pro-inflammatory activation of human endothelial cells on Ti6Al4V alloy. *Biomaterials* 2013, 34, 8075–8085.
- [111] Kasemo, B., Biological surface science. *Surface Science* 2002, 500, 656–677.
- [112] Kasper, C., Witte, F., Pörtner, R. (Eds.), Tissue Engineering III: Cell - Surface Interactions for Tissue Culture, Springer Berlin Heidelberg, Berlin, Heidelberg 2012.
- [113] Landolt, D., Corrosion and Surface Chemistry of Metals, 0 ed., EPFL Press, 2007.
- [114] Wimmer, M.A., Fischer, A., Büscher, R., Pourzal, R., et al., Wear mechanisms in metal-on-metal bearings: The importance of tribochemical reaction layers. *J. Orthop. Res.* 2009, n/a-n/a.
- [115] Yan, Y., Neville, A., Dowson, D., Williams, S., et al., Effect of metallic nanoparticles on the biotribocorrosion behaviour of Metal-on-Metal hip prostheses. *Wear* 2009, 267, 683–688.
- [116] Wimmer, M.A., Sprecher, C., Hauert, R., Täger, G., et al., Tribochemical reaction on metal-on-metal hip joint bearings. *Wear* 2003, 255, 1007–1014.
- [117] Espallargas, N., Fischer, A., Igual Muñoz, A., Mischler, S., et al., In-situ generated tribomaterial in metal/metal contacts: Current understanding and future implications for implants. *Biotribology* 2017, 10, 42–50.
- [118] Zeng, P., Rana, A., Thompson, R., Rainforth, W., Subsurface characterisation of wear on mechanically polished and electro-polished biomedical grade CoCrMo. *Wear* 2015, 332–333, 650–661.
- [119] Pourzal, R., Theissmann, R., Williams, S., Gleising, B., et al., Subsurface changes of a MoM hip implant below different contact zones. *Journal of the Mechanical Behavior of Biomedical Materials* 2009, 2, 186–191.
- [120] Wimmer, M.A., Loos, J., Nassutt, R., Heitkemper, M., et al., The acting wear mechanisms on metal-on-metal hip joint bearings: in vitro results. *Wear* 2001, 250, 129–139.
- [121] Herrera Hernández, H., M. Ruiz Reynoso, A., C. Trinidad González, J., O. González Morán, C., et al., Electrochemical Impedance Spectroscopy (EIS): A Review Study of Basic Aspects of the Corrosion Mechanism Applied to Steels, in: El-Azazy, M., Min, M., Annus, P. (Eds.), *Electrochemical Impedance Spectroscopy*, IntechOpen, 2020.

- [122] Oechsner, H. (Ed.), Thin Film and Depth Profile Analysis, Springer Berlin Heidelberg, Berlin, Heidelberg 1984.
- [123] Mischler, S., Mathieu, H.J., Landolt, D., Investigation of a passive film on an iron–chromium alloy by AES and XPS. *Surf. Interface Anal.* 1988, 11, 182–188.
- [124] Igual Munoz, A., Espallargas, N., Mischler, S., Tribocorrosion, Springer International Publishing, Cham 2020.
- [125] Hang, R., Ma, S., Ji, V., Chu, P.K., Corrosion behavior of NiTi alloy in fetal bovine serum. *Electrochimica Acta* 2010, 55, 5551–5560.
- [126] Lavos-Valereto, I.C., Wolyneć, S., Ramires, I., Guastaldi, A.C., et al., Electrochemical impedance spectroscopy characterization of passive film formed on implant Ti–6Al–7Nb alloy in Hank’s solution. n.d., 5.
- [127] Aziz-Kerrzo, M., Conroy, K.G., Fenelon, A.M., Farrell, S.T., et al., Electrochemical studies on the stability and corrosion resistance of titanium-based implant materials. *Bio-materials* 2001, 22, 1531–1539.
- [128] Yu, W., Qiu, J., Zhang, F., In vitro corrosion study of different TiO<sub>2</sub> nanotube layers on titanium in solution with serum proteins. *Colloids and Surfaces B: Biointerfaces* 2011, 84, 400–405.
- [129] Souza, M.E.P., Lima, L., Lima, C.R.P., Zavaglia, C.A.C., et al., Effects of pH on the electrochemical behaviour of titanium alloys for implant applications. *J Mater Sci: Mater Med* 2009, 20, 549–552.
- [130] Robin, A., Meirelis, J.P., Influence of fluoride concentration and pH on corrosion behavior of titanium in artificial saliva. *J Appl Electrochem* 2007, 37, 511–517.
- [131] Rämö, J., Saarinen, K., Sillanpää, M., Uniform corrosion of titanium in alkaline hydrogen peroxide conditions: influence of transition metals and inhibitors calcium and silicate. *Materials and Corrosion* 2002, 53, 898–901.
- [132] Bao, Y., Kudo, T., Cao, S., Igual Munoz, A., et al., Passivation Charge Density of CoCrMo Alloy in Different Aqueous Solutions. *J Bio Tribo Corros* 2020, 6, 58.
- [133] Valero Vidal, C., Olmo Juan, A., Igual Muñoz, A., Adsorption of bovine serum albumin on CoCrMo surface: Effect of temperature and protein concentration. *Colloids and Surfaces B: Biointerfaces* 2010, 80, 1–11.
- [134] Valero Vidal, C., Igual Muñoz, A., Electrochemical characterisation of biomedical alloys for surgical implants in simulated body fluids. *Corrosion Science* 2008, 50, 1954–1961.
- [135] J.L. Genilloud, A. Igual Muñoz, S. Mischler, Influence of different sterilization methods on the corrosion behaviour of biomedical alloys. *In Progress* n.d.



- [136] Tamilselvi, S., Murugaraj, R., Rajendran, N., Electrochemical impedance spectroscopic studies of titanium and its alloys in saline medium. *Materials and Corrosion* 2007, 58, 113–120.
- [137] Shinagawa, T., Garcia-Esparza, A.T., Takanabe, K., Insight on Tafel slopes from a microkinetic analysis of aqueous electrocatalysis for energy conversion. *Sci Rep* 2015, 5, 13801.
- [138] Movasaghi, Z., Rehman, S., ur Rehman, Dr.I., Fourier Transform Infrared (FTIR) Spectroscopy of Biological Tissues. *Applied Spectroscopy Reviews* 2008, 43, 134–179.
- [139] Rege, S.U., Yang, R.T., A novel FTIR method for studying mixed gas adsorption at low concentrations: H<sub>2</sub>O and CO<sub>2</sub> on NaX zeolite and  $\gamma$ -alumina. *Chemical Engineering Science* 2001, 56, 3781–3796.
- [140] Chen, Z., Wu, D., Monodisperse BSA-conjugated zinc oxide nanoparticles based fluorescence sensors for Cu<sup>2+</sup> ions. *Sensors and Actuators B: Chemical* 2014, 192, 83–91.
- [141] Haxaire, K., Maréchal, Y., Milas, M., Rinaudo, M., Hydration of polysaccharide hyaluronan observed by IR spectrometry. I. Preliminary experiments and band assignments: IR Observation of HA Hydration. I. *Biopolymers* 2003, 72, 10–20.
- [142] Dreissig, I., Machill, S., Salzer, R., Krafft, C., Quantification of brain lipids by FTIR spectroscopy and partial least squares regression. *Spectrochimica Acta Part A: Molecular and Biomolecular Spectroscopy* 2009, 71, 2069–2075.
- [143] Derenne, A., Vandersleyen, O., Goormaghtigh, E., Lipid quantification method using FTIR spectroscopy applied on cancer cell extracts. *Biochimica et Biophysica Acta (BBA) - Molecular and Cell Biology of Lipids* 2014, 1841, 1200–1209.
- [144] Oliviero, F., Frallonardo, P., Peruzzo, L., Ramonda, R., et al., Evidence of Silicon Dioxide Crystals in Synovial Fluid of Patients with Osteoarthritis. *The Journal of Rheumatology* 2008, 35(6), 1092–5.
- [145] Castle, J.E., Practical surface analysis by Auger and X-ray photoelectron spectroscopy. D. Briggs and M. P. Seah (Editors). John Wiley and Sons Ltd, Chichester, 1983, 533 pp., £44.50. *Surf. Interface Anal.* 1984, 6, 302–302.
- [146] Milošev, I., Kosec, T., Strehblow, H.-H., XPS and EIS study of the passive film formed on orthopaedic Ti–6Al–7Nb alloy in Hank's physiological solution. *Electrochimica Acta* 2008, 53, 3547–3558.
- [147] Nie, B., Stutzman, J., Xie, A., A Vibrational Spectral Maker for Probing the Hydrogen-Bonding Status of Protonated Asp and Glu Residues. *Biophysical Journal* 2005, 88, 2833–2847.
- [148] Kong, J., Yu, S., Fourier Transform Infrared Spectroscopic Analysis of Protein Secondary Structures. *Acta Biochim Biophys Sinica* 2007, 39, 549–559.

- [149] Chittur, K.K., FTIR/ATR for protein adsorption to biomaterial surfaces. *Biomaterials* 1998, 19, 357–369.
- [150] Derfus, B.A., Kurian, J.B., Butler, J.J., Daft, L.J., et al., The High Prevalence of Pathologic Calcium Crystals in Pre-operative Knees. *The Journal of Rheumatology* n.d., 5.
- [151] Yavorsky, A., Hernandez-Santana, A., McCarthy, G., McMahon, G., Detection of calcium phosphate crystals in the joint fluid of patients with osteoarthritis – analytical approaches and challenges. *Analyst* 2008, 133, 302.
- [152] MacMullan, P., McMahon, G., McCarthy, G., Detection of basic calcium phosphate crystals in osteoarthritis. *Joint Bone Spine* 2011, 78, 358–363.
- [153] Nalbant, S., Martinez, J.A.M., Kitumnuaypong, T., Clayburne, G., et al., Synovial fluid features and their relations to osteoarthritis severity: new findings from sequential studies. *Osteoarthritis and Cartilage* 2003, 11, 50–54.
- [154] Rosenthal, A.K., Update in calcium deposition diseases. *Current Opinion in Rheumatology* 2007, 19, 158–162.
- [155] Molloy, E.S., McCarthy, G.M., Calcium Crystal Deposition Diseases: Update on Pathogenesis and Manifestations. *Rheumatic Disease Clinics of North America* 2006, 32, 383–400.
- [156] F. Barrere, M. M.E. Snel, C. A. van Blitterswijk, K. Groot, et al., Nano-scale study of the nucleation and growth of calcium phosphate coating on titanium implants. *Biomaterials* 2004, 25, 2901–2910.
- [157] Alla, R.K., Ginjupalli, K., Upadhy, N., Shammash, M., et al., Surface Roughness of Implants: A Review. n.d., 7.
- [158] Sivakumar, B., Pathak, L.C., Singh, R., Role of surface roughness on corrosion and fretting corrosion behaviour of commercially pure titanium in Ringer's solution for bio-implant application. *Applied Surface Science* 2017, 401, 385–398.
- [159] Arslan, E., Totik, Y., Demirci, E., Alsaran, A., Influence of Surface Roughness on Corrosion and Tribological Behavior of CP-Ti After Thermal Oxidation Treatment. *J. of Materi Eng and Perform* 2010, 19, 428–433.
- [160] Chi, G., Yi, D., Liu, H., Effect of roughness on electrochemical and pitting corrosion of Ti-6Al-4V alloy in 12 wt.% HCl solution at 35 °C. *Journal of Materials Research and Technology* 2020, 9, 1162–1174.
- [161] Cheng, X., Roscoe, S.G., Influence of Surface Polishing on the Electrochemical Behavior of Titanium. *Electrochem. Solid-State Lett.* 2005, 8, B38.
- [162] Olsson, C.-O.A., Igual-Muñoz, A.N., Mischler, S., Adsorption of organic matter on titanium surfaces with nano- and micro-scale roughness studied with the electrochemical quartz crystal microbalance dissipation technique. *Biointerphases* 2021, 16, 051001.

- [163] Kim, S.K., Park, I.J., Lee, D.Y., Kim, J.G., Influence of surface roughness on the electrochemical behavior of carbon steel. *J Appl Electrochem* 2013, 43, 507–514.
- [164] Lucas, L.C., Buchanan, R.A., Lemons, J.E., Investigations on the galvanic corrosion of multialloy total hip prostheses. *J. Biomed. Mater. Res.* 1981, 15, 731–747.
- [165] Soares, F.M.S., Elias, C.N., Monteiro, E.S., Coimbra, M.E.R., et al., Galvanic Corrosion of Ti Dental Implants Coupled to CoCrMo Prosthetic Component. *International Journal of Biomaterials* 2021, 2021, 1–11.
- [166] Geng, H., Zhang, D., Chen, K., Wang, Q., Galvanic corrosion behavior between Ti6Al4V and CoCrMo alloys in saline solution. *Mat Express* 2014, 4, 213–220.
- [167] Mellado-Valero, A., Muñoz, A., Pina, V., Sola-Ruiz, M., Electrochemical Behaviour and Galvanic Effects of Titanium Implants Coupled to Metallic Suprastructures in Artificial Saliva. *Materials* 2018, 11, 171.
- [168] Cortada, M., Giner, L., Costa, S., Gil, F.J., et al., Galvanic corrosion behavior of titanium implants coupled to dental alloys. n.d., 7.
- [169] Jia, J.X., Song, G., Atrens, A., Influence of geometry on galvanic corrosion of AZ91D coupled to steel. *Corrosion Science* 2006, 48, 2133–2153.
- [170] Arslan, H., Çelikkan, H., Örneç, N., Ozan, O., et al., Galvanic corrosion of titanium-based dental implant materials. *J Appl Electrochem* 2008, 38, 853–859.
- [171] Songür, M., Çelikkan, H., Gökmeşe, F., Şimşek, S.A., et al., Electrochemical corrosion properties of metal alloys used in orthopaedic implants. *J Appl Electrochem* 2009, 39, 1259–1265.
- [172] Höök, F., Vörös, J., Rodahl, M., Kurrat, R., et al., A comparative study of protein adsorption on titanium oxide surfaces using in situ ellipsometry, optical waveguide lightmode spectroscopy, and quartz crystal microbalance/dissipation. *Colloids and Surfaces B: Biointerfaces* 2002, 24, 155–170.
- [173] G Sauerbrey, Verwendung von Schwingquarzen zur Wägung dünner Schichten und zur Mikrowägung. *Zeitschrift Für Physik* 1959, 155, 206–222.
- [174] Galliano, F., Olsson, C.-O.A., Landolt, D., Flow Cell for EQCM Adsorption Studies. *J. Electrochem. Soc.* 2003, 150, B504.
- [175] Keiji Kanazawa, K., Gordon, J.G., The oscillation frequency of a quartz resonator in contact with liquid. *Analytica Chimica Acta* 1985, 175, 99–105.
- [176] Vergé, M.-G., In-situ electrochemical quartz crystal microbalance studies of anodic film growth on valve metals. 2005.
- [177] Ullevig, D.M., Evans, J.F., Albrecht, M.Grant., Effects of stressed materials on the radial sensitivity function of a quartz crystal microbalance. *Anal. Chem.* 1982, 54, 2341–2343.

- [178] Kelly, J.J., Rahman, K.M.A., West, A.C., Effect of Current Distribution on Quartz Crystal Microbalance Measurements. *J. Electrochem. Soc.* 1998, *145*, 7.
- [179] Kern, P., Landolt, D., Adsorption of organic corrosion inhibitors on iron in the active and passive state. A replacement reaction between inhibitor and water studied with the rotating quartz crystal microbalance. *Electrochimica Acta* 2001, *47*, 589–598.

## Curriculum Vitae

Yueyue Bao  
Chemin des Triaudes 4C,  
1024 Ecublens VD, Switzerland

+41782550811  
[linkedin.com/in/ybao93](https://www.linkedin.com/in/ybao93)

### EDUCATION

---

PhD study in Institute of Materials Oct 2018 - Jan 2023  
*Swiss Federal Institute of Technology Lausanne (EPFL)* *Lausanne, Switzerland*

Thesis on in-vivo investigation of electrochemical reactions of Ti and CoCrMo alloy in human synovial fluids

M.E. Degree in Materials Science and Engineering Sep 2015- Jan 2018  
*University of Science and Technology Beijing (USTB)* *Beijing, China*

Thesis on tribological properties and lubricating mechanism of SiO<sub>2</sub> nanoparticles in water-based fluids.

B.E. Degree in Mechanics and Materials Sep 2011 - Apr 2015  
*Hohai University (HHU)* *Nanjing, China*

### PUBLICATIONS

---

- **Bao Y Y**, Munoz AI, Olsson COA, Mischler S. Surface Analysis of Ti Samples Exposed to in-vivo Synovial Fluids. In progress.
- **Bao Y Y**, Munoz AI, Olsson COA, Jolles BM, Mischler S. The electrochemical behaviour of Ti in human synovial fluids. *Materials*, 2022 Feb 25;15(5):1726.
- **Bao Y**, Kudo T, Cao S, Munoz AI, Mischler S. Passivation charge density of CoCrMo alloy in different aqueous solutions. *Journal of Bio-and Tribo-Corrosion*. 2020 Jun;6(2):1-0.
- **Bao Y Y**, Sun J L, Kong L H. Effects of nano-SiO<sub>2</sub> as water-based lubricant additive on surface qualities of strips after hot rolling. *Tribology International*, 2017, 114: 257-263.
- **Bao Y Y**, Sun J L, Kong L H. Tribological properties and lubricating mechanism of SiO<sub>2</sub> nanoparticles in water-based fluid [C]//IOP Conference Series: Materials Science and Engineering. IOP Publishing, 2017, 182(1): 012025.
- Kong L H, Sun J L, **Bao Y Y**. Preparation, characterization and tribological mechanism of nanofluids. *RSC Advances*, 2017, 7(21): 12599-12609.
- Kong L H, Sun J L, **Bao Y Y**, et al. Effect of TiO<sub>2</sub> nanoparticles on wettability and tribological performance of aqueous suspension. *Wear*, 2017, 376: 786-791.

- Kong L H, Sun J L, **Bao Y Y**. Research on the physicochemical and tribological properties of nano-TiO<sub>2</sub> in the aqueous rolling liquid. Tribology-Materials, Surfaces & Interfaces, 2016, 10(4): 172-177.

## PATIENTS

---

- Jianlin Sun, **Yueyue Bao**, Linghui Kong et al. A water-based rolling liquid containing nano-SiO<sub>2</sub> and its preparation method. [CN106635359A]

## HONORS, AWARDS & SCHLARSHIPS

---

- China Scholarship for Studying Abroad
- National Scholarship, USTB
- Miyoshi Outstanding Graduate Student, USTB

## CONFERENCE

---

- Eurocorr 2022 Tribocorrosion, August 28th - September 2nd, 2022, Berlin, Germany. “Galvanic corrosion between Ti and CoCrMo alloy in human synovial fluids”.
- ICC INTERCORR WCO 2021, July 20th - 23rd, 2021, Brazil. “In-vivo investigation of electrochemical reactions of Ti in human synovial fluids”.
- Swiss Corrosion Science Day 2020, Corrosion Research: Challenges, Opportunities and Applications, March 3, 2020, Empa, Switzerland. “Coupling titanium and CoCr alloys in bio-medical implants: which risk of galvanic corrosion?”
- Eurocorr 2019 Tribocorrosion, September 9th -13th, 2019, Seville, Spain. “Passivation Charge Density of CoCrMo Alloy in Different Aqueous Solutions”.

## PROFESSIONAL SKILLS

---

- Master and usage of: NOVA/IVIUM electrochemical workstation, Electrochemical impedance spectroscopy (EIS), Electrochemical quartz crystal microbalance (EQCM)
- Master and usage of surface techniques: SEM/EDX, FTIR, XPS, AES, Profilometer (KEYENCE)
- Microsoft Office                      Origin                      MultiPAK                      ImageJ

## Languages

---

Chinese: Native language

English: Fluent

French: A1

